DISSERTATION / DOCTORAL THESIS

Titel der Dissertation / Title of the Doctoral Thesis

„Advanced membrane architectures for multimode optomechanics“

verfasst von / submitted by

Dipl.-Phys. Claus-Markus Gärtner

angestrebter akademischer Grad / in partial fulfilment of the requirements for the degree of

Doktor der Naturwissenschaften (Dr. rer. nat.)

Wien, 2020 / Vienna 2020

Studienkennzahl lt. Studienblatt / degree programme code as it appears on the student record sheet:	A 796 605 411
Dissertationsgebiet lt. Studienblatt / field of study as it appears on the student record sheet:	Physik
Betreut von / Supervisor:	Univ.-Prof. Dr. Markus Aspelmeyer

ADVANCED MEMBRANE ARCHITECTURES FOR MULTIMODE OPTOMECHANICS

A WALTZ WITH LIGHT IN THREE VERSES

CLAUS-MARKUS GÄRTNER
University of Vienna
Faculty of Physics
Quantum Optics, Quantum Nanophysics and Quantum Information
Aspelmeyer Group

Claus-Markus Gärtner: *Advanced membrane architectures for multimode optomechanics,* © March 17, 2020

To my mum, the most precious and loving soul

To all my teachers

It doesn't interest me what you do for a living.
I want to know what you ache for –
and if you dare to dream of meeting your heart's longing.
It doesn't interest me how old you are.
I want to know if you will risk looking like a fool –
for love – for your dreams – for the adventure of being alive.

— Oriah Mountain Dreamer

PREFACE

It was early 2012, I was graduating with a Diploma in physics – slightly more than seven years ago – it should mark the start of an incredible journey with many unexpected yet interesting and rewarding outcomes along the road. Thinking back about that time, I can confidently say now that quite a lot has changed, if not even going further in saying *everything has changed*. Back then, I just decided to not stay back at home, pursuing a PhD where I graduated – even though I had the chance to do so. I was standing there without any idea of where life would take me, just at the moment when I thought I was ready for it to accelerate. The decision to trust my feeling and being brave enough to follow up on it, is what lead me on this great journey that I am about to tell. The ship was ready to sail, I just needed to get onboard. Sometimes – as I start to believe very often even so – life unfolds in interesting and unexpected ways whilst the name of the game is surrendering to where life takes us without letting our minds get in the way of how it should play out.

I was bridging the time with working in the same lab where I graduated, continuing what I loved working on: the entire process flow from the idea, to simulations, over to fabrication and finally the characterization of designed devices in order to just start the iteration process all over again, until the device performance would meet our requirements. I loved the work, it just wasn't the right thing anymore to do this back at home for another somewhat five years and I could not deny this ever so slightly increasingly loud voice in my head. And so it happened, that I stumbled upon this interesting sheet of paper hanging on the blackboard in our department advertising the field of optomechanics – seemingly combining all the aspects that I wanted in my PhD life yet to come. It was from Tobias Kippenberg's group, interestingly enough though, I would never even consider applying, let alone going there. I had found out about Markus' group in Vienna. It just felt right, and the rest... not so much.

It still took quite some time. The application process itself, visiting Vienna in November and meeting all the group members back then, figuring out how it feels to be there until the final decision was made in early 2013 that I really wanted to start working in this exciting field that combines many of the aspects that triggered my interest in the first place. The stage was set for an amazing somewhat five years of dedicated work and contributions to the field. Little did I know, life again had different plans for me. Vienna only had me for more or less one and a half years, before my ship was taking turns. The part of working in the clean room was always the one I would look forward to the most, yet Vienna turned out to not be the right place for this endeavor. I started working with Garrett – who used to be the fab guy in our group up until the point when he moved back to Santa Barbara, CA, USA. I cannot deny that living and working in Santa Barbara was something I would have expected but boy was it a pleasant surprise. Later on, we decided to continue working together with Simon's group in Delft, the Netherlands – one of Markus' former students with already existing strong collaborations. As you can imagine, leaving California for the – assuming – rainy Netherlands was not something I would look forward to, but it was the right choice at that time and it surely not only became the phase of my life that this whole dissertation is based on but it also became my home.

Traveling back in time in my memories over the past somewhat seven years, yes, I can definitely say that everything has changed. I left what I called my home for all my life in order to explore the world and put myself on this journey towards not only becoming a doctor, but merely a new person. It was surely not the journey of what most PhD students would experience – which is always true since the personal journey is unique for each and everyone. It is only much later on that we see how the dots connect, whereas during our travels we *just* cannot see but need to trust it is for our greater good. Maybe this is an easy one to say for me, as we do not have control over it anyways and what is there to do if all we need to do is giving up control over the things we cannot control? We don't get to choose another outcome, we don't get a second chance going back in time to make a different decision. It is always about making decisions in the now, the present moment, confidently living with the decisions made, taking responsibility for them and – if desired – adapt so that we can meet our dreams, visions and create different outcomes. My journey is unique in many ways, with outcomes and turns I was not able to foresee that certainly have lead me towards a new me that I was meant to become. It was a journey on which I have met many new friends, colleagues and special people that helped me becoming a better person and scientist. I am grateful for that, but much more am I thankful for the personal growth that is undeniably linked to each and everyone that I had the pleasure to cross paths with. It means everything to me, more than anything else. I don't think, personal growth and scientific maturing can hardly be separated anyways as we – again – make decisions in our life as a scientist as the person we are. We always get to choose, if we grow beyond what life throws at us, if we accept the situations and oftentimes challenges that come along with it, or if we resist. I have never been good at resisting what I felt was the right thing to do, no matter what I was being told or meant to do. But understanding, that the right thing to do for one person can be a total different thing from someone's else perspective, is something important to be aware of. It takes – most of all – compassion, empathy and understanding for each other, for the complexity of life itself in order to smoothly sail through this – at times – stormy and furious sea called life. It is not only the communication with oneself but also with others that we need to lead recklessly, honestly and fearlessly, expressing what is important to us making sure we stay true to ourselves on the path that we are walking with others, while not forgetting that we stay gentle and kind in a world full of competitiveness. I hope to maintain and never forget what it means to see the human being first above all, to never forget to reflect on my actions and thoughts and to always be my authentic true self while respecting all of life.

We think too much and feel too little.
More than machinery, we need humanity.
More than cleverness, we need kindness and gentleness.

— Charlie Chaplin

Delft, May 2019

ABSTRACT

Cavity optomechanics studies the interactions between light and mechanical motion. Its advancements are intrinsically linked to the fabrication of novel devices with superior optical and mechanical properties. Driving mechanical systems into the quantum regime requires the optomechanical coupling to enter the regime of strong cooperativity, in which the cavity-enhanced coherent coupling rate exceeds both the optical and mechanical decoherence rates.

Recent efforts have focused predominantly on employing thin membranes, which can feature small decoherence rates. The coupling strength in these macroscopic optomechanical systems, however, is inherently weak. Additionally, when clamped in optical cavities, membranes are susceptible to acoustic radiation loss, which ultimately precludes obtaining full coherent quantum control of these macroscopic objects.

In this thesis, we overcome the challenge of clamping-induced acoustic radiation loss by fabricating phononic bandgap structures that decouple the membrane modes from the environment. Our square membranes of 350 µm in side length exhibit mechanical frequencies above 1 MHz, a crucial feature in order to minimize effects of classical laser noise. We measure consistently high, clamping-independent quality factors of 2×10^6 (7×10^6) at room (cryogenic) temperature for all modes within the designed bandgap that are now intrinsically limited by the membrane dimensions and thin-film quality. This enables the optomechanical system to enter the multimode strong cooperativity regime provided sufficient laser power. This paves the way towards the observation of quantum effects such as stationary entanglement between light and mechanics.

In a second approach towards accomplishing strong cooperativity we focus on increasing solely the coupling strength. Optomechanical arrays consisting of photonic crystal membranes constitute ideal candidates for this endeavor. These arrays promise coupling enhancements by orders of magnitude, depending on the cavity array finesse and length. Here we realize double-membrane arrays consisting of two high-reflectivity SiN membranes monolithically fabricated on a single chip.We characterize the optical spectra and losses of these 200 µm long Fabry-Pérot cavities, measuring finesse values of up to 140, currently limited by diffraction losses due to their plane-parallel configuration. We demonstrate coupling enhancements for the center-of-mass mode with respect to the single-membrane case. When operated on

resonance, thus addressing the collective breathing mode, these arrays promise cooperativity enhancements of four orders of magnitude for our current system parameters.

Combining both approaches of simultaneously increasing the coupling strength whilst maintaining membranes of consistently low decoherence paves the way towards obtaining full coherent quantum control of these massive mechanical objects.

ZUSAMMENFASSUNG

Optomechanik studiert die Wechselwirkungen zwischen Licht und mechnischer Bewegung. Ihr Fortschritt ist wesentlich mit der Herstellung neuer Bauelemente mit außergewöhnlichen optischen und mechanischen Eigenschaften verknüpft. Um mechanische Systeme in das Quanten-Regime zu bringen bedarf es optomechanischer Kopplungen, die es erlauben in das Regime starker Kooperativität einzudringen, sodass die durch den Hohlraum-Resonator erhöhte kohärente Kopplungsrate die optischen und mechanischen Dekohärenzraten übertrifft. In optomechanischen Freiraum-Experimenten lag der jüngste Fokus überwiegend auf der Verwendung von dünnen Membranen mit kleiner Dekohärenz, während die Kopplungsstärke grundsätzlich niedrig blieb. Allerdings erfahren die Membranen, sobald sie in optischen Hohlraum-Resonatoren eingebunden werden, höhere akustische Strahlungsverluste, das letztendlich das Erlangen voller Quanten-Kontrolle dieser makroskopischen Objekte verhindert.

In dieser Arbeit überwinden wir die Herausforderung der durch das Festklammern induzierten akustischen Strahlungsverluste durch die Herstellung phononischer Bandstrukturen, die die Membranmoden von der Umgebung entkoppeln. Unsere quadratischen Membranen mit 350 µm Seitenlänge weisen Eigenfrequenzen von mehr als 1 MHz auf, ein wesentliches Merkmal um Effekte klassischen Laser-Rauschens zu minimieren. Wir messen einheitlich/konsistent hohe, befestigungsunabhängige Gütefaktoren von 2×10^6 (7×10^6) bei Raumtemperatur (Tieftemperaturen) für alle Moden innerhalb der konzipierten Bandlücke, welche nun intrinsisch durch die Membrandimensionen und Materialqualität bestimmt sind. Damit ist es nun möglich das starke Kooperativitäten-Regime für eine Vielzahl an Moden zu erreichen, das den Weg zu der Beobachtung von Quanteneffekten, wie zum Beispiel der stationären Verschränkung zwischen Licht und Mechanik, bereitet.

In einem zweiten Ansatz zum Erreichen starker Kooperativitäten zielt auf der alleinigen Erhöhung der Kopplungsstärke ab. Optomechanische Arrays bestehend aus Photonischen Kristall Membranen stellen

optimale Kandidaten für dieses Bestreben dar. Diese Arrays versprechen Kopplungserhöhungen mehrerer Größenordnungen, was von der Länge und Finesse des Arrays abhängt. Wir realisieren Doppel-Membran-Arrays, bestehend aus zwei hoch-reflektierenden Silizium-Nitrid Membranen, die monolithisch aus einem einzigen Chip fabriziert wurden. Wir charakterisieren die optischen Spektren und Verluste dieser 200 µm langen Fabry-Pérot Hohlräume und messen Finesse-Werte von bis zu 140, welche gegenwährtig durch Beugungsverluste aufgrund ihrer planparallelen Anordnung limitiert sind. Wir demonstrieren Kopplungserhöhungen für die Massenschwerpunkts-Mode im Vergleich zu dem Fall mit einer einzelnen Membran. Wenn diese Arrays auf Resonanz betrieben und damit die relative Kollektivbewegung beider Membranen ausgenutzt wird, dann versprechen diese Arrays Erhöhungen der Kooperativität von ungefähr vier Größenordnungen mit unseren derzeitigen Systemparametern.

Die Kombination beider Strategien sowohl die Kopplungsstärke signifikant zu erhöhen, als auch konsistent niedrige Dekohärenzraten zu gewährleisten, ebnet möglicherweise den Weg volle, kohärente Quantenkontrolle dieser massiven, makroskopischen mechanischen Objekte zu erlangen.

PUBLICATIONS

[1] Maximilian Bückle, Valentin C. Hauber, Garrett D. Cole, **Claus Gärtner**, Ute Zeimer, Jörg Grenzer, and Eva M. Weig. “Stress control of tensile-strained In1-xGaxP nanomechanical string resonators.” In: *Applied Physics Letters* 113.20 (Nov. 2018), p. 201903. ISSN: 00036951. DOI: 10.1063/1.5054076. URL: http://aip.scitation.org/doi/10.1063/1.5054076.

[2] Garrett D. Cole, Pen Li Yu, **Claus Gärtner**, Karoline Siquans, Ramon Moghadas Nia, Jonas Schmöle, Jason Hoelscher-Obermaier, Thomas P. Purdy, Witlef Wieczorek, Cindy A. Regal, and Markus Aspelmeyer. “Tensile-strained InxGa1-xP membranes for cavity optomechanics.” In: *Applied Physics Letters* 104.20 (May 2014), p. 201908. ISSN: 00036951. DOI: 10.1063/1.4879755. URL: http://aip.scitation.org/doi/10.1063/1.4879755.

[3] Moritz Forsch, Robert Stockill, Andreas Wallucks, Igor Marinković, **Claus Gärtner**, Richard A. Norte, Frank van Otten, Andrea Fiore, Kartik Srinivasan, and Simon Gröblacher. “Microwave-to-optics conversion using a mechanical oscillator in its quantum ground state.” In: *Nature Physics* (Oct. 2019), pp. 1–6. ISSN: 1745-2473. DOI: 10.1038/s41567-019-0673-7. arXiv: 1812.07588.

[4] **Claus Gärtner**, João P. Moura, Wouter Haaxman, Richard A. Norte, and Simon Gröblacher. “Integrated Optomechanical Arrays of Two High Reflectivity SiN Membranes.” In: *Nano Letters* 18.11 (Nov. 2018), pp. 7171–7175. ISSN: 1530-6984. DOI: 10.1021/acs.nanolett.8b03240. arXiv: 1809.06372. URL: http://pubs.acs.org/doi/10.1021/acs.nanolett.8b03240.

Thankfulness is the beginning of gratitude.
Gratitude is the completion of thankfulness.
Thankfulness may consist merely of words.
Gratitude is shown in acts.

— Henri Frederic Amiel

ACKNOWLEDGMENTS

'*Gratitude is the completion of thankfulness. Thankfulness may consist merely of words*'. I wish my words to be understood as genuinely felt words from the bottom of my heart. I hope that the following lines resonate as much with you as they did with me when I was putting them down on paper. May my deep gratitude reach all of you – spoken, written and felt.

Without a doubt, the work presented in this thesis would have not been possible without the help of many that have significantly contributed to the success in one way or another. Truly, I am thankful for every even so little contribution made and support provided.

If I had to pick one of your many qualities that I learned to appreciate over the years, it would be your ability to motivate people intrinsically such that it never felt they should work *for* you but rather *with* you on an exciting project of sheer endless possibilities. Whenever we personally met after what felt like eons there was a genuine and heart-warm felt welcoming which of course was due to the fact that I was everywhere but in Vienna. I not only feel truly blessed with you as my (official) supervisor but even more so I feel grateful for the person I was allowed to get to know on a personal level. Your efforts to provide the best possible work environment for me to pursue my research interests and giving me room to develop my skills – despite all the upcoming challenges – will always stick out to me. For that, I am deeply grateful for. Thank you *Markus*!

Simon, oftentimes, I would think to myself, that there is a second Markus 'growing' up. Don't get me wrong, this is totally a good thing and I want to emphasize that you are not a copy but rather another unique person I was allowed to get to know on a personal as well as professional level. It is just, that I would recognize many of 'his' qualities in you, too, as if you had shared some of your years together – I could swear! I truly cannot thank you enough for taking me into your group as if I was one of your own students. We were always joking about me being the borrowed PhD student and quite frankly, I am totally fine with it. Not only have I personally grown tremendously over the four years with you – both as a scientist and human being – but also did I get to appreciate your sparkling and contagiously motivating personality and your great enthusiasm for science. What started as a journey of unknown duration obviously turned out to be much more than that for me. It took some time to adapt, but I truly see my four years in Delft as my real PhD – not only because (almost) everything I share in my thesis has come to life during that time, but also because it just became what it was – my home! Thank you for trusting the process, your patience that I pushed to the limits, just thank you, *Simon*, for everything!

Garrett, what can I say, thank you so much for moving back to Santa Barbara! Well, seriously 'thank you!'. Jokes aside, I am happy that you were still in Vienna when I applied. I remember vividly sitting in your office, you taking your time explaining everything in detail. I could have not wished for a better person to get started with. Your knowledge when it comes to fabrication and your ability to guide, as well as unique personality made it easy to be around and feel comfortable with. Of course, I am also more than happy that I could experience your California life with you and your personal and CMS[1] family. I also owe them my deepest gratitude. *Paula* and *Dave*! You have been always there for me in the cleanroom whenever I had immediate questions and you never got tired of taking the time! Maybe at this point, it makes sense to say thank you to the entire cleanroom staff in Santa Barbara. I was lucky to work in such a professional environment where I could focus on getting better by the day. I asked so many questions and luckily for me the support I received was outstanding. Maybe it is true what *Tom Reynolds* said when I left SB '*Sooner or later, they all come back.*'. There sure is a deep-seated, yet still dormant pull in me.

Richard, what I find most astounding about you is your seemingly never-ending overflowing motivation and passion for fabrication. Not only are you a hard-working physicist that puts ideas into reality, but also one that comes up with so many new ideas himself. If any help or feedback was needed, you always came up with an answer from the depths of your ocean of knowledge which I am very grateful for. Thank you!

Witlef, my first one and a half years in Vienna are undeniably linked to you. When we started working together on the membrane experiment, I got to come across your expertise in the field of quantum optics. You are truly an amazing personality to work with who pushed and kept the experiment running. Your guidance and also patience in the optical lab was invaluable as we would always find answers in you when things were what seemed beyond fixable. I would not say that I ever really fully warmed up to working in the optics lab, but I still today feed from all the knowledge I gained from you about quantum optics! I am also very happy that you got the chance to start your own group now where you can pass on your knowledge to future generations. Thank you!

---

[1] https://www.crystallinemirrors.com/

Jason and *Ramon*, you turned out to be the soul of the membrane experiment. *Jason*, I truly admire you for your work ethics and the humble and pure person you are. It was a true blessing working with and learning from you. *Ramon*, very similar to my situation, it seems at some point Vienna became what Delft turned out to be for me. I still remember us measuring mechanical Q factors right before the Christmas Quantum Party in Vienna, which we of course joined much later because of that. I wanna thank you for – eventually – making use of the phononic shield membranes, providing me with valuable data for my thesis. *Josh*, a little bit of the outcast on the already sinking ship. You joined the membrane experiment at the very end, trying to reach land when the ship was already drowning. Your guidance was much needed and your efforts in communicating between the various parties are the credits belonging to you. *Corentin*, our guy who does magic to the raw data! Your magic is – still – very much needed and I believe(d) in you. Now that a little bit more time has passed, I am happy that you finally published a paper on the efforts put in. It is well-deserved! In addition, I wanna thank all the students that have worked with us on this project. In particularly, *Thomas Zauner*, for his significant contributions to the entire team. Personally, the simulations for the double membrane structures have greatly benefited from his early coding work.

A special thanks goes out to *Ramon*, *Josh*, *Jonas*, *Florian* (where is this guy even) and of course *Philipp*. What do you guys all have in common? Exactly, you surprised me with a birthday visit in Amsterdam in the most amazing way possible (I will just assume it was not self-interest at all). It is such a fond memory that I love dwelling in whenever I think back to my first half year of my Delft experience. I should have known that something was fishy when *Philipp* – selflessly – offered to take care of accommodation even though Amsterdam was my hood now. Plus, I was really getting annoyed that everyone always wanted to see Amsterdam over Delft. Funnily, it took *Philipp* another three years to finally make it to Delft for arguments I thought would never be a winning argument. It should be mentioned here as well – just to rub it under your nose – that even *Josh* made it to Delft much sooner, even though for different reasons.

As being part of the Aspelmeyer group for so long, I came across so many wonderful people. For those sharing my first two years with me I want to make sure you all know how much you contributed to this beautiful work environment. To those that arrived later after I had 'abandoned' Vienna, I should have come up with a better story, something along the lines of 'Cast away'. Stranded on an lonely island, doing fabrication and, yet here is this guy graduating out of nowhere. What a legend! Thanks to all the Aspels! Never forgotten shall be our theory guy *Hofi*, the levitation people *Uros* (Thank you so so much for showing me Belgrade and being part of your wedding. I feel truly blessed having been part of it!) and *David*, pulsed peeps *Ralf* and *Sungkun*, the BigG octopuses *Hans*, *Tobias*, *Jeremias* and *Mathias* – this project was painful I have to admit, but nevertheless, I am very happy to hear that results are coming along.

João, what can I say. Of course, we could not know in the beginning we would share the entirety of our PhD lives together. I want to thank you for having been a constant for me in Delft. Your wisdom and maturity paired with your work ethics were very inspiring to be around. I, in particularly, want to express my gratitude towards you putting all your efforts into our common scientific goals. I am proud of the results that we have achieved together on the double membranes and you are such an invaluable part of it all. Thank you!

In general, I felt very welcomed by each and everyone in Delft which should not be taken for granted. All of my fellow colleagues in Simon's group have become wonderful companions of my scientific journey, some even more than that. I want to thank all of you, especially *Rob* and *Moritz* who have become far more than just coffee buddies – even though I stopped drinking coffee in the end. *Maarten* for introducing me to Jenever and appeltaart met slagroom. *Igor* for being always true to his authentic self, something I appreciate so much in you and humans in general. *Andreas*, the stoic, hard-working Schwarzwald ambassador for sharing all your knowledge.

Thank you all of the Kavli Nanolab Delft without whom cleanroom work would have not been as smooth. In particularly, I want to give credit to *Marc*, *Arnold* and *Marco* who I have worked most closely together with and who supported me by keeping the tools running – let us just quietly forget about the III-V etcher, *Marco*.

I also want to thank my collaborators in Konstanz, Germany. Especially *Maximilian* in the group of *Eva M. Weig* who has significantly contributed to a better understanding about the nasty and everlastingly stubborn InGaP structures which has lead to a jointly published paper under your lead role!

Thanks everyone for proof-reading parts of my thesis. Without you, it would have been an impossible endeavor that I cannot give enough credit to (amongst others): *Witlef*, *Garrett*, *Bas*, *Moritz*, *Matthijs*, *Rodrigo*, *Maximilian* and of course *Simon* and *Markus*, thank you so much! A special thanks in that regard goes out to *Rob* who literally pushed me over the finish line and has been of invaluable support when it was needed the most.

Las but certainly not least, my deepest gratitude goes out to those who tirelessly supported and maybe more importantly taught me invaluable life lessons. This goes out to a handful of people whose contributions to my success are beyond what words can describe. Among them my dear *family*, especially my *mum* who I love endlessly for all the showers of love she gives to this world. *Rose*, who has become more than just my beacon in the dark, who certainly molded me into the person I have become and has always been there for me in ways no one else could. *T.A.F.*, you left a mark on me during the first part of my PhD like no other. Your shared wisdom and knowledge, compassion and empathy, the way you taught me about love and life. Your existence simply makes this world a better place. Thank you for your patience and love beyond time and space, even though very challenging and yet rewarding at times! *Willemijn*, you have always been part of my Delft life in one way or another. What started with being colleagues in the cleanroom has lead to living and enjoying life with you in the most wonderful way. I love your sparkling nature towards science and life itself besides your 'overly' serious – and for me very enjoyable – approach to most things you do. You have taught me so much in ways I could not foresee, which I am truly grateful for and are of immeasurable value to me. You shine your light in a way that not only makes me smile from the inside but also everyone around you!

I can truly say that – after all – I am content with the past seven years and more than grateful for experiencing life the way it unfolded. I thank life itself, for its lessons, challenges, and the ups and downs. I am grateful for the challenges within which gently or forcefully molded me into who I am today. I could not feel any more grateful for this life that I am allowed to live. I wished everyone could feel the warmth radiating outwards from the bottom of my heart. I have plenty to give and will try to continue giving in a world that asks us to be more gentle to each other, in a world that requires us to remind ourselves that being human is greater than any personal achievements to be reached. I have this deeply felt wish for us to walk alongside with mutual compassion, empathy, understanding and joy for one another.

Develop an attitude of gratitude,
and give thanks for everything that happens to you,
knowing that every step forward
is a step toward achieving something bigger
and better than your current situation.

— Brian Tracy

And so I wanna conclude – according to one of my favorite quotes – what is essential is invisible to the eye. May you all feel my deepest gratitude!

It is only with the heart that one can see rightly;
what is essential is invisible to the eye.

— Antoine de Saint-Exupéry, The Little Prince

CONTENTS

1 INTRODUCTION 1
  1.1 Scope of this thesis 4

I THE OPTOMECHANICAL SYSTEM

2 CAVITY OPTOMECHANICS 9
  2.1 Mechanical oscillators 10
  2.2 The optical cavity 11
  2.3 Optomechanical interaction 12
  2.4 Membrane implementations 15
    2.4.1 Membrane-in-the-middle setup 15
    2.4.2 Optomechanical arrays 17
    2.4.3 Electromechanics 18
3 MICROMECHANICAL MEMBRANES 21
  3.1 Introduction 21
  3.2 Growth of high stress films 22
  3.3 Optical properties of thin films 24
  3.4 Fabrication 28
  3.5 Mechanical modes of a 2D membrane 34
  3.6 Dissipation 36
  3.7 Engineering optical and mechanical properties 40
  3.8 Conclusion 42

II MICROFABRICATED MEMBRANE ARCHITECTURES

4 PHONONIC SHIELD MEMBRANES 45
  4.1 Introduction 46
  4.2 Device design 47
    4.2.1 Phononic shield design simulations 48
  4.3 Device fabrication 52
    4.3.1 Fabrication overview 52
    4.3.2 Deep silicon etching 55
    4.3.3 DRIE process development 58
    4.3.4 A closer look on certain aspects 61
  4.4 Phononic shield membranes for electromechanics 64
    4.4.1 The choice of metal 65
    4.4.2 Metallization procedures 66
  4.5 Results and discussion 69
    4.5.1 Characterization in an optomechanical setup 69
  4.6 Conclusion and outlook 73
5 INTEGRATED OPTOMECHANICAL ARRAYS OF SIN MEMBRANES 77
  5.1 Introduction 78
  5.2 Device design 79
  5.3 Fabrication 80

- 5.4 Device characterization 84
  - 5.4.1 Device limitations 87
- 5.5 Results and discussion 98
  - 5.5.1 Optical characterization 98
  - 5.5.2 Mechanical characterization 100
  - 5.5.3 Optomechanical characterization 101
- 5.6 Conclusion and outlook 105

6 III-V TERNARY INGAP MEMBRANES FOR MULTIMODE OPTOMECHANICS 109
- 6.1 Introduction 109
- 6.2 Device design 111
  - 6.2.1 Distributed Bragg reflector 113
  - 6.2.2 Membrane array 114
  - 6.2.3 The optomechanical double-membrane-cavity system 115
  - 6.2.4 Design limitations 122
- 6.3 Fabrication 126
- 6.4 Results and discussion 129
  - 6.4.1 Dry etching 130
  - 6.4.2 Sacrificial wet release 137
- 6.5 Conclusion and outlook 146

7 CONCLUSION AND OUTLOOK 149

III APPENDIX

A TRANSFER MATRIX METHOD 155
- A.1 Double-membrane cavity calculations 156
- A.2 Optomechanics with InGaP membranes 157
  - A.2.1 Single membrane 157
  - A.2.2 Double-membrane arrays at the endmirror 159

B CHARACTERIZATION SETUPS 167
- B.1 Optical characterization 168
- B.2 Mechanical characterization 169

C PROCESS RECIPES 171

D III-V WAFER DESIGNS 179

BIBLIOGRAPHY 183

LIST OF FIGURES

Figure 1.1 Overview of microfabricated optomechanical systems 3
Figure 2.1 Schematics of an optomechanical setup 9
Figure 2.2 Finite-element simulation of a tethered membrane 10
Figure 2.3 Intensity transmission of a lossless Fabry-Pérot cavity 12
Figure 2.4 Schematics of the membrane-in-the-middle setup 15
Figure 2.5 Resonance frequency of a membrane-in-the-middle (MIM) cavity as function of membrane displacement 16
Figure 2.6 Schematics of an optomechanical multi-membrane setup 18
Figure 2.7 Mechanical compliant LC-circuit 19
Figure 3.1 Lattice structure of strained crystalline layers 24
Figure 3.2 Optical properties of thin films 26
Figure 3.3 Schematics of a square membrane with important design parameters 30
Figure 3.4 Essential fabrication steps of square membranes 31
Figure 3.5 Mode profiles of a square membrane 35
Figure 3.6 Extrinsic and intrinsic sources of dissipation for mechanical resonators 36
Figure 3.7 Example of the reflection spectrum of a PhC membrane exhibiting Fano-type resonances 41
Figure 4.1 Artistic illustration of a phononic shield membrane 45
Figure 4.2 Schematics of the exploited phononic shield cross structure and its parameters 49
Figure 4.3 Bandgap design simulations of the unit cell 51
Figure 4.4 Bandgap design simulations for the full 3D structure 52
Figure 4.5 Fabrication flow of phononic shield membranes 53
Figure 4.6 Photographs of final phononic shield devices 55
Figure 4.7 Deep reactive ion etching of test structures 59
Figure 4.8 Deep reactive ion etching of two different phononic shield designs 60
Figure 4.9 Notching issue for deep reactive ion etching 62
Figure 4.10 Design adaptations for improved deep reactive ion etching 63
Figure 4.11 Schematic overview of metallization fabrication procedures 66

Figure 4.12 Microscope images of the metallized SiN membrane at various fabrication steps 68
Figure 4.13 NbTiN lift-off 69
Figure 4.14 Phononic shield membrane and bandgap characterization 71
Figure 4.15 Q measurements for phononic shield membranes at room and cryogenic temperatures 72
Figure 5.1 Device design parameters for tethered PhC membranes 80
Figure 5.2 Schematics of possible single and double membrane devices 81
Figure 5.3 Schematic representation of the essential steps for the fabrication of various double-membrane arrays 82
Figure 5.4 Design challenges for tethered PhC membranes 83
Figure 5.5 Fully suspended double membrane device 84
Figure 5.6 Low finesse double membrane array consisting of a tethered PhC and square membrane 85
Figure 5.7 High finesse double-membrane arrays with two tethered PhC membranes of wavelength-dependent reflectivity 86
Figure 5.8 Influence of mismatched mirror reflectivity on obtained double-membrane spectra 88
Figure 5.9 Influence of the photonic crystal (PhC) design parameters on its resonance wavelength 89
Figure 5.10 Influence of baking time on the fabrication of PhC holes between front- and backside mirror 91
Figure 5.11 Reflectivity characterization of a single PhC membrane in an optomechanical cavity 92
Figure 5.12 Mode profile analysis of single and double membranes in reflection and transmission 94
Figure 5.13 Measured and fitted transmission peaks in the high-finesse regime of double-membrane arrays 96
Figure 5.14 Reflection spectra of single and double membrane arrays of varying finesse 99
Figure 5.15 Investigation of dispersive behavior of single and double-membrane arrays in an optomechanical cavity 103
Figure 5.16 Comparison of center-of-mass optomechanical coupling between single membranes and double-membrane arrays of varying finesse 104
Figure 5.17 Single tethered PhC membranes with 500 µm central pads 107

Figure 6.1 From membrane-in-the-middle (MIM) to membrane-at-the-endmirror (MATE) configuration 111
Figure 6.2 DBR-double-membrane system parameters 112
Figure 6.3 Optical transmission properties of the multilayer heterostructure DBR dependent on wavelength and number of mirror pairs 113
Figure 6.4 Double-membrane arrays in their transmissive and reflective regime 115
Figure 6.5 Full optomechanical cavity-double-membrane system and its parameters 116
Figure 6.6 Double-membrane arrays made of InGaP in the reflective optomechanics regime 120
Figure 6.7 Double-membrane arrays made of InGaP in the transmissive optomechanics regime 121
Figure 6.8 Overview of possible device designs for the fabrication based on the epitaxial wafer 126
Figure 6.9 Fabrication flow of single InGaP membranes atop of a DBR 128
Figure 6.10 SiN hard mask etching of tethered PhC membranes made of InGaP 131
Figure 6.11 Chlorine based dry etching of the epitaxial layer structure 133
Figure 6.12 Laser reflectometry of epitaxial heterostructure 136
Figure 6.13 Aluminum hydroxide fluoride byproducts from AlGaAs etching in HF 138
Figure 6.14 Low stress indium gallium phosphide (InGaP) tethered membrane suspended atop the DBR 141
Figure 6.15 Fabrication flow of the modified wet release 142
Figure 6.16 Low stress InGaP tethered membranes with the adapted deep non-selective wet release and SiN hard mask 144
Figure 6.17 Low stress InGaP tethered membrane with the adapted deep non-selective wet release 145
Figure 6.18 High stress InGaP tethered photonic crystal membrane with the adapted deep non-selective wet release 146
Figure A.1 Overview of parameters used for TMM simulations of a double-membrane array at the end-mirror 157
Figure A.2 Comparison of a single InGaP membrane in both MIM and MATE configurations 158
Figure A.3 Individual mode displacement results for the reflective optomechanics regime at the end-mirror with $d_1 = 3\lambda$ 160

Figure A.4 Collective mode displacement for double-membrane arrays made of InGaP in the transmissive optomechanics regime 161
Figure A.5 Individual mode displacement results for the reflective optomechanics regime at the endmirror with $d_1 = 3.25\lambda$ 162
Figure A.6 Individual mode displacement results for the transmissive optomechanics regime at the endmirror with $d_1 = 3\lambda$ 163
Figure A.7 Collective mode displacement for double-membrane arrays made of InGaP in the transmissive optomechanics regime 164
Figure A.8 Individual mode displacement results for the transmissive optomechanics regime at the endmirror with $d_1 = 3.25\lambda$ 165
Figure B.1 Schematic of the optical characterization setup 168
Figure B.2 Schematic of the mechanics characterization setup 169

LIST OF TABLES

Table 4.1 Material properties of SiN and Si 49
Table 4.2 Etch rates of PECVD SiO_x and LPCVD SiN in concentrated and dilute HF 64
Table 5.1 Influence of Fabry-Pérot etalon design parameters on finesse and transmission 97
Table 5.2 Photonic crystal parameters used in this study. 99
Table 6.1 TMM simulation parameters used for double-membrane arrays in a membrane-at-the-endmirror (MATE) configuration 117
Table 6.2 TMM simulation results for double-membrane InGaP arrays at the endmirror configuration 118
Table 6.3 Material properties of III-V ternary semiconductors 123
Table 6.4 Etch rates and selectivity of semiconductors during chlorine-based dry etching 135
Table A.1 Coupling strengths obtained for a single InGaP membrane in both MIM and MATE configurations 158
Table A.2 Comparison of coupling results obtained for single- and double-membrane arrays in both MIM and MATE configuration 159

ACRONYMS

AR	anti-reflection
AlGaAs	aluminum gallium arsenide
(Al)GaAs	(aluminum) gallium arsenide
AlSi	aluminum silicon
ARDE	aspect ratio dependent etch
COM	center-of-mass
CPD	critical point drying
CW	continuous wave
CTE	coefficient of thermal expansion
DBR	distributed Bragg reflector
DC	defect cell
DI	deionized
DM	double-membrane
DMF	dimethylformamide
DRIE	deep reactive ion etching
DSiE	deep silicon etch
EBL	electron-beam lithography
FSR	free spectral range
FOM	figure of merit
FWHM	full-width at half-maximum
GaAs	gallium arsenide
HAR	high aspect ratio
HCl	hydrochloric acid
HF	hydrogen fluoride
HWHM	half-width at half-maximum
ICP	inductively coupled plasma

In	indium
IPA	isopropyl alcohol
InGaP	indium gallium phosphide
KOH	potassium hydroxide
LF	low frequency
LIGO	Laser Interferometer Gravitational-Wave Observatory
LPCVD	low-pressure chemical-vapor deposition
LT	low temperature
MATE	membrane-at-the-endmirror
MBE	molecular beam epitaxy
MEMS	micro-electro-mechanical systems
MIBK	methyl isobutyl ketone
MIM	membrane-in-the-middle
NbTiN	niobium titanium nitride
NEMS	nano-electro-mechanical systems
NMP	N-methyl-2-pyrrolidone
NPS	noise power spectrum
OMIT	optomechanically induced transparency
PECVD	plasma-enhanced chemical-vapor deposition
PhC	photonic crystal
PL	photolithography
PMMA	poly methyl methacrylat
ppm	parts per million
PR	photo resist
PS	phononic shield
RIE	reactive ion etching
RMS	root mean square
RF	radio frequency
RT	room temperature

RTO	rapid thermal oxidation
sccm	standard cubic centimeters per minute
SEM	scanning electron microscope
SM	single-membrane
Si	silicon
SiN	silicon nitride
SiO	silicon oxide
TMAH	tetramethylammonium hydroxide
TMM	transfer matrix method
UC	unit cell
XRD	x-ray diffraction

1

INTRODUCTION

Imagine a world without laptops, cell phones, the internet or even cars and planes. After decades of miniaturization and optimization, micro-electro-mechanical systems (MEMS) – constituting the backbone of our information age – have matured into energy and footprint efficient high-performance devices with well-defined engineered functionalities. With their use as e. g. pressure and acceleration sensors, electronic filters and optical switches, they are crucial components that enable communication, navigation and transportation as we know it today. Improved fabrication techniques with control down to the nanoscale have driven the field towards the fundamental limits of solid state physics, entering the regime of nano-electro-mechanical systems (NEMS) governed by quantum mechanical properties, consequently paving the way into the era of quantum technologies.

The research field of cavity (quantum) optomechanics combines expertise from a diversity of research fields such as quantum optics, cryogenics, solid-state physics, material science and the ability to engineer properties with the toolbox of micro-machining [4]. The study of these novel light-matter hybrid systems, exploiting the interaction between light and vibration, oftentimes relies on high-quality optomechanical devices and architectures.

Thanks to advancements in micro-machining, design control on the nanoscale opened up avenues towards novel resonator architectures of unprecedented quality and consequently the exploration of yet unexplored regimes. As a consequence, quantum properties of massive macroscopic mechanical resonators are appearing within reach after what has formerly been unthinkable [93]. Instead of making devices smaller in order to reveal quantum features, one endeavor in the field has become to push the boundaries of quantum mechanics into the macroscopic world.

The interest in optomechanics is manifold in both fundamental as well as applied sciences thanks to their ability to couple to a variety of other quantum systems. From the perspective of fundamental sciences, studying quantum effects of massive macroscopic mechanical oscillators can e. g. lead to a better understanding at the interface of quantum mechanics and gravity. From an application point of view, these systems can be exploited as novel sensing architectures or constitute potential candidates in future quantum networks as transducers [29, 41].

Over the past two decades, cavity optomechanics has developed into a thriving field that features a variety of optomechanical systems, including a broad spectrum of mechanical oscillators. Size, mass and consequently frequencies of these resonators range from kg mirrors at LIGO detectors [61], over µm-sized on-chip structures (e. g. [15, 16, 54, 97] and Figure 1.1), to cold atoms trapped in optical cavities [99].

Thanks to sophisticated device designs and architectures, experimental control, as well as sophisticated micro-machining technologies, optomechanical systems can now be routinely operated in the quantum regime.

To highlight only a few, this includes optical ground state cooling [14, 103], ponderomotive squeezing [10, 89], entanglement in both the optical [83] and microwave [76] regime, as well as achieving mode hybridization in the strong coupling regime [33] and coherent quantum control [109].

All of these achievements require a strong laser drive, which consequently means giving up the intrinsic non-linear optomechanical interaction on the single quanta level. Conducting these experiments on a single photon level remains an outstanding goal in cavity optomechanics. Efforts towards reaching this regime have predominantly focused on producing optomechanical systems with stronger interaction strengths, i. e. larger conversion efficiencies between single quanta of photons and phonons, while simultaneously minimizing the individual decoherence rates. This would pave the way towards controlling massive mechanical oscillators in the non-linear quantum regime, opening up possibilities for the exploration of entirely new quantum phenomena.

One of the most successful optomechanical systems to date are on-chip photonic crystal structures that integrate both optical and mechanical resonators on the same chip (Figure 1.1b). Due to their strong mode confinement and large modal overlap, these structures feature high coupling strengths while maintaining reasonably low loss. In addition, these resonators exhibit mechanical frequencies in the GHz-regime allowing to prepare the mechanical system in its quantum ground state when operated at mK-temperatures without the need for additional laser cooling. There has been a number of remarkable experimental verifications over the past few years, where researchers have succeeded in revealing quantum features of these micro-meter sized objects. This includes the manipulation of single phonons [84], i. e. the generation and readout, the verification of entanglement between light and mechanics [76], as well as entangling two disparate structures with one another [83].

Another particularly successful direction is to dispersively couple vibrating objects in rigid optical cavities. The combination of independent optical and mechanical degrees of freedom allows for the

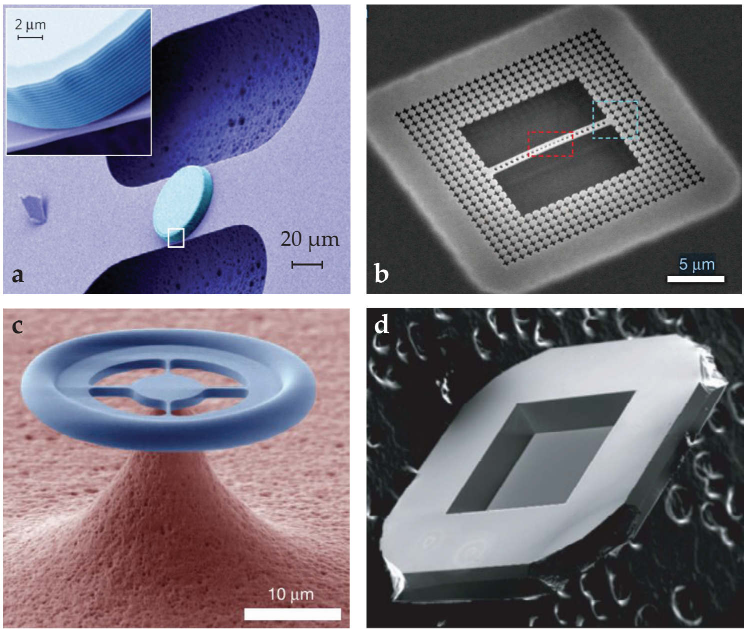

Figure 1.1: Overview selection of microfabricated optomechanical systems. **a** Doubly-clamped SiN beam with a distributed Bragg reflector (DBR) on top [33, 34]. **b** Patterned silicon nanobeam with external phononic shield [13]. **c** *Spoke-anchored toroidal resonator* [109]. **d** Square SiN membrane of 1 mm side length [104]. Images courtesy of given references.

use of high-finesse cavities to study a broad range of mechanical devices, ranging from levitated sub-micron silica particles [52] over to micrometer-sized doubly-clamped beams (Figure 1.1a), and to various membrane designs with millimeter dimensions [104] (Figure 1.1d).

Even though the large optical mode volumes lead to inherently small coupling strengths, remarkable and interesting experiments could have been achieved in the past. From fundamental aspects of proof-of-principle cooling experiments [34] and reaching strong coupling [33], over to sensing [73, 82] and transducer [41] applications, free-space cavity optomechanics constitutes an exciting direction within the research field.

For instance, researchers have successfully manipulated levitated silica particles of around 150 nm in diameter trapped within the standing light field of the optical cavity [52]. Just recently, the improved level of control has resulted in preparing such a levitated particle in its motional quantum groundstate without the need for cryogenic pre-cooling [25]. The preparation of mechanical resonators in its quantum ground state is an important starting point for the observation of quantum features on the single quanta level, while still enabling to operate the system at room temperature.

Even though this particular system does not rely on microfabricated mechanical devices, most other experimental realizations of cavity optomechanics are intrinsically linked to advancements made in the field of micro-machining. In this context, membranes have established as a very popular, and particularly successful alternative due to their flexibility in design, possible low mass and exceptional high mechanical quality factors (Figure 1.1d).

During the last few years, and along the scope of this thesis, novel membrane designs advancing beyond the state-of-the-art have lead to remarkable experimental results in the quantum regime [85, 106]. This is only one of many examples where the success of cavity optomechanics is intrinsically linked with advancements made in microfabrication resulting in novel device architectures with superior engineered optomechanical properties.

1.1 SCOPE OF THIS THESIS

In particular, this thesis seeks to advance the state-of-the-art for membrane architectures which can be utilized for free-space cavity optomechanical experiments. The approaches towards diving deeper into the quantum regime of such macroscopic vibrating objects is twofold. Firstly, producing membranes of better mechanical quality, i. e. lower thermal decoherence, overcoming the device limitations of state-of-the-art membranes when rigidly embedded in optical cavities. Secondly, exploiting multi-membrane architectures that not only promise to overcome the inherently weak interaction strength in membrane-in-the-middle (MIM) experiments, but also open up avenues towards multimode optomechanics.

Experimental success in optomechanics is intrinsically linked with advancements made in micro- and nanofabrication

In Part i of the thesis, I introduce the theoretical background of quantum cavity optomechanics that is intended to provide the basic toolbox for later chapters in Part ii. It is divided into two chapters, where Chapter 2 gives a brief introduction to the fundamental concepts of mechanical resonators, optical cavities, and cavity optomechanics, including a quick review of MIM setups and the concept of optomechanical arrays. Chapter 3 focuses on the mechanical aspects of free-space cavity optomechanics where we discuss the optical and mechanical properties of high-stress thin films and introduce the toolbox of microfabrication exploited for producing high-quality membranes with engineered properties.

Part ii highlights a selection of novel membrane devices and architectures with added functionality, focusing on design and fabrication with in-depth discussions about challenges and future directions.

In Chapter 4 I introduce phononic shield membranes which show superior mechanical properties compared to standard square silicon nitride (SiN) membranes. We show that these membranes exhibit consistently high mechanical quality factors for mechanical modes within the designed bandgap independent of their clamping procedure in an optomechanical cavity, ultimately allowing the system to enter the multimode strong cooperativity regime.

Chapter 5 outlines the vision and realization of optomechanical arrays with two monolithically integrated high-reflectivity SiN membranes that promise significant enhancements of the coupling strength compared to single membranes. I focus on fabrication-related details and show experimental results that characterize their optical, mechanical and optomechanical properties when incorporated in an optical cavity.

Finally, Chapter 6 depicts the advancement of the double-membrane arrays introduced in the previous chapter. In contrast, this system is realized on the III-V semiconductor material platform exploiting the unique properties of crystalline ternary alloys. Thanks to the material's crystalline nature and available growth techniques this approach promises to overcome the observed device limitations for the SiN arrays by enabling the fabrication of much shorter membrane arrays which ultimately paves the way towards even higher coupling enhancements.

Part I

THE OPTOMECHANICAL SYSTEM

Part i covers the basics of free-space cavity optomechanics where thin membranes are incorporated in macroscopic free-space optical cavities.

In Chapter 2, we first introduce the full optomechanical system where we focus on covering basic aspects. We distinguish between various system configurations depending on where the membrane is placed within the optical cavity, and derive the most important figures of merit.

Chapter 3 zooms in on the membranes made from high-stress thin films. Thereby, we discuss their optical and mechanical properties, and focus on fabrication-related aspects that provide the basic understanding for later chapters in Part ii.

2

CAVITY OPTOMECHANICS

Optomechanical systems exist in a large variety of different physical implementations, many of them can be described by the canonical picture of cavity optomechanics: the Fabry-Pérot cavity with an oscillating mirror (Figure 2.1).

Due to radiation pressure, the internal cavity optical field influences the moving element which leads to changes in the cavity length and thus the optical resonance frequency. This frequency change upon adding one phonon to the mechanical excitation is referred to as the bare optomechanical coupling rate.

We will use this system to introduce the most important features of cavity optomechanics that deals with light-matter interactions between optical cavities and employed mechanical resonators. More specifically, throughout the scope of this thesis, we work with membranes as mechanical element which are incorporated in optical cavities comprising two macroscopic mirrors. Typically, both optical and mechanical degrees of freedom can be described as harmonic oscillators which are one of the most important and fundamental physical systems, and are essential in understanding an optomechanical system.

This chapter is meant to introduce the fundamentals of cavity optomechanics whereas I restrict myself to a very basic description. All of the topics presented are well known and extensively discussed in the literature. I closely follow the reviews by Hofer and Hammerer [43] and Aspelmeyer, Kippenberg, and Marquardt [4], as well as the textbook by the same authors [5]. Furthermore, there is an abundance of great theses out there with a stronger, more detailed focus on the optomechanical insights (e. g. Hoelscher-Obermaier [42], Nia [71], and Wilson [113]). More sources are referenced upon necessity.

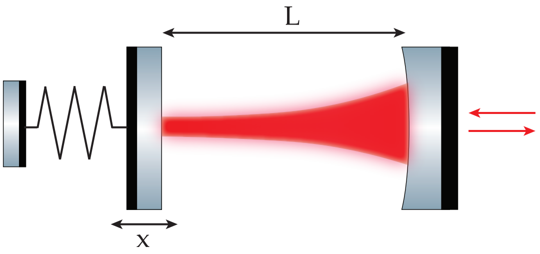

Figure 2.1: Schematics of an optomechanical setup where the cavity length $L(x)$ is modulated by the motion of the mechanical oscillator.

2.1 MECHANICAL OSCILLATORS

Mechanical oscillators are at the heart of optomechanical systems and come in various physical implementations, differing in their size, mass and geometry. Due to their relatively large size, mechanical oscillators possess a multitude of mechanical eigenmodes whose features are determined by the geometry and choice of material. For most geometries, the mechanical modes can take the form of arbitrarily complex shapes, which can be described by a characteristic modal displacement field $\boldsymbol{u}(\boldsymbol{r},t)$. Separation of the characteristic displacement field in its spatial-dependent eigenmodes $u_n(r)$ and respective time-dependent amplitudes $\boldsymbol{u}_n(\boldsymbol{r})$ contains knowledge about the modes' eigenfrequencies and modal shapes, where the subscript n denotes the mode number of the n-th mechanical eigenmode.

$$\boldsymbol{u}(\boldsymbol{r},t) = \sum_n x_n(t)\boldsymbol{u}_n(\boldsymbol{r}) \tag{2.1}$$

The eigenfrequencies and modal field displacements can either be calculated or simulated, where we later briefly derive the differential equations for the specific case of a square tensile-strained membrane (see Section 3.5). Figure 2.2 shows two examples of different eigenmodes of a trampoline resonator (tethered membrane) exploited throughout the scope of this thesis. Their amplitudes can be sufficiently well described by a fully classical damped harmonic oscillator.

$$\ddot{x}_n(t) + \gamma_n\dot{x}_n(t) + \omega_n^2 x_n(t) = \frac{F_{\text{ext}}}{m_{\text{eff}}^{(n)}} \tag{2.2}$$

Here ω_n and γ_n (expressed as the full-width at half-maximum (FWHM)) are the angular resonance frequency and damping term of the n-th eigenmode, m_{eff} denotes the effective mass which is dependent on the modal displacement field $\boldsymbol{u}_n$ and F_{ext} denotes the sum of all external forces that a specific mode of the mechanical resonator

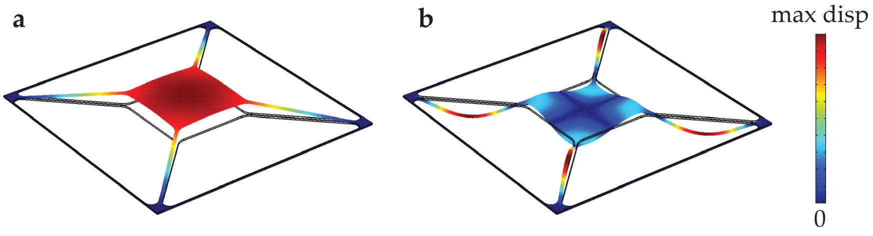

Figure 2.2: Finite-element simulation of a tethered membrane. Depicted are the fundamental (**a**) and a higher-order mechanical mode (**b**).

experiences. Typically, many different damping terms contribute to γ_n, which we can for now describe as the resonator coupling to its support, equivalent to energy leaking out into the resonator's environment. At the same time, the support acts as thermal environment of temperature T and depicts an important system parameter in optomechanical experiments. A bath environment of temperature T – at equilibrium following the Bose-Einstein distribution – results in a resonator's phonon occupation number $\bar{n}(\omega) = [\exp(\hbar\omega/k_B T) - 1]^{-1}$ ($\hbar$ being the reduced Planck constant and k_B the Boltzmann constant). Thus, a mechanical resonator of sufficiently high frequencies – typically in the GHz-regime – can be prepared in its mechanical quantum ground state by means of cryogenic cooling down to 50 mK, equivalent to a phonon occupancy smaller than unity. In contrast, the mechanical resonators exploited within the scope of this thesis exhibit a finite number of phonons at typical cryogenic bath temperatures due to their lower mechanical frequencies in the MHz-regime. As an example, a membrane mode of around 1 MHz exhibits approximately 10^3 phonons at 50 mK ($\approx 10^5$ at 5 K). This directly influences the effective thermal decoherence rate of mechanical oscillators which – in the high-temperature limit – is given by $\bar{n}\gamma \approx k_B T/\hbar Q$, where we defined the mechanical quality factor (Q-factor, Q), $Q = \omega/\gamma$. It becomes apparent that in order to have low thermal decoherence the incorporation of high-Q mechanical oscillators in a low-temperature bath environment is crucial.

A qualitative discussion about the dominant damping mechanisms (total γ_n) in state-of-the-art mechanical oscillators can be found in a later section of this thesis (see Section 3.6).

2.2 THE OPTICAL CAVITY

I have already briefly introduced our optomechanical toy model: the Fabry-Pérot cavity with a moving mirror. Fabry-Pérot cavities consist of two (typically weakly) transmissive mirrors, separated by a vacuum gap of length L, giving rise to an interference condition that builds up standing waves inside the cavity. These resonances are given by the angular frequency $\omega_n = n \cdot \pi c/L$, n being the integer mode number distinguishing between longitudinal modes. The resonances of a Fabry-Pérot cavity are equally spaced in frequency by $\omega_{\text{FSR}} = \pi c/L$, the free spectral range (FSR) of the cavity.

$$\omega_{\text{FSR}} = \pi \frac{c}{L} \tag{2.3}$$

The cavity transmission becomes maximal whenever the resonance condition $\omega_n = n \cdot \omega_{\text{FSR}}$ is fulfilled. For equal mirror reflectivities, all of the light is transmitted, whereas for mismatching mirrors, a fraction of the light is reflected. In general, the resonances show a Lorentzian profile with a linewidth κ (FWHM) dependent on the intensity transmission T_i of each mirror as well as the cavity length L, and the speed of light c inside the resonator (more generally, the cavity linewidth depends on the sum of all optical losses δ, i. e. transmission loss T_i of each mirror, scattering and material absorption).

$$\kappa = \frac{c}{2L}\delta = \frac{c}{2L}(T_1 + T_2 + \delta_{sc} + \delta_{abs}) \tag{2.4}$$

Rewriting this equation with respect to the cavity FSR, we can derive an expression known as the cavity finesse $\mathcal{F}$, which is independent of the cavity dimensions and only a measure of losses.

$$\mathcal{F} = \frac{\omega_{\mathrm{FSR}}}{\kappa} = \frac{\pi c}{\kappa L} = \frac{2\pi}{\delta} \tag{2.5}$$

Intuitively, the finesse of a cavity describes the average number of round-trips for a photon inside the cavity before it leaks out or is absorbed. Additional optical losses, such as scattering and material absorption, contribute to an increased (decreased) cavity linewidth κ (Finesse $\mathcal{F}$).

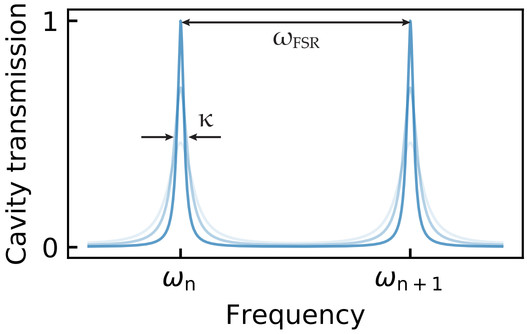

Figure 2.3: Intensity transmission of a lossless Fabry-Pérot cavity. Shown are two longitudinal cavity resonances separated by ω_{FSR}, the FSR of the cavity, for three different cavity linewidths κ (finesse $\mathcal{F}$). The mirror reflectivity of one mirror is fixed at $R_1 = 0.9$, whereas the second mirror varies from $R_2 = 0.5$ (light blue) to $R_2 = 0.9$ (dark blue), resulting in differences in peak transmission and cavity linewidth.

2.3 OPTOMECHANICAL INTERACTION

The starting point of our discussions will be the Hamilton operator H_0 for the case where both optical and mechanical degrees of freedom are treated as uncoupled harmonic oscillators. Note, that the descriptions presented here follow the review of optomechanics by Aspelmeyer, Kippenberg, and Marquardt [4]. For the uncoupled system, consisting of only one mechanical (ω_{cav}) and optical (ω_m) mode, respectively, the Hamiltonian reads

$$\hat{H}_0 = \hbar\omega_{\text{cav}}\hat{a}^\dagger\hat{a} + \hbar\omega_m\hat{b}^\dagger\hat{b} \tag{2.6}$$

where we used the creation and annihilation operators for both optics and mechanics. Note, that for the sake of simplicity, we restrict our discussion to a single mechanical mode with frequency ω_m and a single optical mode ω_{cav} that is closest to the frequency of the laser drive.

If we now allow length changes of the cavity to happen due to a moving end mirror, we can replace the cavity resonance ω_{cav} to be dependent on the mirror position x. Assuming further, that the displacements happen on length scales much smaller than the cavity length L, we can express the resonance frequency as a Taylor expansion around its equilibrium position.

$$\omega_{\text{cav}}(x) \approx \omega_{\text{cav}} + \frac{\partial\omega_{\text{cav}}}{\partial x}x + \mathcal{O}(x)^2 + \cdots \tag{2.7}$$

For the purpose of most experimental realizations to date where we deal with small displacements and interaction strengths, it suffices to only take the linear term into account while neglecting higher order terms $\mathcal{O}(x)^{\geq 2}$. We identify the linear term of the Taylor expansion as the frequency shift per displacement $G = -\partial\omega_{\text{cav}}/\partial x$, where the minus sign reflects the fact, that the cavity resonance reduces for an increase in cavity length, corresponding to positive displacements $x > 0$ if $G > 0$. Inserting 2.7 into equation 2.6 gives rise to the position dependent harmonic oscillator term representing the coupling between optics and mechanics

$$\hbar\omega_{\text{cav}}(x)\hat{a}^\dagger\hat{a} \approx \hbar(\omega_{\text{cav}} - G\hat{x})\hat{a}^\dagger\hat{a} \tag{2.8}$$

We can identify the first term in 2.8 as the bare Hamiltonian of the uncoupled light field, the second term now representing the interaction part of the Hamiltonian of the following form

$$\hat{H}_{\text{int}} = -\hbar g_0\hat{a}^\dagger\hat{a}(\hat{b} + \hat{b}^\dagger) \tag{2.9}$$

where we made use of the displacement operator $\hat{x} = x_{\text{zpf}}(\hat{b} + \hat{b}^\dagger)$ and introduced the vacuum/bare optomechanical coupling strength.

$$g_0 = Gx_{\text{zpf}} \tag{2.10}$$

quantifying the interaction between a single photon and phonon. It can be interpreted as the frequency shift of the optical cavity due to motion of the vibrating end-mirror in its mechanical ground state. The so-called zero-point-fluctuation x_{zpf} denotes an important quantity for quantum mechanical oscillators which is expressed by the oscillator's frequency ω_m and effective mass m_{eff}.

$$x_{\mathrm{zpf}} = \sqrt{\frac{\hbar}{2m_{\mathrm{eff}}\omega_m}} \tag{2.11}$$

The resulting radiation pressure force for the above derived optomechanical interaction is then governed by

$$\hat{F}_{\mathrm{rad}} = -\frac{d\hat{H}_{\mathrm{int}}}{d\hat{x}} = \hbar G \hat{a}^\dagger \hat{a} \tag{2.12}$$

Since the optomechanical coupling of single quanta is however an inherently weak interaction, optomechanical experiments are typically conducted with optical cavities of high finesse. This enhances the coupling by the strong intracavity driving field, whilst however sacrificing the inherent non-linearity of the optomechanical interaction in Equation (2.9).

By applying a strong, coherent input light field of the form $\hat{a} = \alpha + \delta\hat{a}$, where α depicts the mean intracavity field and $\delta\hat{a}$ small fluctuations around the mean value ($\delta\hat{a} \ll \alpha$), the interaction Hamiltonian (Equation (2.9)) can be linearized. The final, linearized interaction Hamiltonian then reads

$$\hat{H}_{\mathrm{int}}^{(\mathrm{lin})} = -\hbar g_0 \alpha (\delta\hat{a} + \delta\hat{a}^\dagger)(\hat{b} + \hat{b}^\dagger). \tag{2.13}$$

where the bare coupling strength g_0 is now enhanced by the mean field amplitude α of the cavity light field, and thus also by the number of photons $\bar{n}_{\mathrm{cav}}$ circulating inside the cavity, which can be tuned by the power of the input laser.

$$g = g_0 \alpha = g_0 \sqrt{\bar{n}_{\mathrm{cav}}}, \tag{2.14}$$

Note, that we restricted ourselves to the case of dispersive optomechanics, where the cavity frequency $\omega_{\mathrm{cav}}(x)$ is a function of the mirror position x. Coupling between optical and mechanical degrees of freedom can as well be identified in other experimental parameters such as the cavity decay rate κ. This case is referred to the so-called dissipative optomechanics, where – instead of the resonance frequency in the dispersive case – the cavity decay rate $\kappa(x)$ is now dependent on the position x of the mechanical resonator.

2.4 MEMBRANE IMPLEMENTATIONS

In cavity optomechanics an abundance of physical implementations have emerged over the last decade, all with their own specific advantages and disadvantages. This thesis focuses on the fabrication of membrane architectures which are suitable for free-space optomechanical systems such as the already introduced canonical optomechanics model of a Fabry-Pérot cavity with an oscillating end-mirror (cf Figure 2.1). Realizing such end-mirror configurations where the mechanical element is part of the macroscopic optical cavity adds additional constraints to the size, shape and functionality of viable mechanical resonator designs. As to ensure high-finesse cavities the mechanical oscillator ideally exhibit high reflectivity which can e. g.be solved by integrating DBRs on top of the resonator geometry [23, 34]. Despite the fact that such cavity configurations reach moderate finesse values, it comes with the disadvantage of increasing the oscillator's mass significantly and thus negatively affecting its mechanical properties.

2.4.1 *Membrane-in-the-middle setup*

Advancing from the end-mirror configuration, it is also possible to incorporate mechanical elements inside the optical cavity which allows for a dispersive coupling between optics and mechanics [104]. This approach has the advantage that it combines independent optical and mechanical components resulting in reducing the formerly limiting constraints on the mechanical elements. These so-called MIM systems (Figure 2.4) allow the use of high finesse cavities to study a variety of mechanical devices (such as nanorods, levitated silica spheres or thin membranes) with attractive features, among them the possibility of integrating small mass, high mechanical-quality factor and exceptionally low optical loss at near-infrared wavelengths.

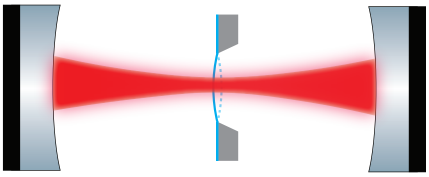

Figure 2.4: Schematics of the membrane-in-the-middle (MIM) setup where the cavity resonance frequency $\omega(x)$ is modulated by the motion of the mechanical oscillator – now independently placed in the middle of the optical cavity.

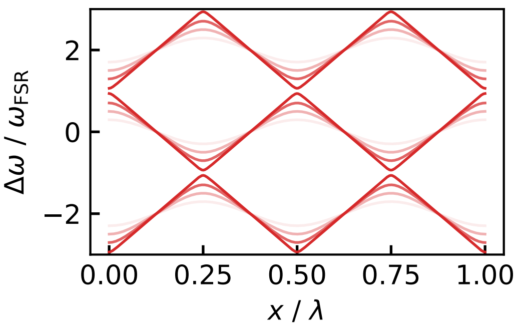

Figure 2.5: Resonance frequency ω of a MIM cavity as function of membrane displacement x. The displacement x is normalized by the laser wavelength. The resonance frequencies of multiple longitudinal modes are referenced to the center laser wavelength and frequency shifts are normalized by the FSR. The membrane intensity reflectivities vary from $R_m = 0.2$ (light traces) to $R_m = 0.99$ (dark traces).

Even though the requirements for the mechanical elements have loosened, highly reflective membranes are still beneficial for reaching larger coupling strengths (cf. Figure 2.5).

Reaching the quantum regime

The single-photon coupling strength g_0, describing the interaction strength between single photons and phonons is rather small – typically many orders of magnitude smaller than the optical cavity decay rate κ or the mechanical resonance frequency ω_m. It depends on geometrical aspects and therefore allows comparing optomechanical systems with one another.

The observation of quantum features for macroscopic mechanical objects is one of the main endeavors in the field of optomechanics. Driving mechanical systems into the quantum regime requires the optomechanical coupling to enter the regime of strong cooperativity, in which the cavity-enhanced coherent coupling rate exceeds both the optical and mechanical decoherence rates ($C_q \gtrsim 1$, $g \gtrsim \sqrt{\kappa\gamma\bar{n}}$).

$$C_q = \frac{4g^2}{\kappa\gamma\bar{n}} \tag{2.15}$$

Another more stringent quantum parameter is the so-called strong single-photon coupling regime, in which $g > \kappa$. Entering the strong coupling regime in the presence of a strong laser pump has been first experimentally shown by Gröblacher et al. [33] while conducting such experiments on the single photon phonon level remains outstanding.

A major disadvantage of dispersively coupled thin membranes in MIM systems is their inherently weak interaction strength due to the large cavity lengths, while simultaneously exhibiting relatively low mechanical frequencies in the hundreds of kHz-regime, further reducing the quantum cooperativity due to the large phonon occupancy $\bar{n}$ even at cryogenic temperatures. In this type of system, the only way to increase the bare coupling rate g_0 is by increasing the membrane reflectivity and/or by making the optical cavity shorter [94].

Under geometrical considerations, forming shorter optical cavities leads to an increase in both the coupling rate g_0 and cavity decay rate κ, as both parameters are inverse proportional with respect to the cavity length. Since the cooperativity scales quadratically with g_0^2/κ, shorter cavities are thus beneficial for reaching the strong cooperativity regime, while the strong coupling parameter g_0/κ stays, however, unaffected.

Considering that g_0/κ for MIM systems are on the order of 10^{-5}, entering the strong single-photon coupling regime seems beyond reach. Also other optomechanical systems, apart from atomic clouds [9], so far have reached ratios well below $g_0/\kappa < 1$.

The best optomechanical systems to date reach ratios of g_0/κ on the order of 2×10^{-3} for optomechanical systems with micro-scale on-chip photonic and phononic crystals [58, 88]. The reason for such large ratios lie in both reducing the optical and mechanical mode volumes while maximizing their modal overlap – leading to a relatively strong interaction between single photons and phonons.

While still orders of magnitude away from entering the single-photon strong coupling regime, continuous and significant effort is invested towards improving beyond the current state-of-the-art. In recent years, research efforts in MIM-type systems have predominantly focused on producing membranes of better quality, i. e. minimizing mechanical dissipation, while at the same time maintaining low optical losses at near-infrared wavelengths. Additionally, the increased flexibility in MIM systems allows for a richer variety of novel resonator (membrane) designs and architectures whose tailored mechanical and optical properties are ultimately limited by the material quality.

2.4.2 *Optomechanical arrays*

Following up on the idea to increase the overlap between optics and mechanics, similar ideas have developed for optomechanical systems where the collective interaction of several mechanical oscillators are predicted to significantly enhance the coupling strength by orders of magnitude without compromising the cavity decay rate [115, 116]. This effect is based on reducing the optical mode volume through arrays of closely spaced mechanical elements whose relative motion leads to frequency shifts much stronger than is the case for single vibrating elements.

Even already for the case of optomechanical arrays consisting of only two membranes (cf. Figure 2.6), enhancement factors for g_0 of up

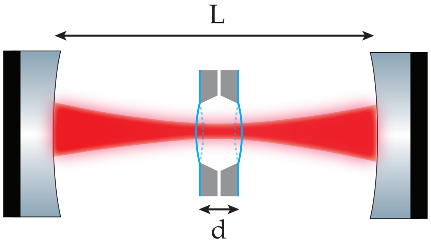

Figure 2.6: Schematics of an optomechanical multi-membrane setup. The membrane array cavity – here comprising two micromechanical membranes – is placed within the macroscopic optical cavity which leads to enhanced coupling strengths when tuned on resonance.

to three orders of magnitude are predicted for ideal, yet challenging system parameters. The most crucial parameter for achieving high enhancements lies in the successful realization of high finesse arrays, i. e. arrays consisting of high-reflectivity membranes, where light effectively spends more time interacting with the mechanical elements. In this case, due to the small optical mode volume of the inner array, i. e. assuming small separations between adjacent mechanical elements, the coupling strength can be greatly enhanced, whilst the cavity decay rate κ is still determined by the macroscopic long outer cavity. Intuitively, photons that leak out from the array cavity are recycled by the outer cavity and can thus interact on longer time-scales resulting in enhanced coupling rates. In the special case of two membranes with single element reflectivities approaching unity, the achievable enhancement factors are determined by the cavity length ratios $L/2d$, L being the length of the outer macroscopic cavity and d the separation between mechanical elements, respectively [60].

This thesis describes efforts towards achieving increased coupling strengths of such collective interactions for optomechanical arrays comprising two highly reflective SiN membranes (Chapter 5) as well as for membrane arrays made of the ternary compound semiconductor indium gallium phosphide (InGaP) (Chapter 6).

2.4.3 *Electromechanics*

So far, we have limited our discussions to optomechanical systems in the optical regime, but analogously, experiments can also be realized in the microwave regime for GHz frequencies. Here, the motion of the mechanical element capacitively couples to the LC-circuit by modulating its total capacitance $C(x)$, that is dependent on the membrane position x [20].

$$\omega_0(x) = \frac{1}{\sqrt{L(C_0 + C_m(x))}} \tag{2.16}$$

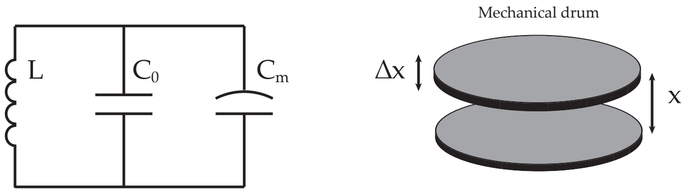

Figure 2.7: Mechanical compliant LC circuit. A traditional LC-circuit is characterized by its inductance L and capacitance C_0, with the inclusion of a parallel capacitor C_m whose spacing x is modulated by the movement Δx of the mechanical drum. (Adapted from Cohen [20])

Assuming that the capacitor can be modeled as parallel plates, its capacitance then writes as $C_m = \epsilon A/x$, where ϵ is the permittivity, A the area of the plates, and x the spacing between the plates. Analogously to the standard optomechanics case, we can derive the cavity pull parameter G

$$G = \frac{\partial \omega_0}{\partial C_m}\frac{\partial C_m}{\partial x} = \frac{\omega_0}{2}\frac{C_m}{C_0 + C_m}\frac{1}{x} \tag{2.17}$$

Essentially, one can see that it is beneficial to have very small gaps between the capacitor plates – one of which is formed by the membrane now – and to optimize the fraction C_m of the total capacitance that is sensitive to the mechanical motion.

3

MICROMECHANICAL MEMBRANES

In the previous chapter, I have introduced the fundamentals of the optomechanical system with its most important properties. In this chapter, the focus lies on the mechanical elements themselves exploited throughout this thesis: thin membranes exhibiting high tensile stress.

3.1 INTRODUCTION

In recent years, SiN has established as the material of choice for free-space optomechanical membrane-experiments due to its high-quality thin films grown on Si substrates. In 2008, Jack Harris exploited the exceptional mechanical and optical properties of commercially available[1] SiN square membranes for studying their dispersive optomechanical coupling inside a Fabry-Pérot cavity [49, 125]. Those membranes exhibit high tensile stress of around 1 GPa and beyond resulting in mechanical frequencies ranging from 100 kHz to several MHz – corresponding to side lengths between hundreds of µm and several mm. High tensile stress benefits the mechanical properties of thin films resulting in higher frequencies and thus enhanced Q factors, assuming the dissipation rates stay unaffected. With novel resonator designs such as tethered membranes, mechanical Q factors have been pushed to higher values for optimized design parameters [73], exceeding those of standard square membranes by one order of magnitude at room temperature. However, their enhanced mechanical Q factors due to their geometry come at a price of reduced resonance frequencies with respect to their square membranes counterpart. In recent years, the focus has been on fabricating devices of lower mechanical dissipation. This has lead to a better understanding of dominant device limitations and thus ways for reaching mechanical quality factors that are ultimately limited by the intrinsic quality of the thin film material. The current trend of engineering optical and mechanical properties constitute the basis of state-of-the-art devices and plays an increasingly dominant role in fabricating novel device designs of unprecedented quality.

This chapter covers several aspects of membrane resonators made of high-stress films, from their basic optical and mechanical properties, fabrication techniques required as well as current directions in device engineering towards overcoming the limitations of square membranes.

---

[1] Norcada Inc., `https://www.norcada.com/products/high-q-si3n4-membrane/`

3.2 GROWTH OF HIGH STRESS FILMS

High stress films are achieved through various growth techniques for both amorphous and crystalline materials. Depending on the goals and requirements of the films to be grown there is a variety of substrate materials to choose amongst. Silicon is likely the most prominent example for its wide-spread use in computer and MEMS technology with its well-developed fabrication techniques.

In recent years, SiN has established as the material of choice for optomechanical membrane experiments due to its ability to be grown on silicon wafers with high film quality. Depending on the growth details, these films exhibit high tensile stress beyond 1 GPa, which beneficially influences mechanical properties such as mode frequencies and dissipation. Obtaining thin films of high quality depends on many factors of the growth process, such as chamber pressure, temperature and gas ratios, which ultimately influence the optomechanical properties and hence quality of the grown film.

Another material platform that gained considerably increased attention is based on compound materials of e. g. III-V groups – such as gallium arsenide (GaAs) as substrate material – with additional functionality due to the intrinsic properties of III-V semiconductors. Moreover, in contrast to SiN, due to its crystalline structure, it is possible to grow more complex multilayer structures consisting of several thin film layers of well-controlled thickness with added functionality. Likely the most relevant example for optomechanics is the realization of high-reflective distributed Bragg reflectors (DBRs) that consist of alternating layers of high and low-index materials.

Additionally, the choice of substrate material can also play an important role for handling and functionality. Wafers of various thicknesses, doping grades, impurities, resistivity values and crystal orientations are available and can influence the choice based on the device requirements.

Amorphous SiN

Amorphous SiN is deposited in a high temperature furnace at temperatures of approximately 800 °C in a process called low-pressure chemical-vapor deposition (LPCVD). Films deposited by LPCVD are typically of higher quality than those grown with other techniques such as plasma-enhanced chemical-vapor deposition (PECVD) (more uniform, lower in defects), the range of materials is, however, limited due to the higher temperatures.

Silicon nitride can be deposited in both stoichiometric form (Si_3N_4) and low-stress (silicon-rich) form depending on the material properties needed. Other interesting properties of the grown films include uniformity and especially surface roughness. It has been shown that depositions at lower temperatures of 770 °C tend to result in higher film qualities when it comes to surface roughness with measured root mean square (RMS) values of 0.3 nm compared to a roughness between 2.5 nm to 5 nm at higher deposition temperatures [105]. Upon cooling down, the SiN layer obtains a high tensile stress of approximately 1 GPa at room temperature due to the difference in coefficient of thermal expansion (CTE) α between SiN and Si ($\alpha_{\text{Si}} = 2.8 \times 10^{-6}\,\text{K}^{-1}$ and $\alpha_{\text{SiN}} = 2.3 \times 10^{-6}\,\text{K}^{-1}$ [19]). In addition, the process details influence the stoichiometry of the film and thus stress, roughness, uniformity and deposition rate.

We grow our SiN films in-house[2] which allows for the fabrication of high quality films of arbitrary thickness, typically ranging from 20 nm to 400 nm, depending on the desired properties and functionality of the SiN layer. In our case, the deposition rate of stoichiometric SiN at a furnace temperature of 800 °C amounts to 0.068 nm/s with an index of refraction of approximately $n = 2$ measured at 638 nm and a tensile stress of 1.2 GPa for 100 nm thick films. Throughout this thesis, we exploit SiN films of 50 nm and 200 nm in thickness with final devices presented in Part ii.

Crystalline semiconductors

In contrast to the stress induced by differences in their thermal expansion coefficients, crystalline heterostructures obtain their stress mainly through mismatches in their lattice constants. Due to their crystalline nature, films with different lattice constants are forced to grow according to the substrate material underneath, which ultimately leads to tensile (compressive) strain $\varepsilon_{\parallel}$ dependent on the mismatch between substrate and grown film (cf. Figure 3.1).

A prominent example of almost lattice matched ternary alloys of the III-V group is gallium arsenide (GaAs) and aluminum gallium arsenide (AlGaAs) for arbitrary aluminum content. Usually, the lattice constants are dependent on the composition of the material and can thus be tuned. Ternary III-V alloys therefore depict an ideal platform for achieving crystalline films of tunable stress dependent on the alloy composition.

In our case, $\text{In}_x\text{Ga}_{1-x}\text{P}$ (InGaP) grown on GaAs is lattice matched for an indium (In) content of 49 % and becomes tensile stressed for lower In contents, resulting in an in-plane strain according to Equation (3.1) [80].

$$\varepsilon_{\parallel} = \frac{a_{\text{InGaP}} - a_{\text{GaAs}}}{a_{\text{GaAs}}} \tag{3.1}$$

Larger lattice mismatches lead to higher film stress while at the same time becoming more prone to crystal growth defects. This is

---

[2] Charles de Boer – Kavli Nanolab, TU Delft

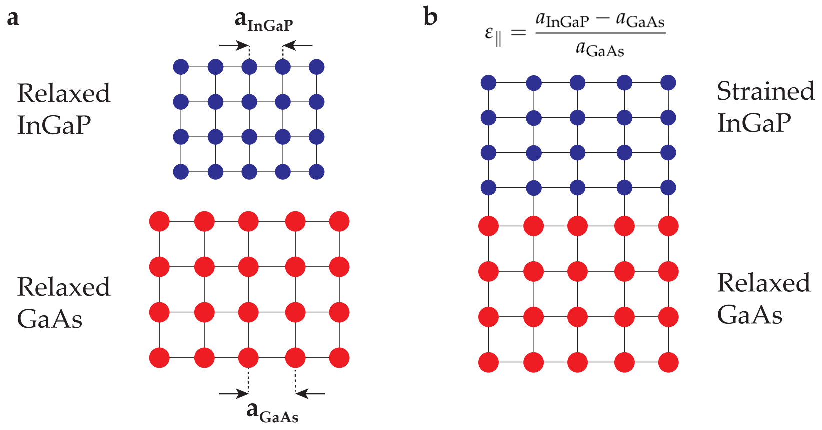
a
a_{InGaP}
Relaxed InGaP
Relaxed GaAs
a_{GaAs}
b
$\varepsilon_{\parallel} = \frac{a_{\mathrm{InGaP}} - a_{\mathrm{GaAs}}}{a_{\mathrm{GaAs}}}$
Strained InGaP
Relaxed GaAs

Figure 3.1: Lattice structure of relaxed InGaP and GaAs (**a**), as well as strained InGaP on relaxed GaAs (**b**)

particularly the case for thicker films above a critical film thickness. It is therefore crucial to not exceed the critical film thickness for a given tensile stress in order to maintain high quality films with as few crystal growth defects possible. There are many different theoretical models to predict the critical thickness for strained layers [46, 64, 78, 108]. In general, larger lattice mismatches result in higher strain but also lower critical film thickness.

In Chapter 6, we make use of crystalline InGaP layers grown on GaAs with two different In contents of both 47 % and 41 %, resulting in films with a nominal tensile stress of 150 MPa and 650 MPa (equivalent to tensile strains of $\varepsilon_{\parallel} = 1.1 \times 10^{-3}$ and $\varepsilon_{\parallel} = 5.5 \times 10^{-3}$), respectively. For the high-stress films with 650 MPa tensile stress the critical film thickness is on the order of a quarter-wave layer, equivalent to 83 nm for InGaP with a refractive index of 3.2.

3.3 OPTICAL PROPERTIES OF THIN FILMS

The film thickness influences both mechanical as well as optical properties. In this section, we briefly discuss the dependence between film thickness and reflectivity. We mainly follow the book chapter "Thin Films" by Gould, Kasap, and Ray [32].

Let us consider the following situation depicted in Figure 3.2a, where an optical beam of light in a medium with refractive index n_0 is incident at an angle ϕ_0 to the normal of a film with refractive index n_1. In order to calculate the amplitude fractions of reflected and transmitted light, r_1 and t_1 respectively, we need to apply the boundary conditions at the interface between two different optical media that can be directly derived from Maxwell's equations. The coefficients r_1 and t_1 – also called Fresnel coefficients – solely depend on the refractive indices of the media involved (n_0 and n_1) and the properties of the impinging light beams (polarization and angle of incidence).

We are interested in the optical properties of a thin film of optical thickness $n_1 d_1$, which consists of two interfaces where multiple partial reflections and transmissions occur. The total amplitude of the reflection (transmission) of such a film is then the result of all partially reflected (transmitted) light fields for which we can find conditions where either constructive or destructive interference occurs (Figure 3.2b). This is accounted for by a *phase thickness* δ_1, that depends on the wave vector k in vacuum (wavelength λ), the optical thickness of the film $n_1 d_1$, and angle of incidence ϕ_1.

$$\delta_1 = \frac{2\pi}{\lambda} n_1 d_1 \cos(\phi_1) \tag{3.2}$$

In our case, where we consider three optical media with two interfaces, the summation of all partial light waves leads to an infinite series. The amplitude reflection coefficient r (and equivalently also transmission coefficient t) then read as

$$r = \frac{r_1 + r_2 \exp(-2i\delta_1)}{1 + r_1 r_2 \exp(-2i\delta_1)} \tag{3.3}$$

$$t = \frac{t_1 t_2 \exp(-i\delta_1)}{1 + r_1 r_2 \exp(-2i\delta_1)} \tag{3.4}$$

In this case, r_1 and t_1 represent the Fresnel coefficients at the first interface between n_0 and n_1, and r_2 and t_2 the coefficients at the second interface between n_1 and n_2, respectively. We can then calculate the power reflectance R and transmittance T by evaluating the complex absolute of the amplitude coefficients with an impedance factor that depends on the refractive indices of incident and final media. Reflectance and transmittance are then given by

$$R = \frac{n_0}{n_0} r r^* = \frac{r_1^2 + r_2^2 + 2 r_1 r_2 \cos(2\delta_1)}{1 + r_1^2 r_2^2 + 2 r_1 r_2 \cos(2\delta_1)} \tag{3.5}$$

$$T = \frac{n_2}{n_0} t t^* = \frac{n_2}{n_0} \frac{t_1^2 t_2^2}{1 + 2 r_1 r_2 \cos(2\delta_1) + r_1^2 r_2^2} \tag{3.6}$$

Inserting the four Fresnel coefficients (r_1, r_2, t_1, t_2) into Equations (3.5) and (3.6) lead to long expressions – even for the case of normal incident light. In general, the power reflectance R and transmittance T only depend on the refractive indices of the three media and and the phase thickness δ_1 and allows for a qualitative discussion for various cases shown in Figure 3.2b. Here, the power reflectance R is plotted versus the phase thickness δ_1 for three different sets of refractive indices $\{n_0, n_1, n_2\}$.

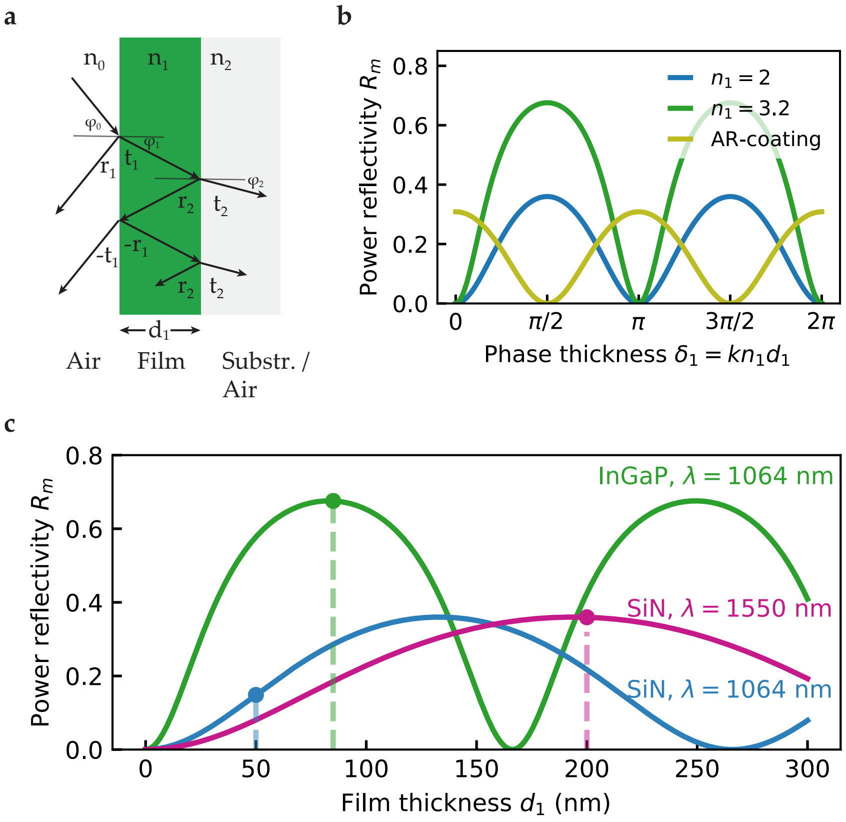

Figure 3.2: Optical properties of thin films. **a** Schematic representation of a thin film (green layer) of thickness d_1 and refractive index n_1 capped by two other optical layers of refractive indices n_0 and n_2, respectively. We distinguish between two cases, where the thin film is surrounded by air/vacuum or alternatively deposited on top of a substrate material with refractive index n_2. The incident optical beam impinges from the left and is partially reflected and transmitted, contributing to the total transmittance and reflectance. **b** Thin film power reflectivity dependence for two different optical materials with refractive index n_1 exhibiting maxima and minima dependent on the optical phase thickness and the refractive index n_1 of the thin film surrounded in air (green and blue curves). When deposited on a substrate material, thin films of optimal optical thickness can also serve as anti-reflection (AR) coatings (green curve). **c** Reflectivity R_m dependent on the film thickness d_1 for two different materials and laser wavelengths used within the scope of this thesis showing the same behavior as in the generalized plot in **b**. The materials used here represent indium gallium phosphide (InGaP) (green curve) and SiN (blue and magenta) with a refractive index of 3.2 and 2, respectively, plotted for two different laser wavelengths of 1064 nm and 1550 nm.

Membranes of various materials and thicknesses

Let us first consider the case, where light of normal incidence impinges on an optical material of thickness d_1 and refractive index n_1, surrounded by air/vacuum and thus referring to the case of a suspended membrane. Most importantly, maxima of the reflectance occur when δ_1 is an odd multiple of $\pi/2$ which corresponds to the case where the optical thickness $n_1 d_1$ amounts to an odd number of quarter wavelengths.

The two refractive indices chosen here represent the choice of materials exploited throughout this thesis, SiN and InGaP membranes with refractive indices of $n_{\mathrm{InGaP}} = 3.2$ (green curve) and $n_{\mathrm{SiN}} = 2$ (blue curve), respectively, in the wavelength range of interest. In addition, the peak reflectance of a membrane in air crucially depends on its refractive index and results in higher values the greater the material's index of refraction is.

For the third curve, let us consider the case, where a thin film is deposited on a substrate with refractive index of $n_2 = 3.5$ (the light impinging medium still being air), roughly corresponding to gallium arsenide (GaAs) and silicon (Si) substrates ($n_0 < n_1 < n_2$). Interestingly now, with the right choice of material, reflectance minima occur at the same phase thickness values where we found maxima in the other cases. At these points unity transmittance can only be achieved when $n_1 = \sqrt{n_0 n_2}$, and films of optical thickness of $d_1 = \lambda/4n_1$. Films with that ability are referred to as anti-reflection (AR) coatings and are widely used in optics.

In Figure 3.2b, we qualitatively analyzed the power reflectance dependent on the phase thickness δ_1, that is a function of wavelength, film thickness and refractive index. In Figure 3.2c, the general case from Figure 3.2b is now plotted for more specific cases of membranes used throughout later chapters of this thesis for varying film thicknesses d_1 (marked as solid dots).

For all three curves, we see the same oscillative behavior of the membrane reflectance R_m observed in Figure 3.2b, however now shifted dependent on the material and impinging optical wavelength. Comparison of the blue and purple curve shows the influence of the optical wavelength for varying film thickness. It is apparent, that larger refractive indices not only lead to bigger reflectance maxima (which allows for larger radiation pressure effects), but also already for thinner membranes, which we will later see is beneficial for obtaining high mechanical quality factors for membranes under high tensile stress.

We will discuss the impact of films with higher refractive indices later on in Chapter 6 when it comes to realizing DBRs as well as membranes made of InGaP. In Chapter 4, membranes of 50 nm thickness are exploited and Chapter 5 will deal with the advantage of thicker films for realizing films of engineered high reflectivity when exploiting PhCs.

It is apparent that unpatterned films of SiN (and other materials for that matter) are not suitable as end-mirrors in a two-mirror optomechanical cavity. However, sophisticated engineering can lead to high-reflectivity membranes by using DBRs with the drawback of increasing its mass significantly [23, 34], or preferably by patterning the film with a repetitive pattern of air holes, so-called PhCs (see Section 3.7 and [73]).

Matrix formalism

The resulting expressions for reflectance and transmittance already become unhandy for only three layers. In particular for films containing several layers – as is the case for e. g. DBRs – transfer matrix methods (TMMs) become a useful tool for determining the reflection and transmission of the entire structure. The transmitted electromagnetic fields can then be expressed by the impinging field components by a 2×2-matrix. The total system matrix then consists of simple matrix multiplication of the individual layers. The electromagnetic field components of adjacent layers are then linked through a characteristic 2×2-matrix. In order to obtain the field components of the entire structure, one has to apply simple matrix multiplication for each layer of the stack, as long as the optical thickness, i. e. refractive index n and thickness d of each layer is known. For these kinds of calculations, optical beams of normal incidence are assumed.

We will make use of this method later on in Chapter 6 for characterizing DBRs as well as entire MIM systems in order to determine membrane configurations of optimized performance. Maximizing the coupling strength with respect to the standing light field inside the optical cavity typically constitutes one of the main goals in that regard. A more detailed description of the TMM can be found in Appendix A.

3.4 FABRICATION

The fabrication of mechanical resonators in high stress films use standard top-down optical or e-beam lithography methods that provide a high level of control and flexibility for the device design and geometry. Usually, at least one lithography step of the device layer is needed to define the two-dimensional geometry of the resonator design that is then transferred into subsequent layers by means of an anisotropic dry etch. Less common are the use of mostly isotropic wet etches for patterning the device layers. The reason lies in the fact that often one is interested in directional anisotropic etching through the rather thin film whose etch boundaries are desirable of high surface quality with a vertical sidewall profile. For these reasons, reactive ion etching (RIE) or inductively coupled plasma (ICP) etching is the standard choice for this endeavor. After the pattern transfer into the device layer, an isotropic dry or wet etch removes a sacrificial layer after which the resonator is suspended. These steps are illustrated in Figure 3.4 based on the fabrication process of a simple square membrane. In principle, more lithography steps can be used for more complex device designs where additional functionality is added by e. g. patterning certain parts with metallic and dielectric layers by means of sputtering and deposition. Most crucial to every fabrication procedure is the availability of selective etching and cleaning procedures that result in pristine films of – in the case of optomechanics – high mechanical and optical quality resulting in low dissipation. However, the quality of the fabricated devices are ultimately defined by the quality of the grown thin films themselves and thus depict an ultimate limit to both optical and mechanical properties – and thus dissipation – of suspended mechanical resonators. In the case of crystalline films this also includes the crystal purity and the amount of defects that ultimately lead to higher dissipation.

In general, every fabrication process relies on the successful and repeatable pattern transfer from a sensitive resist layer into subsequent layers through addition (e. g. deposition and sputtering), modification (i. e. surface treatments) and removal of material (i. e. etching). The quality of the fabrication process can be quantified by a few figures of merit [95]:

- Etch rate – it is desirable to have good control and reproducibility over the processing conditions. Depending on the process details, higher etch rates for increased throughput or lower etch rates for better process control are favorable. However, this also crucially depends on other important figures of merit that are described in the following, such as selectivity.

- Selectivity – it is a measure of how fast the desired material is etched relative to the etch rate of the masking material. Sometimes, depending on the etch details, the selectivity for a material to be etched with respect to a resist layer can be too low and thus requires the use of another intermediate harder material – also referred to as hard mask. Typical hard masks are PECVD silicon oxide or silicon nitride as well as thin metal layers depending on the desired material to be etched.

- Anisotropy – describes the verticality of the etch profile. In many cases, vertical and smooth sidewall profiles are desired and usually obtained by directional dry etching. In contrast, wet etching is typically isotropic in nature with potassium hydroxide (KOH) etching of silicon as likely the most prominent example which is depending on the crystal-orientation.

- Damage – closely related to the process selectivity and the ability of the etch process to passivate and protect areas that are not supposed to be etched. Any surface damage of films with important functionality acquired from processing steps lead to a degradation in film quality and thus increased optical and mechanical losses.

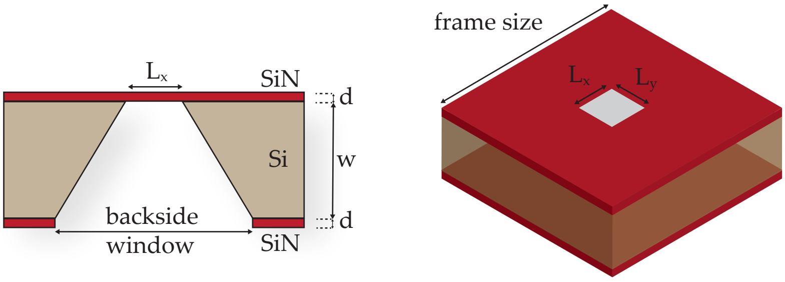

Figure 3.3: Schematics of a squared membrane with important design parameters. Design parameters include the choice of wafer thickness w and deposited film thickness d. Upon pattern transfer of the backside window into the SiN layer and subsequent KOH etching, the released membrane has smaller dimensions due to the characteristic crystal orientation-dependent Si etch of an angle of 54.7° for (100)-silicon wafers.

With the available toolbox of processing technology at hand, we can now discuss the necessary steps for fabricating mechanical resonators out of high quality SiN films. Here I will stick to the exemplary fabrication of square membranes, however, the general ideas presented are readily transferable to other material platforms and resonator designs, and will be made use of in later chapters in Part ii. Details of the fabrication process can be found in Appendix C.

Wafer cleaning

1. Most crucial for the successful fabrication of high quality membrane resonators is to grow thin films of high quality in the first place. This not only includes an optimized deposition process (which is not part of this thesis) but also providing clean and pristine substrates for ideal growth conditions with the least amounts of contaminants present. Therefore, the 4-inch (100)-Si wafers are cleaned with two standard cleaning procedures (RCA1 and RCA2) that subsequently remove organic and metallic compounds off the Si surface. Both cleaning steps are performed at elevated temperatures of 75 °C, whereas RCA1 consists of $NH_4OH/H_2O_2/H_2O$ (1:1:5) and RCA2 of $HCl/H_2O_2/H_2O$ (1:1:5), respectively. A final HF dip is recommended to strip the oxidized Si surface which leaves behind a clean and smooth substrate for optimal growth conditions. In order to minimize

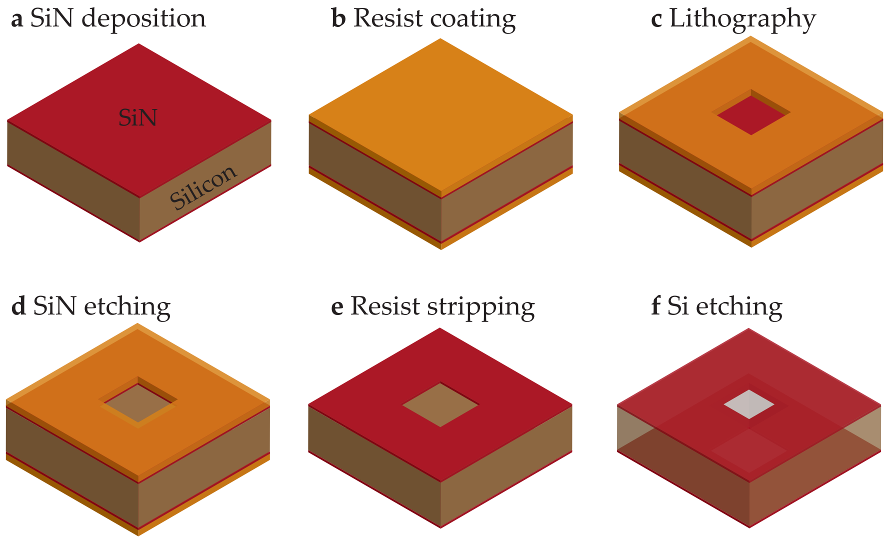

Figure 3.4: Essential fabrication steps of square membranes consisting of SiN deposition, lithography, SiN and Si etching.

re-contamination of the exposed Si surface, the LPCVD deposition process[3] is immediately performed right after wafer cleaning.

Chip preparation

2. After deposition, the 4-inch wafers are diced in smaller chips of arbitrary, in our case 10 mm, side lengths. This is beneficial for the purpose of optimizing both device geometries as well as fabrication processes. Before dicing, the wafer surfaces are covered with a photoresist that protects the SiN device layers from contamination and scratches during dicing and handling. The protective resist coating can then later be stripped using an appropriate solvent such as acetone right before starting the fabrication process. For highly contaminated surfaces by organic compounds, we clean the chips in a more thorough cleaning solution consisting of sulfuric acid and hydrogen peroxide, called Piranha solution.

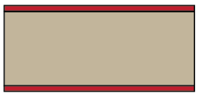

Lithography

3. Depending on the smallest feature size during the pattern transfer, we can choose between photolithography (PL) and electron-beam lithography (EBL). PL has the advantage of transferring patterns with much higher throughput down to features of approximately 1 µm with reasonable effort. The drawback is that for every change in device design one requires a new chrome mask that transfers the device patterns into the photo-sensitive resist layer. In contrast, EBL has a much lower throughput, but provides the flexibility of writing arbitrary patterns without the need for adapting the chrome mask design (Note that other optical techniques such as laser-writing are available that do

---

[3] Performed by Charles de Boer, Kavli Nanolab, TU Delft

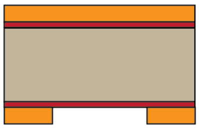

not require the use of chrome masks and still allow for quickly adapting design geometries). EBL allows for smaller feature sizes that can go down to approximately 20 nm assuming optimized process parameters and thin resist layers. The general work flow during lithography consists of dispersing the resist, spinning it uniformly on the chip surface with an appropriate spin speed resulting in the desired thickness, baking on a hotplate or in an oven, exposing the resist, developing and finally drying. The choice of resist depends on the film thickness, the geometry and feature sizes to be transferred, aw well as the achieved etch selectivity. Small features and thick device layers typically require thicker resists for successfully transferring the device pattern. In particular for the fabrication of square membranes, we spin the positive electron-beam resist AR-P6200.09[4] at a spin speed of 3 krpm resulting in resist thicknesses of around 250 nm, followed by tempering the resist on a hotplate at 150 °C for 3 min. The resist-coated chips are then exposed with the design geometry to be transferred into the SiN device layer underneath and afterwards developed in an appropriate solution. Here, we use subsequent rinses of pentyl-acetate, methyl isobutyl ketone (MIBK)-IPA(1:1) and isopropyl alcohol (IPA) of 1 min each, followed by blow-drying the chips with a nitrogen gun.

Pattern transfer

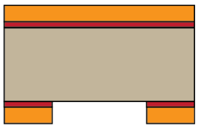

4. The developed resist layer contains the information of device design to be transferred into the layers underneath. Usually, this can be either done by means of wet or dry etching processes. In our case, the resist pattern is transferred in to the SiN layer using RIE etch tools. In particular, SiN layers are etched with a fluorine based chemistry, typically CHF_3 or similar, which etches the SiN both chemically and physically. The ions are generated at a source and the plasma is accelerated towards the sample surface, both physically sputtering and chemically reacting with the material to be etched on the surface. Usually, the advantage of using dry etching lies in achieving directional/anisotropic, often non-selective etches, leading to (deep) vertical and smooth sidewalls for optimized process parameters. Wet chemistry usually provides isotropic etching with good selective etches available. A prominent exception for anisotropic wet etching is silicon etching with KOH, whose etch rate and angle is crucially dependent on the crystal orientation of the silicon. After the pattern transfer, the remaining resist layer is thoroughly stripped in order to guarantee clean sample surfaces for further processing. More complex fabrication procedures consists of many of these described lithography and pattern transfer steps. Most importantly for every process is the compatibility of etch chemistry and parameters such that important functional layers are nei-

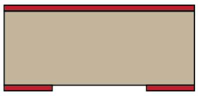

---

[4] AR-P 6200 series, https://www.allresist.com/csar-62-ar-p-6200/

ther harmed nor damaged. Most of the fabrication consists of cleaning surfaces off of organics and non-organic compounds that might damage or even destroy the functionality of the final device performance.

Si etching with KOH

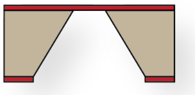

5. Now that the SiN film is patterned in the shape of the membrane design geometry, we can start etching away the exposed silicon for finally releasing the SiN membrane. This is done by immersing the entire chip in a solution of 30 % potassium hydroxide (KOH) at 75 °C (other temperatures and concentrations can be applied for controlling both etch rate and surface quality of the silicon surface) which etches the silicon at a rate of 1 µm/min along the (100)-crystal plane. Note that a characteristic feature of silicon etching in KOH is the crystal-orientation dependent etching which results in well-defined etch profiles along the (111)-crystal-planes. For that reason, if etched on (100)-wafers, the silicon is etched under a characteristic angle of 54.7°. This in turn means, that the released SiN square membrane after fully etching through the entire thickness of the wafer is smaller than the defined square on the backside, ultimately depending on the wafer thickness. As an example, for suspending membranes of 350 µm in side length on 500 µm thick silicon wafers, the backside window requires a size of approximately 1050 µm, which can be obtained by simple geometrical considerations.

Cleaning procedures

6. As a final step, we apply various cleaning procedures to the released membrane. In general, when going from one etchant into another, it is crucial to properly rinse the samples in various water baths to avoid cross-contamination as well as to reduce the risk of undesired exothermic chemical reactions. Therefore, after the KOH etching, we rinse our samples in two consecutive water baths for making sure that the sample is free of any KOH residues. However, often we would find traces of KOH crystals on the sample surface, which we can clean off in a diluted hydrochloric acid (HCl) solution (3 parts HCl:1 part water) for 10 min. Additionally, if needed, the removal of organic compounds can be done in a so-called Piranha solution, consisting of three parts of sulfuric acid and one part of hydrogen peroxide (3:1) for 10 min at 100 °C. After these steps, the samples are again rinsed in consecutive water baths, followed by two final IPA rinses before being carefully blow-dried with a nitrogen gun. It is crucial that all liquids are quickly removed such that no residues are left behind on the surface before evaporation. If blow drying with a nitrogen gun leaves residues behind, a more time-consuming but effective drying process can be performed which – in particular – for deep silicon etches of 1 mm turned out to be useful. The process of critical point drying (CPD) is usually used for drying

fragile suspended structures that are more sensitive to surface tension and consequently a collapse onto the substrate. By using liquid CO_2 the occurring forces during drying are significantly reduced resulting in a process that dries sensitive structures in a gentle, controlled and repeatable manner.

3.5 MECHANICAL MODES OF A 2D MEMBRANE

We model the motion of an elastic tensile-strained membrane that is stretched and then fixed along its edge. Considering the forces at play, a partial differential equation can be derived that we identify as the wave equation in two dimensions with the speed of sound c only depending on the tensile stress T and mass density ρ of the membrane [3].

$$\frac{\partial^2 u}{\partial t^2} - c^2 \Delta^2 u = 0 \quad \text{with} \quad c^2 = \sigma/\rho \tag{3.7}$$

In order to obtain the solutions to this problem, we can separate the trial functions into a time-dependent and spatially dependent part and solve it for membranes fixed along their edge as boundary conditions. A detailed derivation of the solution can be found in standard textbooks which is governed by the following expressions

$$u_{mn}(x, y, t) = a_{mn} \cos(\omega_{mn} t) \sin(m\pi x/l_x) \sin(n\pi y/l_y) \tag{3.8}$$

$$\omega_{mn} = c\pi \sqrt{\frac{m^2}{l_x^2} + \frac{n^2}{l_y^2}} \tag{3.9}$$

Here, $u_{mn}(x, y, t)$ now describes the time-dependent displacement of (in general) rectangular membranes with side lengths l_x and l_y, respectively, that are normalized to the maximum displacement of each mode a_{mn}. Due to the existing boundary condition of membranes fixed to their edge, the characteristic eigenmodes are denoted by integer mode indices $m, n \geq 1$ with ω_{mn} being their corresponding eigenfrequencies.

It is now interesting to note that, depending on l_x and l_y, several eigenmodes – with differing mode shape distributions of the displacement and nodal lines – correspond to the same eigenfrequencies ω_{mn}. This is the case, in particular, for square membranes, where $l_x = l_y$ and thus $\omega_{mn} = \omega_{nm}$ holds (cf. Figure 3.5). However, due to fabrication imperfections, these modes are never fully degenerate due to their slightly different side lengths.

In addition, the eigenfrequencies ω_{mn} depend on their mode indices and material parameters of the film, namely stress σ and mass density ρ. Membranes of higher stress and/or smaller side lengths thus exhibit higher mechanical frequencies.

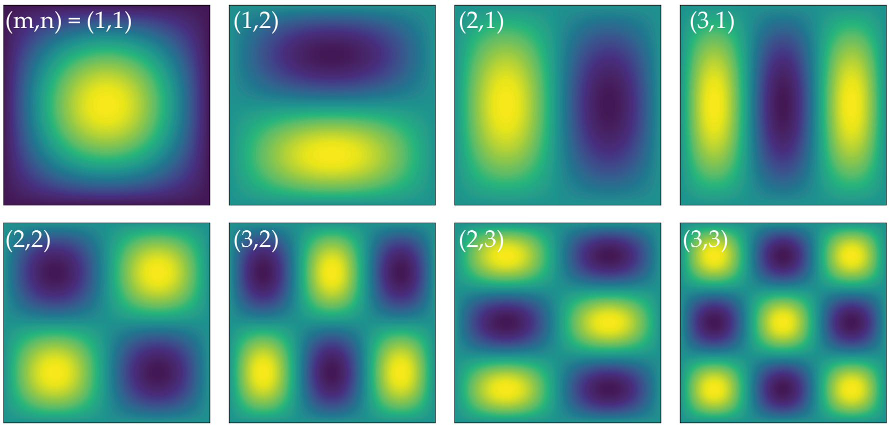

Figure 3.5: Mode profiles of a square membrane. The membrane is fixed along its edge and shows displacement maxima (yellow) and minima (blue) according to Equation (3.8) where we omit their time dependency (Note that for the fundamental mode blue corresponds to zero displacement). The mode numbers (m,n) determine the number of displacement maxima whereas the number of antinodes is given by (m-1,n-1) along the (x,y)-direction.

The mode spectrum of such membranes can be measured with a simple phase-sensitive setup (as described in Appendix B.2).

3.6 DISSIPATION

Dissipation plays a major role for both optical and mechanical degrees of freedom. In particular, better understandings and models for mechanical systems have lead to resonators with unprecedented high quality factors through advanced fabrication techniques and sophisticated novel resonator designs. In this Section I will focus on some aspects of damping mechanisms, that pose a limitation to achieving higher Q-factors. Note that the discussion here is by far not complete and the interested reader is referred to the various papers and reviews out there [47, 51, 110, 119]. We closely follow the review by Imboden and Mohanty [47] and the book by Schmid, Villanueva, and Roukes [91]. In particular for the discussion of damping mechanisms present in state-of-the-art square membranes, I recommend following the model derived by Villanueva and Schmid [110] based on earlier work from Yu, Purdy, and Regal [119], which distinguishes between material-specific intrinsic and external loss channels.

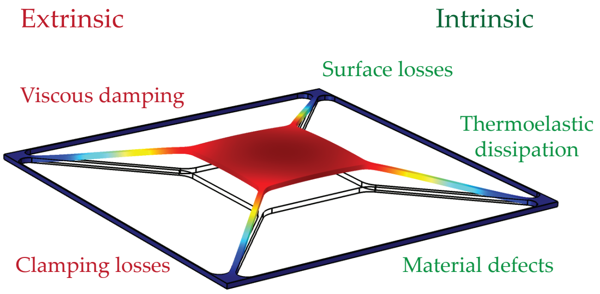

Figure 3.6: Extrinsic and intrinsic sources of dissipation for mechanical resonators. Here, the displacement profile of a tethered membrane is shown where red (blue) colors correspond to larger (smaller) displacements of the fundamental mode.

Dissipation – according to Imboden and Mohanty [47] – can be e. g. sorted into two broader categories: extrinsic and intrinsic sources. In general, damping attributed to intrinsic sources are related to the resonant material and a matter of film quality and appropriate fabrication techniques that – at least – do not additionally harm the (surface) quality of the resonator. When referring to extrinsic sources, we consider effects that can typically be manipulated through engineering and design, as well as dissipation mechanisms related to the resonator's environment, such as ambient gas pressure.

Acoustic radiation into the environment, i. e. coupling to the substrate material has been identified as one of the major limiting dissipation contributions over recent years. Geometrical considerations play a significant role here in minimizing these losses, whilst, in the case for square membranes, the geometry is limited to the choice of side length and film thickness, as well as internal material parameters such as residual tensile stress. With other design geometries such as cantilever, doubly-clamped beams or tethered membranes, additional design parameters such as fillet radii at the clamping points seem to play an important role. Just recently, geometrically engineering the clamping points of doubly-clamped nanobeams has proven to increase the mechanical quality factors [7, 87], which might also be of valuable input for other device designs such as tethered membranes [55, 73, 82]. For square membranes, unprecedented Q-factors were achieved by patterning 30 nm thin films with a periodic air-hole structure. All of these recent developments take advantage of the creation of phononic bandgaps, engineering strain and applying soft-clamping to the structures [28, 31, 72, 106, 107, 117]. Understanding and further controlling above mentioned extrinsic contributions are crucial for reaching mechanical Q factors that are ultimately limited by intrinsic loss mechanisms of the resonator material itself.

In general, there is an abundance of loss mechanisms present in mechanical resonators which would go beyond the scope of the discussions here. However, especially for the case of square membranes (as well as beams and cantilevers), a model by Villanueva and Schmid [110] has been derived based on earlier studies [119]. In particular, this model predicts the maximally achievable, intrinsically-limited Q-factors for tensile-strained resonators when acoustic radiation loss is effectively suppressed. Note, that other contributions such as viscous gas damping are not considered as a limiting factor as residual gas pressures of high vacuum are standardly achieved with reasonable effort.

The total inverse mechanical Q factor can be expressed as the sum of all individual inverse Qs, where we will only discuss the influence of acoustic radiation Q_{rad} as an extrinsic loss source and express all intrinsic contributions in the total – stress-enhanced – intrinsic Q-factor $Q_{\mathrm{int},\sigma}$.

$$Q^{-1} = \sum Q_i^{-1} = Q_{\mathrm{int},\sigma}^{-1} + Q_{\mathrm{rad}}^{-1} + \cdots \tag{3.10}$$

Let us first discuss the acoustic radiation term Q_{rad} in Equation (3.10), which reads as

$$Q_{\mathrm{rad}} \approx \frac{\rho_s}{\rho_r} \eta^3 \frac{n^2 m^2}{(n^2+m^2)^{3/2}} \frac{L}{d} \tag{3.11}$$

where ρ_r and ρ_s are the mass densities of the substrate and resonator, respectively. L and d are the side length and thickness of the membrane, and η being the phase velocity ratio between the substrate and resonator, respectively.

$$\eta \approx \sqrt{\frac{E_s}{\sigma} \frac{\rho_r}{\rho_s}} \tag{3.12}$$

Here, E_s is the Young's modulus of the substrate and σ being the residual stress in the resonator. Acoustic radiation describes the process when energy leaks into the supporting substrate. Mechanical energy of the resonator couples to substrate modes that eventually dissipate, assuming that the radiated energy does not couple back to the resonator. The amount of dissipated energy due to acoustic radiation crucially depends on the geometry, materials, modes and frequencies of both resonator and supporting material. With m, n being the characteristic mode numbers of square membranes, lower order modes are more susceptible to acoustic radiation losses than higher order modes. This has been experimentally observed by numerous groups working with such membranes. Furthermore, it shall be noted that low-stress SiN membranes usually suffer less from acoustic radiation due to their larger acoustic mismatch (phase velocity ratio η). Due to the coupling of energy into the substrate, these losses are strongly dependent on the way how membranes are mounted onto the chip holder, and thus often also referred to as clamping losses. We will later in Section 3.7 introduce a way how to avoid the leaking of energy into the substrate by engineering the supporting structure and/or the membrane itself alone with a periodic pattern that supports the rising of phononic bandgaps and thus avoids the propagation of phonons into its environment and vice versa.

Q-enhancement through stress-engineering

The first term on the right-hand-side in Equation (3.10) describes the intrinsically limited Q-factors in the presence of high tensile stress. As we have seen in this chapter residual stress generated during the growth process can affect several properties (frequencies and damping) and reliability (fracturing under tension, buckling under compression, inelastic deformation) which has proven beneficial to achieving high Q-factors. There are two factors that contribute to higher Qs. Firstly, higher stress in the material increases the stored energy, and secondly, leads to stress-induced changes in dissipation. Here, the stress-enhanced intrinsic quality factor $Q_{\mathrm{int},\sigma}$ can be expressed in terms of the intrinsic Q_{int} multiplied by an enhancement factor that is a function of λ.

$$Q_{\mathrm{int},\sigma} = Q_{\mathrm{int}} \left[2\lambda + (n^2 + m^2)\pi^2\lambda^2 \right]^{-1} \tag{3.13}$$

where m,n are the mode numbers and λ reads as

$$\lambda = \frac{d}{L}\sqrt{\frac{E}{12\sigma}} \tag{3.14}$$

The left term of the enhancement factor in square brackets in Equation (3.13) is independent of the mode numbers and can be attributed to the bending of the resonator at the clamping points with the support structure. The right term, however, depends on the mode numbers and can thus be linked to the bending at the antinodes. In order to achieve large enhancements of the intrinsic Q_{int} the expression in the square bracket has to become minimal, which translates to minimizing λ. It becomes obvious now, that the membrane dimensions crucially influence the enhancement by its aspect ratio of side length L and thickness d as the curvature of their mode displacements happen further away from the clamping periphery. Additionally, increasingly large axial strains ϵ ($\epsilon = \sigma / E$ with E being Young's modulus of the resonator material) in the square root further contributes to minimizing the enhancement factor. Note that since $\lambda \ll 1$, the first term linear in λ dominates over the quadratic term. We want to highlight though, that one possible way to minimize contributions from large curvatures close to the membrane periphery can be achieved by fabricating patterned membranes that exhibit localized modes further away from the clamping periphery [106]. Certainly, design engineering of mechanical resonators plays a major role in achieving ever-increasing quality factors that are ultimately and intrinsically limited by the resonator material itself.

Intrinsic dissipation

There is an abundance of loss contributions (thermoelastic dissipation, internal friction,...) that are discussed in much greater detail in above mentioned references, however, we will restrain ourselves to the qualitative discussion by expressing the intrinsic Q_{int} in loss contributions attributed to the surface Q_{surf} and bulk (volume) Q_{vol} material.

$$Q_{\mathrm{int}}^{-1}(d) = Q_{\mathrm{surf}}^{-1}(d) + Q_{\mathrm{vol}}^{-1} \tag{3.15}$$

For SiN membranes of thicknesses up to 200 nm, as studied within the scope of this thesis, Q_{int} is dominated by Q_{surf}, which depends linear on the thickness d with a fitting parameter β that is determined by experimental data found in literature. It is important to note, that $Q_{\mathrm{int}}(d)$ decreases for thinner membranes and counteracts the advantageous behavior for the enhancement factor in Equation (3.13). Nevertheless, it becomes clear, that surface losses pose a fundamental limitation to increasingly high Q-factors, that ultimately depend on the quality of the source material itself. The origin of these losses are possibly related to – among others – surface roughness, impurities and defects. Crucial to every fabrication procedure is thus the successful processing of materials with high selective etching and effective cleaning steps while at the same time gaining a deeper understanding of surface altering chemical processes (such as oxidation or undesired deposition of thin contaminated layers).

Low-temperature behavior

Optomechanical experiments are typically performed at cryogenic temperatures in order to observe quantum features that otherwise would be inaccessible. Mechanical resonators of sufficiently large frequencies and low enough temperatures can be prepared in their mechanical ground state without additional required optical cooling techniques. This typically the case for mechanical oscillators in the GHz-regime and at temperatures below 50 mK. Even more interestingly from the viewpoint of fabrication is the observation of increased quality factors at cryogenic temperatures orders of magnitude higher than those at room temperature [120, 125]. For temperatures below approximately 10 K, a first plateau of increased Q-factors can be observed, but even more interestingly a second steep increase below 200 mK could be measured for square membranes in a microwave circuit (despite the fact that they were coated with a thin and lossy metal). This low temperature (LT) behavior suggests that intrinsic material loss contributions are temperature-dependent with effectively lower dissipation at low temperatures. However, it should be noted, that such a monotonic increase in Q-factors as seen with SiN for decreasing temperatures is crucially material-dependent. For instance, the dissipation of crystalline AlGaAs has been found to be non-monotonic at cryogenic temperatures [6].

3.7 ENGINEERING OPTICAL AND MECHANICAL PROPERTIES

Engineering and designing devices with superior/new properties has emerged as a branch of physics where optical and mechanical properties can be arbitrarily tailored [2, 50]. Possibly the most prominent examples for such devices are metamaterials and photonic crystal (PhC) structures where the electromagnetic properties of a material layer are altered by geometric patterning. In PhC structures, the specific optical properties arise due to a periodic variation in the materials' respective refractive indices on length scales comparable to the wavelength of the impinging light. Figure 3.7 gives an example of a thin film of thickness t that is periodically patterned with air holes of radius r and lattice constant a. These structures exhibit Fano-type resonances that can be tuned by adapting before-mentioned design parameters [123]. Very similar to their electronic counterpart – where an electron in the vicinity of periodic occurring potentials of the positively charged atom cores – optical dispersion diagrams arise with allowed and forbidden wavelength ranges for impinging photons. These so called bandgaps lead to wavelength ranges where photons are not allowed to propagate, effectively depicting a mirror for photons with wavelengths within the bandgap. This lead to the development of new chip architectures with photon waveguides, photonic crystal defect cavities, DBRs [33, 34, 112] and many more applications. DBRs are maybe the easiest and most widespread example of such a composite material system. These mirrors consist of alternating layers of high and low refractive index, respectively. At each boundary between the layers the partial reflected and transmitted waves interfere. Depending on their optical thickness DBRs can be tuned such that all partially reflected waves constructively interfere leading to high reflective mirrors. The maximum reflectivity depends crucially on the number of layers and can thus be arbitrarily tuned, which we will make use of in later chapters and has also been part of very successful early-stage experiments in the field of optomechanics.

Equivalently, bandgaps can also be designed for phonons when creating a repetitive modulation of the materials' mechanical properties. By either using different materials with distinguishing Young's Modulus or/and alternating geometrically designed structures, we can also create bandgaps for phonons. This has been extensively used in so-called phoxonic structures, where cavities for both photons and phonons provide small optical and mechanical mode volumes with large modal overlap. Therefore, such on-chip structures exhibit (unprecedented) high coupling strengths making them one of the most successful experimental optomechanical platforms to date.

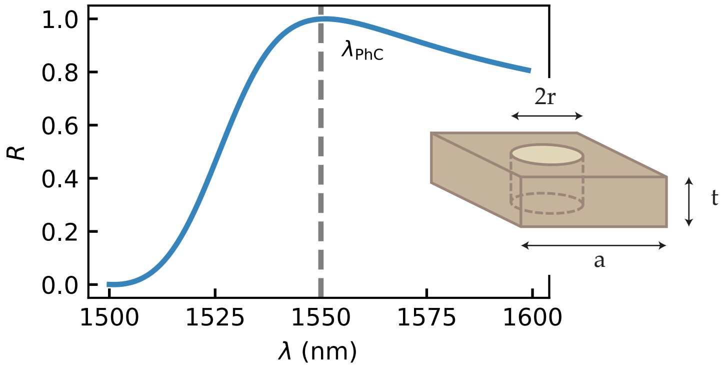

Figure 3.7: Example of the reflection spectrum of a PhC membrane exhibiting Fano-type resonances. The resonance wavelength λ_{PhC} depends on the design parameters of the PhC pattern, as illustrated with a air hole structure with lattice constant a, hole radius r and film thickness t.

In summary, manipulation of the photonic and phononic dispersion relation is achieved by changing the respective material properties (Young's modulus for phonons, permittivity for photons) on length-scales comparable to the wavelength. I have introduced two different examples of how such bandgap structures can be realized, which will be exploited in later chapters of this thesis. For one, in the case of DBRs, the rising of bandgaps come from an alternation of (at least) two materials with varying optical properties. In the case depicted in Figure 3.7, the variation is achieved through geometric patterning.

These two approaches differ in the ways of realization, where DBRs are realized by growing alternating layers of differing optical materials (bottom-up approach), whereas for PhCs top-bottom procedures by means of micro-machining are used.

3.8 CONCLUSION

In this chapter, we have given an overview of mechanical resonators standardly used in free-space optomechanical experiments with SiN membranes. Their exceptional mechanical and optical properties make them ideal candidates for numerous successful implementations in the field of cavity optomechanics. However, a well-known limitation of these devices is their susceptibility towards the mounting procedures in (cryogenic) cavity systems that can lead to a significant degradation in their mechanical Q factors due to acoustic radiation losses. Even though high mechanical quality factors can be achieved, usually tight mounting typically results in degraded Q factors that are unreliable and irreproducible. With groups working on understanding the limiting factors, dissipation models can predict the achievable stress-enhanced quality factors of square membranes when acoustic radiation losses are successfully avoided. For this matter, in particular, using the above mentioned engineering possibilities and techniques that microfabrication provides are extensively and successfully exploited in recent years that ultimately overcome the limitations of standard square membranes. Advanced device designs by engineering optical and mechanical properties by means of geometrical patterning are the basis of state-of-the-art devices and play a increasingly dominant role in fabricating more complex devices of unprecedented mechanical and optical quality by means of soft-clamping, stress engineering and the exploitation of phononic shield structures [72, 106, 107, 117].

In particular for the chapters to follow in Part ii, we will make great use of fabricating membranes with engineered optical and mechanical properties.

Part II

MICROFABRICATED MEMBRANE ARCHITECTURES

The second part of the thesis introduces novel membrane architectures with engineered mechanical and optical properties, superior to standard bare single square membranes. Each device chapter starts with a brief motivation, current limitations of the state-of-the-art and reasons why the novel devices show superior properties. Each chapter focuses on fabrication related topics. We dive into the specifics of device designs and fabrication with in-depth elucidations on challenges, solutions and future improvements. Upon availability, we also show the devices' optical, mechanical and optomechanical characterization of the engineered features.

This part contains knowledge of the fabrication for phononic shield membranes (Chapter 4), integrated optomechanical arrays of two high reflectivity SiN membranes (Chapter 5), and integrated optomechanical arrays with III-V ternary semiconductor membranes (Chapter 6). In-depth process recipes for the fabricated devices are provided in Appendix C.

4

PHONONIC SHIELD MEMBRANES FOR MULTIMODE ELECTRO- AND OPTOMECHANICS IN THE QUANTUM REGIME

Acoustic radiation loss of square SiN membranes inside optical cavities constitutes a challenge for reaching the multimode strong quantum cooperativity regime in an inherently multimode optomechanical system. However, for the observation of quantum features such as entanglement between optics and mechanics, reaching the strong cooperativity is typically a key criterion. A particularly successful way in circumventing the current limitations is engineering phononic bandgap structures that effectively shield the center square membrane from outside excitations promising intrinsically-limited quality factors, i. e.limited by surface losses of the material itself, for all modes within the designed bandgap. Here, we realize phononic bandgap shielded membranes by patterning the entire silicon chip with a periodic structure in a through-wafer deep silicon etch. By optimizing the device design, we achieve bandgaps of 2.5 MHz width that effectively shield the first ten mechanical modes from undesired outside excitations. We confirm the existence of the designed bandgap when incorporated in an optomechanical cavity by measuring suppressed noise power spectra and consistently high mechanical quality factors of around 6×10^6 at cryogenic temperatures for all modes within the designed bandgap. This paves the way towards entering the strong cooperativity regime for a multitude of modes ultimately enabling the observation of strong quantum correlations and as such entanglement between optics and mechanics.

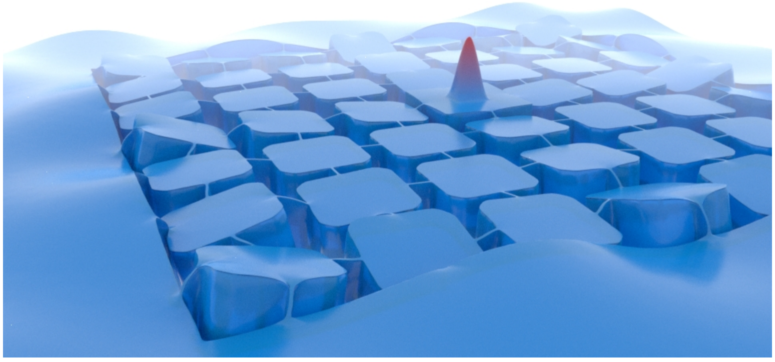

Figure 4.1: Artistic illustration of a phononic shield membrane (©Moritz Forsch, GroeblacherLab, TU Delft). Illustrated are a collective mode of the lattice and central square membrane.

4.1 INTRODUCTION

One of the outstanding goals in free-space optomechanical systems is the generation and detection of non-classical states between light and mechanics such as entangled states. This goal has already been achieved in the microwave regime [76] and for on-chip platforms with photonic and phononic crystal patterned nanobeams [83, 84]. In the case of the latter, the generation and detection of entanglement has been shown in the pulsed optomechanics regime using red and blue detuned pulses and subsequent detection of resonantly scattered photons. In contrast, modifying the ideas from pulsed entanglement schemes by Hofer et al. [44], the developed protocol for MIM setups uses continuous wave (CW) light that resonantly drives the optical cavity and also accounts for the inherent nature of the multimode membranes [42]. More precisely, in the resonantly driven case, the optomechanical interaction creates sidebands that are red- and blue-detuned by the mechanical frequency. We detect the cavity interacted light with homodyne detection and evaluate both amplitude and phase quadratures of the generated sidebands in post-processing. For more insights into the experimental realization and applied post-processing schemes I want to refer to the theses of my colleagues Hoelscher-Obermaier [42] and Nia [71].

Determining factors and figures of merit

For the generation of entanglement, we need to typically satisfy $C_q \gtrsim 1$, the quantum cooperativity of the optomechanical system being on the order and greater than unity. On the fabrication side that means – as per usual – fabricating mechanical resonators with mechanical quality factors as high as possible. Square SiN membranes such as those introduced in the Chapter 3 are ideal candidates for meeting the requirement of mechanical resonators exhibiting low decoherence rates $\bar{n}\gamma = k_b T/\hbar Q$. Depending on the side length of those membranes, Q factors of several tens of millions have been reported at room temperature with even larger Q factors at cryogenic temperatures [120].

From single-mode to multi-mode entanglement

Despite the fact that we have measured mechanical Q factors as high as 3.5×10^7 for higher order modes, especially low-order modes are more susceptible to acoustic radiation losses and thus constitute a challenge to the generation of entanglement in an inherently multimode mechanical system. The main challenge for the generation and detection of entanglement is to guarantee sufficiently low thermal decoherence rates of many modes across a wide range of frequencies whilst at the same time providing large interaction rates $4g^2/\kappa$, effectively satisfying operation in the strong quantum cooperativity regime. However for the case of membranes with a densely spaced mode spectrum, low-Q neighboring modes effectively constitute a source of noise, which makes the verification of entanglement impossible.

In addition, increasing the intermode frequency spacing between adjacent modes turns out to be of importance for the preservation of entanglement whilst providing consistently high mechanical quality factors. However, it is well-known that membranes rigidly mounted (that means e. g. clamped or glued) on a holder plate suffer from additional acoustic radiation losses into the substrate [113]. The way forward to circumvent induced clamping loss is to mechanically shield the membrane modes from its environment, which has been suggested and successfully implemented using phononic band gap structures [72, 107, 117, 118]. It has been shown, that all the modes within the designed band gaps are effectively shielded from unwanted outside excitations and follow the expected dissipation rates for intrinsically limited quality factors for given dimensions.

The issue of classical laser noise

Even though the fabrication of larger and thinner membranes are usually beneficial for achieving lower decoherence rates, the accompanying reduction of their resonance frequency, however, poses an issue with introduced classical laser noise. Another important boundary condition for observing quantum features is shot-noise limited drive and detection, which – in our setup – is provided for mechanical frequencies above 1 MHz. Initially, in order to fulfil this condition, we addressed mechanical modes of higher order that promised to meet the requirements of sufficiently large mechanical frequencies and Q factors. Unfortunately, post-processing the recorded data showed that the dense spacing for higher order modes presumably poses a significant challenge for the preservation of entanglement if one cannot guarantee high Q factors for all mechanical modes.

Nevertheless, for the achieved quality factors of state-of-the-art membranes, entering the strong cooperativity regime is feasible already with cavities of moderate finesse values of several thousand and sufficiently strong input power [71].

4.2 DEVICE DESIGN

In the previous section, we have introduced important boundary conditions for the design properties of the mechanical membranes. We aim for frequencies greater than 1 MHz while being able to mount them in a cryogenic cavity and still maintain highest quality factors. Assuming a tensile stress of around 1 GPa requires membranes with side lengths of approximately 350 µm (cf. Equation (3.9)). Considering a cavity beam waist of 50 µm, both conditions of large enough frequencies while still being able to avoid optical clipping losses are fulfilled. (Actually, we have seen that even membranes as small as 300 µm can still be successfully aligned without seeing a noticeable degradation of the cavity finesse caused by clipping losses). In principle, smaller laser beams at the cavity waist would also be possible for slightly adapted cavity designs and thus allowing for even smaller membranes, however with slightly reduced quality factors (cf. Section 3.6 in Chapter 3).

Membranes in the MHz*-regime*

Membranes of 350 µm in length exhibit frequencies of their fundamental mode of around 1.18 MHz, thus fulfilling the requirement of shot-noise limited detection. In terms of mechanical Q factors, as seen in the chapter before, bigger aspect ratios are advantageous.

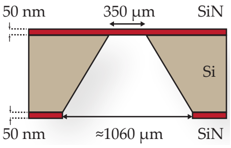

Thinner membranes with similar lateral dimensions only show slightly larger Qs, while at the same time smaller reflectivity and thus coupling strength. In addition, by changing the membrane thickness, we also affect its mass. Taking all parameters into consideration with the aim of maximizing the cooperativity, we decided to exploit membranes of 50 nm thickness.

4.2.1 *Phononic shield design simulations*

In order to effectively avoid mechanical energy of the membrane to dissipate into the substrate we aim to design bandgaps that fit as many mechanical modes possible by periodically patterning the entire substrate with a repetitive structure. Considering above mentioned criteria on the eigenfrequencies of the membrane, we analyze various designs and optimize their geometry for bandgaps as wide as possible starting from around 1 MHz based on designs found in the literature [72, 107, 117, 118]. The calculations of the band diagrams are carried out in COMSOL[1] through the eigenfrequency analysis, where we first study the geometries of various unit cells with Bloch-Floquet boundary conditions. This assumes an infinite structure with periodicity of the size of the unit cell and calculates the eigenfrequencies for various wave vectors in the 3D lattice – along the reduced Brillouine zone in two dimensions.

We can estimate the length of the unit cell by using the relationship between wavelength, speed of sound and frequencies for phonons. With the speed of sound in silicon of 2200 m s^{-1} and target frequencies for the bandgap of around 1 MHz, this translates to unit cell (UC) sizes of roughly 1 mm, which we will keep fixed in the following. Changing this parameter mainly effects the center frequency of the created bandgaps and can thus be adapted for phonons of different frequencies.

---

[1] `https://www.comsol.com/`

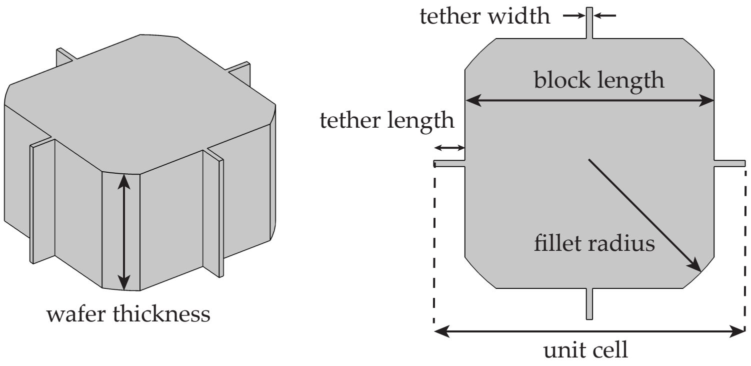

Figure 4.2: Schematics of phononic shield cross structure and its parameters.

MATERIAL PROPERTY	VALUE FOR SIN	VALUE FOR SI
Young's modulus, E (GPa)	250	170
Poisson ratio, ρ	0.23	0.28
Tensile stress, T (MPa)	$800 - 1200$	-
Densitiy, ρ ($10^3\,\mathrm{kg/m^3}$)	3.1	2.3

Table 4.1: Material properties of SiN and Si, taken from the COMSOL library.

Figure 4.2 shows an overview of tested design geometries and their varied parameters. The main objective for this project was to find a geometry that can effectively shield as many mechanical modes of the square membrane as possible in order to avoid additional acoustic radiation losses – especially for the lower order modes more susceptible – induced by the mounting procedure inside an optical cavity. The design parameters such as tether length and width, block size, fillet of the block corners as well as wafer thickness all contribute to changes in the resulting bandgaps. We have found that wider bandgaps are achieved on thicker substrates and thus limit the discussion to substrate thicknesses of 500 µm. All of the geometries considered provide bandgaps in the desired frequency range with only small deviations in the bandgap size. We will later see that some geometries are more suitable for the feasibility in fabrication than others, especially when it comes to the etching of large aspect ratios in deep silicon etch (DSiE). The designs taken into consideration all require a deep silicon etch through the entire wafer thickness. Deeper etches with small feature sizes – i. e. larger aspect ratios – are more challenging to carry out. We thus restrict ourselves to substrate thicknesses of 500 µm that result in broad bandgaps at our desired frequency range. Taking these fabrication related challenges into consideration and since all geometries show similar performances, we focus on analyzing the simpler cross design depicted in Figure 4.2b. This design only differs from the slightly more complex trefoil design Figure 4.2a by not having (ideally) small feature cuts around the tethers which ultimately makes this design more challenging to be carried out in deep reactive ion etching (DRIE).

Thin tethers for better bandgaps

One of the most crucial parameters on the bandgap is the tether width. It has been shown, that narrow tethers lead to wider bandgaps. For increasingly large tether widths above 20 µm we find that the lower bandgap mode shifts to higher frequencies, which we need to avoid such that the fundamental frequencies of the square membrane is still considerably larger. Note, that increasing the fundamental mode frequency is a possibility but due to constrictions in both mechanical Q factors as well as optical beam sizes, we decided to keep the membrane size of $\approx$ 350 µm – equivalent to a fundamental mode frequency of around 1.2 MHz – fixed.

Another aspect is to consider the influence of design parameters in terms of fabrication imperfections. This raises the question how well the design parameters can be matched, especially for design parameters that have a stronger influence on the bandgap for small variations in design dimensions. Essentially, we have found that the tether width depicts the most crucial design parameter, as it defines the mass ratio between the heavy block region and the tethers.

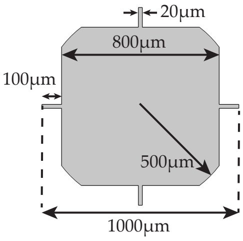

After systematically sweeping the above mentioned design parameters, we have found the design shown on the side the most appropriate for our purposes. The analyzed design results in a bandgap ranging from 1 MHz to 3.6 MHz with one additional eigenmode of the lattice sitting at around 2.7 MHz (cf. Figure 4.3). Since this mode seems to be independent of the wave vector k we consider this mode to not play a significant role for as long as one of the mechanical resonances does not get significantly close in order for them to couple. We want to note here that this mode can be effectively shifted above the upper bandgap mode by reducing the radius of the block fillet from 500 µm to 400 µm with the drawback of also shifting the lower bandgap mode to slightly above 1.2 MHz. As elucidated before, we prefer keeping the lowest bandgap mode as low as possible and sacrifice the rising of a lattice mode that - presumably - does not negatively affect the shielding of sufficiently far away mechanical modes.

Full 3D design simulations

In order to verify whether the found geometry really exhibits a bandgap within the found frequency band, we execute full 3D bandgap simulations in the frequency domain. Figure 4.4 shows the results of

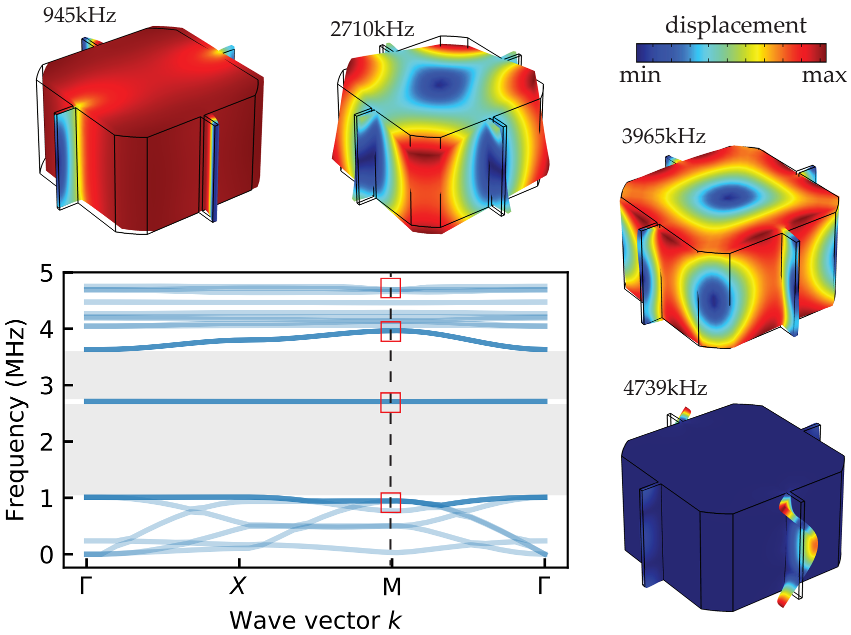

Figure 4.3: Bandgap design simulations of the unit cell along the irreducible Brillouin zone including mode profiles of various frequencies evaluated at wave vector M.

the entire structure under investigation including the defect center cell hosting the square membrane of 350 µm in side length. Note, that due to fabrication related reasons, the defect cell measures 1050 µm in length without rounded corners and is thus slightly bigger than the designed unit cell. The entire chip has a side length of 10 mm and can therefore fit seven unit cells in total. The outer region of the chip design is assumed to be excited with a prescribed displacement. In order to effectively determine and quantify the effectiveness of the shielding, we calculate the ratio of the elastic strain energy (evaluated in COMSOL by volume integration) stored in the defect cell (DC) normalized to that in the entire structure – according to the bandgap analysis performed by Yu et al. [118] (Equation (4.1)). We also refer to the ratio as a partition coefficient ϵ where lower values are thus an indicator for good shielding from outside excitations with values orders of magnitude lower than for frequencies outside the bandgap.

$$\epsilon = \frac{\int_{\mathrm{DC}} \rho(x) u(x)^2 d^3x}{\int_{\mathrm{whole}} \rho(x) u(x)^2 d^3x} \tag{4.1}$$

The results of the 3D simulations are shown in Figure 4.4 and clearly show the shielding effectiveness of the periodic pattern. In the gray-shaded region obtained from the bandgap simulations of the unit cell alone (cf. Figure 4.3), we can identify a reduction of the partition coefficient by orders of magnitude with respect to values outside

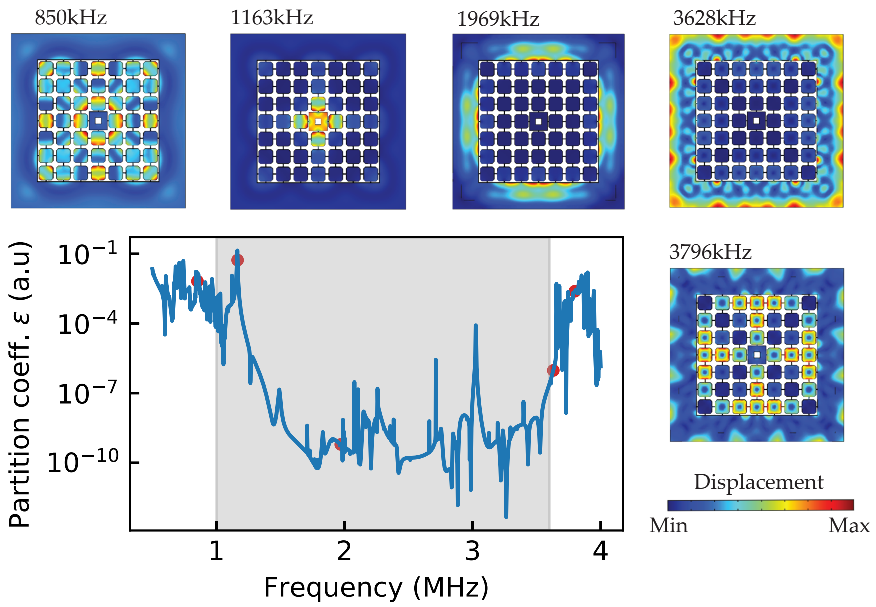

Figure 4.4: Bandgap design simulations for the full 3D structure. The graph shows the evaluated partition coefficient ϵ for optimized phononic shield design parameters resulting in wide bandgaps. Low values correspond to effective shielding, whereas high values correspond to frequencies outside the bandgap. In addition, chosen mode profiles for lattice eigenmodes both inside and outside the bandgap are depicted, showing the effectiveness of shielding the center defect cell from outside excitations (also marked as red points in the graph).

the bandgap. The observed shielding coincides well with the results from the unit cell simulations. Additionally, we also show various eigenfrequencies of the entire structure for frequencies inside and outside the bandgap, which visually underline the effectiveness of the bandgap structure.

4.3 DEVICE FABRICATION

4.3.1 *Fabrication overview*

Our devices are fabricated in 50 nm thick stoichiometric SiN deposited via low-pressure chemical-vapor deposition LPCVD on a plain 500 µm-thick Si substrate. As a first step, we fabricate a square membrane with a side length of around 350 µm in order to meet the requirements for mechanical frequencies larger than 1 MHz. A more detailed description of the fabrication of square membranes is given in Chapter 3 and will only be discussed briefly here. Alternatively to the fabrication of custom-made membranes, one can directly start with the ones com-

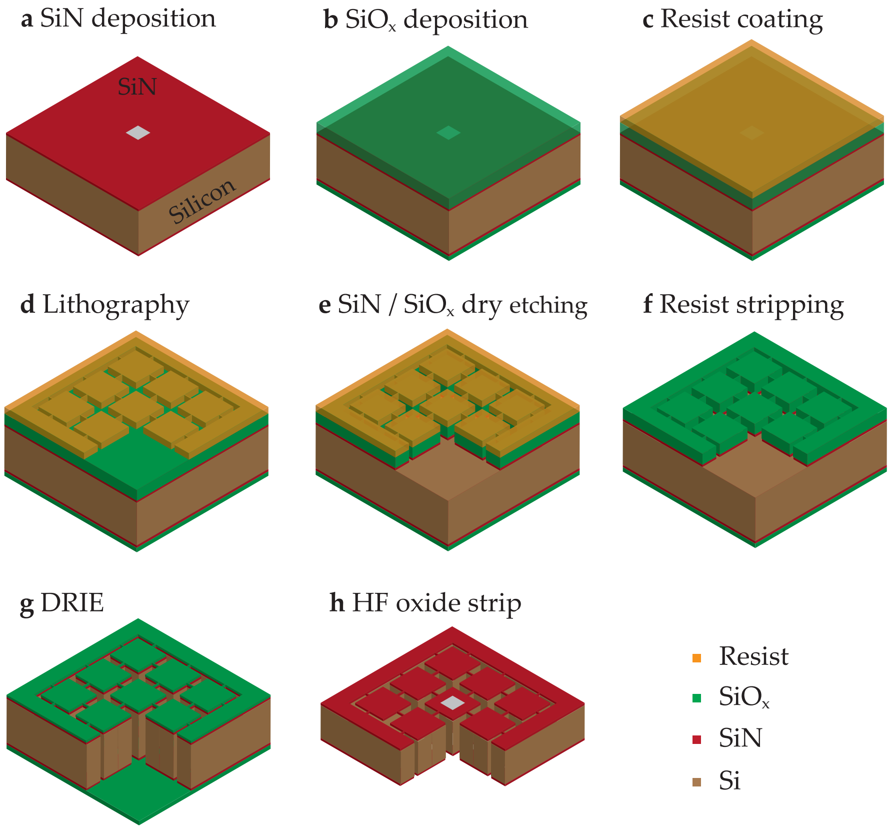
a SiN deposition
b SiO$_x$ deposition
c Resist coating
SiN
Silicon
d Lithography
e SiN / SiO$_x$ dry etching
f Resist stripping
g DRIE
h HF oxide strip
Resist
SiO$_x$
SiN
Si

Figure 4.5: Fabrication flow of phononic shield membranes. **a** Starting point is a simple SiN square membrane on a silicon wafer, followed by deposition of the oxide hard mask (**b**) and standard lithography of the phononic shield (PS) design (**c-d**). The PS pattern is subsequently transferred into the oxide hard mask and the remaining resist is stripped (**e-f**). Then, the entire thickness of the silicon wafer is fully etched by means of deep reactive ion etching (DRIE) until reaching the oxide etch stop layer at the bottom (**g**). Finally, the remaining oxide hard mask is stripped in (dilute) HF and dried by critical point drying (CPD) (**h**).

mercially available from Norcada[2], if standardized membrane sizes meet the experimental requirements.

The membranes are defined by patterning the backside of the wafer with a square that is further transferred into the SiN layer by means of a fluorine-based RIE-process (CHF_3). For membranes with side lengths of 350 µm on 500 µm thick <100> Si substrates, the backside window measures approximately 1050 µm – 708 µm wider in order to account for the characteristic orientation-dependent Si etching in KOH. The resist is stripped with an appropriate solvent and optionally, additionally cleaned with hot Piranha solution at 100 °C, making sure that all organic residues are thoroughly cleaned off the surface. The square membranes are released during the KOH etch through the entire thickness of the wafer, followed by a 10 min diluted HCl solution that cleans off KOH residues of the exposed surfaces. Note, that cleaning the chip before the KOH step is not necessarily required as it is stripped during the long etching step itself. Additionally, we have found that the hot Piranha cleaning step can be done both before or right after the KOH release itself to have a pristine chip ready for further processing.

---

[2] https://www.norcada.com/products/high-q-si3n4-membrane/

In the second part, we fabricate the PS structure into the substrate with the already released membrane. We, therefore, first deposit 3.5 µm of PECVD silicon oxide at 300 °C that serves as a hard mask followed by spin-coating a positive electron-beam resist (AR-P 6200.18) at 3 krpm, resulting in 1 µm thickness. Additionally, we also deposit 700 nm SiO_x on the backside with the same recipe right after front side deposition. For one, it protects the membrane from undesired contamination by the heat conducting oil during later etching steps and secondly acts as an etch stop layer during DRIE[3]. We then lithographically define the resist layer in the front in the shape of our PS structure and transfer the pattern into the oxide layer with a $C_4F_8/He/CH_4$ plasma etch. The remaining resist layer is afterwards stripped completely and the chip is mounted on an oxide carrier wafer for the through-wafer-etching by means of DRIE, ensuring vertical sidewall profiles within an angle of 1 %. Heat removal during the DRIE is crucial[4] and partly ensured by He-backside cooling and contacting with a thermal heat conducting oil between chip and carrier wafer, the choice of platen temperature for reproducible etch results. After etching through the entire wafer, the formed passivation layer during the DRIE process is removed with a 10 min oxygen plasma inside the DRIE chamber. It is crucial here, that the platen temperature does not exceed 200 °C that the conducting oil does not change its chemical properties and makes it impossible to remove the sample off the carrier wafer. Removing the chip off is then done by first rinsing the wafer in ethanol and gently pushing and lifting it off the surface, followed by more thorough cleaning steps for removing remaining organic residues consisting of a 10 min hot bath in PRS at 80 °C and a hot Piranha clean at 110 °C. This ensures that the entire chip is thoroughly cleaned off the conducting oil. As a final step we strip the remaining oxide hard mask in a (diluted) solution of hydrogen fluoride (HF), followed by consecutive rinses in water and IPA before drying the chip in a CPD.

---

[3] Note, that in principle, a resist-only process could be worked out even for 500 µm thick substrates which we will see later can be advantageous when working with certain metals. Furthermore, it should be also noted that the fabrication of PS devices does not require the usage of EBL, however, due to convenience of adapting design parameters and availability, we continued using EBL over PL.

[4] Even more important for resist masks that suffer from resist burn

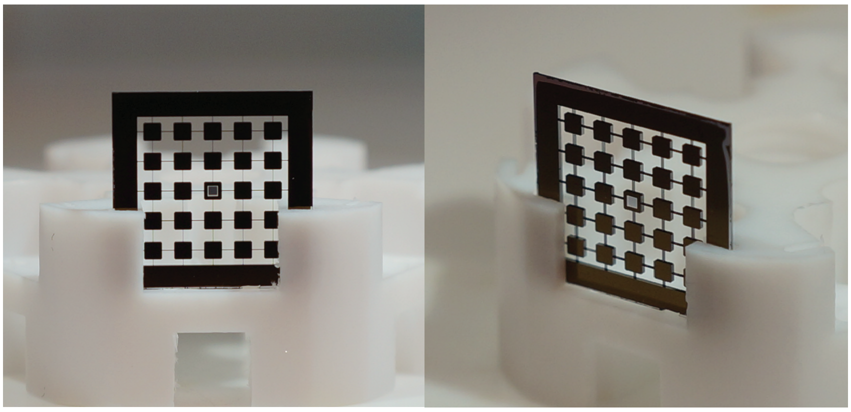

Figure 4.6: Photographs of final phononic shield devices. Devices shown here are fabricated on $10 \times 10\mathrm{mm}^2$ chips fitting five unit cells of 1.5 mm in total. Here, the square membrane in the center defect cell is coated with a 20 nm-thin metal film of an aluminum-silicon alloy.

4.3.2 *Deep silicon etching*

In the following, we want to discuss details of the DSiE since it constitutes the most crucial step in the fabrication of PS devices based on patterning the entire thickness of the wafer. We first introduce DSiE in a more generic fashion before moving on to a more detailed description of the process used during the fabrication of our PSs – the standard BOSCH DRIE process for through silicon etching.

General aspects

DRIE or also DSiE is a process widely used in MEMS technology for etching structures with high aspect ratios and the need for vertical sidewall control. Modern DRIE tools nowadays come with advanced hardware allowing to have more process control and thus exploiting a wider range of possible applications with adapted etch recipes. Usually, DSiE is a very fast etching process for arbitrary feature sizes. However, the etching process crucially depends on the features to be etched with higher etch rates for increasingly large features. This situation is usually referred to as aspect ratio dependent etch (ARDE) which implies same feature sizes on a single etch process for best etch results.

In principle, modern DSiE tools provide two different types of etching. The standard DRIE consists of a repetitive cycle alternating between an isotropic etching step with SF_6 and a subsequent passivation step with C_4F_8 as illustrated on the side. With optimized process parameters between etching and passivation, one can achieve the typical vertical sidewall profile for DSiE with its characteristic scalloping. The faster the switching times between the cycles and the shorter the etch duration, the smaller the scalloping becomes, which can result in very

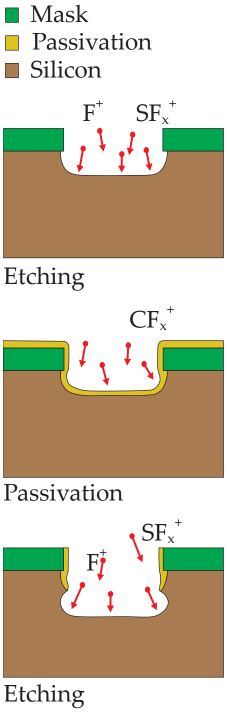

smooth sidewalls. Achieving even smoother sidewalls without any sort of scalloping can only be achieved with a continuous etch, where both etching and passivation happens at the same time. This process is usually referred to as cryogenic silicon etching where sidewall profile control is primarily achieved by adjusting the temperature and gas ratio (SF_6/O_2).

Especially for increasingly complex structures, a larger range of process parameters is desirable to adapt and optimize etch recipes to one's specific needs. For instance, important aspects are etching processes with high etch rates while maintaining a high selectivity between the silicon and masking material. Maximum selectivity is achieved by adding an additional step to the two-step etch-passivation cycle where the bias is only on during the so-called breakthrough step. This reduces the etch rate of the masking material while maintaining the high isotropic etch rate of the silicon, thus becoming more selective. Other interesting applications involve high aspect ratio (HAR) etching, where the etch depth becomes relatively large with respect to the feature sizes. This requires to significantly increase the relative amount of polymerization during the process in order to protect the sidewalls from damaging. Especially in deep and narrow features, the charged sidewalls lead to an increase in ion deflection which threatens to penetrate the existing protective passivation layer of the sidewalls. To obtain best results, the process can additionally be split into several different stages, as the optimal process balance changes with increasing etch depths.

Nowadays with advanced processing tools, i. e. better hardware in terms of faster gas switching times, increased process parameter control and etch depth dependent process details, the amount of control and flexibility for all sorts of DSiE is steadily improving, which is also of great significance for the fabrication of phononic shield devices.

Specific aspects

During DRIE a significant amount of heat is generated by the continuous deep etching, often resulting in photo resist (PR) burning. One way to avoid burning of the PR is to reduce the heat load by e.g. reducing the ICP power, the table temperature or increasing the Helium backside pressure for better cooling. On the PR side, switching to multiple layers of thin resists might be more resistant to a single layer of thick resist. Alternatively, a hard bake step after development can improve resist resistivity further. In terms of sample mounting, it is recommended that both for mounting purposes as well as heat conductance, an appropriate oil or heat paste is used. In our case, we use PFPE oil. Together, these steps are sufficient to completely eliminate the burning of the PR and thus provide good control over the resist selectivity and cleanliness for further processing.

Alternatively, especially also recommended for very deep etching where the selectivity poses a limiting factor, PR masks can be replaced by harder masking layers such as silicon oxide (SiO), which is the use of choice throughout the fabrication of phononic shielded membranes within the scope of this thesis.

After performing first initial etch tests at etch depths targeting about half the thickness of the wafers, slightly re-entrant side wall profiles are observed. Since DSiE is ARDE, meaning that the etch characteristic depends on both feature sizes to be etched and their etch depth, a etch depth dependent recipe is needed to maintain good side wall control throughout the entirety of the wafer. The process was adjusted to improve profile and extended to near full depth, while introducing staging that modifies process parameters with depth. This is essential to achieve best process results in through wafer etching of relatively small features with strict requirements for vertical side walls. This plays an even more important role for our design where the fabrication of narrow bridges of only 20 µm requires very good control over maintaining the vertical etch profile throughout the entire wafer thickness. This is the reason where staging and faster gas flows with overall better etch control helps tremendously in achieving the realization of devices with strict design parameters.

Optimization of the process parameters for various depths leads to nearly perfectly vertical, smooth sidewalls for 50 µm trenches, while the etch profile for increasingly large features remains slightly re-entrant. Large amounts of excess polymer formation on the side walls are cleaned off in a post-DRIE 10 min O_2 polymer strip. The overall process shows excellent profile and good sidewall quality for the target features of around 50 µm.

Up until this point, all samples used were etched without the usage of a stop layer on the bottom side of the wafer, which resulted in exposure to the PFPE oil upon breakthrough. It is recommended to apply an etch stop layer on the back side of the chip such that the sample is protected from the mounting oil. For final samples, a 500 nm thick etch stop layer of PECVD oxide was also deposited on the backside. This not only protects the etched features from exposure to heat conducting oil, but also protects the backside of the already suspended SiN membrane from it. Additionally, subsequent additional cleaning steps of the oil removal can be done while stripping the oxide masks without the actual chip surfaces ever getting in contact with the oil.

However, using a dielectric etch stop layer can lead to increased lateral etching near the bottom oxide, usually referred to as notching. In order to reduce this effect when a bottom oxide layer is present, a recipe using pulsed low frequency (LF) power is desirable. This process can be extended in depth in a similar fashion as described above in order to reduce notching effects. Again, especially for narrow bridges, the reduction of notching is desirable in order to maintain perfect etch profiles according to the design. Taking into consideration that notching occurs only at the bottom of a thick wafer with only small relative changes with respect to the phonon wavelength, we do not expect the resulting bandgaps to shift tremendously compared to their simulated frequency range and has thus not been optimized at this stage of the project. However, for the sake of completeness, it shall be noted that notch control can be achieved upon necessity.

4.3.3 *DRIE process development*

Wafer preparation

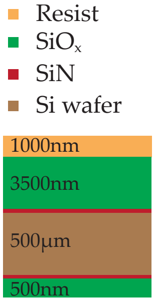

Optimization of process parameter that satisfy the requirements on sidewall profile and quality usually demands several iterations of tweaking the vast parameter space. It is therefore recommended – for issues of effective time management – to prepare a whole wafer with test chips. Our chips contain several designs of studied phononic shields with a finite amount of unit cells as well as etch test lines that later allow an easy and efficient characterization of the etch results in a scanning electron microscope (SEM). It is sufficient to start the fabrication of said DRIE test wafer without the LPCVD SiN device layer and just start depositing the oxide hard mask right away. In our case, we deposit 3.5 µm of PECVD silicon oxide at 300 °C, followed by spin coating AR-P6200.18 positive e-beam resist at a speed of 3 krpm, resulting in a sufficiently thick resist layer of approximately 1.0 µm thickness. In the following, the main objective is to optimize the process parameters for reaching vertical sidewalls with sufficiently large etch selectivity between the various layers.

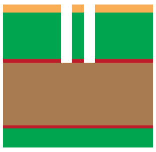

Dry etching

Oxide hard mask etching

For the pattern transfer into the oxide hard mask we use a C_4F_8 based gas mixture at 10 °C. It is important that the bias is high enough to overcome the threshold above which etching of oxide occurs. Otherwise, polymer deposition occurs at the chip surface which seals the etch openings and stripping both resist and oxide layer becomes necessary. For optimized process parameters, an etch selectivity of around 4 to 5 can be achieved for RF biases just above the threshold for oxide etching with decreasing etch selectivity for increasing RF powers (meaning that the oxide etch rate is 4 to 5 times that of the resist). With that selectivity at hand, oxide masks of up to approximately 4 µm can be successfully prepared for subsequent processing steps which will be sufficient for etch selectivities achieved in the subsequent DRIE process. It shall be mentioned here, that the etch details are slightly different for full wafer processing in comparison to those of smaller chips. As an example, we have found necessary to increase the RF power significantly in order to achieve similar etch rates on the wafer with respect to achieved etch rates on smaller chips. Additional aspects to keep in mind – among chief – are uniformity, etch rates and thus selectivity, and load, i. e. areas to be etched.

After having successfully opened the oxide hard mask layer, the wafers are then ready to be diced in individual $10 \times 10\text{mm}^2$ chips which we will now use for the DRIE optimization process. A 4-inch wafer fully covered contains roughly 49 chips of said size giving plenty of opportunity to tweak the process without the need of repeating the earlier steps of oxide deposition, lithography and oxide etching.

Deep reactive ion etching

DRIE

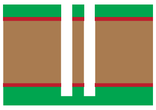

We mount individual chips on an silicon carrier wafer with a 5.3 µm thick thermal oxide layer on top that protects the silicon from being etched during the DRIE process. Exposure of entire silicon wafers to the etch chamber would result in totally different etch results due to the increased load and thus have to be avoided. A heat conducting oil not only holds the chips in place but also guarantees proper thermalization during the continuous heat-producing DRIE process which is crucial for reproducible etch results. In general, the temperature of a process significantly influences the etch results and therefore plays a major role in maintaining the process balance for optimized gas ratios and temperatures that leads to the desired etch profiles.

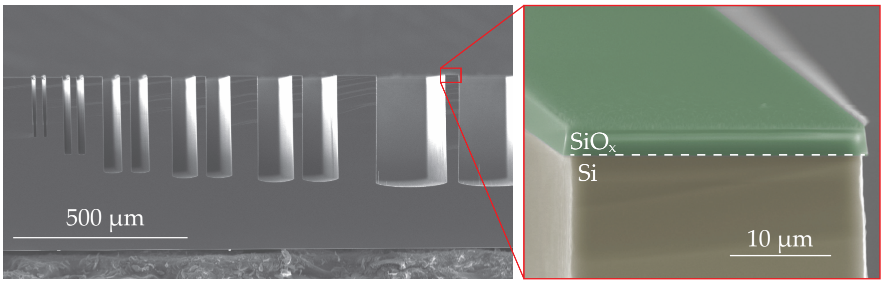

Figure 4.7: Deep reactive ion etching (DRIE) of test structures. Etch test lines of various feature sizes are etched into an oxide hard mask and subsequently etched into the silicon wafer. Inspection under cross-section is performed with a SEM revealing the aspect ratio dependent nature of the etch process up until a certain feature size beyond which the etch rate remains constant. The image on the right shows a zoom-in with which the etch rate of the oxide hard mask (green) and thus selectivity can be determined.

Figure 4.7 shows early stage etch results investigated with a SEM. The cleaved chips are mounted such that the sidewalls can be inspected under various angles. We observe an aspect ratio dependent etch which means that the etch rate varies with feature size. For that purpose the etch test lines in the design have varying widths from

20 µm to 300 µm. An important figure of merit for the successful etching is the achieved side wall profile and accompanying etch selectivity between oxide mask and silicon which can be determined by measuring the layer thickness and etch depths, respectively, before and after the etching for a given etch duration. In Figure 4.7, inspection with an SEM under a cross-sectional view reveals the silicon etch depths and remaining oxide layer.

Additionally, with the already available etch parameters at hand, we perform full through-wafer etching for designs initially considered with the etch results shown in Figure 4.8. In addition to the simulated cross design (right structure in Figure 4.8), we also tested the slightly more challenging trefoil design with the main difference between both designs being the narrow feature cuts around the tethered region (It shall only be mentioned here that decreasingly small features – as small as only 20 µm – lead to wider bandgaps). With the observed feature size dependent etching above, it becomes clear now that through-wafer-etching of simultaneously small and big features lead to differing breakthrough times, meaning that larger features with higher etch rates can thus be etched through the entire wafer significantly faster than is the case for small features. Moreover, with lower etch selectivity for smaller features due to their lower silicon etch rate, we opted for a minimum feature size of 50 µm in order to successfully perform full through-wafer etching without the need to adapt the current fabrication flow.

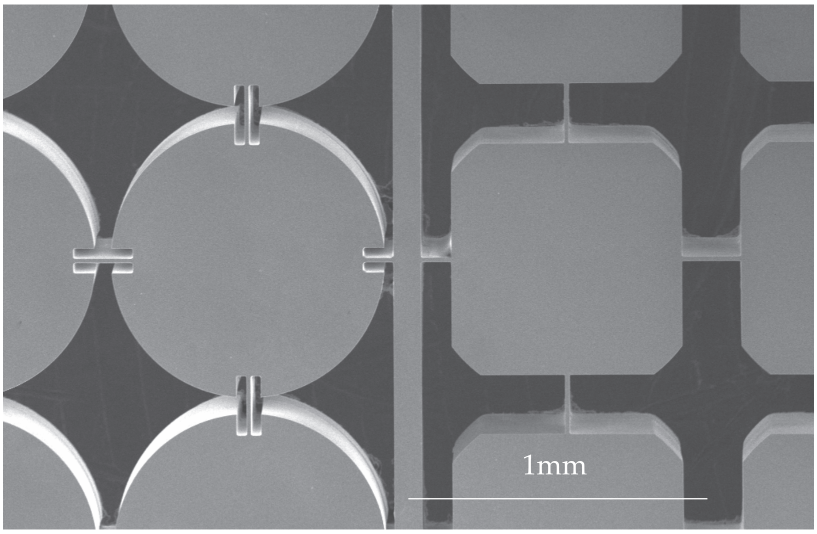

Figure 4.8: Deep reactive ion etching of two different phononic shield (PS) designs. The structures are etched through the entire thickness of a wafer and inspected with a SEM from the top.

Optimized DRIE process

We summarize the most important aspects for improved DRIE performance concerning both etch related as well as design related considerations. Vertical side wall profiles for through-wafer etching of 500 µm thick wafers are achieved for features of around 50 µm by introducing staging, i. e. the process details are controlled and adapted dependent on the etch depth. We can determine the etch rate of the etched silicon features (8.1 µm/min) and compare it to the etch rate of the oxide hard mask (47 nm/min), resulting in a selectivity of around 173. Higher values of 200 can be achieved with slightly adapted etch details that mainly reduce the oxide etch rate. The optimized recipe includes adaptations to existing issues that are further discussed in the section to follow. To summarize them, we make adaptations to the design by making sure that only similar features of 50 µm in size are exposed in order to ensure consistent etching and vertical side wall profile. This greatly reduces the over etch duration and thus notching, i. e. undesired lateral etching at the bottom of the wafer after breaking through the bottom SiN layer. Moreover, we introduce an oxide etch stop layer that protects the backside from exposure to the conducting oil which can then subsequently and more conveniently cleaned off without possibly compromising the SiN film quality of the already suspended membrane.

4.3.4 *A closer look on certain aspects*

Notching

The primary cause of notching in DSiE processes are charging effects at the dielectric interface at the bottom of the sample. Accelerated (positively charged) ions towards the bottom of the etch are deflected towards the sidewalls that are also positively charged leading to an increased passivation removal at the base and hence an occurring subsequent lateral isotropic etching. As a secondary cause, heating of areas with – especially thin – Si tend to have reduced sidewall passivation which results in a breakthrough at the base. This becomes even more dominant the thinner the bridges become. How much this effect matters for 20 µm thin bridges in our design has not been studied thoroughly enough. Controlling notching effects for very deep etches with very thin Si features becomes increasingly important. Nevertheless, even small notching effects of a few µm are not assumed to have a strong effect on the bandgap, since only a small percentage of the whole substrate thickness is effectively thinned down. Usually, notching occurs mainly when small feature sizes are present – as e.g. for small deep trenches, vias or pillars, where larger fractions of ions hit the sidewalls. Equally bad are long overetching durations since the lateral sidewalls are much more exposed at the etch stop layer.

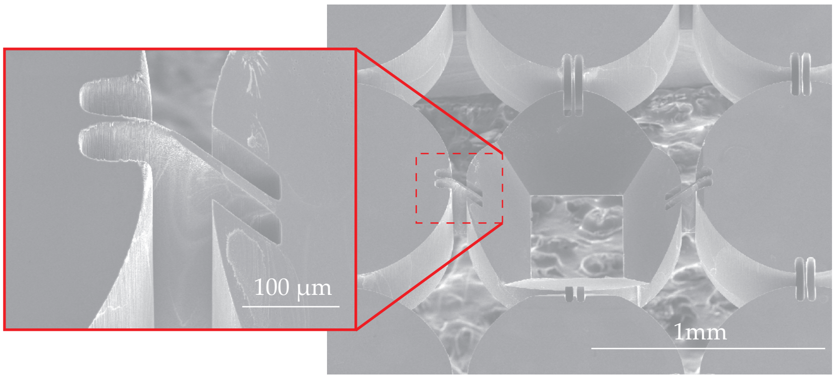

Figure 4.9: Notching issue for deep reactive ion etching. SEM images taken from the backside of a fully etched chip including the central defect cell with a broken membrane. Common issues of notching especially at the tether regions with small features can be observed (zoom-in). In addition, larger center defect cells adapted for the large membrane backside opening due to the angle dependent etching in KOH might be desirable.

Solutions to the notching issue are to minimize the overetch, the increase of passivation during the overetch and faster switching times that refreshes the polymer formation on the sidewalls. In order to minimize an overetch, one should use similar feature sizes such that the entire wafer is fully etched through at similar times, ideally combined with sacrificial layers with endpoint detection.

In addition, using a LF plasma mode helps in reducing charging compared to the standard high-frequency bias. Reduced charging ultimately reduces the ion deflection and hence notching.

Breakdown

Breakdown describes the process of undesired removal of the passivation layer on the sidewalls. This is dependent on the depth of the etch and can thus be adjusted gradually by e. g. increasing the ratio of passivation and etching step throughout the entire process (staging). Alternatively, increasing the deposition power, flow and time, as well as reducing the ion flux due to a reduction in etch bias and time can help solve the problem. Since this issue crucially depends on the aspect ratio and feature sizes to be etched, it is beneficial to design the entire structure with similar feature sizes. This allows to optimize the etch characteristic of specific features with a well-balanced etch process for well-protected, passivated sidewalls.

Improved designs with similar feature sizes

As elucidated above, DSiE is ARDE which leads to different breakthrough times through the bottom of the wafer for differing feature sizes, which makes it impossible to reduce both over etching and notching to a minimum. In addition, optimization of the etch profile can only simultaneously achieved for similar features since the etch characteristic changes significantly with varying feature size. It is therefore recommended that feature sizes are similar for a single etching process by adapting the design pattern to be etched with dummy silicon islands that are disconnected from the structure after finishing the through-wafer-etching.

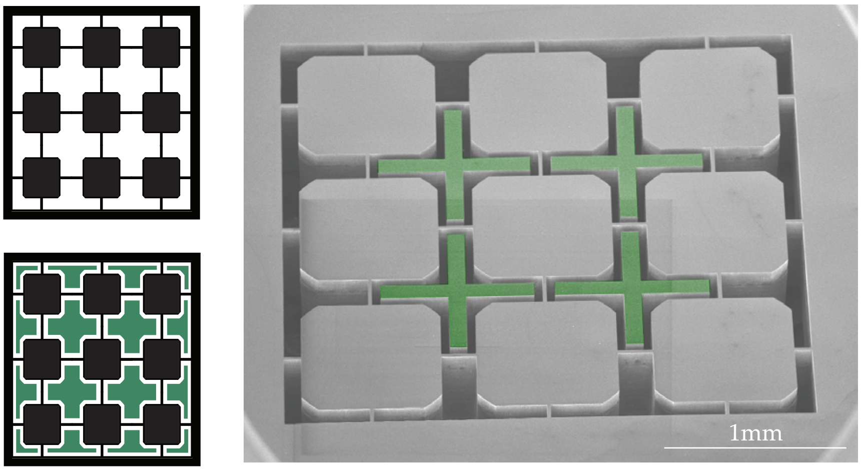

Figure 4.10: Design adaptations for improved deep reactive ion etching. Shown are schematics of a chip design with and without silicon dummy islands (green), as well as a SEM image of an etched test structure.

Alignment between membrane and phononic shield

The alignment of phononic shield patterns does not require additional alignment markers on the chip. Despite the fact that the entire front side of the chip is covered with a 3.5 µm thick oxide hard mask and a 1 µm thick electron-beam resist, the already suspended membrane can still be seen with a standard optical microscope. By determining two corners of the membrane, we can set the center of the phononic shield patterns to be written right in the center of the membrane. With this procedure, a misalignment of 10 µm to 20 µm are within range, only limited by the uncertainty and error propagation during the determination of various coordinates. Ideally, in standard optical lithography, one would use back- or frontside alignment which would possibly allow for more accurate alignment results.

HF strip of oxide hard mask

One open question remains whether and if so by how much the final oxide stripping in concentrated (dilute) HF compromises the film quality of the SiN. We have therefore determined the etch rates for both LPCVD-grown SiN and PECVD SiO_x for two different HF concentrations.

The results are obtained by ellipsometry and summarized in Table 4.2. Since LPCVD SiN is of higher quality the etch rates are much lower than those of PECVD-grown layers, even more so the case for SiO_x. SiN is effectively only etched in concentrated 40 % HF with an etch rate of $8\,\mathrm{nm\,min^{-1}}$. In contrast, even after leaving the sample in dilute 4 % HF for several minutes, no change in thickness was observed. For the PECVD oxide, the etch rates in highly concentrated HF are that high, that a thick layer of 2.6 µm has been fully stripped within 10 s of etching which gives us a lower bound of $15.6\,\mathrm{\mu m\,min^{-1}}$. The etch rate in dilute HF could have been measured as high as $600\,\mathrm{nm\,min^{-1}}$.

Crucially, in order to exclude negative effects of the final oxide strip, our samples are etched in dilute HF as it provides highly selective etching between LPCVD SiN and PECVD SiO_x without any expected SiN etching for the duration of the oxide strip.

Material	HF (40 %)	HF (4 %)
LPCVD SiN	8 nm/min	not measurable
PECVD SiO_x	>16 µm/min	600 nm/min

Table 4.2: Etch rates of PECVD SiO_x and LPCVD SiN in concentrated and dilute HF. The etch rates are determined by means of ellipsometry.

4.4 PHONONIC SHIELD MEMBRANES FOR ELECTROMECHANICS

Phononic shield devices can easily be adapted for using them in electromechanical circuits by coating the membrane with a thin metal layer that allows to capacitively couple to the microwave circuitry. The gap between bottom and top plates of the capacitor is modulated by the membrane oscillations, thus effectively modulating the resonance frequency of the LC-circuit. Similarly to optomechanics, this shift in resonance frequency $\delta\omega$ dependent on the membrane movement δx determines the coupling strength of the mechanical and microwave degrees of freedom. Intuitively, smaller gaps of the capacitor results in larger relative changes due to the membrane oscillations and thus leads to larger frequency shifts (cf. Section 2.4.3). Small gaps of a few µm already promise large frequency shifts that allow operation well within in the strong cooperativity regime with current setup parameters.

Q factor measurements of SiN membranes coated with a thin layer of aluminum show an increase of their mechanical Q factor by orders of magnitude when going below 200 mK [120]. Since these measurements have been observed for SiN membranes without a phononic shield and thus being sensitive to clamping losses, phononic shield devices possibly result in even higher, but maybe more importantly more reliable, clamping-independent mechanical quality factors.

Therefore, in a collaboration with the group of Gary Steele in Delft, we adapt the introduced phononic shield membranes by extending the existing fabrication procedure by coating the membrane with a thin layer of a superconducting metal.

4.4.1 *The choice of metal*

The apparent choice of metals to be used in the field of electromechanics are niobium titanium nitride (NbTiN) and aluminum, whose properties we will compare briefly (actually, the aluminum contains 1 % of silicon, however for convenience we simply refer to the metal alloy as aluminum silicon (AlSi)).

Superconductivity

In terms of superconductivity, both metals distinguish in its critical temperature below which the metal becomes superconducting. For AlSi, this temperature is slightly lower than for NbTiN, however, since experiments are usually conducted at sub-K-temperatures, both metals are suitable for these kind of experiments. We will not go into details here about whether why one could prefer one metal over the other in terms of other properties and simply focus on fabrication related questions.

Mechanical properties of SiN

Secondly, it is crucial that the mechanical properties of the SiN are not compromised. That means that either fracturing, buckling or wrinkling can be successfully avoided and the resulting effective stress of the membrane-metal double-layer remains unaltered.

Compatibility and feasibility with fabrication process

Ideally, the current fabrication process does not require any adaptations and additional process steps for the metallazation are simply added. Therefore, urgent and important questions cover topics of selectivity and feasibility for the metallization procedure with respect to the already existing recipe. As an example, since we use an oxide hard mask during DRIE a final HF etch is required for stripping the remaining oxide. However, AlSi is etched by HF and thus suffers from loss of quality. In general, most important is the guarantee that additional processing steps do not comprise the quality and functionality of both SiN membrane and metal layers involved.

4.4.2 *Metallization procedures*

There are various ways of how to coat the released membrane with a thin layer of metal which are listed below. Note that these the first two approaches come before the phononic shield (PS) processing, whereas the last approach of shadow mask evaporation comes last. A schematic overview of both standard pattern transfer and lift-off is shown in Figure 4.11.

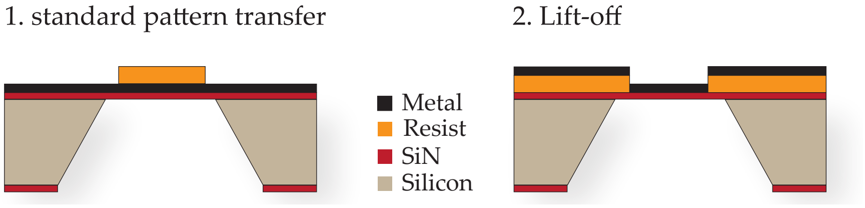

Figure 4.11: Schematic overview of metallization fabrication procedures. The left schematic describes the standard pattern transfer where the entire chip is first metallized and consecutively patterned by means of standard lithography and wet/dry etching. The right schematic depicts the lift-off approach where the resist is patterned before metallization. Areas of undesired metals are then lifted off afterwards in an appropriate resist solvent.

1. Standard pattern transfer approach: evaporation/sputtering of the metal layer first, followed by standard lithography and selective etching. This requires an etch process that is highly selective between the metal to be etched and the SiN membrane, such that the quality of both films is maintained.
2. Lift-off approach: The lithography step comes first, followed by the metallization step. The areas where metals are undesired are lifted off in an appropriate resist stripper. The process needs to be tuned in terms of choosing an appropriate lift-off resist resulting in a negative profile.
3. Shadow mask evaporation approach: independent of metal, but external alignment with large uncertainty and much effort after the entire processing is done. Less flexibility than with the other two approaches, however independent of etch selectivity and compatibility. This approach has not been exploited here.

AlSi metallization

Aluminum is a common choice in electromechanics due to its well-known properties. We follow the first approach introduced above, where we begin with the metallization of the entire chip, followed by lithographically protecting the square area on the membrane with a negative resist layer during the etching step.

We use AR-N 7700.18 spun at 4000 rounds per minute resulting in a thin protective resist layer during the subsequent aluminum etching. The spun resist is baked at 90 °C for 90 s before and post-exposure-baked for another 2 min at 110 °C after e-beam exposure. We develop the exposed resist layer with MF321 for 130 s, followed by consecutive rinses in water for 30 s and IPA for another 15 s. Conveniently, both development and aluminum etching happen in the same processing step since MF321 is based on tetramethylammonium hydroxide (TMAH) which etches aluminum. The remaining resist layer is finally stripped in PRS3000 at 90 °C until fully cleaned.

Evaporation and spinning of negative resist, development and etching of AlSi with the same chemistry allows for an easy and convenient process step of patterning the metal layer. Alignment in simply done with an optical microscope by determining the center point of the membrane itself which results in metal layers that are aligned within an accuracy of a few tens of µm. The remaining fab steps stay the same as described in the fab sections before. The most critical step comprises of the oxide hard mask strip while making sure that the metal layer is not negatively compromised. It turned out that using vapor HF over a pure 40 % HF etch is beneficial in terms of not attacking the AlSi at all, although leaving some oxide residues behind on the surface that are then eventually cleaned off by a quick HF dip of highest concentration. This is suggested as AlSi etches faster in low HF concentrations due to the increased water content. Even though we expected the surface of the AlSi to not be influenced by the short HF dip of 1 s only, we see some structural changes under the microscope, which is currently under further investigation whether the properties of the metal layer are compromised. Resistivity measurements don't suggest a significant harming of the metallic layer, however, measurements in a cryogenic setup have lead to the conclusion that its properties are indeed negatively altered. It must be further noted that already depositing the oxide hard mask seems to alter the metal-oxide layer irreversibly (cf. Figure 4.12b).

Adaptations to the standard recipe

One way to circumvent the uncertainty to what a HF treatment and the oxide deposition itself does to the AlSi layer is to fully avoid the usage of an oxide hard mask during DRIE and switch to a resist only through-wafer-etch. Initially, the aim was to fabricate phononic shields with largest bandgaps for multimode entanglement protocols, where thick Si substrates are desirable. Here, the main interest lies in shielding one mode – the fundamental mode – only, proving thinner Si substrates of 200 µm to be sufficient. Admittedly, even for 500 µm thick Si, one could use a resist-based DRIE process with a bit of effort, but oxide

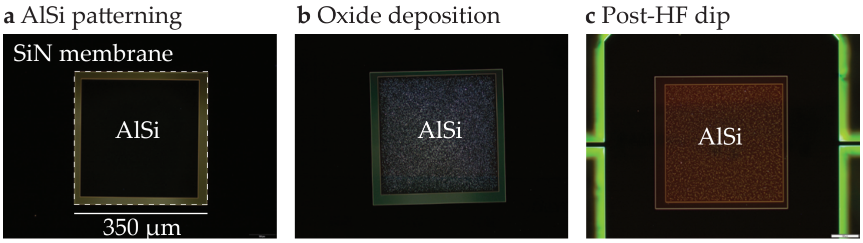

Figure 4.12: Microscope images of the metallized SiN membrane at various fabrication steps. The microscope images depict the suspended SiN membrane from a top view. **a** The membrane of 350 µm side length (marked in white dashed lines) is patterned and consecutively etched resulting in a square AlSi layer. **b** After oxide deposition, the metal layer looks grainy at the interface between metal and deposited transparent oxide. **c** Central defect cell with the metallized suspended square membrane. The grain structure even after the HF dip is still observable.

hard masks offer some benefits over using resist masks for such deep etches.

NbTiN as choice of metal

On the other hand, NbTiN has proven to be compatible with the current fabrication recipe as it is not etched by any concentrations of HF. Patterning the NbTiN layer can be successfully done in multiple ways by e. g. dry and wet etching or by means of a lift-off approach. SF_6/O_2 plasmas etch NbTiN but also attack the underlying SiN device layer slightly, whereas wet etching might provide high selective etching between SiN and NbTiN. Lift-off approaches of sputtered films on the other hand usually leave residues on the edge boundaries behind – so-called dog ears. However, this does not seem to be the case for sputtered metal films with high tensile stress such as the case with NbTiN.

We use a double-resist-layer of poly methyl methacrylat (PMMA) (PMMA 495 A4 as bottom layer, PMMA 950 A3 as top layer) consecutively spun at 4000 rpm and baked for 5 min at 185 °C on a hotplate which results in a quasi negative resist profile, essential for a successful lift-off. After e-beam exposure, we develop the resist layers in subsequent solutions of MIBK:IPA (1:3) for 60 s, followed by 60 s rinses in IPA. Afterwards, a 25 nm thick NbTiN layer is sputtered onto the developed resist. The final step consists of lifting off the undesired areas covered with metal by immersing the sample in hot N-methyl-2-pyrrolidone (NMP) at 80 °C for 20 min finished off by a 5 min oxygen plasma in order to fully clean off resist residues, leaving behind a pristine metal layer as depicted in Figure 4.13.

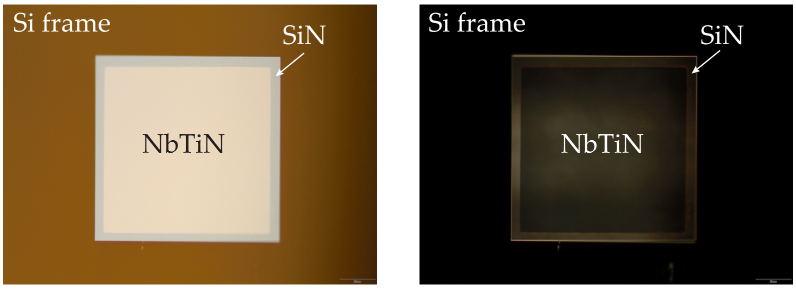

Figure 4.13: NbTiN lift-off. Normal (left) and dark field (right) microscope images of the NbTiN metallized SiN membrane after lift-off.

4.5 RESULTS AND DISCUSSION

The main results presented here were obtained and measured by Nia [71] in Vienna who used the fabricated PS membranes (without metal layer) in a MIM setup. An independent attempt of analyzing the mechanical Q factors in a dedicated fiber-based characterization setup was unsuccessful. Exciting the membrane modes within the bandgap with a piezo drive was only possible in rare cases where the fundamental mode was close to the edge of the bandgap. However, it should be noted, that in the dedicated setup, we did not tightly clamp down the membrane frame to the stage which presumably significantly reduces the amount of piezo power transmitted. Additionally, the piezo drive was mounted further away which seemed to prohibit the successful excitation of membrane modes within the bandgap. We took that as an indirect sign of the existence of the designed bandgap. In most cases, only the fundamental mode and higher modes outside the bandgap could be excited.

4.5.1 *Characterization in an optomechanical setup*

For this part, I would like to refer to the work by Nia [71], who characterized the optomechanical properties of the fabricated PS membranes in a MIM setup. A more detailed description about the experimental setup and the experiments done with those membrane can be found in his PhD thesis [71]. In the following, we will restrict ourselves to the mechanical properties associated with the shielded membranes with respect to the verification of the phononic bandgap and accompanying measured mechanical quality factors. The fabricated phononic shield devices are therefore incorporated in a typical MIM setup with tight clamping and the possibility to drive the membrane's motion mechanically and optically which is then monitored with a phase-sensitive homodyne detection system. Figure 4.14a shows the central part of the phononic shield membrane with a properly aligned cavity beam (white spot) with design parameters specified in Figure 4.14b. Here, it shall be noted that in contrast to other devices, the defect cell still is of the shape of all the other unit cells.

We want to quickly mention a few experimental challenges that come with the characterization of membranes exhibiting phononic bandgaps. Firstly, mechanical modes are usually excited with a piezo drive in the vicinity of the membrane. However, due to the acoustic shielding, exciting mechanical modes within the bandgap is stronly suppressed. Secondly, radiation pressure effects in the cavity alter the mechanical dissipation rate by optical cooling or amplification depending on the detuning with respect the cavity resonance. Since we are interested in mechanical properties unaffected by radiation pressure effects, we probe the mechanical motion with a laser beam at a wavelength of 1550 nm, non-resonant with the optical cavity.

For these reasons, in order to measure the mechanical quality factors of bandgap modes, two alternative methods have been exploited. Firstly, an intensity-modulated laser beam at 1550 nm wavelength can enhance the membrane's motion by experiencing a modulated force. Secondly, a blue-detuned laser at 1064 nm leads to an amplification of the membrane motion dependent on the laser detuning and thus can also be used to excite the mechanical motion of a given mechanical mode. With both methods, upon switching off the drive, we monitor the characteristic decay time by means of ringdown measurements.

Phononic shield characterization

In order to experimentally verify the existence of a bandgap within the desired frequency range, we measure the membrane's noise power spectrum (NPS) by probing its displacement monitored by a phase-sensitive homodyne detection system. Figure 4.14a and b show the central part of a phononic shield membrane and a schematic of the defect cell dimensions, respectively. We can measure the NPS by probing the displacement with an optical beam as depicted in Figure 4.14a, where the TEM00 mode of the optical beam (here 1064 nm) is aligned to the center of the membrane, whilst the entire chip is excited by white noise from a strongly driven piezo actuator. Alternatively, we can move the optical spot onto the defect cell frame slightly off the membrane itself.

The results are depicted in Figure 4.14c that shows the mechanical spectrum of a square membrane of 350 µm (red) with a fundamental frequency at around 1.2 MHz and the NPS obtained from probing the defect cell (blue). We measure several orders of magnitude less noise power within the expected (simulated) frequency range of the bandgap between 1 MHz to 3.6 MHz (gray area). At the low-frequency end of the bandgap between 1 MHz to 2 MHz, we still see quite some noise peaks coming up, whereas the shielding between 2 MHz to 3.8 MHz seems to be more effective. In addition, we can clearly identify

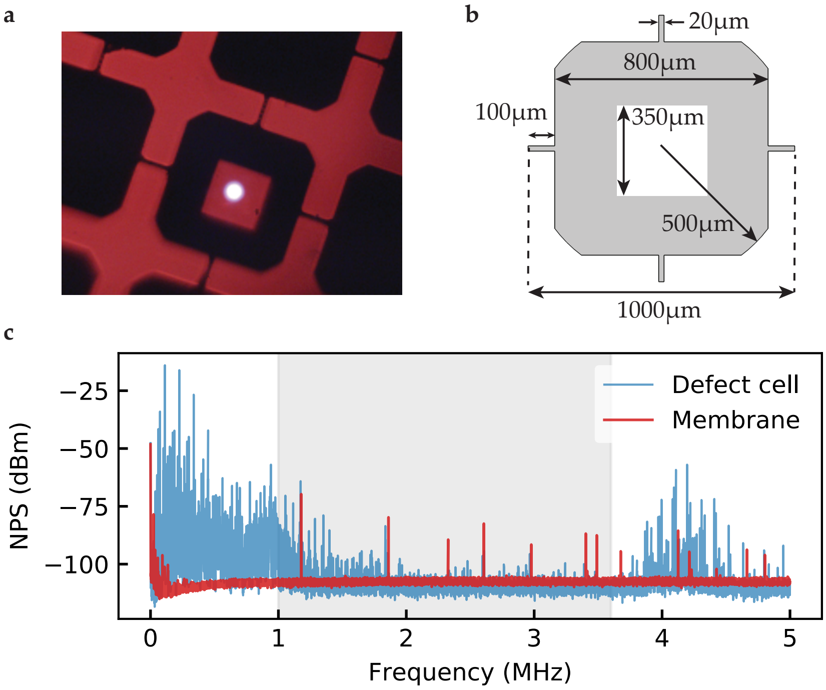

Figure 4.14: Phononic shield membrane and bandgap characterization. **a** shows a photograph of a phononic shield membrane used in one of our optomechanical setups. Depicted are the central defect cell hosting the SiN membrane itself with the fundamental optical light mode aligned to it. The PS has the dimensions as stated in **b** with a membrane of side length 350 µm resulting in a fundamental mechanical frequency of around 1.2 MHz. **c** shows the noise power spectrum (NPS) measured on the membrane (red) and on the defect cell (blue) while white noise is applied to the chip holder and therefore exciting both lattice and membrane modes of the entire device. Modes within the (simulated) bandgap are strongly suppressed (gray shaded area) whereas modes outside the bandgap can be more strongly excited. External phonons at frequencies outside the bandgap thus couple less to the membrane modes and vise versa, effectively prohibiting energy from dissipating into the environment via mechanical modes of the lattice.

the end of the bandgap at around 3.8 MHz, where additional noise can be observed again. The measured noise power spectra are in good agreement with the simulated ones in Figure 4.4 with maybe a slight shift to higher frequencies, which we attribute to fabrication imperfections and simulation uncertainties.

Characterization of mechanical Q factors

With the measured noise power spectra, we can now individually excite single mechanical membrane modes with a blue-detuned cavity drive and determine their quality factors at room and cryogenic temperatures by means of ringdown measurements. The results for two similar devices (devices are marked with circles and triangles, respectively) are summarized in Figure 4.15, where the red and blue data points correspond to measurements at room and cryogenic temperatures, respectively. The quality factors at room temperature (RT) show values between 1×10^6 to 2×10^6 measured for modes mostly outside the bandgap due to technical difficulties. However, for LT measurements, a full set of Q factors could have been measured with values at around 4×10^6 for device one (blue circles) and slightly larger values for device two (triangles) of up to 8×10^6 within the bandgap.

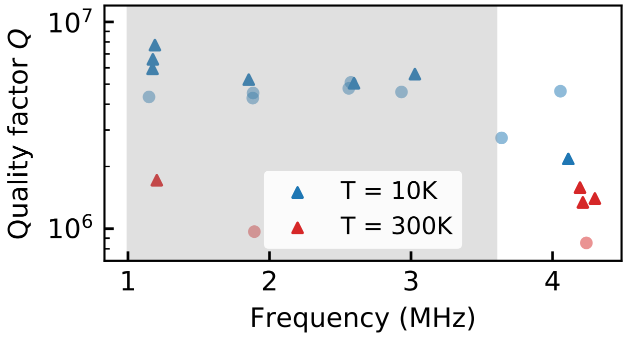

Figure 4.15: Q measurements for two different phononic shield membranes (marked as circles and triangles) at room (red) and cryogenic (blue) temperatures. All measurements yield quality factors above 10^6 at room temperature, except for one of the highest measured modes above 4 MHz, which lies outside of the designed bandgap (gray shaded region). At cryogenic temperatures, both membranes measured here exhibit consistently high Q factors greater than 4×10^6 for all modes within the bandgap.

Comparison between shielded and non-shielded square membranes

We have measured the mechanical quality factors of square membranes with and without phononic shield in order to quantify possible negative effects originating from the fabrication process itself. For the shielded membranes of 350 µm side length and 53 nm thickness, the measured quality factors of around 2×10^6 at room temperature are well in agreement for surface loss limited quality factors predicted by [110] (corresponding to $Q_{\mathrm{surf}} = \beta d$, where d is the membrane thickness and $\beta = 6 \times 10^{10}$ a fitting parameter; cf. Section 3.6). In contrast to the measured Qs of the shielded devices, we have noticed slightly higher quality factors for the unpatterned, non-shielded devices of similar dimensions by a factor of two (corresponding to $\beta = 1.2 \times 10^{11}$). Despite the lack of statistical relevance and the fact that the compared quality factors are measured from different devices, the degradation of mechanical quality after the PS fabrication can now be interpreted in various ways:

1. Negative influence of the PS fabrication process in general. In particular, the final HF oxide strip might appear to have a negative effect on the surface quality of the SiN.

2. The suspended SiN film quality decreases over time due to surface-altering effects which reduces the intrinsic quality factor limited by surface losses.

In the above mentioned paper about the origin of surface losses, it is also noted that devices with a final HF treatment generally show quality factors slightly below average due to added surface impurities [110]. In addition, the question remains whether surface effects (e. g. oxidation) gradually worsen the film quality of fabricated devices over time. It has to be noted, that the measurements of the non-patterned standard square membranes have been conducted within hours right after finishing the fabrication process, whereas the measurements of the phononic shield devices happened months after their completion. It is thus an open question whether and if so on which time-scales a degradation due to surface-altering effects occurs.

4.6 CONCLUSION AND OUTLOOK

We have developed a fabrication process for providing clamping independent square membranes of 350 µm side length and 53 nm thickness with reliably high mechanical Q factors of around 8×10^6 at 10 K. These so-called PS membranes effectively provide a platform for reaching the strong cooperativity regime for the first ten mechanical modes which seems to be necessary for the generation and detection of entanglement between optics and mechanics in an inherent multimode system. The mechanical quality factors achieved for membrane modes within the phononic bandgap follow the predictions of a dissipation model for square membranes [110], proving that their intrinsically limited dissipation rates are reached for the membrane parameters given, despite rigid mounting in an optical cryogenic cavity setup. Square membranes with side lengths of around 350 µm exhibit fundamental frequencies of around 1.2 MHz, sufficient to work in the regime where laser operation is shot-noise limited – a crucial feature for observing quantum effects in optomechanical experiments. The developed fabrication process is readily applicable for the usage in microwave circuits by depositing a superconducting metal layer on top of the suspended membrane itself. We have worked out methods that are compatible with the current fabrication as well as for slightly adapted processes.

Future directions

Possible improvements include using a photoresist only and fully avoiding the need for a oxide hard mask during the DRIE process. Using only a PR as mask could exclude the possibility that a (dilute) HF oxide strip negatively alters the surface quality of the SiN film. A resist-only recipe is more likely to be implemented for thinner substrates as the selectivity between resist and silicon etching is significantly worse compared to that of a hard mask, which ultimately requires very thick resist layers.

Lifting mode degeneracy

The operation in the strong cooperativity regime for – ideally – all mechanical modes is a necessary condition for the successful observation of quantum effects for multimode systems. One of the remaining questions is still whether larger frequency spacings between adjacent modes are beneficial to verify entanglement. Degenerate modes of square membranes naturally impose a problem to that, which can be circumvented by fabricating rectangular membranes, ultimately providing a multimode system with largest spectral spacing between adjacent mechanical modes where $\omega_{i,j} \neq \omega_{j,i}$ holds.

Mirrors for increased coupling strength?

Another way to increase the cooperativity further with the current resonator design is by patterning the membrane as a PhC. Depending on the thickness of the membrane, this allows to boost its reflectivity and thus the cooperativity which scales quadratically with the coupling strength. Note, that we mention this for completeness knowing that the overall net gain is rather small, whilst the situation still demands answers on whether a PhC patterned membrane suffers from additional scattering losses that dominate the positive aspect of increased membrane reflectivity and thus coupling strength.

Ultrahigh Q factors towards single-mode operation?

In general, largest mode separations and lowest mechanical decoherence rates are desirable for preserving entanglement. Recent developments of mechanical resonators with unprecedented, orders of magnitude higher Q factors [106] than presented here prompts the question whether an inherently multimode mechanical resonator can eventually again be treated as a single-mode system for sufficiently large quality factors and mode separations.

Entanglement between light and mechanics?

Finally, stationary entanglement between light and mechanics in free-space cavity optomechanics is an outstanding goal yet to be achieved. Tremendous progress has been made over the last couple of years towards the understanding of existing challenges for both optical and mechanical degrees of freedom with ever improving mechanical resonators that make the operation in the multimode strong cooperativity regime possible. However, remaining technical challenges are yet to be overcome for direct proof that entanglement is generated in such systems [38].

It should be mentioned that strong optomechanical quantum correlations in the form of ponderomotive squeezing have been observed in a basically identical system which promises the observation of entanglement [72].

5

INTEGRATED OPTOMECHANICAL ARRAYS OF TWO HIGH REFLECTIVITY SILICON NITRIDE MEMBRANES

Multi-element cavity optomechanics constitutes a direction to observe novel effects with mechanical resonators. Several exciting ideas include superradiance, increased optomechanical coupling, and quantum effects between distinct mechanical modes among others. Realizing these experiments has so far been difficult, because of the need for extremely precise positioning of the elements relative to one another and due to the high reflectivity required for each element. Here we overcome this challenge and present the fabrication of monolithic arrays of two highly reflective mechanical resonators in a single chip. We characterize the optical spectra and losses of these 200 μm-long Fabry-Pérot interferometers, measuring finesse values of up to 140. In addition, we observe a slight enhancement of the coupling rate between the cavity field and the mechanical center-of-mass mode compared to the single membrane case. Further enhancements in coupling with these devices are predicted, potentially reaching the single-photon strong coupling regime, giving these integrated structures an exciting prospect for future multimode quantum experiments.

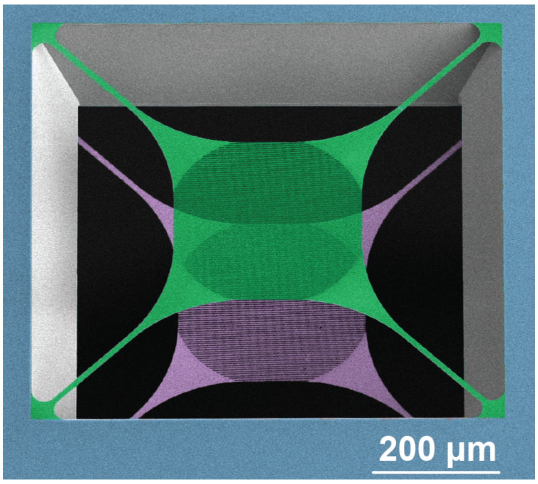

Parts of this chapter have been published together with J. Moura, W. Haaxman, R.A. Norte and S. Gröblacher in Nano Letters **18**, 7171 (2018) [30].

5.1 INTRODUCTION

Cavity optomechanics explores light-matter interactions by using the established control techniques of optical resonators to manipulate highly sensitive mechanical oscillators [4]. A particularly successful direction is to dispersively couple suspended silicon nitride (SiN) membranes to a rigid optical cavity [104]. These so-called membrane-in-the-middle (MIM) systems combine independent optical and mechanical oscillators, allowing the use of high-finesse cavities to study a variety of mechanical devices. Although recent years have seen tremendous progress in quantum optomechanics and in particular with experiments observing quantum behavior of the mechanical mode [45, 75, 83], most have focused on single mechanical or noninteracting modes. Studying the behavior of multiple directly coupled modes could however allow probing new and exciting regimes of optomechanics [8], like superradiance, phonon lasing [35, 53], synchronization [121], the study of exceptional points [114], quantum information processing [92], as well as the direct entanglement of mechanical resonators [39]. It has also been suggested that the collective interaction of several mechanical oscillators can allow reaching the single-photon strong coupling regime [115]. This effect is based on reducing the effective optical mode volume through an array of closely spaced mechanical systems and it becomes stronger as the reflectivity of the individual systems R_m is increased.

Tethered SiN membranes patterned with a PhC constitute ideal candidates for this type of architecture, as they have excellent mechanical properties, low mass, and high reflectivity. ThePhC can also be engineered to operate at a large range of wavelengths [73, 82]. To date, experimental efforts have focused on using independent mechanical membranes to create a mechanical array [70, 79], relying on the intrinsic reflectivity of the bare SiN with one recent attempt to fabricate a membrane on each side of the same chip [112].

In the present work, we monolithically combine two tethered SiN membranes on a single chip and control their reflectivity using PhC patterns. This avoids having to manually align the mechanical elements to each other, which to date has been a major challenge with such high-reflectivity resonators. To compare the properties of devices with different reflectivity R_m, we fabricate pairs of single and double-membranes for three different PhC parameter sets, spanning R_m from 33 % to 99.8 % at an operating wavelength of 1550 nm. The optical spectrum of the arrays exhibits Fabry-Pérot interference, which allows us to study the optical loss mechanisms present in the system. The optomechanical coupling rate of the center-of-mass (COM) mode of single- and double-membranes to an optical cavity are compared. By changing the incident laser wavelength, we can operate the double-membrane stacks in their reflective or transmissive regimes, corresponding to enhanced or null COM optomechanical couplings, respectively.

5.2 DEVICE DESIGN

Monolithically combining two tethered SiN membranes on a single chip and controlling their reflectivity using PhC patterns promises to meet the design requirements for enhancing the coupling strength in free-space optical cavities by orders of magnitude. The most crucial requirement for our devices is forming double-membrane arrays of high optical finesse $\mathcal{F}$, i. e. arrays consisting of two high-reflectivity membranes, that are operated in the transmissive regime. At the heart of our devices is a central mirror pad on the tethered membranes. It is patterned with a two-dimensional PhC consisting of a periodic array of holes etched into the SiN device layer. Such a periodic change in the refractive index creates a band gap that can be tailored to a specific wavelength, resulting in reflectivities $> 99.9\,\%$ [17, 73]. Using S^4, a Rigorous Coupled-Wave Analysis software, we simulate the spectrum of a given PhC pattern [63]. During fabrication, we can accurately tune the PhC resonance to our desired wavelength by adjusting the lattice constant a and hole radius r. In the past, we have extensively worked on optimizing and characterizing PhC patterned membranes – both for large square membranes [68] as well as tethered membranes [73]. Reaching high reflectivities with PhC membranes depends on various design parameters such as the optical thickness of the material slab, the impinging optical beam radius, and the size of the central mirror pad itself [68].

Unpatterned tethered membranes with pad sizes four times the size of the cavity beam waist have proven to be sufficient for maintaining a high optical finesse, i. e. without introducing additional scattering loss from the membrane edges [82].

It seems intuitive that larger pad sizes can only be beneficial when it comes to avoiding additional clipping loss from the membrane edges which ultimately means fabricating membranes with central mirror pads as large as possible.

Trampolines with large mirror pads

In the past, the fabrication of tethered PhC membranes with large central pads has been challenging and was limited to pad sizes of around 100 µm, barely enough to host cavity beam waists of several tens of µm without clipping the optical beam.

On one hand, using sufficiently small beam waists is beneficial for avoiding clipping losses but on the other hand possibly results in smaller membrane reflectivity which crucially depends on the optical thickness of the material slab that the holes are patterned into [68]. PhC membranes require sufficiently large beam waists in order to achieve the maximum achievable reflectivity plateau. Thicker device layers are here beneficial as they allow reaching the high reflectivity regime already for smaller beam waists. To give some numbers, using SiN layers of 200 nm allows to work with optical beam waists of around 50 µm while still promising to reach membrane intensity reflectivities greater than 99.9 %.

In contrast to the design optimization performed in earlier works [73], that typically aimed at maximizing the Qf-product for ground state cooling experiments from room temperature, there are no further design requirements than maximizing the membranes' reflectivity and consequently the maximum achievable coupling enhancement.

We thus aim for tethered membranes with central mirror pads of at least 250 µm in 200 nm thick SiN and 200 µm Si wafers – effectively determining the spacing of the double-membrane-array. In general, shorter arrays ultimately promise larger coupling enhancements when working with membrane reflectivities close to unity [60], however they pose challenges involving the handling of thinner chips.

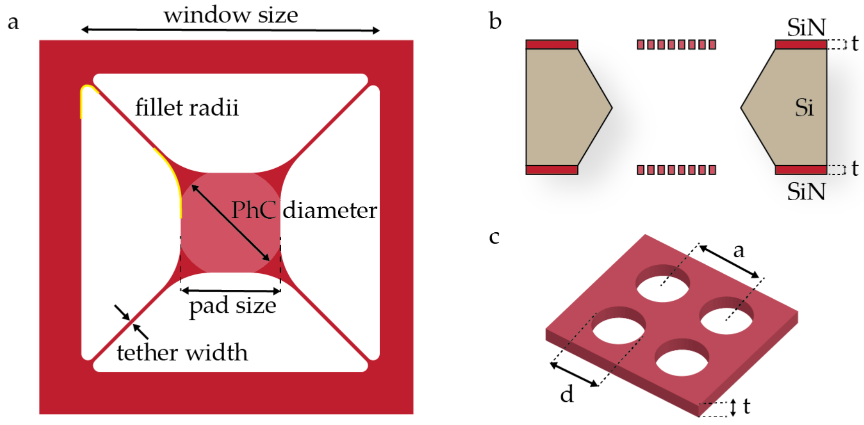

Figure 5.1: Device design parameters for tethered PhC membranes. **a** Tethered membrane, **b** wafer thickness, and **c** PhC design specifications.

5.3 FABRICATION

With the available standard SiN/Si wafers, we can now start to fabricate different devices in a very simple process flow. Single tethered PhC membranes are used for simple studies of the optical properties of our PhCs and for optimizing the yield of designs with increasing pad size where we can choose to either fully or only partially etch through the entire silicon wafer dependent on whether optical properties are studied in transmission (cf. Figure 5.2a and b).

For the case of double membrane arrays, we can decide to either also lithographically pattern it with one of our PhC trampolines (Figure 5.2d) or, alternatively, leave the backside of the chip unpatterned

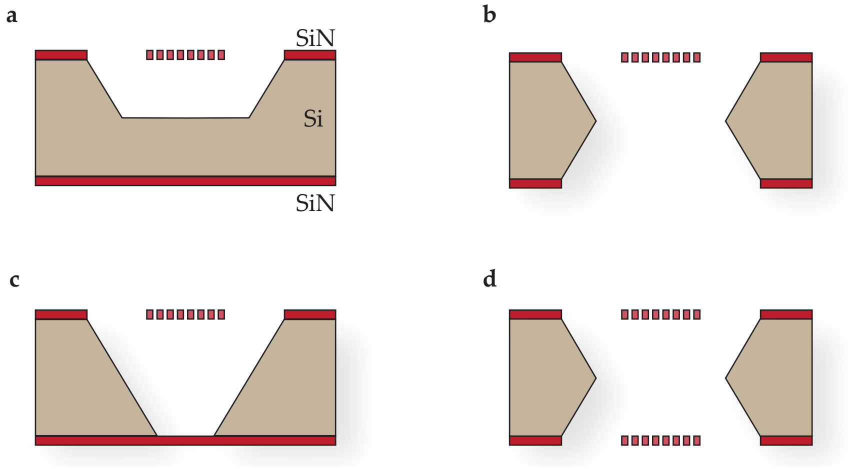

Figure 5.2: Schematics of possible single (**a** and **b** in upper row) and double membrane (**c** and **d** in bottom row) devices fabricated from a standard LPCVD SiN coated silicon wafer.

(Figure 5.2c). By performing the latter, we form our first simple double-membrane arrays, consisting of one tethered PhC membrane with wavelength-dependent and a square membrane of basically constant but low reflectivity. Eventually, both sides of the chip are patterned with PhC tethered membranes for forming arrays of highest finesse crucially dependent on the reflectivity of each PhC membrane.

General fabrication flow

Our devices are fabricated in 200 nm thick stoichiometric SiN deposited via low-pressure chemical-vapor deposition (LPCVD) on a plain 200 µm-thick Si substrate. We then lithographically define a 500 nm thick electron-beam sensitive resist (AR-P 6200.13)[1] in the shape of our photonic crystal trampolines and transfer the pattern into the SiN device layer with a CHF_3/O_2 plasma etch (cf. Figure 5.3a-e). In the case of our single PhC trampolines the backside of the wafer is then patterned with square openings to fully etch through the entire Si wafer without forming a double membrane array. For fabricating double-membrane arrays, we first thoroughly strip the remaining electron beam resist with a suitable remover at elevated temperatures (Baker PRS-3000 at 80 °C) to ensure a clean surface after the first pattern transfer step. We then repeat the same procedure of transferring the trampoline pattern into the second device layer while protecting the already patterned front side as to minimize exposure of both device layers to the clean room environment. This cannot fully be avoided as both device layers will get in contact during the spin coating procedure, i. e. with both the spin coater chuck and the hot plate surface during tempering.

---

[1] http://www.allresist.com/csar-62-ar-p-6200/

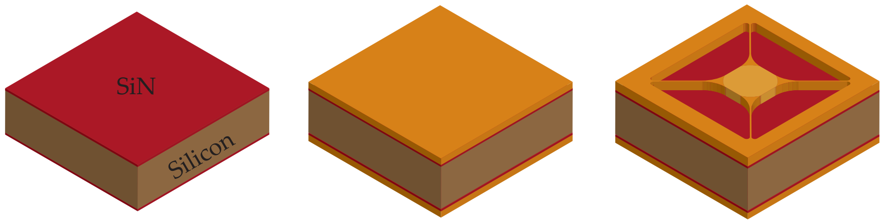

a SiN deposition **b** Resist coating **c** Lithography

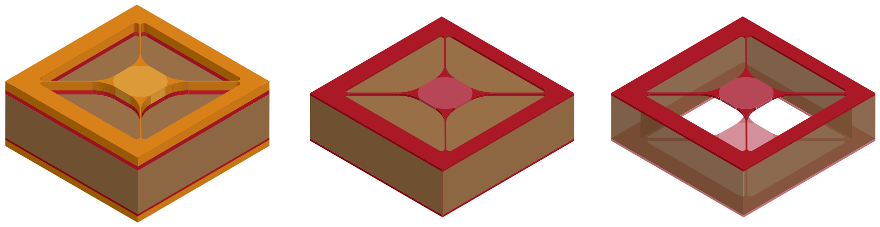

d SiN etching **e** Resist stripping **f** Si etching

Figure 5.3: Schematic representation of the essential steps for the fabrication of double-membrane arrays consisting of two tethered PhC membranes. Illustrated is only the whole process flow for the pattern transfer of a single membrane (**a**-**e**). For forming double-membrane arrays, the chip is flipped around and process steps a-e are repeated, before eventually releasing both devices in a final KOH etch (**f**).

Despite that fact, we do not see evident negative effects on either the mechanical or optical properties of our resonators. After the pattern transfer into both SiN layers, we again clean the chip surfaces thoroughly from any organic compounds. We first use Baker PRS-3000 at 80 °C to remove the remaining electron resist off the surface followed by a hot Piranha solution at 110 °C. To release the trampolines, the chips are briefly rinsed in various water baths and then transferred to a 30 % potassium hydroxide (KOH) solution at 75 °C. The silicon is etched through the entire wafer for about two hours at a rate of 1 µm/min. After the release, a 10 min hydrochloric acid (HCl) etch cleans off KOH residues of the exposed resonators surfaces. We then carefully transfer them into subsequent rinsing baths of water and isopropyl alcohol (IPA) before drying them using critical point drying (CPD) to avoid their exposure to viscous forces and surface tension.

Alignment between front and back membrane

We align front and backside using an optical microscope to determine the coordinates of the patterns to be written with respect to one corner of our chips. By using this method, we introduce uncertainties to the correct coordinates between front and backside, leading to misalignments between 10 µm and 30 µm with good reproducibility, effectively reducing the overlap between both mirrors. This could possibly be improved by using topological alignment markers reaching through the entire chip, e.g. by deep reactive ion etching (DRIE). This would lead to better alignment between both membranes with the drawback of adding additional fabrication steps. Ideally, one would use optical lithography with backside alignment for patterning the tethered membranes themselves instead of using electron-beam lithography (EBL). By doing so, entire wafers could be fabricated more time-efficiently while still being able to fine tune the PhC resonances in a separate EBL step.

Increased fabrication yield

Tethered PhC membranes with increasingly large pad sizes become more susceptible to large stress during wet release. Several membrane designs with varying pad size of around 300 µm, tether length and

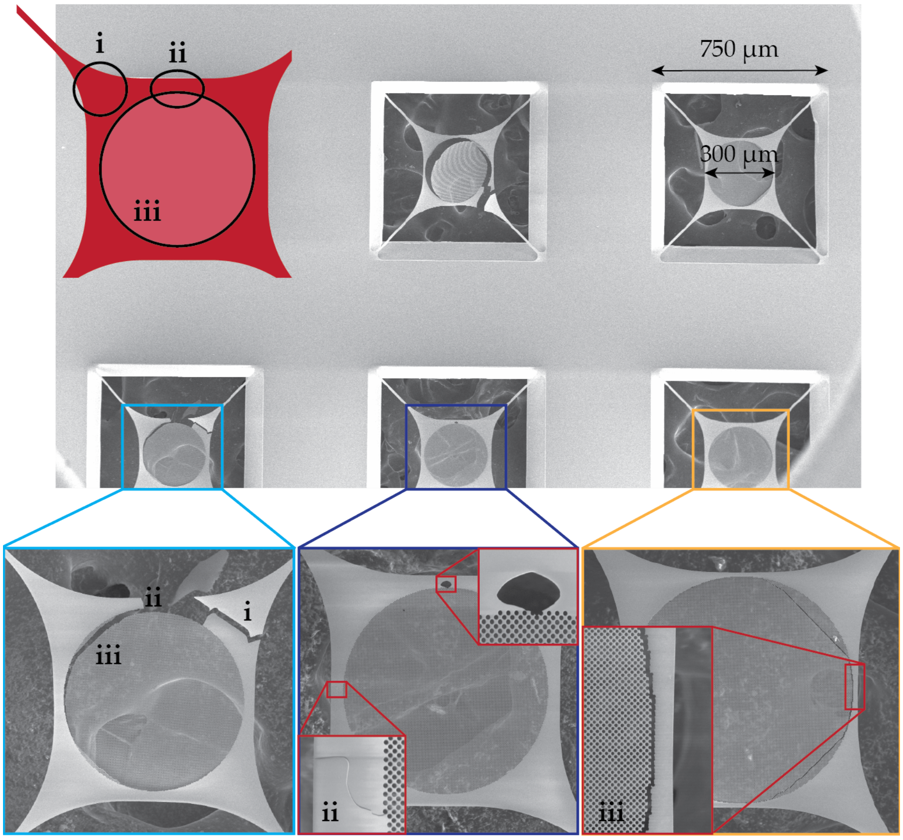

Figure 5.4: Design challenges for tethered PhC membranes. First devices would regularly result in cracks, fracturing or full device failure. Shown are scanning electron microscope (SEM) images of devices with these design issues revealing points of large stress during release (as also indicated in the schematic).

width, as well as PhC related adaptations have often resulted in cracks, fracturing or full device failure (cf. Figure 5.4). We have found that by patterning the entire central pad with PhC holes, even on its edges, as shown in the zoom-in of Figure 5.5c, the fabrication yield increases considerably to almost 100 %. Increasing the PhC diameter such that we cover more of the central pad with etch holes seems to reduce part of the large stress on the membranes which presumably is causing their rupture during release. This allows us to explore a much wider range of possible design parameters with even larger pad sizes, which significantly improves on challenges like alignment between both membranes which are ultimately related to finite aperture losses (see Section 5.4.1.2), or using bigger beam waists in an optical cavity. With the improved design, we are able to successfully release devices with pads of up to 500 µm in side length, tethers of 5 µm in width and large window sizes of 1.3 mm (see Figure 5.17).

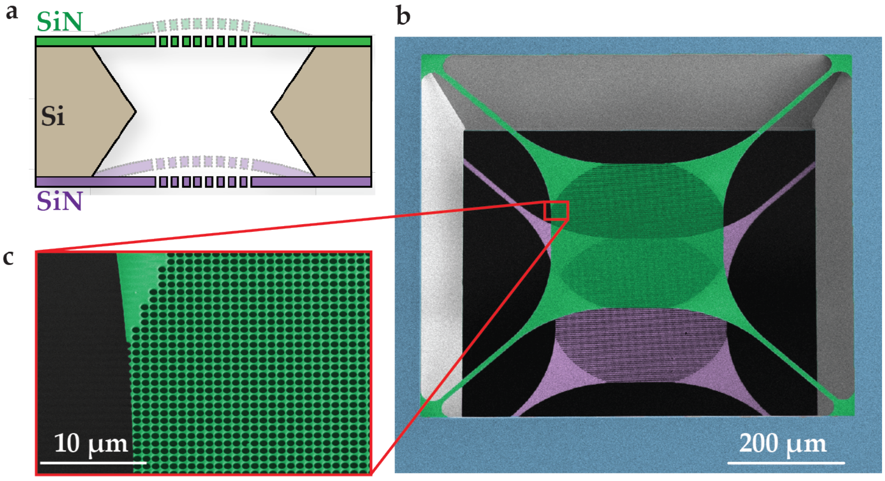

Figure 5.5: Fully suspended double membrane device. **a** Cross-sectional schematic of a released double membrane stack. **b** False-colored SEM image from the top under an angle of 37° showing a stack of two membranes as depicted in **a**. The top (green) and bottom (purple) SiN trampolines form a Fabry-Pérot cavity. **c** Zoom-in of the PhC patterned central pad area of the upper membrane.

5.4 DEVICE CHARACTERIZATION

Low finesse arrays

We form our first double-membrane arrays by patterning one side of the chip as a PhC tethered membrane and simply etch through the entire silicon wafer (cf. Figure 5.2c). The KOH etch stops at the bottom SiN layer and forms a double-membrane array of relatively low finesse consisting of a tethered membrane on one side with varying reflectivity of the PhC resonance and on the other side a square membrane of

200 nm thickness exhibiting a constant reflectivity of around 37 % (cf. Figure 5.2c).

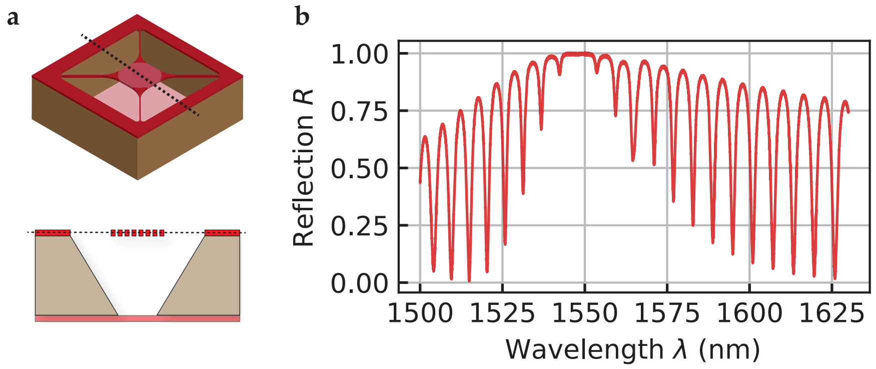

Figure 5.6: Low finesse double membrane array consisting of a tethered PhC membrane with wavelength-dependent reflectivity and a square membrane of constant reflectivity. **a** 3D and cross-sectional schematics of the fabricated arrays and **b** the resulting spectra obtained in reflection.

Figure 5.6b shows the measured transmission spectra characteristic for Fabry-Pérot etalons with peak transmissions crucially dependent on the single element reflectivity mismatch between both membranes. This is particularly dominant where the tethered membrane has its PhC resonance at around 1550 nm. At this wavelength the transmission peak vanishes completely whereas it starts to increase again for better matching membrane reflectivities. The various transmission peaks are separated by roughly 6 nm, the free spectral range (FSR) of the array, determined by the membrane separation and thus substrate thickness of 200 µm. Further, because of the wavelength-dependent PhC resonance, we observe a decrease (increase) in linewidth (finesse) of the transmission peaks of the etalon reaching its minimum (maximum) at the PhC resonance.

High finesse arrays

When patterning also the backside of the chip as a highly reflective PhC trampoline, we form double-membrane arrays of higher finesse and larger transmission values when compared to the low-finesse arrays.

In order to better understand the measured double-membrane spectra and additionally have the possibility to measure multiple devices within the same fabrication run, we pattern 3x3 arrays of tethered membranes and squares on each side of the chip, ensuring that – with neat arrangement – both single (SM) and double membranes (DM) can be measured on the same chip produced within the same process flow. By doing so, we end up with a chip consisting of six double-membrane arrays and one single membrane on each side (and an additional square opening for aligning the empty cavity). This allows us to gain knowledge about the individual mirror spectra (blue spectra in Figure 5.7) and identify the PhC resonances belonging to front- and backside, allowing to further compare them to the obtained double-membrane spectra composed of the individual ones.

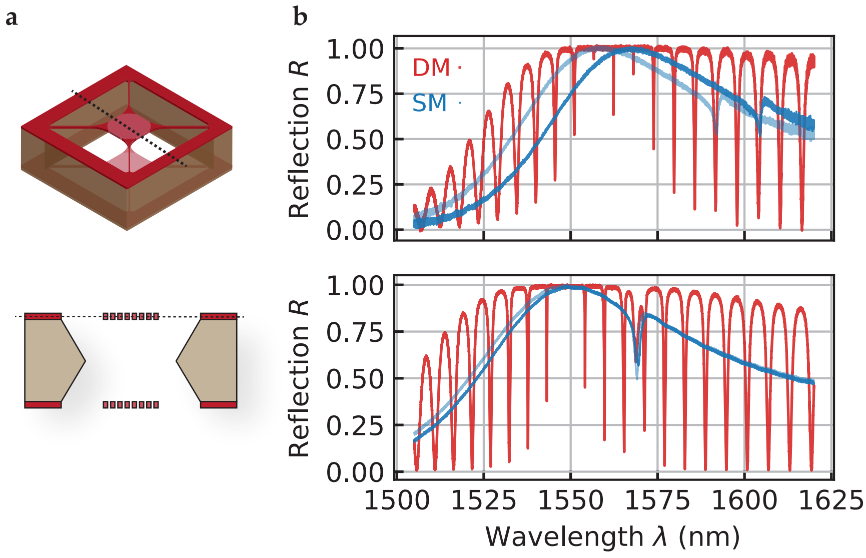

Figure 5.7: High finesse double-membrane arrays with two tethered PhC membranes of wavelength-dependent reflectivity. **a** 3D and cross-sectional schematics of the fabricated arrays and **b** the resulting spectra obtained in reflection for the case of unmatched (top) and relatively well matched (bottom) mirrors. Spectra of individual single-membrane (SM) are plotted in (light) blue with the resulting double-membrane (DM) spectra (red) for arrays composed of the individual membranes, respectively.

To our surprise, studying the individual mirrors revealed mismatching resonance wavelengths between both mirrors of nominally identical PhC design (cf. Figure 5.7, upper plot). At first, this was attributed to imperfections in the fabrication process, but ultimately turned out to be reproducible for all the arrays on the same as well as on other chips produced in subsequent process runs. We have noticed that the PhC resonances of the mirror originating from the second exposure are shifted towards lower wavelength, equivalent to larger hole sizes. We mainly attribute these systematic shifts to fabrication-related effects during EBL which we will elaborate later on in Section 5.4.1.1.

For the characterized membranes these systematic shifts amount to resonance shifts of around 5 nm, corresponding to changes in hole diameter of approximately 13 nm, equivalent to relative changes of approximately 1 % with respect to the initial hole diameter of 1050 nm.

In order to test how much the reduced transmission dip depths can be attributed to mismatching mirror reflectivities, we fabricated double-membrane arrays with varying PhC design parameters. We keep the devices on one side of the chip fixed while sweeping the lattice constants a on the other side by ± 1.5 nm (and an offset accounting for the discrepancy between both mirror resonances), effectively tuning λ_{res} by more than 5 nm. We found that upon better resonance matching, we could increase the dip depth of the high finesse array resonances noticeably (Figure 5.7b, lower plot). However, when the array resonance coincides with the maximum of the PhC resonance we usually observe that the transmission peak completely disappears even for relatively well matched resonances. This is the case where both membranes exhibit their highest reflectivity resulting in arrays of high finesse (narrow linewidth). In this regime, even minute differences in mirror transmission already lead to large reductions in dip depth.

5.4.1 *Device limitations*

5.4.1.1 *Importance of matching mirror resonances*

In order to understand the importance of matching the reflectivities between both mirrors, we plot the theoretical transmission T of the Fabry-Pérot cavity with respect to the ratio R_1/R_2 of its individual mirror reflectivities (see Figure 5.8). The transmission (without losses) follows the following equation for normal incident light

$$T = \frac{(1-R_1)(1-R_2)}{(1-\sqrt{R_1 R_2})^2}.$$

One can see that the transmission only reaches unity for matching mirror reflectivities and drops quicker the higher the finesse of the cavity becomes, i. e. for increasing R_1 and R_2. In the case of $R_1 = 90\,\%$, mismatches of up to 10 % do not cause a big drop in transmission yet (red curve, see also low and mid R transmission plots in Figure 5.14). For very high mirror reflectivities above $R_1 = 99.99\,\%$ even small mismatches between both mirrors already lead to a significant and rapid reduction in transmission (blue curve, high R plot in Figure 5.14).

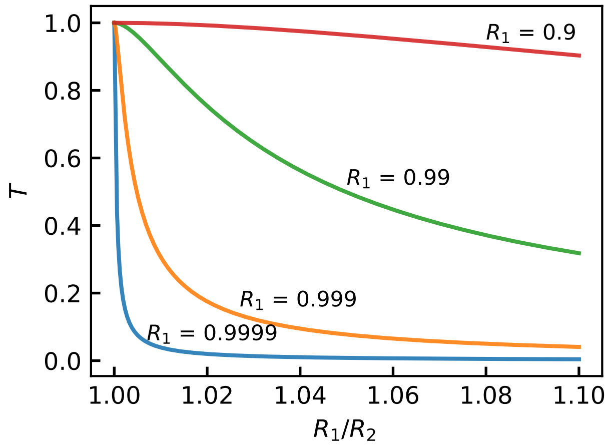

Figure 5.8: Influence of reflectivity mismatches between both mirrors. Plotted is the transmission T versus the ratio of both mirror reflectivities R_1/R_2. For low finesse Fabry-Pérot cavities, bigger mismatches do not have as big of an influence on the the transmission as for the high finesse cases.

PhC resonance tuning

It is crucial to have good control over the tuning of our PhC resonances in order to account for mismatches between both mirrors induced by fabrication imperfections, especially in high-finesse cavities. We therefore fabricated single membranes with various PhC parameters in order to see its influence on the maximum of their resonance λ_{res} (see Figure 5.9). We vary their radius r as well as lattice constant a and find a linear behaviour around our operating wavelength of 1550 nm. Taking the measured values of the lines with three data points, we can determine the slopes to be $\Delta\lambda_{\text{res}} \propto 1.81 \cdot \Delta a$ for a fixed radius of $r = 550\,\text{nm}$, and $\Delta\lambda_{\text{res}} \propto -0.76 \cdot \Delta r$ for a fixed lattice constant of $a = 1380\,\text{nm}$.

With this knowledge, we can account for fabrication-related mirror mismatches and tune the resonances to the desired wavelength. This becomes particularly important for arrays of increasingly high finesse where already small differences between both mirrors lead to large reductions in peak transmission (blue curve in Figure 5.9) with an even further reduction attributed to other (dominating) loss contributions.

Origin of mirror mismatch

We have seen that good control over the PhC resonances is a crucial tool for the fabrication of DM arrays exhibiting highest finesse and transmission.

Of utmost importance is to understand the origin of these occurring fabrication-related resonance shifts between various membranes of nominally identical design. We therefore measured PhC resonances of devices on the same side of the chip and between various chips,

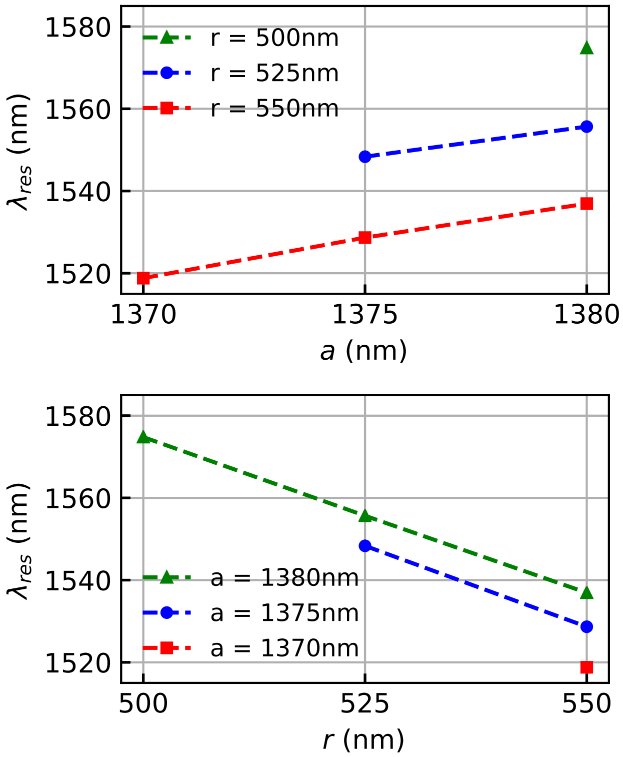

Figure 5.9: Influence of the PhC design parameters on its resonance wavelength λ_{res}. Plotted are measured resonance maxima for varying lattice constants a and radii r. For increasing lattice constants, the maximum of the PhC resonance shifts to higher wavelengths, whereas it decreases for increasing radii.

and have consistently found greatly overlapping resonances among all devices. However, when comparing mirrors from front- and backside of the same chip, we consistently measure significant resonance shifts of around 5 nm. Thereby, the mirror on the backside systematically exhibits resonances shifted to shorter wavelengths, equivalent to bigger holes. As can be extracted from Figure 5.9, a resonance shift of 5 nm corresponds to absolute hole diameter changes of approximately 13 nm, equivalent to a relative changes on the order of 1 % with respect to the initial hole diameter of 1050 nm.

This proves that the fabrication process is reproducible which rules out the possibility of random fluctuations during e. g. the RIE pattern transfer. However, it also shows that there are systematic contributions that we think arise from lithography.

E-beam lithography as source of uncertainty

Due to the inherent nature of the tempering processes in our fabrication recipe, baking times between front- and backside exposure differ by 3 min.

Generally, the pattern transfer into the resist layer depends on baking time and temperature which ultimately influences the sensitivity of the exposed resist. For positive-tone resists, longer baking times harden the resist, i.e. make it less sensitive to the impinging electrons, consequently leading to slightly smaller features after exposure and development. In our case, because of the fabrication process of protecting the already patterned frontside of the chip, the baking time for the fabrication of each mirrors differs by 3 min and thus leads to slightly different PhC features between front- and backside.

Additionally, whether and if so by how much the already patterned SiN on the frontside introduces proximity effects due to additional backscattered electrons has not been quantified but could be an additional contribution for the observed differences in hole size. Ultimately, adjusting the baking time for both lithography steps possibly results in matched mirror resonances without the need for additional resonance tuning.

Photonic crystals of smaller features

Our monolithic double membrane arrays not only promise to enhance the single-photon coupling strength in a rigid Fabry-Pérot cavity but also already constitute a multimode optomechanical system of disparate mechanical resonators in itself. The Bouwmeester group in Leiden has shown coherent optomechanical state transfer in a similar system [112]. Their devices are also fabricated on a single chip whereas one of them acts as an end-mirror in a Fabry-Pérot-type cavity. They showed that even for non-degenerate mechanical modes coherent optomechanical state swapping between two spatially and frequency separated resonators is possible by using an intermediary optical mode.

Since our double membrane arrays have PhC optimized for 1550 nm, we fabricated trampoline membranes with resonances at 1064 nm for their existing optical setups. The challenges here involve tuning the PhC design parameters as an initial step. Resonances at lower wavelength implies down-scaling of the PhC parameters as well, resulting in smaller hole diameter and lattice constants of 720 nm and 850 nm, respectively. Due to the smaller features and thus dense spacing between adjacent holes, we have noticed a systematic overexposure for the PhC patterned central mirror pad during the second exposure – despite using the very same design parameters for both lithography steps (cf Figure 5.10). This supports the earlier assumption that EBL related effects such as baking time and proximity effects lead to differences in hole sizes during pattern transfer into the resist.

We assume that this effect is also responsible for the systematic shift of the PhC resonances at 1550 nm, but has just not been visible under the optical microscope due to the bigger PhC features. Since matching mirror reflectivities are crucial for optimized membrane arrays, it

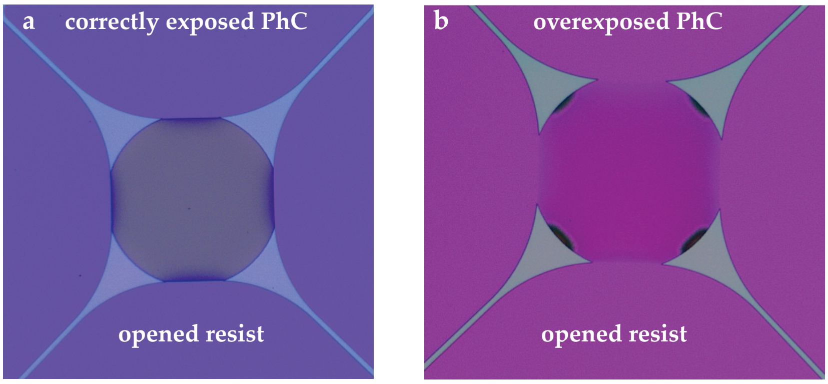

Figure 5.10: Influence of baking time on the fabrication of PhC holes between front- and backside mirror. Shown are microscope images of nominally identical tethered PhC membranes (lattice constant of 850 nm and hole diameter of 720 nm) on both front- and backside of the same chip after resist development. **a** The PhC pattern during the first lithography step on the frontside is clearly visible and correctly exposed whereas in **b** the central mirror pad originating from the second lithography on the backside is significantly overexposed, emphasizing the influence of shorter baking times.

might be beneficial to avoid differences in baking times between front- and backside mirrors. By doing so – assuming all other subsequent process steps to stay the same – one could end up with optimally matched PhC resonances without the additional need for PhC tuning.

In conclusion, we have shown that we can accurately account for fabrication-related systematic shifts and match both mirrors reasonably well resulting in larger peak transmissions even at increasingly large finesse. With the measured single membrane spectra on each side of the chip we can estimate the expected transmissions of the array dependent on the individual single mirror reflectivities. However, we still find a significant discrepancy between model and measured data which we attribute to additional optical losses that start to dominate over the wavelength-dependent mirror transmissions, even in the case of perfectly matched mirrors.

5.4.1.2 *Estimation of optical losses*

Single-membrane minimum transmission

To obtain a more accurate estimate of the maximum reflectivity achievable with our PhC membranes, we place a sample with a PhC resonance at 1565 nm in the cavity setup described before. Figure 5.11 (top) shows the cavity reflection as a function of laser frequency and membrane displacement x. The membrane divides the cavity into two half-cavities whose mode frequencies are a function of membrane displacement x. As x increases, the length of the half-cavity above (below) the membrane increases (decreases), changing the mode frequency as indicated by the dashed red (blue) line. If the membrane

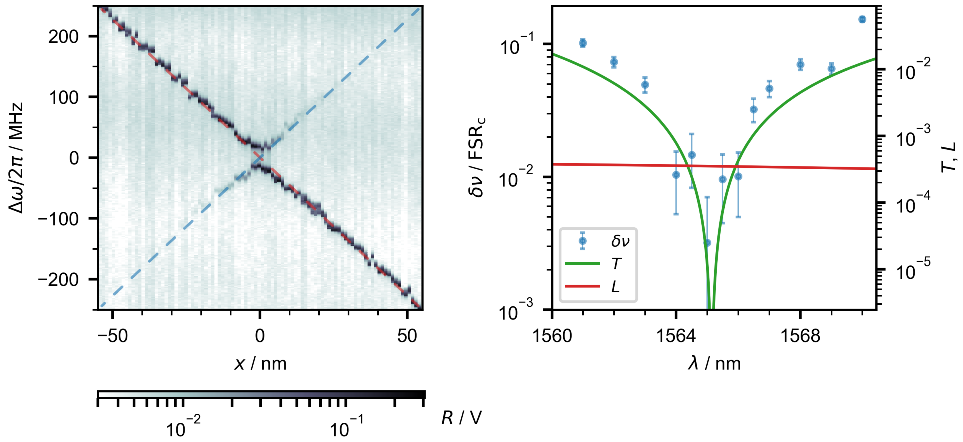

Figure 5.11: Left: Reflection of the optical cavity as a function of laser frequency $\Delta\omega$ and membrane position x at a wavelength of 1566 nm. Here, we study a sample with a PhC resonance at 1565 nm and measure the splitting of the avoided crossing $\delta\nu$. Right: The points indicate the measured $\delta\nu$, normalized by the cavity free spectral range $\mathrm{FSR_c}$, as a function of the laser wavelength, close to the PhC resonance. These data can be converted into a membrane transmission, which is indicated on the right axis. The traces are the result of an S^4 simulation of the transmission (green) and absorption losses (red) of a single PhC membrane with similar geometry as the measured sample and an imaginary part of the refractive index of 1.9×10^{-5}.

was perfectly reflective, both half-cavity mode frequencies would become degenerate at a particular x. Realistically, the membrane has a non-zero transmission which allows some light to leak between the two half-cavities. This lifts the degeneracy and gives rise to an avoided crossing whose frequency splitting $\delta\nu$ can be used to extract the membrane transmission [17, 98].

We repeat this measurement for multiple wavelengths close to the PhC resonance. The frequency splittings normalized by the free spectral range are plotted as blue circles in Figure 5.11 (right). The smallest $\delta\nu/\mathrm{FSR_c}$ measured for this sample was 3.2×10^{-3} at 1565 nm. Using the method of Stambaugh et al. [98], this corresponds to a a minimum PhC transmission of 2.5×10^{-5}.

Double membrane transmission loss

In each round-trip, some light inside the double membrane etalon is transmitted through the PhC mirrors. If both membranes had exactly the same PhC resonance wavelength and if the highest finesse peak was exactly at the same wavelength as that resonance, this would result in a round-trip transmission of 5×10^{-5}. However, the double-membrane peak is not, in general, at the PhC resonance. For a double-membrane with similar PhC resonances, the peak can be, at most, 3 nm (approximately $\mathrm{FSR_{DM}}/2$) away from the PhC resonance. According to

Figure 5.11, this sets an upper boundary to the round-trip transmission of 2.6×10^{-2}.

Material losses

When light interacts with the SiN layer, some of it will be absorbed by the material or scattered away due to fabrication imperfections. To estimate the magnitude of these effects, we use S^4 to simulate the reflection and transmission through a PhC with similar parameters to those of Figure 5.11. We have considered the material to have an imaginary part of the refractive index of 1.9×10^{-5} [98], which accounts for not only absorption but also other loss mechanisms such as scattering [17], and we calculate the losses as $L = 1 - R - T$, where R is the reflection and T the transmission coefficients. The simulation results are shown on the lower part of Figure 5.11. We see that the measured transmission follows the simulation quite well. Within this wavelength range, the losses are approximately constant and have a value of 3.5×10^{-4}.

Finite aperture loss

Any Fabry-Pérot inteferometer with a finite aperture will lose some of the light through diffraction at the mirror edges [96, 102]. These losses are higher for smaller mirrors and for increasing cavity stability parameter. In particular, a plane-parallel Fabry-Pérot cavity has a stability parameter $g = 1$, which makes it particularly susceptible to finite aperture losses.

To estimate these, one can calculate the cavity Fresnel number $N = a^2/L\lambda$, where a is the mirror radius and L is the cavity length, and obtain the estimated losses per cavity round-trip from tables in literature [96, 102]. Given a mirror diameter of 260 µm, the Fresnel number of our devices is 54, which corresponds to a loss per round-trip of 2×10^{-3}.

Notice that this effect could be directly mitigated either by making the PhC membranes larger, or by controlling the wavefront of the field with one of the PhC, effectively realizing a focusing mirror [36]. This would reduce the stability parameter of the cavity, making it less susceptible to finite aperture losses.

Total losses

Taking into account the previous results, we can estimate the total losses of the double-membrane array if its highest finesse peak is at the resonance wavelength of the PhC or if it is 3 nm away from it. Using the finite aperture loss, the measured transmissions and the simulated material losses, we reach round-trip total losses of 2.8×10^{-3} and 2.9×10^{-2}, corresponding to cavity finesse values of 2243 and 217. The lower bound of this range is in good agreement with the maximum finesse we measure in our devices of about 140. However, most of our samples show maximum finesses which are approximately a factor of 5 smaller. This could be due to underestimations of scattering and diffraction losses, or due to additional absorption by material residues on the SiN layers.

Mode profile analysis

The reflection and transmission beam profiles can also help in understanding the behavior of our devices. We install flip mirrors in our setup which can send the optical beams to an IR-sensitive camera and record the beam profiles for single and double membranes, shown in Figure 5.12 a and b, respectively.

For the single membranes we obtain the beam profiles slightly detuned from the maximal reflectivity, around 95 %, as otherwise the transmission is below the sensitivity of the camera. The measured modes have an overlap of approx. 83 % with a Gaussian distribution, highlighting that the PhC structures distort the transmitted optical beams only slightly.

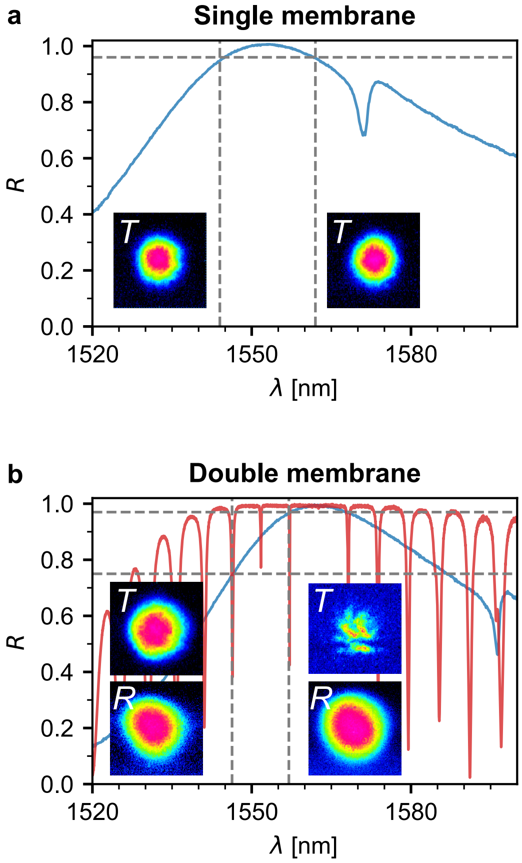

Figure 5.12: Shown are the reflection spectra, together with the transmitted (T) and reflected (R) beam mode profiles of single **a** and double membranes **b**. The dashed lines indicate the reflectivity and wavelength at which the mode profiles were measured.

In Figure 5.12b we plot the reflection spectrum of a double membrane (red) which individual membranes have a spectrum similar to the one shown in blue. The resonance with the highest finesse occurs at 1562 nm, however its low dip depth makes the mode difficult to measure with our camera. The adjacent resonance at 1557 nm shows the second highest finesse ($\mathcal{F} = 144$), corresponding to single membrane reflectivities of around 97 %. Here we are able to measure the beam profiles for the transmitted and reflected light. While the reflection is mostly unaffected, the transmitted beam appears distorted. As the single membrane transmission does not show such behavior, we suspect the distortion results partly from scattering losses, as described in Section 5.4.1.2. This loss mechanism becomes more dominant as the number of cavity round-trips, i.e. the finesse, increases. Indeed, for the resonance at 1546 nm with a lower finesse of only 21, corresponding to a single element reflectivity of 75 %, the transmitted and reflected beam profiles have an overlap with a Gaussian distribution of more than 84 %.

In addition, we would also like to note that the tip/tilt alignment becomes more important in double membrane arrays with high finesse, since the incident beam has to be properly mode matched to the cavity. This is further complicated by the plane-parallel geometry of our PhC cavities and could therefore be another main contribution to the observed mode distortion. This problem could be ameliorated by making one of the PhC mirrors a so-called *focusing* PhC [36], which can decrease the cavity stability parameter, making the mode matching and alignment easier.

5.4.1.3 *Challenges and perspectives*

The limitations of our current monolithic design is reflected in the observed reduction of the peak transmission for increasingly large mirror reflectivities, i.e. high finesse arrays. For a lossless Fabry-Pérot cavity, unity transmission is reached only for matching mirror reflectivities, whereas additional losses due to absorption, scattering or diffraction will inevitably contribute to a further reduction in its peak transmission.

In the low finesse regime, we observe peak transmissions close to unity since the individual mirror transmission losses exceed the additional loss terms. In this regime, the peak transmission is mainly determined by their mirror mismatch where even large differences in the intensity reflectivity of the individual mirrors do not contribute at all (red curve in Figure 5.8).

For the high finesse case, things become more complicated, since both effects of mirror impedance mismatch and other loss contributions exceeding those of the mirror transmission losses start to significantly contribute and effect the measured double-membrane spectra. In terms of impedance mismatching, we tried to overlap both

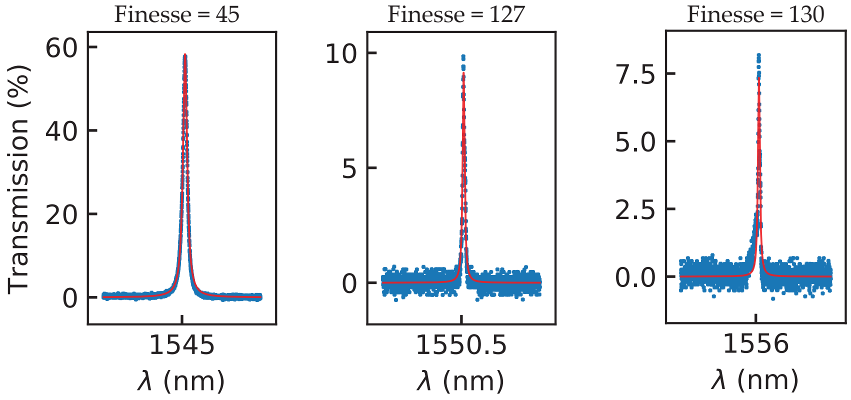

Figure 5.13: Largest transmission peaks in the high-finesse regime of double-membrane arrays with measured finesse values of up to 130 and accompanied peak transmissions of around 8 %.

mirror resonances as good as possible with slight improvements in the achieved finesse and dip depth (cf. Figure 5.13). This leads to the assumption, that – despite relatively well matching mirror transmissions – the main contribution to the reduction of array peak transmissions come from additional other losses related to scattering, diffraction and material absorption. This ultimately results in very low peak transmissions in the high finesse regime where mirror reflectivities approach unity.

For our best arrays we achieve finesse values of up to 140 with dip depths in the single digit regime of around 10 % (center graph in Figure 5.13). Comparing the performance of our best arrays with the expected finesse and transmission peaks with the help of an online etalon designer tool[2], we find good agreement for mirror reflectivities R_1 and R_2 of around 99.8 %.

The upper rows in Table 5.1 correspond to our array design where the mirror separation L_{DM} and aperture, i. e. PhC diameter d_{PhC}, are 200 µm and 300 µm, respectively. Assuming individual mirror intensity reflectivities of 99.8 % results in the observed finesse and peak transmission values in the planar case mainly independent of additional loss contributions due to material absorption δ. The online tool also suggests that the limiting contributions stem from the plane-parallel configuration and are thus attributed to diffraction/finite aperture losses. Interestingly and worth mentioning for the case of plane-parallel arrays with even unpatterned square membranes, the second highest limiting finesse contribution comes from surface irregularities of the membranes themselves (not shown here). Assuming a reasonable surface roughness of 5 Å [105] and neglecting the limitations arising from the current array settings result in a maximum achievable finesse of 660. In order to circumvent the accompanied per-

---

[2] `https://lightmachinery.com/optical-design-center/etalon-designer/`

L_{DM} (µm)	d_{PhC} (µm)	R_1 (%)	R_2 (%)	Loss δ (ppm)	$\mathcal{F}$ (T) planar	spherical
200	300	99.95	99.95	50	142 (2 %)	5710 (91 %)
200	300	99.8	99.8	50	141 (9 %)	1531 (98 %)
200	300	99.8	99.8	5000	135 (9 %)	448 (28 %)
200	300	99.0	99.0	50	129 (41 %)	311 (100 %)
200	300	99.9	99.7	50	141 (7 %)	1531 (73 %)
200	300	99.9	99.7	5000	135 (6 %)	448 (21 %)
200	500	99.8	99.8	50	334 (21 %)	1531 (98 %)
50	500	99.8	99.8	50	560 (36 %)	1531 (98 %)

Table 5.1: Influence of Fabry-Pérot etalon design parameters on finesse $\mathcal{F}$ and peak transmission T predicted by an online etalon designer tool for plane-parallel arrays and those with at least one focusing element. L_{DM} and d_{PhC} being the length double-membrane array and diameter of the PhC, R_1 and R_2 the individual mirror intensity reflectivities, and losses δ attributed to material absorption and scattering. Upper four rows: our array configuration for various mirror reflectivities resulting all in similar finesse and transmission peak predictions. Middle two rows: our configuration with mismatched mirrors and varying loss. Last two rows: shorter arrays with larger, matching mirrors resulting in higher finesse and peak transmission.

formance limitations due to the plane-parallel configuration, we can form a spherical cavity array, which promises significantly higher finesse and peak transmissions due to the absence of diffraction limiting contributions (last column in Table 5.1). By how much the non-perfect etching and surface smoothness of the etched PhC holes contribute to additional scattering losses can only be fully understood when currently dominating loss contributions are minimized. So far, scattering due to the holes and material absorption do not seem to be the main contributors, but surely should be kept in the back of the mind when aiming for double-membrane arrays of highest finesse and peak transmissions.

In order to quantify the influence of mismatching mirror reflectivities, we assumed small reflectivity differences of 0.2 % points for maximum values as high as 99.9 % (middle rows of Table 5.1). Interestingly, in this regime, the discrepancy between both mirrors only contributes minimally to a reduction in peak transmission when compared to the case of perfectly matched mirrors. However, we have also often noticed close to zero transmission at peaks corresponding to highest finesse (cf. Figure 5.7) and/or alternatively larger mismatches (cf. Figure 5.6). This additional reduction in dip depth can be attributed to small mirror mismatches in the very high finesse regime, where minor differences between the mirrors already significantly contribute to a reduced transmission even without existing losses (cf. Figure 5.8). In general, low peak transmissions close to zero are the result for very high finesse arrays, where additional loss contributions exceed the (very small) mirror transmission losses significantly, even for the case where both mirrors are assumed to be perfectly matched. In addition, small mirror mismatches again start to significantly contribute when working with mirrors at their PhC resonance with highest reflectivity.

Indeed, increasing the mirror size and reducing the separation between them leads to slightly higher finesse with significantly larger peak transmission. However, it seems apparent that reaching highest finesse arrays with close to unity peak transmission can only be achieved by forming a stabler spherical cavity with at least one focusing element. We have – to a reasonable amount – ruled out that the reduced peak transmissions arise from mismatching mirror reflectivities when not operated at the PhC resonance with reflectivities beyond 99.9 %. In general, additional losses exceeding those of the mirror transmissions will always result in a large reduction of peak transmission especially for increasingly large array finesse, i. e. being mirror transmission loss limited is crucial and with the current design only possible for arrays with lower finesse.

5.5 RESULTS AND DISCUSSION

For a more systematic study of the optomechanical properties, we design three PhC patterns in order to obtain different R_m at our operating wavelength of 1550 nm. We refer to these patterns as *Low*, *Mid*, and *High R*, and their geometries and measured R_m at 1550 nm are specified in Table 5.2. The optical beam we use to probe the PhC has a waist size of about 50 µm. To avoid clipping losses, the central mirror pad has a side length of 300 µm, while the tether length and width are 318 µm and 10 µm, respectively. Figure 5.5 shows a cross-sectional schematic of a final double membrane stack, as well as a false-colored SEM of one of our released devices.

For each PhC pattern (cf. Table 5.2), we fabricate a single- and a double-membrane, which allows us to test all designs on a single chip, greatly facilitating the measurements. In the following subsections, we characterize their optical, mechanical, and optomechanical properties.

5.5.1 *Optical characterization*

Single membranes

We first obtain the optical spectra of the single devices by scanning a tunable laser from 1510 nm to 1600 nm and measure the reflected and transmitted signals from the PhC trampolines, which are shown in Figure 5.14. At 1550 nm, we measure reflectivities of 33 %, 56 %, and

	a (nm)	r (nm)	R_m @1550 nm
Low R	1240	475	33 %
Mid R	1310	500	56 %
High R	1372	525	99.8 %

Table 5.2: Lattice constant a and hole radius r of the PhC patterns used in this work, as well as their measured reflectivity R_m at our operating wavelength of 1550 nm.

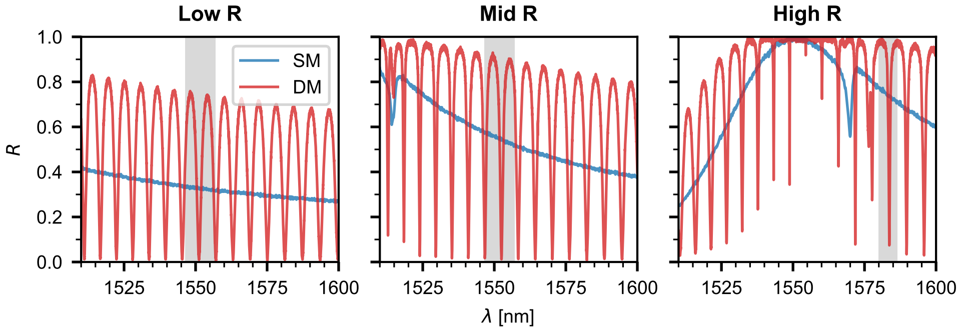

Figure 5.14: Reflection spectra of the devices. The photonic crystal pattern of each device is indicated at the top of each figure, according to the parameters in Table 5.2. The blue traces correspond to devices composed of a single-membrane (SM), whereas the red traces are from double-membrane stacks (DM). The gray-shaded regions correspond to the wavelength ranges where the center-of-mass optomechanical coupling was measured (see Figures 5.15 and 5.16).

99.8 % for the Low, Mid, and High R samples, respectively. Because this measurement procedure has an uncertainty of 0.5 %, we determine the dispersive effect of a device similar to the High R sample on an optical cavity to obtain a lower bound on its transmission at resonance [17, 98]. We measure a transmission of 2.5×10^{-5}, comparable to the best reported results in the literature [17]. Finally, we simulate a PhC membrane with an imaginary component of the refractive index of 1.9×10^{-5} [98], and estimate that a fraction of 3.4×10^{-4} of the light is lost when interacting with the devices, due to either absorption or scattering from fabrication imperfections (cf. Section 5.4.1.2).

Double-membrane arrays

The double-membrane arrays have the same PhC design as the individual membranes and we determine their optical response in a similar way, shown in Figure 5.14. These structures can be modeled as plane-parallel etalons (Figure 5.5) and the characteristic features of Fabry-Pérot interferometers can be clearly observed in their spectra. The free spectral range $\mathrm{FSR_{DM}}$ of 750 GHz, or 6 nm at a wavelength of 1550 nm, is, as expected, defined by the 200 µm thickness of the Si substrate that separates the two membranes. The linewidth of the resonances becomes smaller as the reflectivity of the individual membranes increases. This is particularly prominent on the High R sample, where the full-width at half-maximum linewidth changes from 176 GHz at 1521 nm to 8.7 GHz at 1554 nm, corresponding to a change in finesse $\mathcal{F}$ from 4.3 to 86. Our best performing samples exhibit linewidths as low as 5.3 GHz ($\mathcal{F} = 140$), suggesting a total loss per round-trip of approximately $2\pi/\mathcal{F} = 4.5 \times 10^{-2}$.

Several sources contribute to this loss. First, using the measurements presented in the previous section, we estimate a lower bound for the round-trip transmission of 5×10^{-5}. However, in general the highest finesse etalon peak is not exactly at the resonance of the PhC, being at most $\mathrm{FSR}_{\mathrm{DM}}/2 = 3\,\mathrm{nm}$ away from it. At this point, the round-trip transmission becomes 2.6×10^{-2}. Second, we expect a round-trip absorption and scattering loss of 6.8×10^{-4}. Finally, some light will be lost due to the finite aperture size of the etalon. Plane-parallel Fabry-Pérot cavities are particularly susceptible to this effect [96, 102], and we estimate it to result in a round-trip loss of 2×10^{-3}. Combining these effects we arrive at estimated total round-trip losses from 2.8×10^{-3} to 2.9×10^{-2} (cf. Section 5.4.1.2 for more details).

Although the maximum finesse measured in our devices fits well to this range, the fact that we generally measure lower values suggests that they are underestimated. Scattering, which has consistently been identified as one of the main loss mechanisms in other PhC membranes [17, 98], could be higher than expected. In addition, these estimates assume that both membranes have the same reflectivity. In both the Low and Mid R samples the reflection drops to zero at the etalon resonances, indicating that the PhC resonances on the front and back membranes are sufficiently well matched in these regimes. However, with increasing reflectivities, mismatches due to fabrication imperfections and small systematic shifts between the individual PhC mirrors become more apparent and lead to smaller dip depths (cf. the High R device in Figure 5.14). In fact, as the reflectivity of the individual membranes increases, the dip depth becomes significantly more sensitive to differences between the two mirrors (see Figure 5.8). This also results in higher round-trip transmission values that can explain the discrepancy between our finesse estimates and measurements.

5.5.2 *Mechanical characterization*

We determine the mechanical quality factor of the fundamental modes of both single and double membrane devices by performing interferometric ring-down measurements. The mode frequencies are approximately 150 kHz and the difference in frequency between the front and back membranes is typically around 170 Hz. The small difference of around 0.1 % in resonance frequency can be attributed to an irreproducibility in the fabrication process. All devices show unclamped quality factors in the range from 1.2×10^6 to 5.6×10^6. These values are in good agreement with measurements on a similar geometry, which showed quality factors of 4×10^6 [73], indicating that the PhC patterning does not negatively effect their mechanical properties.

5.5.3 *Optomechanical characterization*

In order to obtain the optomechanical characteristics of the devices we place them inside an optical cavity. The optical modes of this larger cavity strongly depend on the position of the membranes inside. By measuring the changes in cavity mode frequency ω_c as a function of the device displacement x, we are able to determine the linear optomechanical coupling between the cavity and the device's center-of-mass mechanical modes, which we define as $G \equiv \max\{|\partial\omega_c/\partial x|\}$. The cavity has a free spectral range $\mathrm{FSR_c} = 3.13\,\mathrm{GHz}$ and an empty cavity half-width at half-maximum of $\kappa/2\pi = 550\,\mathrm{kHz}$. We align our tunable laser to the cavity and measure the transmitted light. The laser frequency is then scanned as a function of the device position, which allows us to directly obtain $\omega_c(x)$ and calculate the optomechanical coupling.

Let us first consider the case of a single-membrane, where the cavity modes are affected by the membrane position and reflectivity R_m, according to $\Delta\omega_c/2\pi = \mathrm{FSR} \cdot \arccos(\sqrt{R_m}\cos(4\pi x/\lambda))/\pi$ [104]. The so-called linear coupling regime occurs when a membrane is placed close to $x = \lambda/8 + n\lambda/4, n \in \mathbb{Z}$. Around these points, the cavity frequency changes linearly with the membrane position and the optomechanical coupling is given by

$$\frac{G}{2\pi} = 4\frac{\mathrm{FSR}}{\lambda}\sqrt{R_m}. \tag{5.1}$$

The first row of Figure 5.15 shows the cavity transmission as a function of laser frequency shift and displacement of the single-membrane samples. The wavelength at which the measurements were taken is indicated above each plot. The points of high transmission correspond to cavity modes. Because of alignment imperfections between the impinging light beam, the cavity and the membranes, in addition to the fundamental cavity mode, we also observe higher order modes, which can be coupled to each other [90]. The fundamental optical mode frequency depends on the membrane position with a periodicity of $x/\lambda = \pi/2$ and the amplitude of the frequency oscillations increases with the membrane reflectivity, as indicated by Equation (5.1). Using these data, we obtain G by numerically calculating $|\partial\omega_c/\partial x|$ and taking its maximum value, which occurs at the positions of linear coupling. The blue data points in Figure 5.16 show the single membranes' coupling around a narrow wavelength window. In addition we plot the coupling as calculated by the reflectivity measured in Figure 5.14 and

Equation (5.1). Within this wavelength range, the reflectivity of each device varies little and therefore G is practically constant. The average measured couplings $G/2\pi$ for the Low, Mid, and High R samples are 3.8(6), 5.7(9) and 7.7(12) MHz/nm, whereas the expected values using Equation (5.1) and $\sqrt{R}$ are 4.5, 5.8, and 6.8 MHz/nm. Despite the large uncertainty, mainly due to the displacement calibration, the results are in good agreement with Equation (5.1).

Finally, we follow the same approach to obtain the coupling rate between the cavity and the COM displacement of the double-membrane chips, schematically represented in Fig. 5.5. The crucial difference between single and double-membranes is that the latter's spectra vary more strongly with wavelength. In particular, over one $\mathrm{FSR_{DM}}$, the device reflectivity can quickly change from zero to one (see Figure 5.14). When the reflectivity is low, the COM mode of the device will interact weakly with the external cavity. Correspondingly, at a reflection maximum, the coupling will be higher than that of a device composed of only one membrane. In rows 2 to 5 of Figure 5.15 the measured cavity dispersion for the three double-membranes studied is shown. We perform these measurements at several wavelengths spanning half a $\mathrm{FSR_{DM}}$, between which the reflectivity varies between its maximum and minimum values. Note that for the High R sample we choose to study a resonance for which $R_m \sim 0.76$ (λ close to 1580 nm) since for higher R_m the laser fine scanning range becomes similar to the resonance linewidth, and the dip depth decreases, making the coupling oscillations less visible. Row 2 corresponds to the reflectivity maxima. When comparing it with row 1, it becomes clear that the cavity frequency varies more strongly than in the single-membrane case. The data in row 5 are taken close to a transmission maximum where, as discussed, the COM motion has little influence on the cavity frequency. Rows 3 and 4 show wavelengths in between the maximum reflection and transmission of the double-membrane stacks. The extracted COM coupling is plotted in red in Figure 5.16. As discussed, the coupling oscillates between almost zero and values larger than those of the individual membranes. The oscillation follows the device's spectral response, indicating that the COM coupling of a double-membrane is well described by Equation (5.1), a model derived from the single-membrane case.

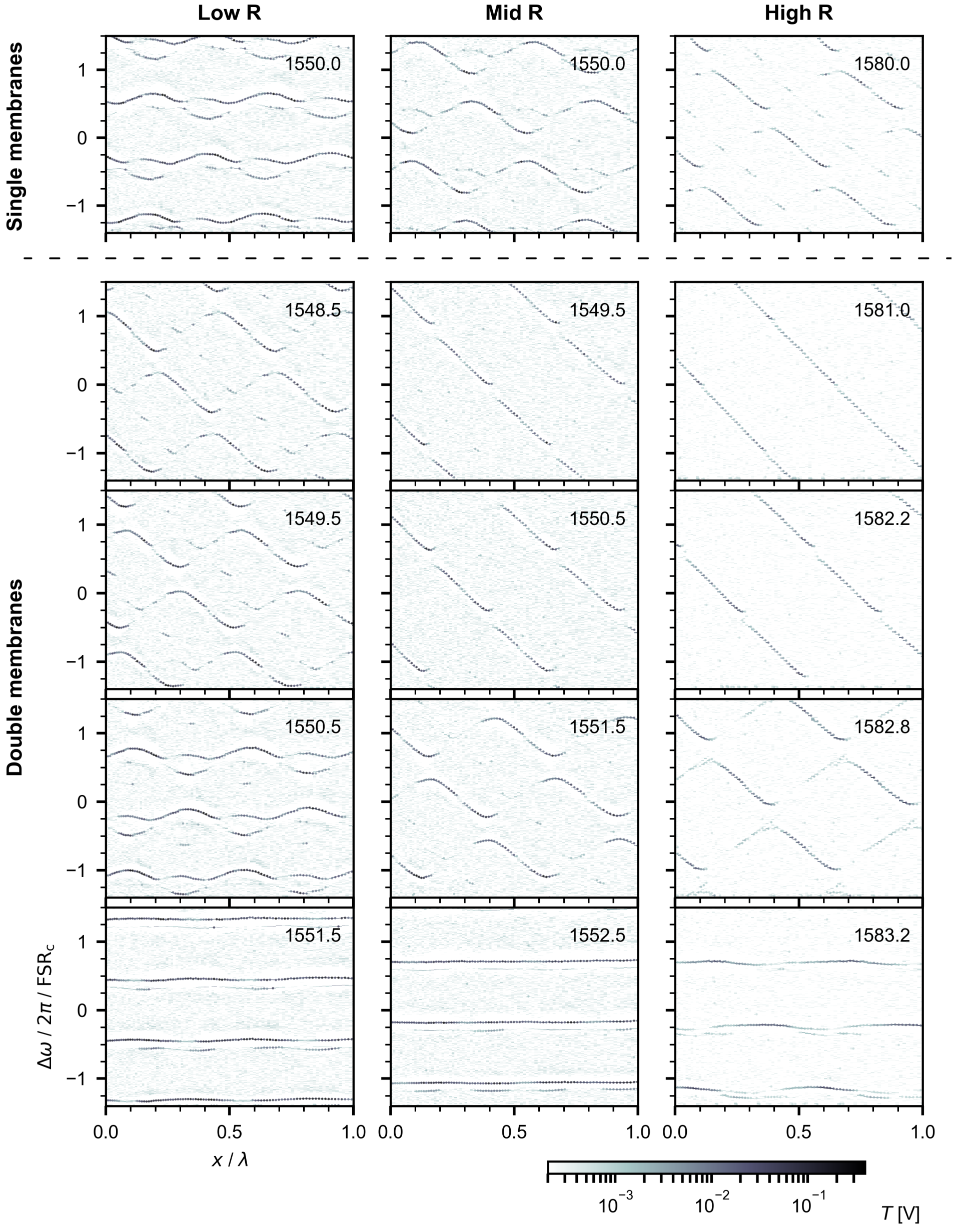

Figure 5.15: Optical cavity transmission T as a function of the frequency shift $\Delta\omega$ of the incident laser and of the displacement x of several mechanical devices placed in the middle of the cavity. $\Delta\omega$ is normalized by the cavity free spectral range $\mathrm{FSR_c} = 3.13\,\mathrm{GHz}$ and x by the laser wavelength λ which is indicated on top of each plot. We measured multiple devices in the middle of the cavity: on the left of the dashed line we study single-membranes and on the right double-membranes. The type of photonic crystal used in each sample is indicated on the left of the figure. Note that in order to work in a regime with a slow reflectivity change and large dip depth, the High R samples were studied at a wavelength for which $\mathrm{R_m} = 0.76$.

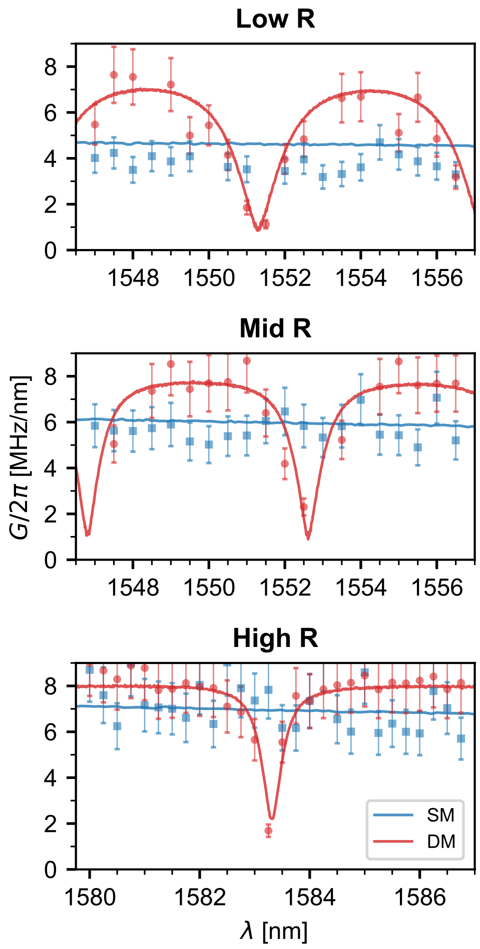

Figure 5.16: Center-of-mass optomechanical coupling $G/2\pi$ as a function of wavelength λ obtained through the derivative of the cavity dispersion $\max\{|\partial\omega_c/\partial x|\}$ (points) and through the membrane-in-the-middle model $4\frac{\mathrm{FSR}}{\lambda}\sqrt{R_m}$ (lines). The blue data are taken from single- (SM) and the red from double-membrane (DM) devices. The corresponding PhC patterns are indicated on top of each figure with the wavelength range studied here marked in gray in Figure 5.14.

5.6 CONCLUSION AND OUTLOOK

In conclusion, we have fabricated and characterized stacks of optomechanical devices that operate in various low to high reflectivity regimes. The devices presented here are patterned onto a single chip without the need for additional bonding steps or micro-positioners. Our devices form a flexible platform in which the finesse can be freely tuned. Placing these devices inside an optical cavity allows the direct comparison of membrane-in-the-middle systems in multiple reflectivity regimes, such as proposed by Xuereb and Domokos [116]. We see slight enhancements of the optomechanical coupling rate between the COM motion of the two membranes and the cavity field as a function of reflectivity, when compared to a single membrane system.

More importantly, by changing the laser frequency we can tune the system such that the COM coupling is practically zero. The theory of the collective motion of optomechanical arrays predicts that at these points the cavity field becomes resonant with the inner cavity and thus couples strongly to the relative motion of the membranes. This is the regime where single-photon strong coupling in an optomechanical system could be achievable [115]. We are currently working on improving the stability of our setup in order to probe these relative motional modes. For devices with large R_m, like the ones presented here, the coupling enhancement of the differential mechanical motion is limited by the ratio $L/2d$ between the length of the optical cavity L and the separation between the membranes d [60]. Given our experimental parameters, this should allow us to observe an enhancement factor of up to 120. Increasing this value further could be done by replacing the Si substrate by a thin sacrificial layer as the spacer between mirrors, considerably decreasing d to values similar to [70] but keeping the advantages of monolithic fabrication presented here.

Even more interestingly, the single-photon cooperativity scales quadratically with the single-photon coupling strength, which in our case could boost this important figure of merit by 4 orders of magnitude, assuming the mechanical and optical dissipation rates stay the same. For many experiments, coherent control in the strong single-photon coupling regime is not necessary but reaching cooperativities greater than one is sufficient for performing several quantum protocols [4, 58]. Other interesting experiments could include synchronization of mechanical modes [121], studying exceptional points in optomechanics with independent mechanical systems, as well as superradiance [35, 53] and state transfer between mechanical systems [112]. In addition, our arrays could serve as rigid, stable free-space optical filters with adjustable finesse. The arrays also constitute an optomechanical system by themselves, whose mirrors are both movable and with engineerable optical and mechanical properties. As both mirrors and mechanical resonators are monolithically combined, the system is inherently stable, greatly relaxing the setup complexity of typical free-space optomechanical setups, and making it an ideal platform for simple studies of radiation-pressure effects.

Ways towards better membrane arrays

Focusing PhC

Highest finesse and transmission values can be achieved by using a cavity configuration with spherical mirrors avoiding the contribution of additional losses attributed to plane-parallel etalons. This problem could be ameliorated by making one of the PhC mirrors a so-called *focusing* PhC [36], which promises to reduce currently dominating diffraction losses, and ultimately leads to cavities exhibiting both high finesse and peak transmissions.

Shorter arrays with larger mirrors

Another apparent approach towards improving current design limitations is to go to shorter arrays consisting of larger mirrors. Assuming a mirror separation L_{DM} of 200 µm and larger mirrors of 500 µm (cf. Figure 5.17) as already successfully fabricated promises slightly increased finesse and peak transmission due to reduced diffraction losses. Ultimately, upon aiming for even further improvements, this implies giving up the approach of monolithically combining both mirrors on opposite sides of the same chip on the Si/SiN material platform where handling of thin substrates becomes impossible. Alternatively, adding additional layers of high-stress LPCVD-grown SiN and an appropriate sacrificial layer could allow for shorter double-membrane arrays with both device layers on the same side of the chip. However, the question remains whether these layers can be grown of sufficient accuracy and quality.

Flip-chip approach with large PhC membranes

Another idea is going away from the monolithic design to a flip-chip approach with two individual chips as already performed by several groups working with bare SiN membranes. This possibly allows to reduce the spacing between both mirrors by using some sort of spacer material that defines the distance between both membranes as exploited in [70]. However, this could introduce additional losses due to a possible misalignment between both mirrors. These tip tilt losses – depending on the amount – can again lead to a limited device performance especially for high finesse arrays. One would need to carefully control the distance between both membranes and make sure, that height difference of the clamping and/or gluing procedure will not lead to a big tilt between the mirror surfaces. Studies on such structures have been shown to work, at least in the low finesse regime

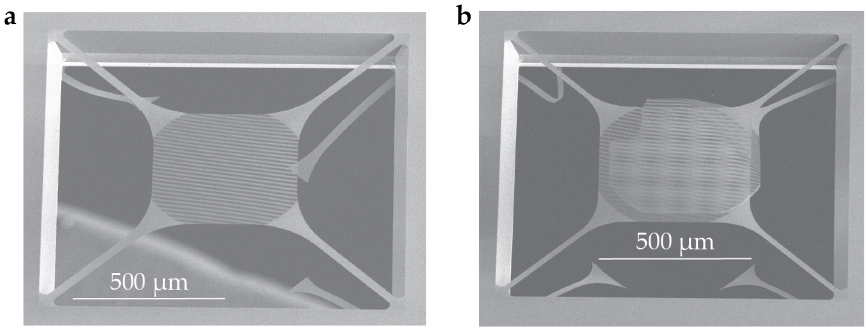

Figure 5.17: Single tethered PhC membranes with 500 µm central pads. Shown are designed double-membrane arrays whereas only one of the membranes survived the fabrication process with remnants of the second membrane still visible. In **a** the entire central pad is gone, whereas in **b** the central pad of the bottom membrane collapsed onto the pad of the upper one revealing points of fracturing at the PhC periphery.

[69, 70]. One additional thing to keep in mind is the fact, that the FSR for shorter cavities becomes much larger, ultimately limiting the minimum spacing one could measure with the available tuning range of the laser. Another issue then will be to perfectly match the resonance of the PhC with the transmission peak of the array which depends on the exact thickness of the spacing. Admittedly, this approach seems to be quite a lot of work considering the promised improvements.

III-V semiconductors as a way out?

Multi-membrane arrays on Si/SiN seem to be limited to maximally two membranes with separations defined by the minimum wafer thickness – at least for our monolithically integrated approach. A possible solution towards that limiting challenge is using the III-V material platform since many layers can be grown in a controllable manner resulting in device layers of high mechanical and optical quality. As mentioned before, the smaller the spacing between membranes become the better the control is needed to accurately hit the membrane cavity resonance as the FSR becomes increasingly large. This can be overcome by either having the possibility to optically tune the laser resonance (one still requires the optical PhC resonance to effectively overlap with the FSR resonance) or having control over the membrane spacing by moving the membranes along the optical axis. Another way towards matching resonances is to accurately control the spacing between both membranes during the growth process. In the following chapter, we will see that molecular beam epitaxy (MBE) allows to possibly overcome those limitations, resulting in multilayer structures of even more than just two membranes and minimal, well-controllable separation among them without the need for additional alignment procedures.

6

III-V TERNARY INGAP MEMBRANES FOR MULTIMODE OPTOMECHANICS

In the previous chapter we introduced the fabrication of monolithic double-membrane arrays of two highly reflective SiN membranes in a single chip. Due to their plane-parallel configuration, these 200 µm-long Fabry-Pérot interferometers are however limited by diffraction losses.

One possible way towards improving the current device performance is by forming significantly shorter cavity arrays, ultimately promising even stronger coupling strengths and lower loss. This in turn requires very accurate membrane positioning.

Here, we present the vision of overcoming these challenges by growing a crystalline multilayer heterostructure based on III-V semiconductors with well-controlled film thicknesses of high quality defined by molecular beam epitaxy (MBE). The membranes are made of the ternary III-V alloy indium gallium phosphide (InGaP) whose tensile stress can be controlled through lattice-mismatch during film growth [11, 21]. This approach not only enables the exploration of arrays with more than two membranes but also allows the monolithic integration of membrane arrays atop a distributed Bragg reflector (DBR).

Placing the array right atop one of the endmirrors raises the question whether the predicted results of enhanced coupling strengths in the transmissive regime in the middle of a cavity breaks down under such highly asymmetric conditions. We answer this question by performing extensive transfer matrix method (TMM) simulations showing that double-membrane arrays in the asymmetric cavity configuration result in the same enhancements for identical array parameters and optimized membrane positioning within the optical cavity. For bare InGaP membranes of 65 % reflectivity, this promises enhancements of the coupling strength by almost one order of magnitude with an outlook to even larger enhancements when exploiting PhC patterned membranes.

With the obtained results, we design a full wafer with optimized film thicknesses for operation at cryogenic temperatures and introduce a full fabrication flow towards the realization of single InGaP membranes integrated atop a DBR.

6.1 INTRODUCTION

SiN as the material of choice has lead to tremendous progress in quantum optomechanics and in particular with experiments observing quantum behavior of mechanical resonances, however most of these previous efforts have focused on single mechanical or noninteracting modes. Studying the behavior of multiple directly coupled modes could however allow probing new and exciting regimes of optomechanics, chief among achieving large coupling enhancements by using several mechanical resonators within an optical cavity. Recent developments toward achieving this endeavor include the investigation of arrays consisting of non-patterned square membranes with single element reflectivity dependent on their thickness.

In the previous chapter, I have introduced the monolithic fabrication of two tethered PhC membranes on the same chip with engineered reflectivity close to unity. Even though this system allows for the observation of enhanced coupling strengths by two orders of magnitude, it has severe drawbacks to be overcome. Due to its plane-parallel configuration, the achievable finesse values of the double-membrane arrays are currently limited to 140 with possible improvements when e. g. going to shorter arrays and larger mirrors. This not only promises to significantly reduce the current dominating losses related to diffraction but also to further increase the maximally achievable enhancement of the coupling strength due to the significantly reduced membrane separation. Shorter arrays have been achieved by separating commercially available bare SiN membranes with appropriate spacers defining its cavity length. However, this approach increases the experimental complexity by requiring careful individual alignment of both membranes without having good control over their separation. In addition, the demand for operation in the transmissive regime requires either the ability to tune the laser wavelength with respect to the membrane separation or vice versa. Shorter cavities however exhibit increasingly large FSRs which makes laser tuning impossible, hence posing a major obstacle towards successfully controlling the array system.

One possible way toward circumventing current design limitations is to form high-finesse cavities with larger mirrors and shorter, well-controlled distances between adjacent membranes. We follow a bottom-up approach by growing thin films of well-controllable thickness by means of molecular beam epitaxy (MBE), which allows the fabrication of membrane arrays with more than two membranes.

Furthermore, I describe initial attempts to not only grow the stack of membranes, but also integrate it with a DBR and thus constituting the majority of a membrane-at-the-endmirror (MATE) configuration (cf. Figure 6.1).

The material platform of choice are ternary III-V semiconductors that allow the growth of mirrors and membranes with excellent mechanical and optical properties. A common material system for the growth of high-quality DBRs is the combination of alternating stacks of high and low refractive index AlGaAs/GaAs[1] [22].

---

[1] https://www.crystallinemirrors.com/

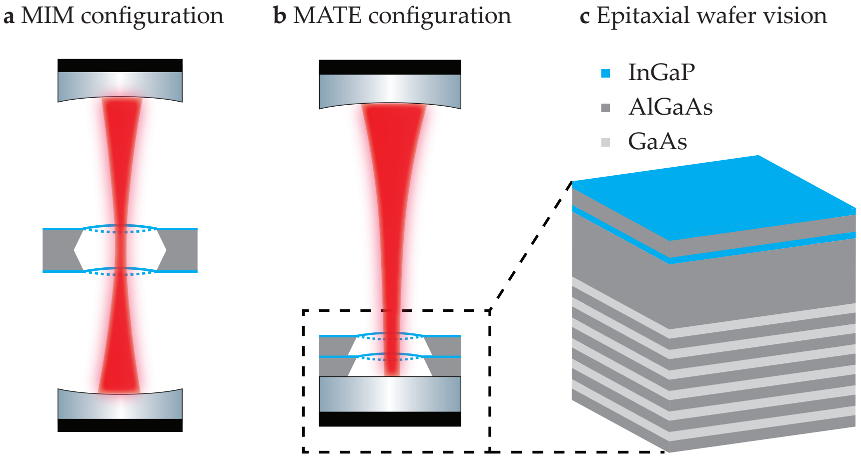

Figure 6.1: From membrane-in-the-middle (MIM) to membrane-at-the-endmirror (MATE) configuration. **a** Typical MIM configuration with a double-membrane array located in the middle of the optical cavity comprising two mirrors, in contrast to the design investigated here, where the membrane-array is monolithically integrated with one of the end-mirrors as depicted in **b**. Realization of the MATE configuration with a molecular beam epitaxy (MBE)-grown heterostructure consisting of alternating quarter-wave (Al)GaAs DBR, and two sacrificial AlGaAs and InGaP device layers, respectively. Depicted are only few double-layers of the DBR.

For the membranes, $In_xGa_{1-x}P$ has recently emerged as alternative resonator material (we drop the subscripts for the sake of readability and specify upon need). We have investigated the optomechanical properties of tensile-strained InGaP nanomembranes grown on GaAs (cf. Cole et al. [21]). This material system combines the benefits of highly strained membranes, similar to those based on stoichiometric SiN, with the unique properties of thin-film semiconductor single crystals, as previously demonstrated with suspended GaAs [62]. The tensile strain can be tuned by the lattice mismatch between substrate and thin-film during epitaxial growth through variations in the alloy composition of ternary InGaP. InGaP is lattice matched with GaAs for an In content of 49 % and exhibits tensile strain for values below. Dissipation dilution through strain engineering, possibly high intrinsic quality factors of single crystalline films and the possibility to stack layers makes this material platform an intriguing candidate for multimode optomechanical experiments with membrane arrays. In addition, the monolithic, integrated approach promises to significantly reduce the experimental complexity as it gives the ability to align the structures in epitaxial growth.

6.2 DEVICE DESIGN

We are interested in an optomechanical system with two membranes close to one of the end-mirrors, in contrary to the more typical MIM-type setup with membranes more centrally located (cf. Figure 6.1). At one end of the cavity, both mirror and double-membrane stack are integrated monolithically and eventually fabricated from a single chip. The other mirror comprising the full optomechanical system can be arbitrarily chosen with commercially available mirrors of arbitrary transmittance and radii of curvature.

Ultimately, we are interested in optimizing the system parameters for maximized optomechanical coupling strength of the entire cavity-membrane system with respect to the standard MIM case with a single membrane.

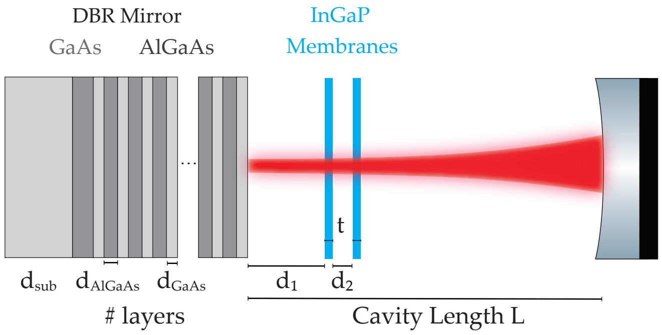

Figure 6.2: DBR-double-membrane system parameters

Since the entire system depends on many parameters, we can first dissect it into subsystems that we analyse individually. Figure 6.2 shows an overview of the parameters under investigation. Note, that for the sake of readability the second mirror comprising the cavity on the right is not depicted as a DBR, it will – however – be treated as such when investigating the whole optomechanical cavity. The simulations are executed by means of a one-dimensional transfer matrix method (TMM) approach which we describe in more detail in Appendix A.

For a successful implementation of TMM simulations, we only require knowledge about the optical properties of the various layers at play with refractive index n and thickness d. Our material system is made of the ternary III-V semiconductors GaAs, AlGaAs and InGaP, whose material properties are summarized in Table 6.3 for the material compositions used. Designing the entire multilayer heterostructure with accurate film thicknesses requires the refractive indices of the compound semiconductors at both cryogenic and room temperatures, as well as their specific coefficient of thermal expansion (CTE), which will be discussed in more detail later on.

In the following, we will have a look at some aspects of the individual subsystems, starting first with the DBR by analyzing its transmittance dependency with respect to the number of double layers. Secondly, we will briefly study the transmittance and reflectance behavior of the double-membrane array for varying membrane separations and fixed laser wavelength. We will identify configurations that belong to either the standard reflective or the transmissive optomechanics regime which has been extensively studied by Xuereb, Genes, and Dantan [115]. Finally, we investigate the entire optomechanical system in a highly asymmetric membrane-at-the-endmirror (MATE) [27] configuration where we identify optimized DBR-array spacings d_1 for arrays operated both in its reflective and transmissive regime, dependent on the membrane separation d_2.

Generally, most of the optimal layer thicknesses during the simulations correspond to quarter-wave layers, which is e. g. the case for high performance DBRs and bare membranes with maximum achievable reflectivity.

6.2.1 *Distributed Bragg reflector*

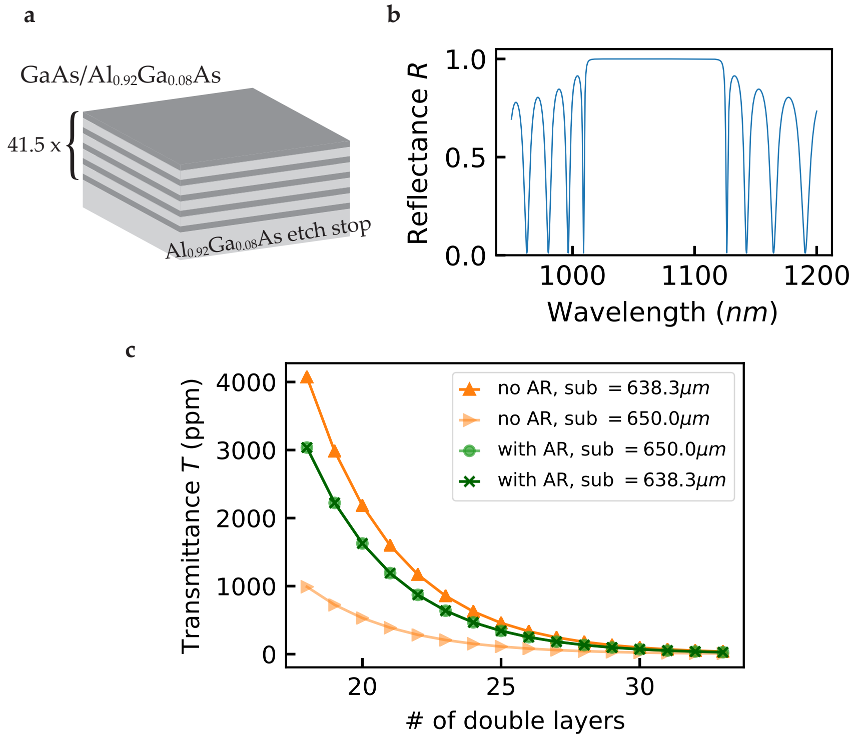

Figure 6.3: Optical transmission properties of the multilayer heterostructure DBR dependent on wavelength and number of mirror pairs. **a** Multilayer heterostructure of the investigated DBR consisting of alternating quarter-wave double-layers of (Al)GaAs with an additional etch stop layer at the bottom. **b** Wavelength-dependent reflectance for the structure depicted in **a** with 41.5 (Al)GaAs double-layers. **c** Dependency of the DBR transmittance with respect to the number of double-layers for DBRs with and without an anti-reflection (AR)-coating.

As already introduced in Section 3.7, DBRs consist of alternating quarter-wave stacks of a GaAs (high index, $n_{\mathrm{GaAs}} = 3.48$ at $\lambda =$

1064 nm) and AlGaAs (low index, $n_{\text{AlGaAs}} = 2.98$ at $\lambda = 1064$ nm) grown on a (100)-oriented GaAs substrate. The base of the DBR stack additionally incorporates an AlGaAs etch stop layer of three quarter-wavelength thickness (cf. Figure 6.3a). This design is based on earlier work by Cole et al. [22] and has proven to achieve mirror coatings of high reflectivity and superior material properties than those typically used in the past[2].

The maximum mirror reflectivity crucially depends on the number of layers and can thus be arbitrarily tuned. When simulating the wavelength dependent transmittance of a DBR consisting of a stack of 41.5 periods of alternating (Al)GaAs optimized for 1064.5 nm, i. e. film thicknesses of quarter-wave optical thickness, we can identify a region of high reflectivity centered around the target wavelength whose bandwidth depends on both the number of layers as well as on the index contrast between both materials (cf. Figure 6.3b).

More realistically, these coatings are grown on a GaAs substrate of in our case approximately 650 µm thickness. When also incorporating the substrate into our simulations, we have noticed deviations of the transmittance with and without the substrate. The reason lies in the fact, that the substrate now adds to the interference pattern and thus leads to a wavelength-dependent transmittance – or equivalently substrate thickness-dependent transmittance for fixed wavelengths.

Therefore, the underlying substrate requires an AR-coating in order to compensate for the uncertainty of substrate thickness, that otherwise leads to large uncertainties for the exact mirror transmission due to interference effects. The effect of an existing AR-coating for substrates of two different thicknesses are shown in Figure 6.3c. Especially for mirrors with higher transmittance, equivalent to less mirror pairs, the discrepancy can become significantly large for varying substrate thicknesses (orange curves). However, incorporating an AR-coating leads to a substrate thickness independent mirror transmittance (overlapping green curves).

Therefore, in the following, we will make use of AR-coated DBRs of ideal refractive index and film thickness [32, 66]. In order to achieve a cavity finesse of around 1000 (for the big macroscopic cavity), these mirrors consist of 18.5 double-layers resulting in a mirror transmittance of approximately 3000 parts per million (ppm).

6.2.2 *Membrane array*

When simply looking at the membrane array consisting of two InGaP membranes of quarter-wave thickness separated by distance d_2, we can identify points of operation where the array is fully transmissive or highly reflective. For a fixed laser wavelength λ, integer multiples of $\lambda/2$ correspond to the transmissive regime, where 100 % of the inci-

---

[2] https://www.crystallinemirrors.com/

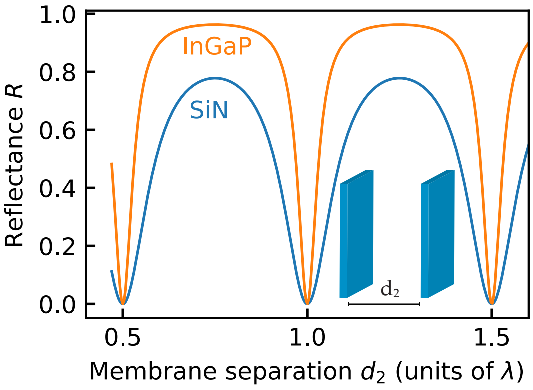

Figure 6.4: Double-membrane arrays in their transmissive and reflective regime dependent on the membrane separation d_2. The transmissive (reflective) regime corresponds to membrane separations where the array exhibits minimum (maximum) reflectance. Illustrated for arrays made of InGaP and SiN. Higher index materials exhibit narrower resonances and simultaneously larger maximum reflectance.

dent light is transmitted when no losses are assumed. For membrane separations shifted by a quarter-wavelength, corresponding to integer multiples of $n\lambda/2 + \lambda/4$, we observe points of lowest transmission and thus high reflectivity. The transmissive regime promises benefits in terms of achieving high coupling enhancements for arrays operated in the middle of an optical cavity [115].

We can readily see that for increasingly large single membrane reflectivities R_m the transmission linewidths become narrower and thus more sensitive for positioning inaccuracies at simultaneously larger couplings. In addition, the peak reflectivity in the reflective regime also increases for increasingly large membrane reflectivities, as is illustrated for arrays made of SiN and InGaP, respectively (cf. Figure 6.4).

6.2.3 *The optomechanical double-membrane-cavity system*

Extensive simulations have been performed for the case of two semiconductor membranes made of InGaP incorporated in a Fabry-Pérot cavity. The stack of these membranes is – contrary to the normal symmetric MIM case – placed right atop of a DBR. In order to maximize the optomechanical coupling of the double-membrane-cavity system, we sweep d_1 and d_2, effectively determining the position of both membranes within the optical cavity. We can distinguish between various membrane configurations, where the array itself as well as its membranes comprising the array is either in the transmissive or reflective optomechanics regime, effectively determined by the choice of d_2. In principle, the choice of d_1 and d_2 can be arbitrary, but we have found two configurations of DBR-array spacing d_1 and inter-membrane sep-

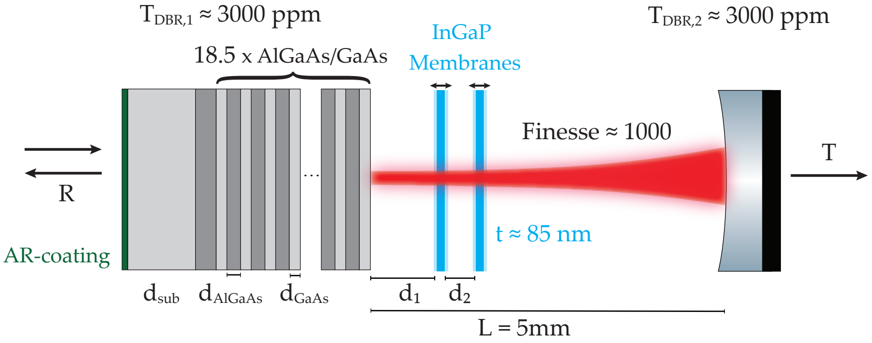

Figure 6.5: Full optomechanical cavity-double-membrane system and its parameters used for the transfer matrix method (TMM) simulations. We obtain intensity reflection R and transmission T when light is incident from the left by exploring various membrane configurations when sweeping d_1 and d_2 collectively.

aration d_2 that result in particularly interesting regimes of enhanced coupling and measurement rates with respect to the standard MIM case.

Configuration 1 with $\{d_1, d_2\} = \{3\lambda, 3.25\lambda\}$ corresponds to the reflective optomechanics case, whereas configuration 2 with $\{d_1, d_2\} = \{3.25\lambda, 3\lambda\}$ to the transmissive case (Additional results for other combinations of d_1 and d_2 can be found in Appendix A.2.2). The other system parameters are fixed with both mirrors exhibiting intensity transmissions of around 3000 ppm, equivalent to an empty cavity finesse $\mathcal{F} \approx 1000$ and a total cavity length of 5 mm. For the DBR, this corresponds to a total of 18.5 quarter-wave double-layers on a 650 µm thick GaAs substrate with an AR-coating of ideal optical thickness [32]. Similarly, in order to achieve the peak reflectivity of a bare InGaP membrane, the slab thickness is also chosen to be a quarter-wave layer resulting in approximately 65 % for 83 nm thick InGaP layers. The full optomechanical double-membrane cavity with the parameters used for the TMM simulations are summarized in Figure 6.5 and Table 6.1 where we also summarize the thicknesses of the various layers given their refractive indices for the material compositions used.

Simulation results

For each initial array configuration $\{d_1, d_2\}$, we plot the cavity resonance ω with respect to the collective array displacement Δx_i from its rest position from which we can derive the coupling strength G by numerically calculating the derivative. More importantly, with the knowledge of how the cavity linewidth (FWHM) changes for changing membrane positions, we can also determine the ratio between G/κ, an important figure of merit (FOM) for reaching the coherent quantum regime, as well as the measurement rate G^2/κ. Additionally, we show the intensity transmission (reflection) of the full optomechanical

PARAMETER, SYMBOL	UNITS	VALUE
Laser wavelength, λ	nm	1064.5
Cavity length, L	mm	5
# of DBR layers	1	18.5
DBR intensity transmission, T_{DBR}	ppm	≈ 3000
Empty cavity finesse, $\mathcal{F}_0$	1	≈ 1000
REFRACTIVE INDICES		
n_{AlGaAs}	1	2.97717
n_{GaAs}	1	3.48041
n_{InGaP}	1	3.21
$n_{\mathrm{AR}} = \sqrt{n_{\mathrm{GaAs}}}$	1	1.87
LAYER THICKNESSES		
$d_{\mathrm{AlGaAs}} = \lambda/4n_{\mathrm{AlGaAs}}$	nm	89.3
$d_{\mathrm{GaAs}} = \lambda/4n_{\mathrm{GaAs}}$	nm	76.7
$d_{\mathrm{InGaP}} = \lambda/4n_{\mathrm{InGaP}}$	nm	82.9
$d_{\mathrm{AR}} = \lambda/4n_{\mathrm{AR}}$	nm	142.6
$d_{\mathrm{substrate}}$	µm	650

Table 6.1: TMM simulation parameters used for double-membrane arrays in a membrane-at-the-endmirror (MATE) configuration.

cavity system when each membrane of the array is simultaneously displaced, according to their individual coupling strengths obtained when individually displaced. This clearly reveals the nature of the configuration under investigation by either showing high transmission (reflection) through the cavity when the array is operated in its transmissive (reflective) regime. Note, that we follow the description of Xuereb, Genes, and Dantan [115] and further discuss the procedure in more detail in Appendix A of how to obtain the total collective coupling strength in a multi-membrane system based on studying the individual displacement of each membrane first.

We plot the simulation results obtained for collectively displacing both membranes of the array in Figure 6.6 (reflective regime) and in Figure 6.7 (transmissive regime) normalized to the maximum values achieved for a single InGaP membrane exactly in the middle of the cavity ($G_{\mathrm{max}} = 0.58\,\mathrm{rad\,GHz/nm}$). Similar plots for the absolute values are given in Appendix A.2.2. We extract the maximum absolute values from these plots for membranes in their rest position $\Delta x = 0$ and summarize them in Table 6.2 for the parameters given in Table 6.1. Interestingly, despite the fact, that the membrane array is now located at the end-mirror thus depicting a highly asymmetric cavity case, we

PARAMETER, SYMBOL	UNITS	VALUE
TRANSMISSIVE OPTOMECHANICS		
Membrane configuration, $\{d_1, d_2\}$	nm	$\{3.25\lambda, 3.0\lambda\}$
Individual coupling, G_1	rad GHz/nm	3.24
Individual coupling, G_2	rad GHz/nm	-3.22
Collective mode coupling, G	rad GHz/nm	4.58
Strong coupling parameter, G/κ	nm^{-1}	25.3
Measurement rate, G^2/κ	rad GHz/nm^2	115.8
REFLECTIVE OPTOMECHANICS		
Membrane configuration, $\{d_1, d_2\}$	nm	$\{3.0\lambda, 3.23\lambda\}$
Individual coupling, G_1	rad GHz/nm	-27.86
Individual coupling, G_2	rad GHz/nm	-3.04
Collective coupling, G	rad GHz/nm	28.03
Strong coupling parameter, G/κ	nm^{-1}	6.1
Measurement rate, G^2/κ	rad GHz/nm^2	168

Table 6.2: TMM simulation results for double-membrane InGaP arrays at the endmirror configuration. Values are extracted from the respective plots at $\Delta x = 0$.

achieve the same coupling enhancements as obtained in the symmetric MIM case suggesting that arbitrary array positions within the cavity lead to the same expected enhancements when operated in transmission and optimized mirror-array separation d_1. In comparison to the SM MIM case, enhancements of almost one order of magnitude are achieved, agreeing well with the results obtained by Xuereb, Genes, and Dantan [115] for InGaP membranes with a bare reflectivity of 65 %. Moreover, it is apparent that the transmissive case benefits collective modes that experience a radiation pressure force (proportional to the individual coupling strengths G_i) in opposite direction, thus depicting the case of a collective breathing mode.

For the reflective optomechanics case, both membranes experience a radiation pressure of the same sign and thus depicting the case of a COM type collective supermode with both membranes oscillating in phase. Very interestingly, in this configuration, we find even higher maximum coupling strengths for the inner membrane enclosed by the mirror and second membrane. The additional enhancement by almost one order of magnitude with respect to the transmissive optomechanics case can be explained by effectively forming a very short cavity with total length $L = d_1 + d_2$ determined by the separation of DBR and second membrane. The inner membrane is now located at a position of maximum coupling equivalent to the standard single MIM case. However, this comes at a price of orders of magnitude increased (reduced) optical linewidth (finesse) due to the significantly reduced effective cavity length which ultimately results in lower values of G/κ compared to the transmissive case. Nevertheless, it has to be highlighted that for the investigated set of parameters the measurement rate G^2/κ is still approximately 40 % higher in the reflective regime which we expect to be eventually outscaled when working with PhC membranes of higher reflectivity.

Here, for the sake of a qualitative analysis, we kept the feasibility of achieving the optical cavity parameters high with moderate finesse values of only 1000 and a cavity length of 5 mm. Further coupling enhancements – especially for the transmissive optomechanics case – are predicted when going to longer external cavities and membrane reflectivities approaching unity that are ultimately limited by the ratio of external cavity length L and membrane spacing d, $L/2d$ [60]. This can be intuitively understood by effectively enhancing the interaction g by reducing the optical mode volume of the resonantly enhanced light field within the array. At the same time, the optical dissipation κ is still determined by the external cavities which reduces for increasingly long cavities, thus increasing the strong coupling parameter g/κ.

It has to be mentioned here that for the first final wafer version, membrane-mirror separations corresponding to the reflective optomechanics configuration have been chosen. In future wafer designs, we would recommend exploiting the transmissive optomechanics case with the predicted beneficial enhancement scaling, especially when PhC membranes of high reflectivity are incorporated. However, choosing one over the other configuration ultimately depends on the conditions and requirements for the experiments under consideration where e. g. higher measurement rates are desired without minding for significantly increased cavity linewidths κ.

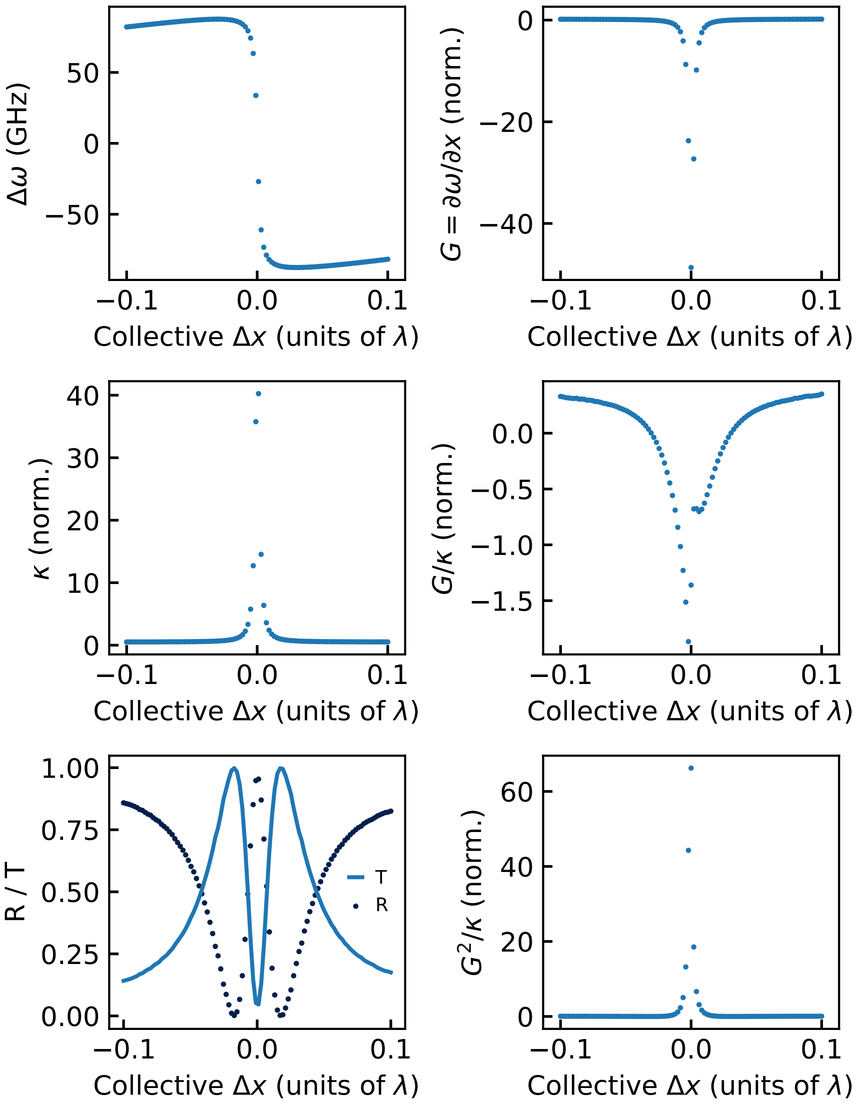

Figure 6.6: Double-membrane arrays made of InGaP in the reflective optomechanics regime. Plotted are changes in cavity resonance frequency $\Delta\omega$ for the collective movement of both membranes, thereof derived frequency pull parameter G, cavity linewidth κ normalized to the empty cavity linewidth, and intensity reflection R and transmission T through the full optomechanical cavity, as well as strong coupling parameter G/κ and measurement rate G^2/κ. All plots in the right column are normalized to the maximum values for the case of a single InGaP membrane exactly in the middle of the cavity. All system parameters are plotted with respect to the membrane positions around their rest position $d_1 = 3\lambda$ and $d_1 = 3.23\lambda$. Displacements are given in units of laser wavelength $\lambda = 1064.5\,\text{nm}$, where negative array displacements are equivalent to membranes being displaced toward the DBR normalized with their individual coupling strengths (COM-type collective mode).

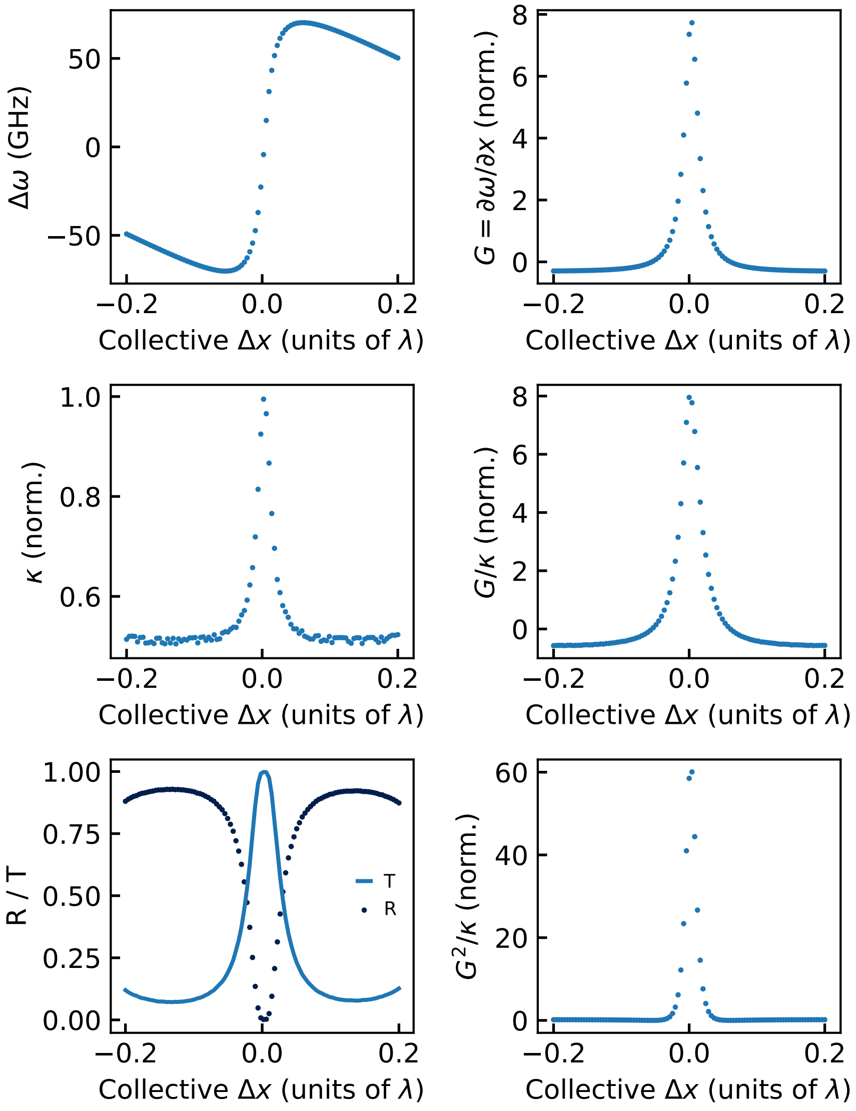

Figure 6.7: Double-membrane arrays made of InGaP in the transmissive optomechanics regime. Plotted are changes in cavity resonance frequency $\Delta\omega$ for the collective movement of both membranes, thereof derived frequency pull parameter G, cavity linewidth κ normalized to the empty cavity linewidth, and intensity reflection R and transmission T through the full optomechanical cavity, as well as strong coupling parameter G/κ and measurement rate G^2/κ. All plots in the right column are normalized to the maximum values for the case of a single InGaP membrane exactly in the middle of the cavity. All system parameters are plotted with respect to the membrane positions around their rest position $d_1 = 3.25\lambda$ and $d_1 = 3\lambda$. Displacements are given in units of laser wavelength $\lambda = 1064.5\,\mathrm{nm}$, where negative array displacements are equivalent to the inner (outer) membrane being displaced toward (away from) the DBR normalized with their individual coupling strengths (breathing-type collective mode).

6.2.4 *Design limitations*

Ultimately, our epitaxial wafers are designed to be operated at cryogenic temperatures with well-defined film thicknesses. In particular, both sacrificial AlGaAs layers (i. e. d_1 and d_2) effectively determine the achievable coupling based on the accuracy of both membrane positioning. This requires careful considerations of film thickness uncertainties originating from temperature-dependent material properties as well as inaccuracies introduced during film growth. In particular for large coupling strengths the optimal membrane position becomes increasingly more susceptible to deviations from its optimal rest position. In the following, we aim to answer the question if it is still feasible to operate the system at points of optimal coupling while sacrificing experimental flexibility and control to move the membranes and/or tune the laser into resonance.

Film thickness uncertainty during film growth

For the success of this monolithic approach, it is indispensable that the nominally defined layer thickness requirements can be accurately met during the epitaxial film growth. Assuming relative growth errors of up to 1 % lead to large absolute thickness deviations dependent on the initial layer thickness[3]. The uncertainty arises from an inaccurate growth rate calibration and thus influences all layers of the same material with the same uncertainty.

Systematic contributions due to material properties

In contrast to the random fluctuations introduced during film growth, contributions from temperature and composition dependent material properties are deterministic and can thus be accounted for. These systematic contributions involve properties that effect the optical thickness of the layers when operated at cryogenic temperatures.

1. Refractive index changes dependent on temperature and material composition
2. Thermal expansion/contraction: Relative layer thickness changes in response to a change of temperature, expressed as $\Delta L/L_0 = \alpha\Delta T$, with α being the linear coefficient of thermal expansion (CTE).

Given the material properties found in literature and summarized in Table 6.3, the main contribution arises from differences in refractive index between room and cryogenic temperatures, whereas the contribution of the CTE are so small as to be negligible on the order of

---

[3] Typical growth errors are at the few tenths of a percent level without active / in-situ film thickness monitoring

MATERIAL	INDEX OF REFRACTION		THERMAL EXPANSION
	(RT)	(LT)	COEFF. ($10^{-6}\,\mathrm{K}^{-1}$)
GaAs	3.4804	3.4173	5.73
$Al_{0.92}Ga_{0.08}As$	2.9772	2.9440	5.24
$In_{0.47}Ga_{0.53}As$	3.2196	3.1134	4.81
$In_{0.41}Ga_{0.59}As$	3.2078	3.1002	4.79

Table 6.3: Material properties of III-V ternary semiconductors for the material compositions used. The refractive indices are specified for a laser wavelength of $\lambda = 1064\,\mathrm{nm}$ and the coefficient of thermal expansion (CTE) values are given at room temperature (RT). Material properties extracted from [1, 48, 59, 86].

0.1 %. Importantly, concerning thermal expansion, these estimations arise from crude calculations where the CTE at room temperature was assumed to be temperature-independent, which is generally not the case. However, especially at low temperatures, the CTE becomes small and we determine an effective temperature change in order to estimate the total length changes on the order of approximately 0.1 %. In comparison to the random fluctuations of up to 1 % introduced by the growth process itself, these values are smaller but deterministic in nature, which can thus be accounted for.

A much bigger influence arises from the refractive index shift between room and cryogenic temperatures. Therefore, for the best estimate of optimal layer thicknesses, we first determine the thicknesses at cryogenic temperatures with their respective refractive indices and then derive the room temperature values considering changes due to thermal contraction. This gives us the layer thicknesses specified for the epitaxial film growth.

However, accounting for these film thickness changes requires accurate knowledge about the material properties and thus remains a source of significant uncertainty. In the following, we will briefly discuss these contributions for the various semiconductors present.

Sacrificial AlGaAs layers

The most crucial parameter is the optimal separation between membranes and DBR, determined by the sacrificial AlGaAs layers. Typically, the optimal membrane positions become more sensitive for increasingly large coupling strengths and thus small deviations from the ideal position due to temperature-dependent material properties have to be taken into account. However, the single biggest contribution of layer thickness uncertainty lies in the accuracy achieved during the growth process. Relative errors of up to 1 % are specified by the manufacturers whereas contributions of thermal contraction are estimated to only account for roughly 0.1 % of the thickness changes. Nevertheless, more reasonably are errors of around 0.5 % which ultimately limit the achievable thickness accuracy of the various layers. In order to keep the absolute thickness errors to a minimum, we therefore decided to aim for thinner sacrificial layers than those simulated of only $\{d_1, d_2\} = \{1\lambda, 0.25\lambda\}$, respectively. For 1 µm thick layers given the crude estimations above, thermal contraction results in absolute thickness changes of up to 1 nm. Keeping in mind that the sacrificial layers are eventually etched away for suspending the mechanical resonators, contributions from refractive index changes of air/vacuum are non-existent.

InGaP membrane

Since the peak reflectivity of the InGaP membrane is fairly insensitive with respect to its optical thickness, low temperature variations in thickness and also refractive index do not play a significant role. Nevertheless, for the final wafer version, we aim for maximizing the reflectivity of a bare InGaP membrane operated at cryogenic temperatures and thus assuming its low temperature index of refraction. This results in membranes approximately 3 nm thicker than their optimal quarter-wave thickness at room temperature.

Calculations of the critical strain for the now 85 nm thick InGaP layer result in a maximum achievable tensile stress of around 700 MPa at 41 % In content. Even though these critical strain estimations are on the edge of what is expected to be safely grown without compromising film quality, the growth manufacturer was confident in successfully growing the designed epitaxial wafer.

Ultimately, we aim for two almost identical wafer versions only differing in the resulting strain of the 85 nm thick InGaP membrane layers determined by its In content. For the highly-strained membranes, we expect a resulting tensile stress of 700 MPa at 41 % In content, whereas the only slightly strained version of same membrane thickness results in an expected tensile stress of 150 MPa at 47 % In content.

DBR

The quarter-wave stacks of the DBR are calculated using the respective refractive indices of (Al)GaAs at cryogenic temperatures. Similar as for the sacrificial AlGaAs layer discussion above, estimated contributions due to thermal expansion amount to only 1 Å for 100 nm thick layers – negligible with respect to the deviations caused from refractive index changes.

Using the obtained optimized parameters for LT operation, we can compare the performance of the DBR by calculating its intensity transmission at both RT and LT. Interestingly, despite deviations from the optimal quarter-wave thicknesses at RT operation, we see slightly, however insignificantly lower mirror transmissions at RT. The reason lies in the index contrast, which is lower at LT compared to the case at RT, thus resulting in larger transmissions despite mirrors with non-optimal quarter-wave-stacks. Most importantly, taking both index changes as well as growth errors of up to 1 % into account, the transmittance of a 41.5 double-layer DBR stays basically unaffected.

We can also see, that by simply adding mirror pairs, the transmission of the DBR becomes smaller. Assuming scatter and absorption losses fall in the range of 4 ppm to 10 ppm, the maximum number of mirror pairs is determined by reaching intensity transmissions anywhere between those values.

Initially, we aimed for single-sided operation in our cavity where the cavity-interacted light is detected in reflection. Contrary to the simulated mirrors with 18.5 double-layers, we therefore designed a DBR with 41.5 layer pairs and expected transmittance of only 4 ppm on the order of scattering and absorption.

Final first wafer design

Ultimately, our epitaxial wafers are designed to be operated at cryogenic temperatures with InGaP membranes differing in their residual film stress (see final wafer design in Appendix D). Taking into consideration the qualitative and quantitative discussion above with systematic errors due to the temperature-dependent material properties as well as random fluctuations during the growth process, we can confidently say that this monolithic approach meets the requirements for successfully operating such a system in interesting regimes while simultaneously sacrificing experimental flexibility and control. The success is crucially dependent on the achieved film thickness accuracy for both sacrificial AlGaAs layers that ultimately determine the optimal membrane positioning and thus points of coupling. We can account – to a certain degree – for systematic thickness changes related to temperature-dependent material properties. However, growth uncertainties pose a major challenge and contribute significantly for increasingly thick layers and coupling strengths. Additional effort during growth might help in keeping these thickness fluctuations to a minimum. Considering that higher coupling enhancements exhibit even narrower resonances ultimately requires even better position accuracy. This will eventually limit the feasibility of the monolithic approach while still being able to ensure operation at points of highest coupling in the transmissive regime.

We can fit the obtained resonances in Figure 6.7 with a Lorentzian and determine its half-width at half-maximum (HWHM). In the transmissive case, these resonances exhibit linewidths of 10 nm comparable to the expected thickness uncertainties in the worst case scenario where a growth error of 1 % amounts to roughly 10 nm for 1 µm thick sacrificial layers. With a reduction of 50 % in this case, significant enhancements for coupling G and measurement rate G^2/κ are still to be expected, proving the monolithic approach feasible. However, in the reflective regime, we find even more stringent position requirements for the more strongly coupled 'inner' membrane incorporated in the sub-cavity of DBR and second membrane. Here, the spread of the resonance is determined to be only 1.6 nm at HWHM, posing a major challenge towards proper alignment without additional positioning control.

6.3 FABRICATION

III-V semiconductors have been established as an alternative material platform for the fabrication of optomechanical devices with unique properties when compared to the standard Si/SiN platform. Especially multilayers based on GaAs and $\mathrm{Al_xGa_{1-x}As}$ are well-established due to their matching lattice constants for basically arbitrary x which allows for the growth of unstressed stacked layers without compromising film quality. In contrary, using $\mathrm{In_yGa_{1-y}P}$ as device layer and controlling its compound composition results in tensile-strained films for In-contents below 49 %. In terms of fabrication feasibility, this system provides highly selective wet etching in HF for $\mathrm{Al_xGa_{1-x}As}$ layers with increasingly large Al-content, whereas at the same time InGaP and GaAs stay unaffected.

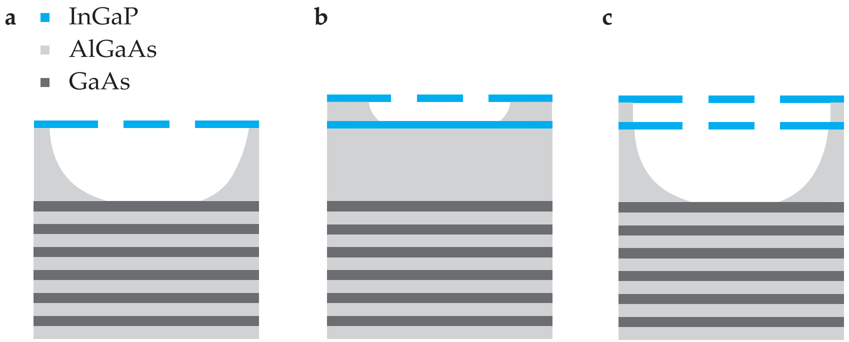

Figure 6.8: Overview of possible device designs for the fabrication based on the epitaxial wafer. Illustrated are **a,b** single and **c** double-membrane devices suspended on top of the DBR (illustrated are only the upper mirror pairs). Single membranes can be either fabricated from the **a** lower or **b** upper InGaP device layer, respectively.

The material stack is grown by molecular beam epitaxy (MBE)[4] on a 650 µm thick GaAs substrate, consisting of a 41.5 double-layer (Al)GaAs DBR and alternating layers of sacrificial $\mathrm{Al_xGa_{1-x}As}$ ($x = 0.92$) and InGaP, as illustrated in Figure 6.9a. Both InGaP device layers are 85 nm in thickness, the bottom and upper AlGaAs sacrificial layers are roughly 1065 nm and 265 nm, respectively. For reasons of growth quality the InGaP device films are capped by 1 nm thick GaAs layers[5] (not depicted in the schematics).

---

[4] `https://www.iqep.com/`

With the designed multilayer structure, we can now start the fabrication process for various device designs, enabling the realization of single and double membrane devices (cf. Figure 6.8). In terms of single membranes we can exploit either one of the two InGaP layers only differing in their sacrificial AlGaAs layer thickness of either λ or $\lambda/4$. Eventually, the goal is to exploit both layers for the fabrication of a double-membrane array on top of the DBR. As in Chapter 5 with the double-membrane devices made of SiN, tethered membranes constitute ideal candidates for the fabrication procedure, where a front-side etch is required and will thus be used as the resonator design of choice. In contrast to the square window for the membranes fabricated on SiN due to its crystal-orientation dependent Si etching, here a circular window of approximately 500 µm is applied due to the isotropic wet release. We aim for tethered membranes with central pads of 100 µm side length, the tether length and width are 200 µm and 10 µm, respectively. Optionally, the central pads are patterned as PhCs for increased membrane reflectivity.

Here, we focus on the fabrication of single membranes. The process flow differs only slightly depending on whether we use the top or bottom InGaP device layer. However, since a thicker sacrificial AlGaAs layer turned out to be beneficial, we made a compromise of fabricating single membranes mainly from the bottom InGaP layer despite the need for additional process steps (cf. Figure 6.8a). Furthermore, using the membrane right atop the DBR would allow to directly implement the fabricated membrane-DBR device by forming an optomechanical cavity with an additional commercially available mirror.

Stripping of upper layers

We start the fabrication process for single tethered membranes atop of a DBR by stripping the top two layers consisting of InGaP and AlGaAs (Figure 6.9b). This can be done by either pure selective wet etching of the respective layers or a combination of both dry and wet etching, where we opted for the latter. A chlorine-based dry etch at elevated temperatures of 190 °C etches into the sacrificial AlGaAs layer before reaching the bottom InGaP device layer. This is ensured by making use of laser monitoring. The remaining AlGaAs is completely removed by a selective wet etch in (dilute) HF, followed by cleaning off accompanying solid, insoluble byproducts by subsequent rinses in heated deionized (DI) water at 80 °C, 30 % KOH, and again in heated DI water at 80 °C.

---

[5] Recommended by the growth manufacturer

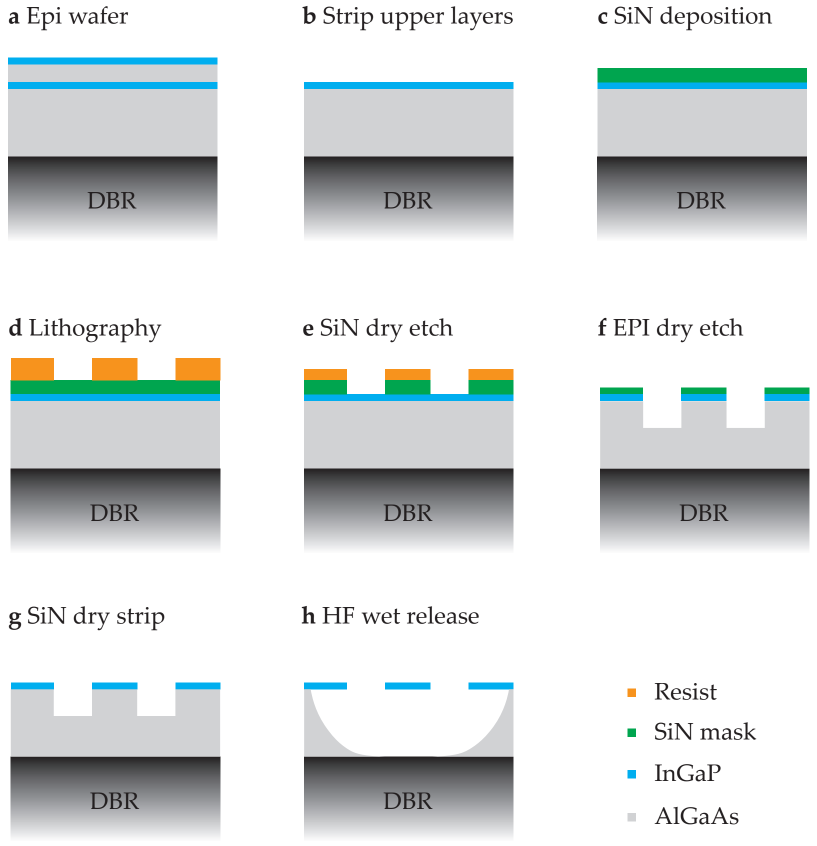
a Epi wafer
b Strip upper layers
c SiN deposition
d Lithography
e SiN dry etch
f EPI dry etch
g SiN dry strip
h HF wet release
DBR
DBR
DBR
DBR
DBR
DBR
DBR
DBR
Resist
SiN mask
InGaP
AlGaAs

Figure 6.9: Fabrication flow of single InGaP membranes atop of a DBR. **a** We start with the grown epitaxial heterostructure and strip the upper two layers, leaving behind a single InGaP device and sacrificial AlGaAs layer. We then deposit the SiN hard mask, followed by e-beam lithography (**c-d**). The patterned resist layer is then subsequently transferred into the hard mask and semiconductors (**e-f**). The hard mask is then stripped right before the sacrificial wet release in HF, and then finished by CPD.

Deposition, lithography and dry etching

After successfully stripping the first two top layers and leaving a clean surface behind, we continue the fabrication process by depositing a plasma-enhanced chemical-vapor deposition (PECVD) SiN hard mask of 210 nm in thickness, immediately followed by electron-beam lithography (EBL) (Figure 6.9c and d). The positive electron-beam resist AR-P 6200.13[6] is spun onto the sample at 3000 rpm and baked at 150 °C for 3 min resulting in sufficiently thick layers for the subsequent pattern transfer into the SiN hard mask. After e-beam exposure resist development is carried out in subsequent rinses of pentyl-acetate, MIBK/IPA (1:1) and IPA, each for 1 min.

The pattern is then transferred into the SiN hard mask by using a CHF_3 etch chemistry commonly used for SiN etching (Figure 6.9e).

---

[6] `https://www.allresist.de/ar-p-6200-csar-62/`

The remaining resist is stripped in an oxygen plasma in the same etch chamber right after the mask opening. In addition, for thorough cleaning of all organic residues the samples are immersed in dimethylformamide (DMF) at elevated temperatures of 80 °C.

After having thoroughly cleaned the chip surface from any organics, we continue transferring the pattern deeper into the second sacrificial layer by exploiting the same chlorine-based dry etch as for stripping the upper layers before (Figure 6.9f). Using the reflectance signal from laser monitoring, we can ensure stopping the dry etch process before damaging the top DBR GaAs layer. Crucially after dry etching of semiconductors with high Al-content, the freshly etched chips require immediate rinsing in DI water in order to slow down the rapid oxidation of the exposed AlGaAs.

Typically, the SiN hard mask is stripped in a selective CHF_3-based etch chemistry right before the sacrificial wet release (Figure 6.9g). However, we will later adapt the fabrication flow by stripping the hard mask after the wet etch in order to make the membranes more resilient to device failure (breaking and collapsing) during the wet release.

Sacrificial wet release

Special care is taken throughout the entire wet etching process in order to avoid surface tension related breaking and collapsing of the released membranes. Therefore, we treat the chip in a gentle ozone/oxygen plasma right before the wet etch in order to prepare a hydrophilic surface. During the wet release in dilute HF we use a surface tension reducing soap, a so-called surfactant, as well a special custom-made chip holder that protects the fragile membranes from turbulences especially during wet transfers from one liquid into another [74]. The released structures are finally rinsed in subsequent rinses of DI water and IPA, before dried by critical point drying (CPD). Note that for most of our fabricated samples we restricted ourselves from thoroughly cleaning the chips from etch residues originating from both dry and wet etching. The reason lies in the fact that we intended to keep the amount of liquid transfers to a minimum in order to increase the fabrication yield. Eventually, upon necessity, thorough cleaning of AlGaAs wet etch residues in (dilute) HF can be applied right after the wet release in before the final CPD step.

6.4 RESULTS AND DISCUSSION

This section summarizes the progress made in fabricating single InGaP membranes according to the process flow introduced above. If not stated otherwise, the fabrication is executed on the low-stress wafers with $In_{0.47}Ga_{0.53}P$ films nominally exhibiting a residual tensile stress of around 150 MPa determined by its In content of 47 %.

We first dive into the individual processing steps, consisting of dry etching, sacrificial wet release and necessary cleaning procedures. We discuss in detail the obtained results and emerging challenges during the fabrication of single membranes made from InGaP, and exploit several adaptations to the standard fabrication flow in order to investigate accompanied issues in material and design.

6.4.1 *Dry etching*

Choice of masking material

In RIE processes, the choice of masking material is crucial in order to guarantee etched features of high structural quality. This becomes especially important for ultimately transferring PhC membrane pattern into both device layers of large separation. As we have seen in Chapter 5, PhC resonances are very sensitive to changes in hole diameter and thus require deep vertical dry etching with sufficient etch control for matching PhC resonances of both membranes.

For the fabrication of single membranes, pattern transfer of even small features such as PhC holes can in principle be realized by simply using a sufficiently thick resist layer in order to etch through the only 85 nm thick InGaP membrane [65]. However, In-containing composite materials such as InGaP benefit from a dry etch process at elevated temperatures above 160 °C in order to achieve smooth sidewalls, and reasonably high etch rates and thus selectivity due to the low volatility of indium chloride based etch products [57]. The use of resist masks in hot plasmas, even at non-elevated substrate temperatures, can lead to resist damage and the formation of carbon-rich compounds which require additional cleaning steps.

Moreover, keeping in mind, that the ultimate goal is etching through the entire membrane array of several µm, we decided to exploit the possibility of using a hard mask. Further, a hard mask provides a greater selectivity of the process, i. e. the ratio between etch rates of masking material and semiconductors, equally crucial for deep pattern transfers through various membranes with large sacrificial layers, in particular for small features.

Standard hard mask materials are plasma-enhanced chemical-vapor deposition (PECVD) grown SiN and SiO_x, both of which have been tested. SiN hard masks are etched more slowly in HF compared to SiO_x, with etch rates depending on the HF concentration. Dependent on the etch duration and the exact etch rate of SiN, this might demand an additional hard mask strip by using a selective dry/wet etching step before/after the wet release. In contrast, SiO_x etch rates are significantly higher, which offers the advantage of simultaneously removing the SiO_x hard mask during the sacrificial AlGaAs undercut, making it a convenient alternative where less processing steps are required.

Even though SiO_x allows for an easy and convenient way of mask removal during the sacrificial wet release, we opted for SiN hard masks of 210 nm thickness with sufficient etch selectivity with respect to the semiconductors and required etch depths. We restrict ourselves here from an in-depth discussion of SiN mask etching (see Figure 6.10) and refer to Chapters 3 to 5 where SiN processing was discussed in more detail. It shall be noted here, that the knowledge of patterning the entire central pad with PhC holes for increased device yield (cf. Chapter 5) was not known at the time and was thus not exploited.

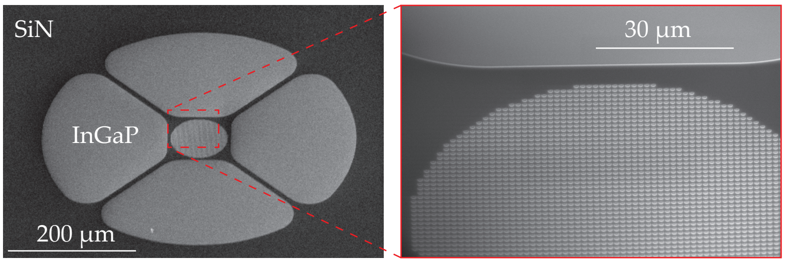

Figure 6.10: SiN hard mask etching of tethered PhC membranes made of InGaP. In contrary to the square window opening suitable for the crystal-orientation dependent KOH etching of Si, here a circular shape for the isotropic HF etching of AlGaAs is recommended. The inset on the right shows a zoom-in of the central pad that is patterned with PhC holes. Dark layers correspond to the SiN hard mask whereas bright layers correspond to the top surface of the InGaP where the SiN has been etched away (Figure 6.9e after resist strip).

Dry etching of III-V semiconductors

Dry etching of III-V seminconductors is achieved with chlorine-based etch chemistries with a variety of different additive gases for both passivation and dilution [56, 57, 65, 77, 100]. The reactive ion etching (RIE) system is equipped with an inductively coupled plasma (ICP) and allows monitoring of the etch progress in real-time using laser inteferometry. This enables the possibility to control and stop the etching process when a desired etch depth and material layer is reached. In our case, we aim for stopping well within the sacrificial AlGaAs layers without damaging the top GaAs layer of the DBR. The etch chamber is connected with a variety of different gases that allows to explore various etch chemistries.

In order to transfer patterns vertically through the epitaxial heterostructure, the gas ratio between both passivation and etching agents needs to be well balanced, among other possibilities to effectively tune the side wall profile and quality. Here, we explore two different etch chemistries differing in the choice of passivation gas, namely boron trichloride (BCl_3) and nitrogen (N_2), whereas chlorine (Cl_2) acts as main etching agent with argon (Ar) as diluting gas.

The task is finding an optimized balance among the etch gases and other system parameters in order to provide smooth and vertical etch profiles. The main difficulty here lies in optimizing the sidewall profile for etching through the various semiconductors present such that defined features are optimally transferred into all the various layers underneath. This is in particularly important for eventually transferring PhC holes into both InGaP layers with ideally identical features for matching PhC resonances.

The main knob to tune the profile is by adjusting the ratio of etch and passivation gases while keeping the total gas flow constant. Low chamber pressures are usually advantageous for achieving straight side wall profiles since larger pressures lead to increased lateral etching. All etches are carried out at elevated temperatures of 190 °C in order for the In-containing by-products to be volatile.

To avoid excessive heating and further guarantee reproducible results, a good thermal contact between the sample and electrode is established. This requires the usage of helium backside cooling between electrode and carrier wafer, as well as a thermal heat conducting oil that not only guarantees good thermal contact between them but also fixates the sample on the Si carrier wafer.

We investigate the quality of the dry etching processes by writing test lines of varying width into the epitaxial heterostructure. The etched samples are then cleaved for a cross-sectional investigation in a SEM (see Figure 6.11). The trenches of approximately 800 nm in width are inspected under a slight angle with etch depths reaching into the inner sacrificial layer, stopping well before penetrating the top GaAs layer of the DBR.

We have noticed that after dry etching, the trenches are filled up with an additional material and – upon deeper investigation – turned out to arise from the etch boundaries of the AlGaAs (color-coded in olive green). This could be later identified as an oxidation process happening instantly after the dry etching upon exposure to atmospheric conditions which leads to a significant swelling of the AlGaAs at its etch boundaries even after only minutes in ambient air [24].

Residual chlorine molecules at the etched surfaces seem to significantly accelerate the oxidation process by attracting water out of ambient air which results in rapid oxidation of the exposed AlGaAs. This oxidation process is usually not observed for AlGaAs layers of lower Al-concentration or at least significantly slowed down and thus attributed to oxidation of aluminum-bearing layers. Nevertheless, for our AlGaAs layers, we have found that this process can be stopped or at least slowed down by immediate rinsing the freshly etched samples in DI water right after the chlorine etch (cf. Figure 6.11c and d).

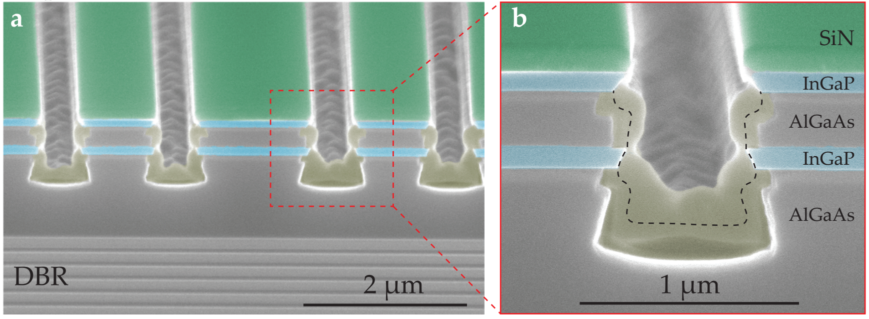

I) BCl_3 / Cl_2 / Ar = 3 / 4 / 25 sccm
p = 1.7 mTorr, P_{ICP} = 800 W, P_{RF} = 100 W

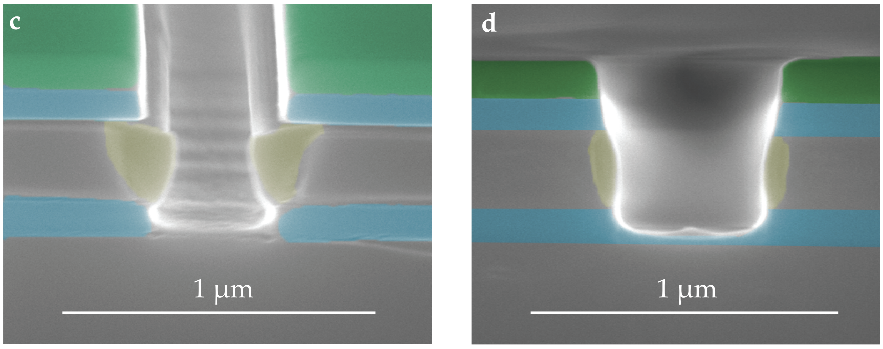

II) Cl_2 / N_2 / Ar = 5 / 5 / 21 sccm
p = 1.8 mTorr, P_{ICP} = 800 W, P_{RF} = 100 W

Figure 6.11: Chlorine based dry etching of the epitaxial layer structure. Shown are the results for two different etch chemistries only differing in the choice of passivation gas, where the first etch chemistry uses BCl_3 (**I**, images **a** and **b**) and the second one N_2 (**II**, images **c** and **d**). The etches are carried out at elevated temperatures of 190 °C and a constant total gas flow resulting in a chamber pressure of approximately 1.8 mTorr. RF and ICP power are fixed to 100 W and 800 W, respectively. The quality of the etch is evaluated by inspection in a SEM under cross-section. The first etch chemistry in the upper row shows the top layers of the epitaxial heterostructure including the first few double-layers of the DBR. The etch trenches are inspected and evaluated by means of vertical and smooth side walls. Zooming in to one of the etched trenches reveals a common issue of high Al-content AlGaAs (**b**). Even after minutes in ambient air a swelling starting from the AlGaAs etch boundary can be observed, eventually closing the entire etch trench. In etch chemistry II the same behavior can be observed (**c** and **d**). Both images originate from the same etch and chip, whereas image **d** has been rinsed in DI water right after the dry etch which prevents or at least slows down the AlGaAs oxidation process. In contrast, image **c** has been left untreated and shows a significantly stronger oxidation under the same conditions. SiN hard mask (green), InGaP (blue), AlGaAs (dark gray), GaAs (light gray), oxidized AlGaAs (olive green, only front facet is color-coded)

The samples originate from the very same chip and dry etch conditions with the difference that sample in Figure 6.11d was immediately rinsed in DI water after the dry etch, whereas sample in Figure 6.11c was left untreated. The chip was then cleaved and inspected within two hours after retrieving the chip out of the etch chamber. Even after such a short exposure time, clear differences in oxidation can be observed with an already noticeable swelling of the AlGaAs.

In contrary, the DI rinsed sample shows only minor however still noticeable swelling. Alternatively, rapid thermal oxidation (RTO) has proven to stop the AlGaAs oxidation with samples unaffected even after a week of exposure in ambient atmospheric conditions [11]. Nevertheless, for future generations in heterostructure design, this suggests the use of AlGaAs layers of lower Al-content between 70 % to 80 %. This still ensures selective etching over GaAs with reasonable etch rates whilst at the same time avoids the undesired rapid oxidation and thus swelling of the AlGaAs.

In terms of etch quality, i. e. achieving smooth and vertical side wall profiles, both etches meet the requirements with possible improvements upon further optimization. For both etch chemistries with only differing passivation agent (N_2 versus BCl_3) operating at low chamber pressures after an initial ignition step resulted in best side wall profiles. For most of our etches, we kept the electrode RF and ICP power constant, using 100 W and 800 W, respectively. We tune the profile by adjusting the gas ratios between etch and passivation gas, while keeping the total gas flow constant at a chamber pressure of around 1.8 mTorr. All etches are carried out at elevated temperatures of 190 °C in order for the In-containing by-products to be volatile.

Starting from the gas ratios found in literature, we have found decent side wall profiles when the $BCl_3/Cl_2/Ar$ flow ratio is set to 3/4/25 sccm, respectively (see Figure 6.11I, images **a** and **b**). The main difficulty here lies in optimizing the profile for both InGaP and AlGaAs while ensuring straight side walls such that the patterned features are similar in both InGaP device layers. This is ultimately required for a successful implementation of PhC patterned membranes where the reflectivity of each membrane mirror is desired to be (perfectly) matched when approaching unity reflectivity. Here, for the chosen gas flows, the transferred features in both InGaP layers are similar in size with however skewed side walls and somewhat funky etch boundaries (as indicated by the black dashed line in Figure 6.11b.

In contrast, using N_2 as passivation gas, we have found reasonably good etching profiles when the $Cl_2/N_2/Ar$ flow ratio is set to 5/5/21 sccm, respectively. The etch profile obtained here is still slightly non-vertical with however now straight etch boundaries throughout all the layers. By increasing the ratio between etch and passivation gas, we expect to further improve the etch profiles eventually resulting in smooth vertical side walls and well-controlled pattern transfer through both device layers.

Both etch chemistries serve as a good starting point for further optimization when smooth and vertical side walls for the fabrication of PhC patterned membranes are desired. Since we aim for the fabrication of single membranes first, we opted to pause the dry etch optimization with an outlook for getting back to it in the future.

With the etch recipes at hand, we can now measure the etch depths and thus determine the selectivity between semiconductors and SiN hard mask. In order to gain additional information over the individual etch rates for the various layers, we performed a deep etch through the entire epitaxial heterostructure. The detected reflectance signal from laser monitoring is compared to the expected theoretical signal obtained by simple TMM calculations[7] and shows good agreement (cf. Figure 6.12). In the data, we can clearly identify the various layers, where the first two peaks correspond to InGaP and the oscillating behavior of the lower signals between and after correspond to the sacrificial layers (marked as gray and blue shaded areas for both AlGaAs and InGaP, respectively). We will later make use of laser monitoring in order to etch into the sacrificial AlGaAs layer without harming the DBR surface underneath.

MATERIAL	ETCH RATE (nm/min)	SELECTIVITY
GaAs	750	17
AlGaAs	910	20
InGaP	510	11
SiN	45	–

Table 6.4: Etch rates and selectivity of semiconductors during chlorine-based dry etching. The etch rates and selectivity with respect to the SiN hardmask are determined by laser interferometry and depict an upper limit due to large area etching when compared to small features such as PhC holes.

In addition, by knowing the layer thicknesses, we can determine the etch rates from the reflectometry measurements. Evaluation of the data results in etch rates of approximately 910 nm/min for AlGaAs and 410 nm/min for InGaP, respectively. In order to determine the etch selectivity between masking material and semiconductors, we extracted the etch rate for the hard mask in a similar fashion for the same etch recipe. Table 6.4 summarizes the results for etch chemistry I with BCl_3 as passivation gas (and at 180 °C), where an higher etch temperatures have shown to increase both etch rates and selectivity significantly.

---

[7] We used an open source software called *Vertical*, developed by Dr. Frank Peters (`http://research.ucc.ie/profiles/D006/fpeters`)

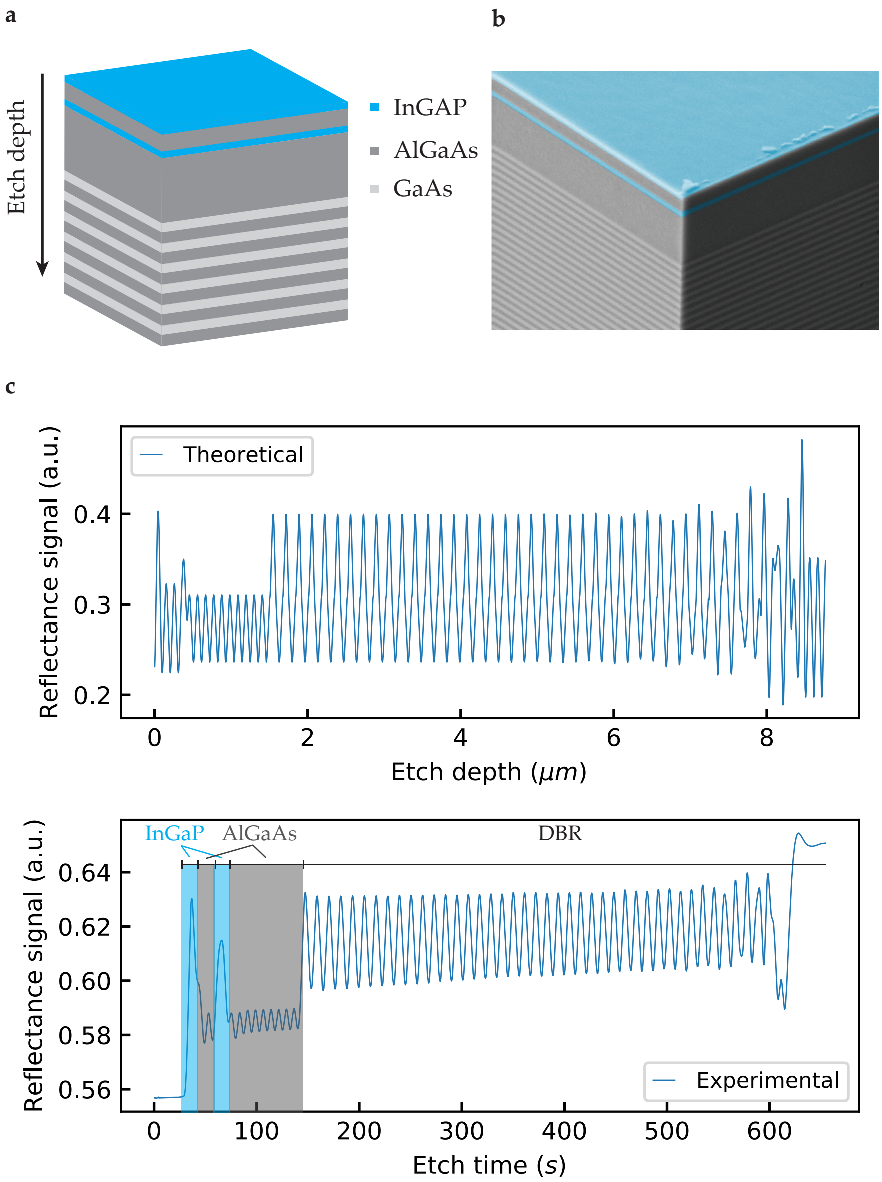

Figure 6.12: Laser reflectometry of epitaxial heterostructure. **a** schematic of the designed wafer showing the first few µm of the epitaxial heterostructure, consisting of the device and sacrificial layers and the first couple of double-layers of the DBR. **b** SEM of the wafer as depicted in **a** with clear distinction between the various layers (SEM image taken by Valentin C. Hauber, group of Eva M. Weig, University of Konstanz). **c** Expected laser reflectance signal and obtained reflectance signal during the chlorine-based through-wafer etching. The features corresponding to the various layers can be clearly identified following the simulated predictions with good agreement.

6.4.2 *Sacrificial wet release*

In order to suspend the InGaP membranes, we need to (ideally) selectively etch the sacrificial AlGaAs layer without harming neither GaAs nor InGaP. Hydrofluoric acid (HF) is known to achieve very selective wet etching of AlGaAs with increasingly high etch rates the higher the Al-content becomes [65]. For our sacrificial layers with an Al-content of 92 % this results in etch rates of 1.4 µm/min when diluted solutions of 1 % HF are used. Therefore, for successfully releasing tethered membranes with central pad sizes 100 µm in side length, a total etch duration of 35 min is required. For comparison, 4 % HF already results in etch rates of around 10 µm/min.

Alternatively, HCl has been suggested as an advantageous etch solution for etching sacrificial AlAs layers resulting in smoother surfaces due to a higher solubility of the etch byproducts [18] with the disadvantage that it also attacks InGaP with high etch rates [56]. However, for reasons of etch selectivity, HCl is not exploited for the sacrificial wet release.

In comparison to SiN, the fabrication of tensile-strained InGaP membranes is significantly more challenging which requires careful handling and treatment during wet processing. In particular, thin membranes of large lateral dimensions and low mechanical stiffness, and at the same time thin sacrificial layers are very susceptible to capillary forces and can thus suffer from device collapse onto the substrate [65].

In order to increase device yield, special attention is paid throughout the entire wet release process. We therefore use a custom-made sample holder in order to avoid device damage due to strong liquid movements that at the same time keeps the chip entirely covered in liquid at all times, especially during the wet transfers from one liquid to another [74]. Additionally, in order to further reduce surface tension related stiction, we prepare the chip surface hydrophilic by applying a gentle oxygen/ozone plasma right before as well as using surface tension reducing soaps, so-called surfactants, during the wet release. As a final measure, the released devices are carefully dried by using critical point drying (CPD).

Types of etch residues

Cleaning of samples from impurities such as organic and inorganic compounds is most crucial for every clean room fabrication. In our case, we mainly deal with two types of compounds that need to be thoroughly cleaned off the surface: organic residues from lithography steps and by-products from wet and dry etching processes. As an example, chlorine based dry etching of indium containing materials requires substrate temperatures above approximately 160 °C due to the relatively low volatility of indium chlorides ($InCl_x$) and thus guaranteeing acceptable smooth surfaces with reasonably high etch rates. On the other hand, HF wet etching of AlGaAs with high aluminum content benefit the formation of solid and hardly soluble compounds (cf. Figure 6.13), crystalline aluminum hydroxide fluoride salts of the form $AlF_y(OH)_{3-y} \cdot H_2O$ $(0 < y < 3)$ which require special treatment [111, 122].

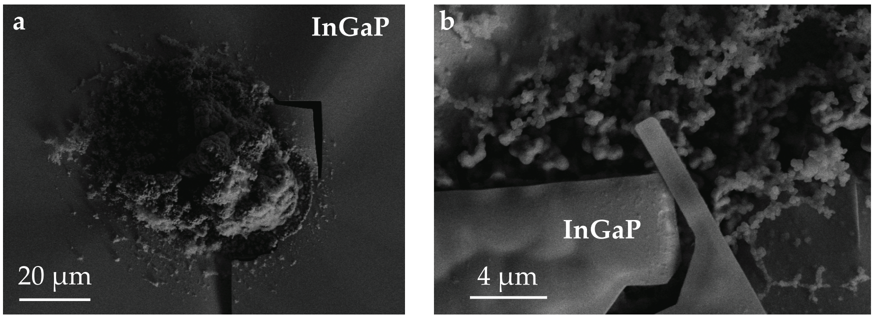

Figure 6.13: Aluminum hydroxide fluoride byproducts from AlGaAs etching in HF. Solid compounds of alumina salts after wet HF etching of the sacrificial layer, trapped in the proximity of etch release holes **a** and etch boundaries in general **b** between the (fractured) InGaP device and bottom layer.

On one hand AlF_3, even though not very soluble, can be easily dissolved in heated DI water for 10 min. On the other hand, aluminum hydroxide is amphoteric in nature i.e., it can either be dissolved in solutions of high or low pH values.

Digital cleaning

In general, etch solutions with hydrogen peroxide (H_2O_2) as oxidizing agent etch most semiconductors in combination with the appropriate acid/base. However, in order to avoid the continuous oxidation and subsequent de-oxidation, i. e. removal of oxide layer in the acid/base, both oxidizing agent and etchant have to be kept separate. Since H_2O_2 oxidize the (GaAs) surface in a controlled manner resulting in well-defined oxide layers of around 15 Å, the process exploiting alternating steps of oxidation and etching happens in discrete steps and is thus called *digital etching* [26, 40].

Digital etching in our case can be used to remove the 1 nm thick GaAs cap layer in a controlled way and in order to clean the chip surface off of organic residues by forming volatile etch products of carbon rich materials when immersed in H_2O_2. Following the elucidations by Midolo et al. [65] a KOH-based etchant is chosen as remover which handily also simultaneously removes the insoluble aluminum hydroxide salts obtained by the AlGaAs wet etching in dilute HF.

Optimal cleaning procedure

Best results in terms of surface cleanliness have been achieved by the following cleaning process flow: The AlGaAs sacrificial layer is removed in dilute HF and thoroughly rinsed in heated DI water at 80 °C. Often, this wet etching would be accompanied by the precipitation of a white powder that can be easily wiped off with a cotton swap. The samples are however cleaned by immersion in 400K developer[8], or alternatively 30 % KOH, for 60 s. Afterwards, the samples are again rinsed in heated DI water at 80 °C. If excessive amounts of organic carbon-rich residues due to e. g. earlier lithography steps are present, an additional oxidizing step – as usually the case for digital etching – can be introduced. However, for only cleaning off by-products from the HF AlGaAs etch this additional oxidation step has not been found urgent in our case. This is true under the assumption that all organic resist residues from any lithography step have been thoroughly cleaned off the chip beforehand.

These cleaning steps are recommended after each AlGaAs etch in HF which happens twice in our described process flow. Firstly, we make use of the procedure after stripping the upper two layers in order to ensure a clean surface for further processing, and secondly after the sacrificial wet release. However, especially after the release, we avoid the additional required wet transfers as to increase the device yield for the already suspended and fragile membranes.

Single tethered membranes

We follow the general description given in the fabrication flow and suspend the patterned InGaP layer by etching the sacrificial AlGaAs underneath. Most membranes regularly break, collapse, show material fracturing or are completely ripped off their anchor points with only few devices fully surviving the wet release (see Figure 6.14). Even our best devices show obvious material deformations that result in collapsing membranes that are in contact with the top surface of the DBR. Typical for all membranes, the central pad shows both buckling and bending, whereas the long tethers sag down completely (Figure 6.14c and d).

Initially, this raised the question whether the grown InGaP film undesirably exhibits a compressive stress. This has however been ruled out by measurements of the stress-dependent resonance frequencies of doubly-clamped beams of varying length and more detailed x-ray diffraction (XRD) analyses [11]. Both methods independently confirmed the grown InGaP layers to exhibit a maximum tensile stress for both low and high stress wafers of 150 MPa and 650 MPa, respectively. In addition, it has been shown, that the tensile strain is dependent on the crystal orientation with deviations of almost 50 % from its maximum values. The observed angular stress dependency is explained by a combination of an anisotropic Young's modulus and a change of elastic properties likely caused by defects within the thin film [11]. The XRD measurements further revealed a variation in In-content within the grown layer which results in a stress gradient and thus possibly leads to some intra-layer strains [81, 101]. Additionally, we often noticed crystal growth defects in the device layer which is the origin for undesired undercuts elsewhere on the chip surface (cf. Figure 6.14a). Another significant contribution to the device fracturing might originate from the rapid oxidation and consequently swelling of the exposed AlGaAs layer, as shown in Figure 6.11. Especially at the etch boundary, we have noticed buckling and fracturing, which we assume is caused from the expanding AlGaAs oxide.

---

[8] `https://www.microchemicals.com/micro/info_az_400k_421k_Developer.pdf`

In comparison to SiN, the fabrication of tensile-strained InGaP membranes is significantly more challenging. It remains an open question whether the observed challenges in fabrication originate from material specific reason, inappropriate handling during processing and/or are related to imperfections in design of both grown heterostructure and resonator itself. In particular, thin membranes of large lateral dimensions and low mechanical stiffness, and at the same time thin sacrificial layers are very susceptible to capillary forces and can thus suffer from device collapse onto the substrate. It has also been shown that simpler resonator designs such as doubly-clamped beams can be successfully suspended of only up to 53 µm in length, which is certainly far from the parameter regime required for the more complex tethered membranes exploited here.

The challenge here was to undercut large membranes in contrast to narrow beams. Therefore, it would be beneficial to minimize undercut distances by patterning the central pad with PhC holes. This not only reduces the big overhang but also promises to simplify the release process.

Nevertheless, even for these simpler structures the oxidation and consequently expansion of the AlGaAs has proven to pose a major obstacle. To summarize, the following points might contribute to the issues experienced in fabrication, some of which we will investigate by modifying the current process flow.

1. Inappropriate handling during wet processing
2. Material specific properties of both InGaP and sacrificial AlGaAs, e. g. AlGaAs oxidation, stress distribution, material stiffness and weakness of InGaP
3. Design related issues, e. g. thin sacrificial layer, resonator design itself

At this point, due to the difficulties experienced during wet release we skipped the introduced cleaning sequence in order to minimize the

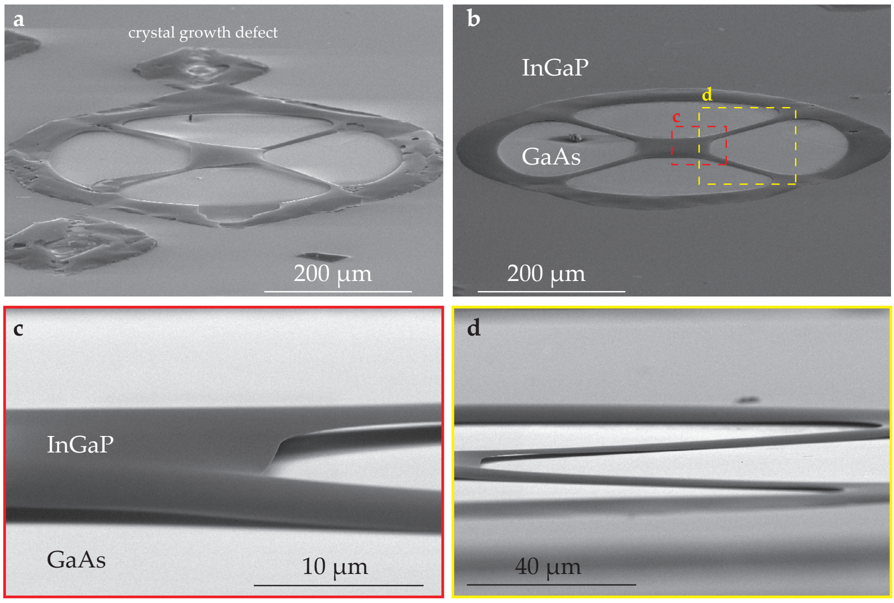

Figure 6.14: Low stress InGaP tethered membrane suspended atop the DBR. **a** Device with typical device failures after the full fabrication flow, showing issues of undesired crystal growth defects, material deformations and fracturing. **b** Best devices when special attention is paid throughout the entire wet process. Images **c** and **d** are zoom-ins from image **b** and highlight issues of material deformations resulting in undesired contact with the surface of the DBR.

amount of wet transfers and focused solely on successfully suspending membranes without the observed issues.

Process adaptations

In the following, in order to test whether the thin sacrificial layer of only 1 µm contributes to the observed challenges in fabrication, e. g. material deformations, we adapt the current process flow by exploiting a non-selective etch that etches deep into the DBR.

Even though non-selective wet etches are not desirable and completely defeat the purpose of the grown heterostructure, deep etching into the DBR effectively gives the possibility to test whether thicker sacrificial layers are enabling the successful release of membranes of larger dimensions. For that purpose, we will exploit a phosphoric acid (H_3PO_4) and hydrogen peroxide (H_2O_2) based solution which etches all of the semiconductors present in our material stack (AlGaAs, GaAs and InGaP). Using $H_3PO_4/H_2O_2/H_2O$ (1:5:15) results in AlGaAs/GaAs etch rates of approximately 1.5 µm/min which requires a total etch duration of 35 min for fully releasing tethered membranes with central pad sizes of 100 µm. In comparison, the etch rate of InGaP for the same etch solution is determined to be 1.5 nm/min and thus results in significantly thinned down membranes due to its low selectivity. With these crude etch rate determinations, whilst fully

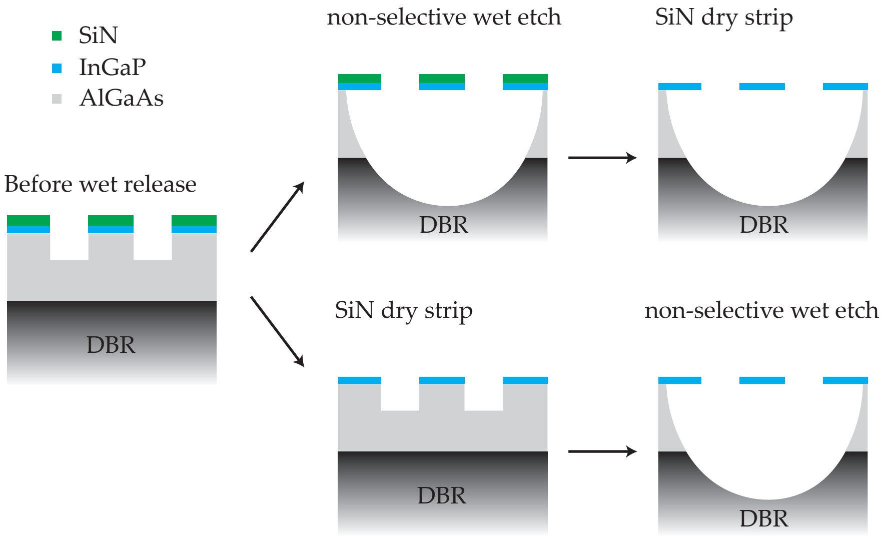

Figure 6.15: Fabrication flow of the modified wet release. After the dry etching step into the sacrificial AlGaAs layer the remaining SiN hard mask (green) can either be stripped before (lower flow) or after (upper flow) the deep non-selective wet etch.

suspending membranes with central pads 100 µm in side length, we even expect the membrane layer to be completely etched away.

Additionally, for enhanced stability during the wet release and to test whether material specific issues of InGaP contribute to the observed challenges, we keep the SiN hard mask during wet etching (approximately 150 nm) and decide to strip it afterwards with a CHF_3 based dry etch. This not only provides enhanced stability for the fragile InGaP membranes, but also protects the top surface from undesired etching.

We can thus distinguish between two recipe modifications for the final wet release step as schematically shown in Figure 6.15, where we exploit a non-selective deep etching with optional stripping of the hard mask before or after.

Deep sacrificial wet release with increased stability

Due to stability and reasons of etch selectivity, we start with the deep etch first while the hard mask is still on top of the InGaP layer. In Figure 6.16, we see two different samples, one of which is fully released whereas the other one was underetched a little too short. When inspecting the non-released samples under almost full cross-section in a SEM, it reveals that the membranes sag down significantly which explains the observed collapse onto the top surface of the DBR during the standard process flow (cf. schematics in Figure 6.16). With tensile stress (and no stress gradients) a doubly-clamped structure should not sag down.

For the fully released samples, it is impossible to notice a difference. The devices look flat under the SEM and no additional cracks or fracturing can be observed. However, stripping the hard mask afterwards causes the samples to break likely due to material and design related reasons. Especially in Figure 6.16 bottom right image, it is clearly visible that the overhang material is so weak that it sags down completely. We further observe a waviness in the overhang region that is presumably stress-related. Whether incomplete stripping of the SiN contributes to these observations cannot be fully excluded.

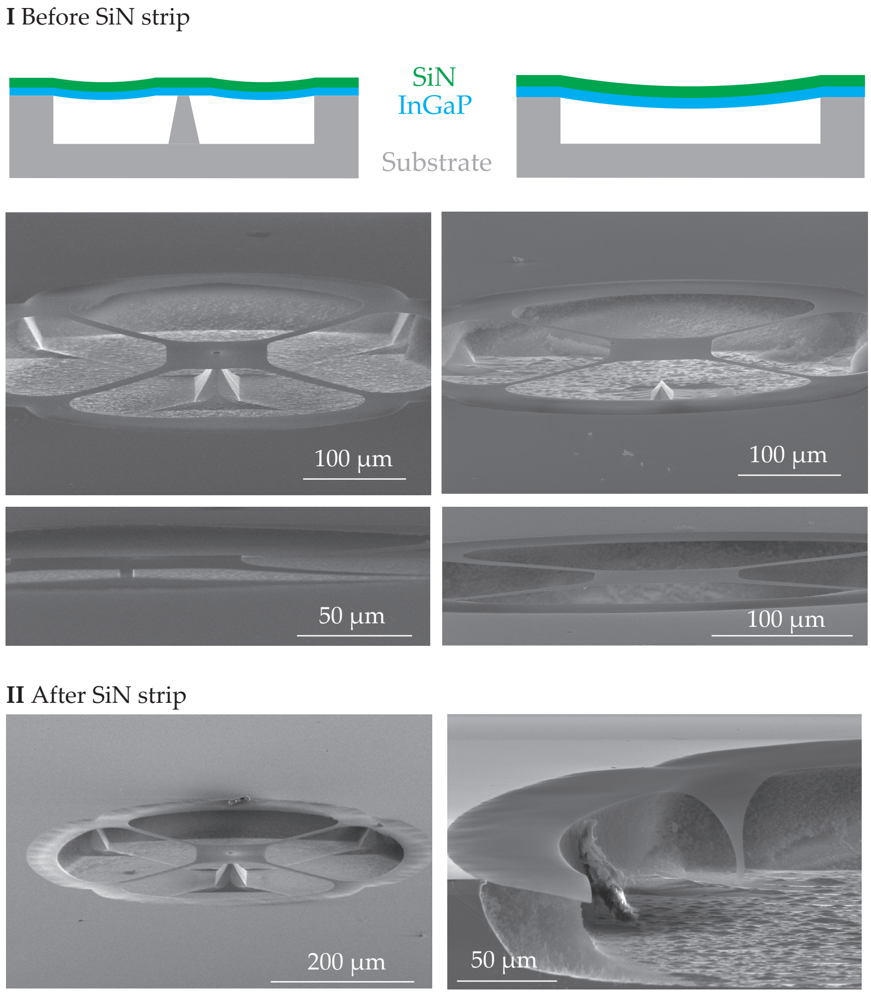
I Before SiN strip
SiN
InGaP
Substrate
100 µm
100 µm
50 µm
100 µm
II After SiN strip
200 µm
50 µm

Figure 6.16: Low stress InGaP tethered membrane with the adapted deep non-selective wet release and SiN hard mask. All devices shown here have been etched with the adapted non-selective deep etch into the substrate while still covered with the SiN hard mask. We show two different chips where one of the shown devices has not been completely released yet in contrast to other. For the unreleased device the material underneath acts as reference height and reveals that parts of the membrane sag down (see schematics). All devices are shown before (**I**) and after (**II**) the final SiN strip.

Deep sacrificial wet release without SiN hard mask

Even though we expected the membranes to be almost completely etched away, we have found devices to survive the non-selective wet-etching resulting in presumably very thin InGaP membranes (see Figure 6.17). This suggests that the obtained etch rate for InGaP in phosphoric acid stated above is overestimated or at least crucially dependent on the etch details. Surprisingly, these thin membranes do not suffer from the various wet transfers and appear to be flat without any wrinkling, which leaves the device layer thickness in combination with the film stress as an important parameter. Another observation is that the large overhang at the support periphery often constitutes a weak point for breaking which can be reduced by minimizing the etch duration. This can be achieved by either reducing the central pad size or/and alternatively pattern it with PhC holes, ultimately determined by the largest features to be underetched.

When placed in a measurement test chamber under vacuum, those very thin membranes show very susceptible to mechanical vibrations especially during chip alignment with piezo actuators. Unfortunately, none of the fabricated devices survived the alignment procedure and their mechanical properties could have therefore not been successfully measured in our test setup.

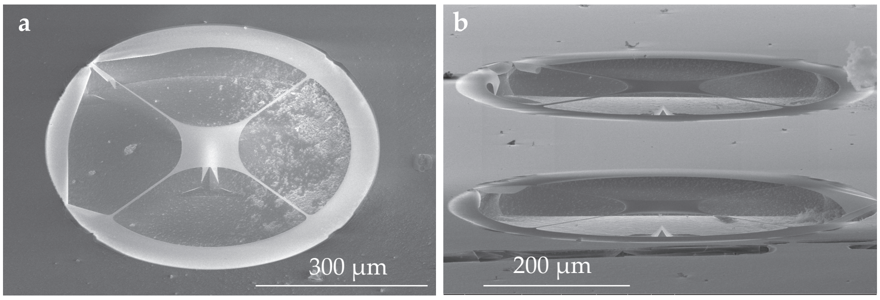

Figure 6.17: Low stress InGaP tethered membrane with the adapted deep non-selective wet release. **a** Fully suspended InGaP membrane under a slight angle from the top. **b** Inspection under almost full cross-section. The membranes are significantly thinned down to an estimated thickness of below 20 nm due to the non-selective wet etch.

InGaP membranes with even higher tensile stress

Similarly to the fabrication of tethered membranes made of the low-stress films, we tried to fabricate high-stress membranes ($\sigma = 650\,\mathrm{MPa}$) exploiting the same deep non-selective etch. Most devices break at their support points and are completely washed away. In Figure 6.18, we show one of the only "surviving" membranes that is still hanging on one of its tethers. This particular sample is patterned with a PhC which reduces the etch duration and thus overhang. It does not seem to have the same material deformations as observed for the low-stress samples even though the SiN hard mask is stripped beforehand, suggesting that higher stress and thinner membranes might solve some of the observed issues. Moreover, breaking at their support points rather hints towards design-related issues exceeding a critical strain beyond which the material fractures. Adapting the device design geometries could thus possibly result in suspended membranes without the material deformations observed for the low stress samples.

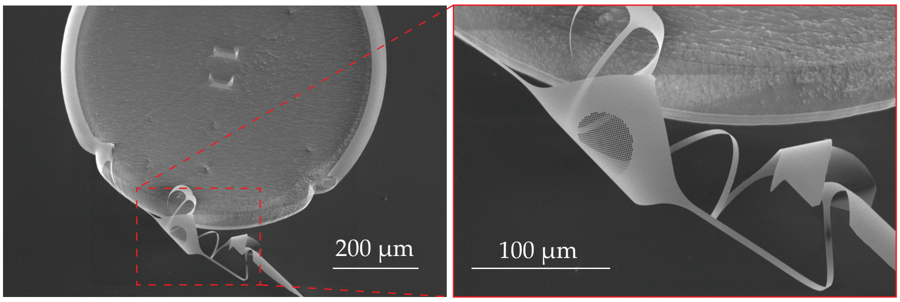

Figure 6.18: High stress InGaP tethered photonic crystal membrane with the adapted deep non-selective wet release. Membranes fabricated from the highly strained InGaP films would regularly break at their support points resulting in most samples completely washed away. Shown is a sole "survivor" that is still hanging on one of its tethers. This particular sample is patterned with a small circular PhC which reduces the underetch duration and thus overhang.

6.5 CONCLUSION AND OUTLOOK

In conclusion, we proposed a bottom-up approach towards achieving a two-membrane cavity system, where both membranes are monolithically integrated on top of a DBR during the growth process. The material system of choice is based on ternary III-V compound semiconductors, where the DBR itself consists of alternating quarter-wave stacks of (Al)GaAs and the membranes of InGaP.

InGaP has recently emerged as an alternative exciting material for optomechanics due to the combination of its unique electro-optic and mechanical properties of crystalline semiconductors, and the ability to tune the internal stress with its compound composition with measured Q factors on the order of 10^6 [21]. Combining the unique properties of ternary III-V semiconductors with the ability to grow multilayer structures of high film quality makes this material platform a promising candidate for optomechanical experiments with multiple mechanical elements, such as enhanced single-photon coupling strengths with membrane arrays.

In contrast to the canonically investigated symmetric case, where the array is placed in the middle of the long macroscopic cavity, here we investigated the MATE configuration, where the array is located close to one of the endmirrors. We found two interesting configurations with optimal membrane-DBR separations corresponding to arrays operated in both their reflective and transmissive regime. In the standard reflective optomechanics case, the inner membrane experiences a coupling strength an order of magnitude larger than the top membrane due to cavity-enhancing effects between membranes and DBR even for the case of an intrinsic membrane-reflectivity of approximately 65 %. However, this strong enhancement comes at a price of significantly increased cavity linewidth. In contrast, when operated in its transmissive regime, the same enhancement factors can be achieved as predicted for the symmetric case where the array is located in the middle of the cavity with even larger enhancements predicted for arrays of higher finesse. Such an all-integrated structure constitutes an interesting multi-element platform in itself with reduced experimental complexity due to its monolithic design with however high demands in accurate layer growth.

We introduced a full fabrication flow towards successfully suspending single tethered membranes as thin as (supposedly) 20 nm. Unfortunately, characterization of their mechanical properties by means of measuring their quality factor remained unsuccessful. In comparison to SiN, the fabrication of InGaP resonators revealed itself as much more challenging. Current challenges involve a better understanding of the material-specific properties and accompanying difficulties during fabrication as well as finding better ways of handling. Nevertheless, doubly-clamped nanobeams of up to 53 µm in length from the same wafer fabricated by our collaborators in the group of Eva M. Weig (Konstanz/Germany) were successfully suspended (both high and low stress) [11]. By changing the beam orientation, a crystal-orientation stress dependence was observed which can be explained by a combination of an anisotropic Young's modulus and a change of elastic properties likely caused by defects within the thin film [11]. This, on one hand, leaves the orientation of resonators as a design parameter, but on the other hand could also explain the observed challenges during fabrication of more complex two-dimensional structures such as tethered membranes with lateral dimensions of several hundreds of µm. We assume that the high aluminum content, the thin sacrificial layers and the membrane thickness constitute the main reasons for the emerging challenges for successfully suspending single- or multi-membrane structures.

Future directions

Possible improvements include adaptations in the epitaxial growth, where changes in layer thicknesses and composition of the compound semiconductors in particularly for the sacrificial AlGaAs and InGaP device layers are recommended in order to avoid current challenges in fabrication while gaining a better understanding of the material properties. Thinner InGaP membranes well below the critical strain might improve the film quality with fewer growth defects whilst however at the same time increasing challenges for achieving highly reflective PhC membranes. Alternatively, instead of using InGaP as device layer, other more matured materials such as GaAs/GaP/InP could be exploited, whilst, however, giving up the possibility of stress tuning. Additionally, thicker sacrificial AlGaAs layers with reduced Al-content promise to significantly improve or even completely solve current obvious challenges in fabrication. Recommended are AlGaAs layers with an Al content between 60 % to 80 % which allows for fast, yet controllable wet etching in (dilute) HF, as well as the avoidance of rapid oxidation in ambient air. Additionally, thicker sacrificial layers are beneficial in successfully releasing membranes without collapsing due to surface tension. However, larger membrane separations defined by the sacrificial layers pose major challenges for meeting the requirement of vertical, smooth side walls during the anisotropic dry etching. Maintaining the pattern design – especially important for tuning the PhC resonances of upper and lower membrane – is believed to constitute a major (insurmountable) obstacle toward the successful implementation of high finesse arrays.

Crucially, for the successful implementation of pre-aligned cavity-membrane systems that rely on accurate layer thicknesses during growth, sagging membranes due to e. g. material fatigue and low stiffness cannot be tolerated and fully defeat the purpose of this monolithic approach. Moreover, as of now, it seems more realistic to just integrate a single membrane on top of a DBR of arbitrary reflectivity or fully avoid the need of patterning the InGaP layers as PhC by just exploiting their non-patterned high reflectivity due to their high refractive index. Exploiting the unpatterned bare membranes still promises coupling enhancements by almost one order of magnitude with an outlook for exploring interesting novel regimes of multimode optomechanics with disparate mechanical resonators.

Nevertheless, membranes made of crystalline semiconductors such as InGaP constitute an interesting alternative for multimode optomechanics with the possibility of growing multilayer structures of custom-designed thickness and functionality. However, challenges in fabrication render it a difficult material platform with many obstacles yet to be overcome. As ultimate goal, we aim for high tensile-strained PhC tethered membranes that will overcome current challenges in fabrication resulting in membrane arrays of high finesse for crystalline semiconductors comparable to those fabricated on SiN. The integration on top of a DBR reduces experimental complexity while still achieving the same coupling enhancements as predicted for arrays in the middle of the optical cavity. However, a better understanding of material properties and accompanying fabrication challenges is crucially required which leaves SiN as the more matured material platform.

7

CONCLUSION AND OUTLOOK

This thesis aimed to make progress towards reaching two major goals: Firstly, providing high-quality membranes that allow to enter the multimode strong cooperativity regime for a MIM system with the main interest in generating non-classical correlations between optics and mechanics. Secondly, making progress towards reaching significantly increased coupling strengths with optomechanical double-membrane arrays. Not only would such a system boost the single-photon strong cooperativity by orders of magnitude, thus potentially allowing to enter the quantum regime with single photons, but also does it allow the study of multimode optomechanics with disparate mechanical resonators.

Entering the multimode quantum regime with phononic shield membranes

Phononic shield structures have become state-of-the-art optomechanical devices that show superior mechanical properties compared to their non-engineered counterparts. The fabricated phononic shield SiN membranes of 350 μm side length (Chapter 4) show reliably high, clamping-independent mechanical quality factors for all mechanical modes within the designed bandgap. Due to the shielding from additional acoustic radiation losses, measured Q factors of approximately 7×10^6 are now intrinsically limited by the membrane dimensions and material quality. Putting those membranes in perspective with further developed structures, nowadays, mechanical quality factors of around 800×10^6 at 1 MHz and room temperature have been demonstrated with an outlook for even higher Qs when operated at cryogenic temperatures [106].

In this case, instead of patterning the entire substrate, the square membrane itself is patterned with a periodic structure that is responsible for the rising of phononic bandgaps and simultaneously localizes the mechanical eigenmodes far away from its clamping points. Therefore, bending losses are greatly reduced beating the intrinsic limitations of their standard square membrane counterpart, which results in unprecedented high quality factors. However, these bandgaps are much narrower and thus shield fewer mechanical modes which seems to be a key criteron for the preservation of multimode entanglement. Even though we have put significant effort in the observation of entanglement between light and mechanics there still seem many technical challenges yet to be overcome and remaining questions to be understood [42, 71].

Entering the single-photon quantum regime

One of the grand goals in optomechanics is reaching the single-photon strong coupling or – less stringent – cooperativity regime, where strong non-linearities dominate the single-photon interaction and allow various single-photon protocols including photon blockade or Schrödinger-cat state generation. Clearly, there is still a very long way to go with many challenges ahead. In the context of membrane optomechanics, strong coupling enhancements are predicted by exploiting optomechanical arrays that promise to push the frontier of optomechanics into the quantum regime, enabling the exploration of exciting novel phenomena with disparate mechanical resonators.

First steps towards this endeavor have been made with groups working on employing membrane arrays that promise to enhance the coupling strength by orders of magnitude based on the array finesse and cavity dimensions. Formerly limited by low finesse, I have successfully fabricated monolithic optomechanical arrays consisting of two highly reflective SiN tethered membranes approaching unity reflectivity due to their photonic crystal pattern (Chapter 5).

In the high finesse regime with finesse values of up to 140, our arrays promise coupling enhancements by two orders of magnitude compared to the single membrane case; an experimental verification of the predicted increased coupling rates still outstanding. Even though these devices are currently limited by diffraction losses due to their plane-parallel configuration, they could potentially be completely overcome by forming stable, spherical cavities with so-called *focusing* PhC membranes.

As an alternative path to minimizing diffraction losses, we aimed to forming significantly shorter arrays with membrane separations of only a few wavelengths by exploiting the unique properties of ternary III-V semiconductors (Chapter 6). Even though shorter arrays of higher finesse ultimately promise significantly larger coupling enhancements, operation in the transmissive regime, and thus accurate membrane positioning, becomes increasingly challenging at the same time. With the purpose of maximizing coupling rates and minimizing diffraction losses, we have designed a multilayer heterostructure that monolithically integrates two closely spaced tensile-strained InGaP membranes on top of a high-reflectivity DBR made of alternating layers of (aluminum) gallium arsenide ((Al)GaAs). Even though our cavity design promises strong coupling enhancements confirmed by TMM simulations, an open question remains whether the requirements of accurate membrane positioning can be achieved during film growth of the designed heterostructure. First of all, the observed challenges in fabricating tensile strained InGaP membranes have to be fully understood and overcome before focusing on other technical experimental challenges that will certainly arise.

While other optomechanical systems can nowadays be operated in the regime of strong single-photon cooperativity [37, 58, 124], the more stringent single-photon strong coupling regime still seems far out of reach. For membrane optomechanics, the conceptual ideas of optomechanical arrays constitute an exciting platform towards overcoming the inherently weak coupling rates in membrane-type system, which ultimately paths the way for membrane architectures to also enter the non-linear single-photon quantum regime.

Undoubtedly, the fast-pace developing field of optomechanics has brought many great achievements to light in recent years. Optomechanical systems of unprecedented quality will continue to reveal quantum properties of massive mechanical resonators, where advancements in fabrication take a major role. Certainly, novel device designs and architectures of improved quality will inevitably enable the exploration of new frontiers and experimental ground, which makes this research field so exciting for the years to come.

Part III

APPENDIX

A

TRANSFER MATRIX METHOD

The TMM is a method that is used to analyze the propagation of electromagnetic fields through a stack of various layers with refractive indices n and thicknesses d, respectively. The reflection and transmission of light from a single interface is described by the Fresnel equations. For structures with multiple interfaces, where light is partially transmitted and reflected from the various interfaces. Depending on the optical path length of the various layers, the wave can destructively or constructively interfere. The total reflection and transmission of the whole structure depends on the interplay between all the partially reflected waves at all the interfaces and can be calculated from a system matrix obtained through simple matrix multiplication of the individual layer matrices. The system matrix of the whole structure then can be converted back into transmission and reflection coefficients.

The reader can find more information in numerous standard optics textbooks or in [12]. We will greatly make use of the TMM in order to obtain the steady-state fields for all of our optomechanical systems under investigation. It allows us to gain useful information, such as the cavity resonance frequency, finesse, as well as transmission and reflection with respect to the membrane's position within the cavity and finally also the coupling strength of the optomechanical system. We will make great use of this approach for even more complicated systems such as realistic multilayer DBRs and as well as for multiple membranes within a cavity (cf. Chapter 6).

There are several TMM python packages available[1], one of them we used as a starting point to analyze our various optomechanical systems where we follow Byrnes [12]. The general idea is the following:

1. In order to calculate the transmission and reflection coefficients of the total system matrix with differing optical layers, we need to provide a list of the refractive indices and thicknesses of each individual layer, respectively ($n = \{n_1, n_2, \cdots, n_n\}$ and $d = \{d_1, d_2, \cdots, d_n\}$). For perpendicular incident light, the results for s- and p-polarized light are identical, so we arbitrarily choose either one of them for the calculations. Lastly, we need to define the wavelength of the light incident to the whole structure.

2. For a given set of input parameters as described above, we obtain the (amplitude) intensity reflection and transmission coefficients $R(\omega)$ and $T(\omega)$, respectively.

---

[1] https://pythonhosted.org/tmm/tmm.html

3. Sweeping over a whole range of wavelengths allows us to obtain the electromagnetic response of our system, basically the fractions of transmitted and reflected light for at each wavelength. With the electromagnetic spectrum at hand, we can further derive useful parameters such as the resonance frequency ω_{res} of our cavity, its line width κ and thus finesse $\mathcal{F}$.
4. In order to determine the optomechanical coupling strength of one (or several) element(s), we repeat above steps for various membrane positions within the cavity.

A.1 DOUBLE-MEMBRANE CAVITY CALCULATIONS

In order to obtain important system parameters such as the optomechanical coupling strength, we determine the resonance frequency with respect to the membrane's position within the optical cavity. This is simple for the case of one membrane only, however, becomes more complicated when dealing with multiple moving elements. The case of arrays with multiple moving elements has been thoroughly analyzed by Xuereb, Genes, and Dantan [115] and the calculations here are based on the paper as well as useful discussions with the author[2] that are summarized in the following. Here, we specifically only investigate the two-membrane case and guide the reader through the thought process in order to remove ambiguity. By moving each membrane individually, we can derive each membrane's coupling strength G_i and thus get to know what the collective supermode is. We can then artificially move all the membranes, with the displacement of the i-th membrane proportional to G_i normalized to the total coupling G. Each transmission point has a different set of G_i, and therefore a different supermode. In particular for the two-membrane case, we can thus distinguish between the *center-of-mass* and so-called *breathing mode*, where both membranes experience a radiation pressure force proportional to their respective coupling G of same and opposite sign, respectively.

For the avoidance of doubt (following strictly the correspondence with André Xuereb):

1. Moving each membrane individually gives us G_i
2. The square-root of the sum of G_i^2 is the overall coupling constant G
3. The Hamiltonian can be expressed as a single-mode system where the optical field couples to one mode (position operator x) with coupling strength G
4. If I move the membranes by an amount $(G_i/G)x$, it is equivalent to displacing this supermode by displacement x

---

[2] Thanks again for the clarifications, André!

5. The shift in the cavity frequency when I displace the supermode directly gives G

If we had known about the existence of the supermode we could have gone to step 4 directly. Alternatively, we can view the G obtained in step 2 and that obtained in step 5 as cross-checking one another.

A.2 OPTOMECHANICS WITH INGAP MEMBRANES

For later comparison, we also briefly summarize the results obtained for configurations already investigated in the literature (MIM configuration for both SMs and DMs as well as a SM at the end-mirror (MATE), cf. Table A.1). We start by comparing the extracted optomechanical performance values for single membranes in both membrane-in-the-middle (MIM) and membrane-at-the-endmirror (MATE) configuration, followed by comparison of the double membrane results obtained for the specific configurations of interest in Chapter 6 (MATE) and the standard MIM setup. We give the results for scanning both membranes individually first which we can extract their respective individual coupling strengths G_1 and G_2, respectively, and thus also follow up with a collective scan based on the coupling ratios obtained by the individual scans. The collective coupling G is obtained by the collective scan method (for the two most interesting cases where collective scan results are shown), but generally agrees well when derived from the individual couplings G_i. The cavity parameters are again summarized in Figure A.1, illustrated for the two-membrane case where we optimize the optomechanical performance by sweeping the spacings d_1 and d_2.

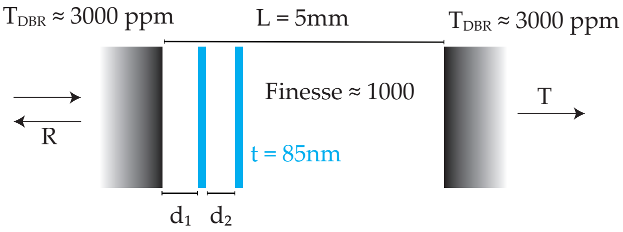

Figure A.1: Overview of parameters used for TMM simulations of a double-membrane array at the end-mirror. Light is incident from the left at 1064.5 nm. The InGaP membrane enclosed by the input mirror and second membrane is labeled as 'membrane 1', whereas the other membrane is labeled as 'membrane 2'.

A.2.1 *Single membrane*

Configuration	G (GHz nm^{-1})	G/κ (nm^{-1})
MIM	0.58	3.2
MATE	3.02	3.7

Table A.1: Coupling strengths obtained for a single InGaP membrane in both membrane-in-the-middle (MIM) and membrane-at-the-endmirror (MATE) configuration. Given are the maximum values for G and G/κ.

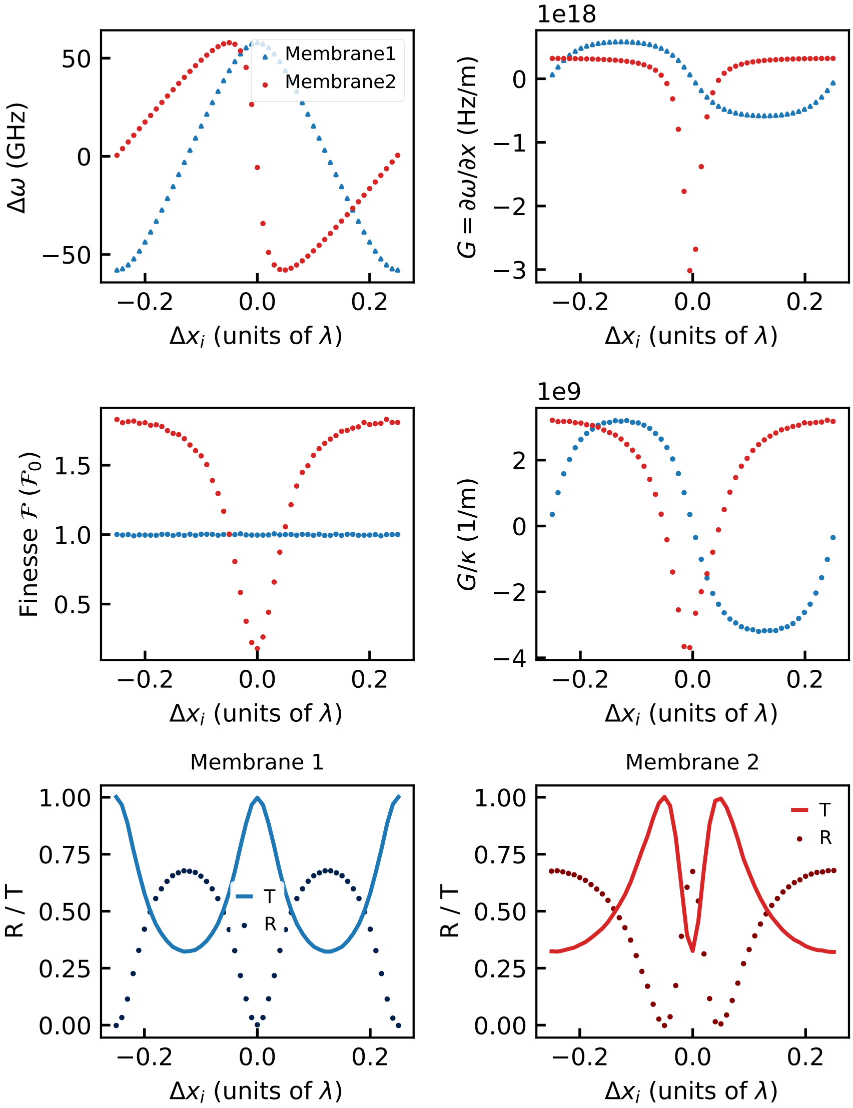

Figure A.2: Comparison of a single InGaP membrane in both membrane-in-the-middle (MIM) and membrane-at-the-endmirror (MATE) configuration. The case labeled as 'membrane1' corresponds to the MIM (blue data), whereas the MATE case is labeled as 'membrane2' (red data).

A.2.2 *Double-membrane arrays at the endmirror*

In this section, we summarize all the results obtained for the various double-membrane arrays made of InGaP in their reflective and transmissive regime. Plotted are changes in cavity resonance frequency $\Delta\omega$ for the individual and collective movement of both membranes, thereof derived frequency pull parameter G, cavity linewidth κ normalized to the empty cavity linewidth, intensity reflection R and transmission T through the full optomechanical cavity, as well as strong coupling parameter G/κ and measurement rate G^2/κ. The cavity linewidth is evaluated as the full-width at half-maximum (FWHM). All results are given in absolute values, whereas we restricted ourselves from applying the zero-point-fluctuation x_{zpf} which depends on specifics of the membrane-light interaction. All system parameters are plotted with respect to the membrane displacements Δx from their rest position specified for each configuration, given in units of laser wavelength $\lambda = 1064.5\,\mathrm{nm}$.

Configuration	d_1	d_2	G_1	G_2	G	G/κ
	(units of λ)			(GHz nm^{-1})		(nm^{-1})
MIM	$L_{\mathrm{cav}}/2$	3	3.25	-3.25	4.49	24.8
MATE	3	3	-0.32	0.32	0.45	1.8
	3.25	3	3.24	-3.22	4.48	25.3
	3	3.23	-27.86	-3.04	28.03	6.08
	3.25	3.25	0.06	0.32	0.33	0.57

Table A.2: Comparison of coupling results obtained for single- and double-membrane arrays in both membrane-in-the-middle (MIM) and membrane-at-the-endmirror (MATE) configuration. Values extracted from the individual and collective scans.

A.2.2.1 *Reflective optomechanics at the end-mirror*

$\{d_1, d_2\} = \{3.0\lambda, 3.23\lambda\}$

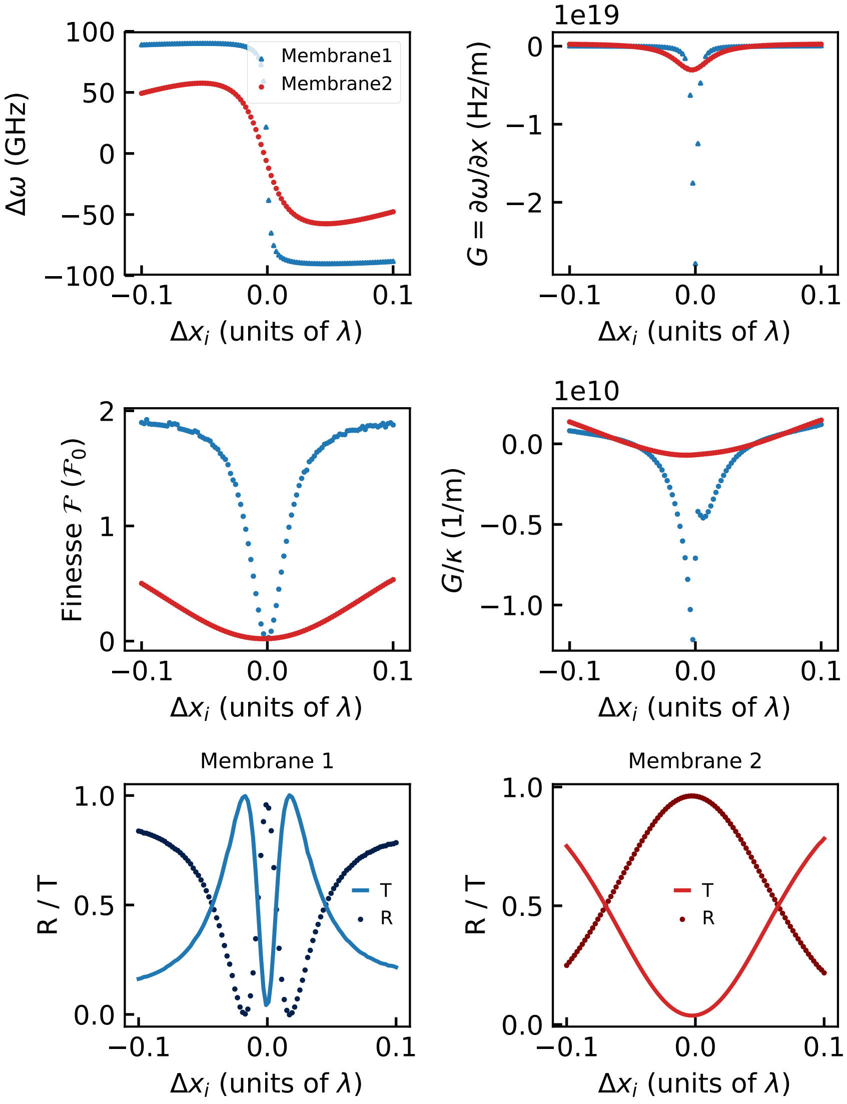

Figure A.3: Individual mode displacement results for the reflective optomechanics regime at the end-mirror with $d_1 = 3\lambda$.

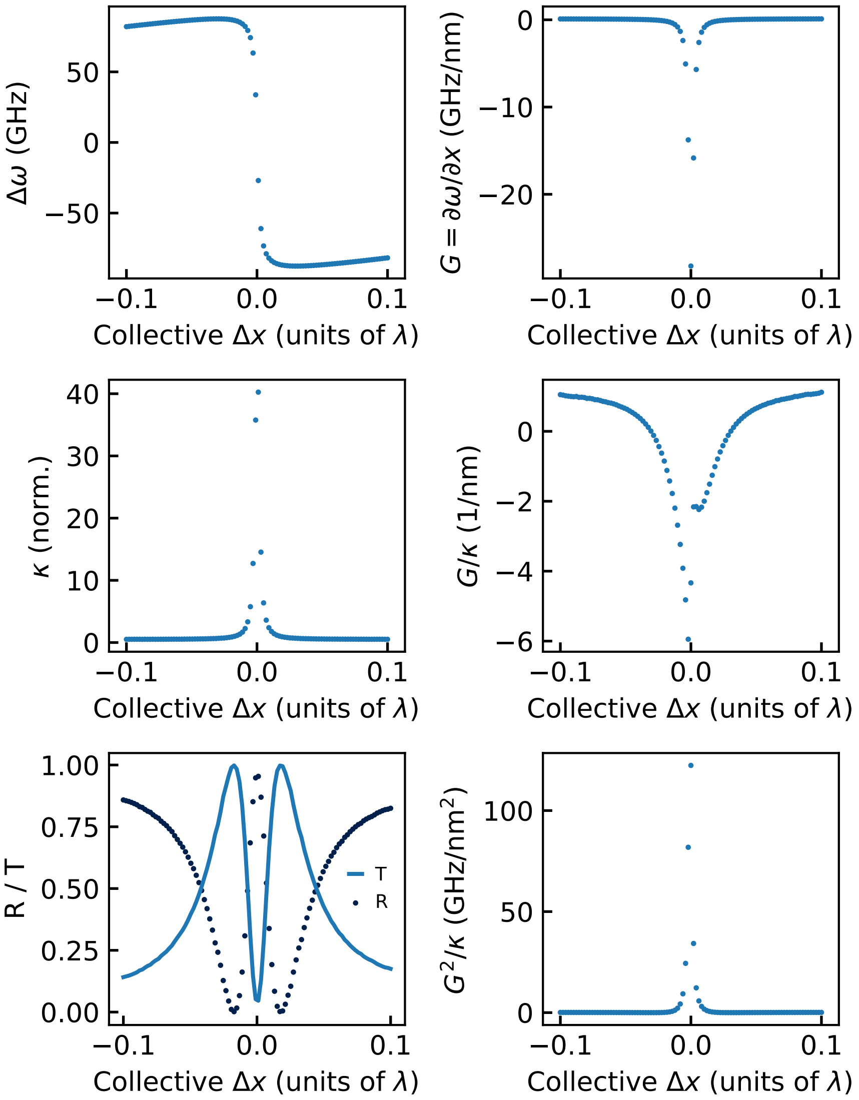

Figure A.4: Collective mode displacement for double-membrane arrays made of InGaP in the transmissive optomechanics regime. All system parameters are plotted with respect to the membrane positions around their rest position $d_1 = 3.25\lambda$ and $d_1 = 3\lambda$.

$\{d_1, d_2\} = \{3.25\lambda, 3.25\lambda\}$

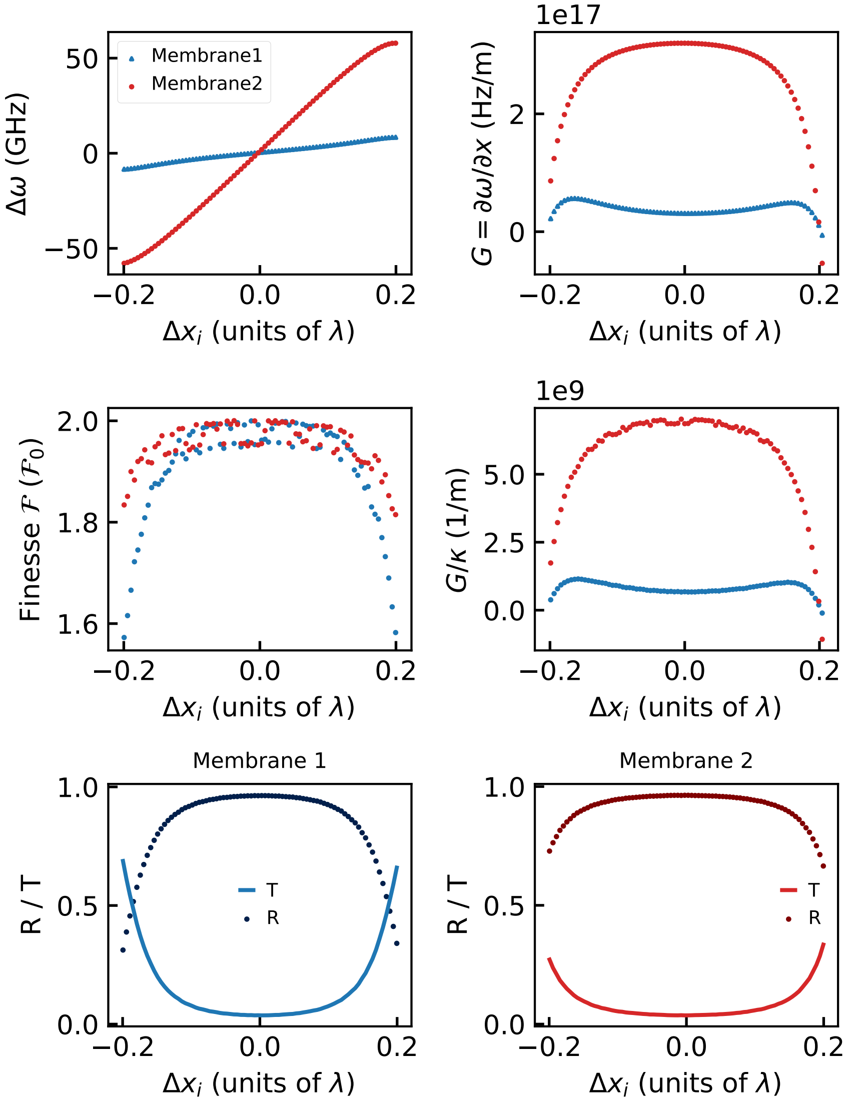

Figure A.5: Individual mode displacement results for the reflective optomechanics regime at the end-mirror with $d_1 = 3.25\lambda$.

A.2.2.2 *Transmissive optomechanics at the end-mirror*

$\{d_1, d_2\} = \{3.0\lambda, 3.0\lambda\}$

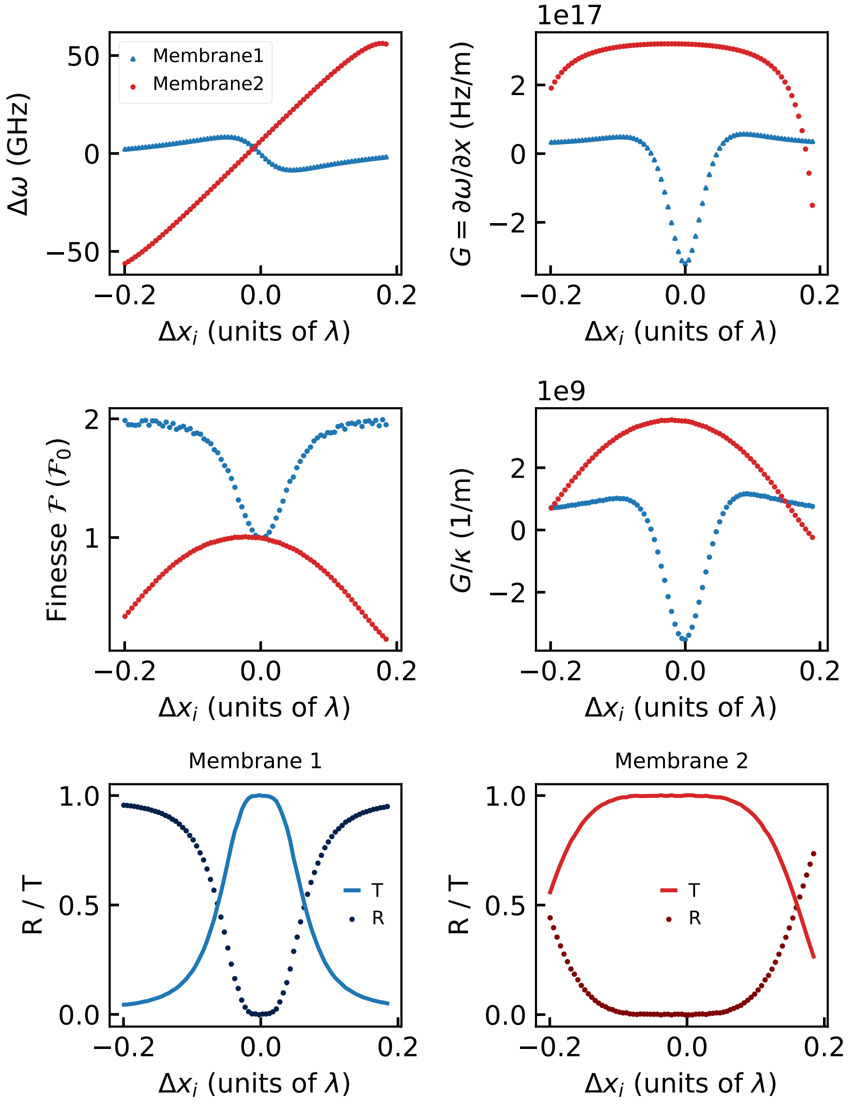

Figure A.6: Individual mode displacement results for the transmissive optomechanics regime at the end-mirror with $d_1 = 3\lambda$.

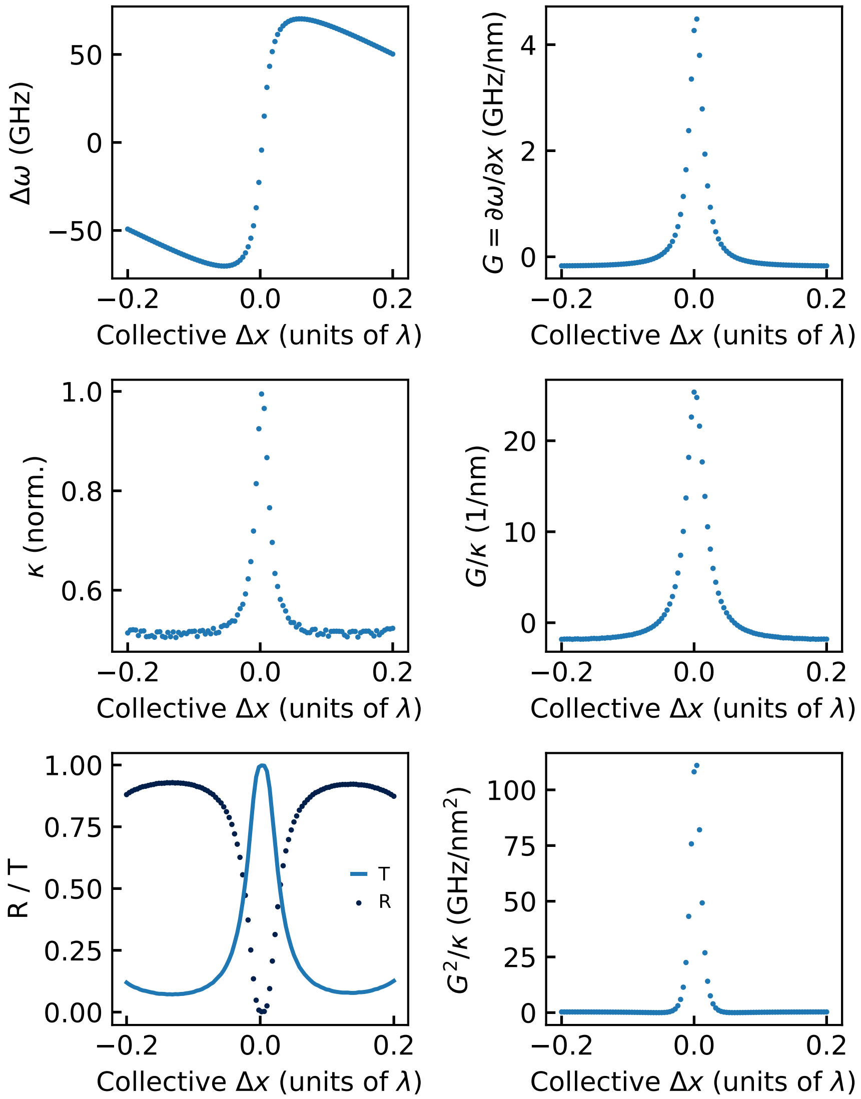

Figure A.7: Collective mode displacement for double-membrane arrays made of InGaP in the transmissive optomechanics regime. All system parameters are plotted with respect to the membrane positions around their rest position $d_1 = 3.25\lambda$ and $d_1 = 3\lambda$.

$\{d_1, d_2\} = \{3.25\lambda, 3.0\lambda\}$

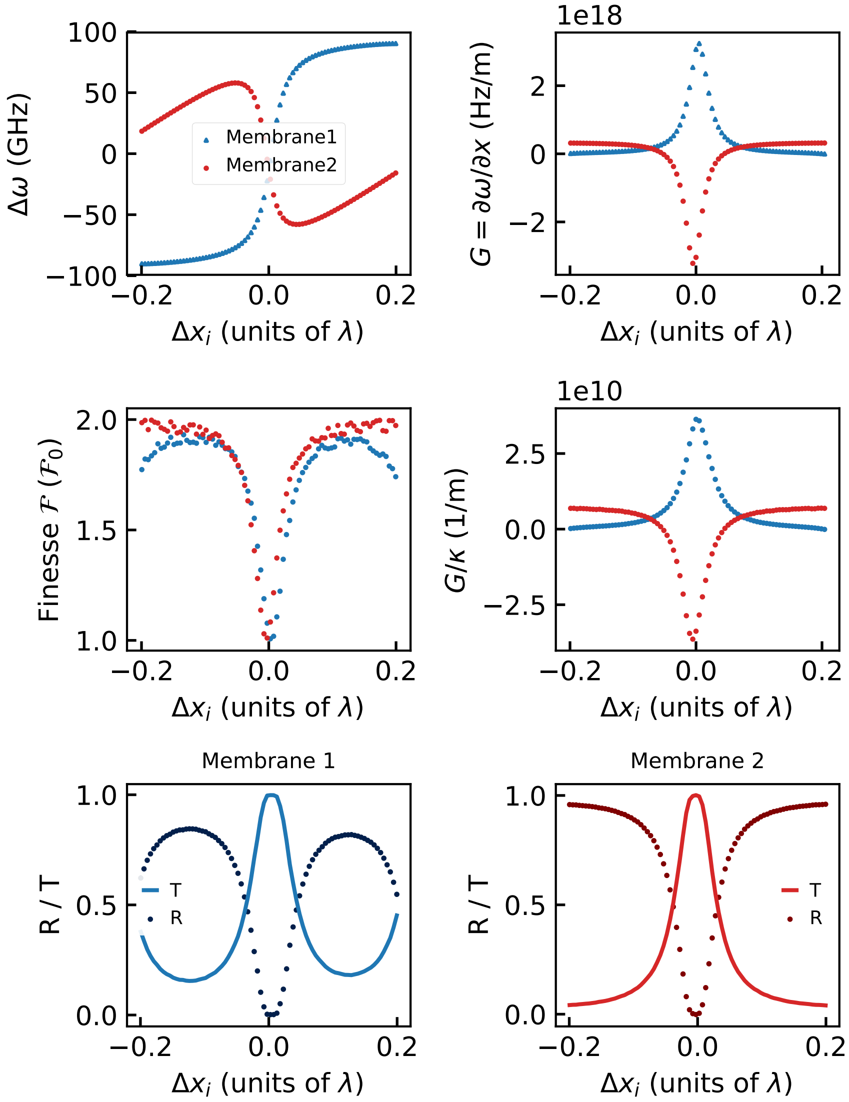

Figure A.8: Individual mode displacement results for the transmissive optomechanics regime at the end-mirror with $d_1 = 3.25\lambda$.

B

CHARACTERIZATION SETUPS

This appendix chapter gives a brief overview over the various setups and methods that can be used for characterizing the optical and mechanical properties of fabricated membrane resonators. The toolbox of quantum optics allows for a thorough and accurate characterization of optomechanical system parameters by using optical cavities. However, due to their complexity and higher effort in operation, it can be useful to use dedicated setups for the characterization of specific properties only. Here, in terms of the characterizing optical and mechanical properties of membranes in particular, we introduce two dedicated setups. First, an optical setup for determining the reflective and transmissive spectral behavior of membrane resonators. Second, a dedicated setup for determining the mechanical quality factors by means of ringdown measurements. With these two setups, we are able to quickly determine membrane properties such as their mechanical spectra and mode-dependent dissipation rates, and wavelength-dependent reflectivity spectrum R_m. However, measurements in optical cavities can usually be obtained with higher accuracy with additional efforts. Later on, we will additionally determine the reflectivity of membranes incorporated in MIM-setups by analyzing the obtained mode splitting [98]. It goes without saying that the characterization of coupling strengths can only be obtained by exploiting methods used in optomechanical setups (e. g. optomechanically induced transparency (OMIT)). However, properties of the individual optical and mechanical systems can – to some extend – independently be studied, as what will be explained in the following. In the case of determining the optical losses induced by scattering and material absorption, the method of choice is to measure the optical finesse $\mathcal{F}$, which contains information about the total (optical) system losses and thus also those induced from the mechanical resonator (κ and thus $\mathcal{F}$). Usually, losses arising from the input and output mirrors comprising the optical cavity are either known and/or can further be determined by measuring the finesse of an empty cavity which is then compared to the finesse of the whole optomechanical system.

For a more in-depth description of characterization methods and setups, especially for the characterization in optomechanical cavities, I refer to the theses of my colleagues. Especially for the membranes introduced in Chapter 4, a full optomechanical characterization has been executed by Nia [71], for the devices introduced in Chapter 5, the optomechanical characterization has been performed by Moura [67].

B.1 OPTICAL CHARACTERIZATION

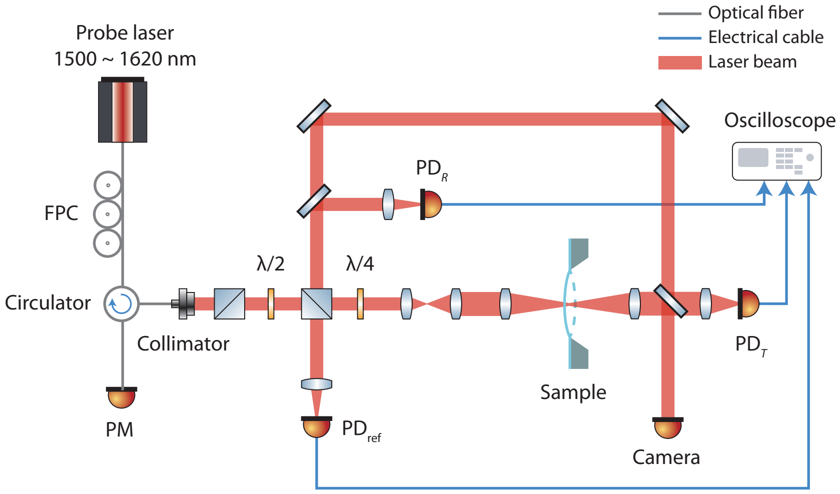

Figure B.1: Schematic of the optical characterization setup (taken from Moura [67]). FPC: fiber polarization controller; PM: powermeter; PD: photodiode.

For the characterization of the optical properties of membranes, in particular for studying the reflectance and transmittance, we use a dedicated setup schematically described in Figure B.1. We obtain the optical spectrum of the devices using a laser tunable from 1500 to 1630 nm. This laser beam is split into a path that is incident on the sample and a reference path, directed onto a photodetector. This serves to correct for drifts in the setup before the interaction with the sample. The incident beam is focused onto the sample with arbitrary beam waists achievable, determined by the choice of the 3-lens-system. Usually, we aim to characterize our samples for beam waists of approximately 50 µm, similar to the beam waist of our optomechanical cavity. Light transmitted through the sample is measured on a third photodetector. Light reflected from the sample follows the same optical path as the incident beam. We split these two, using a combination of a polarization beam splitter and a quarter-wave plate, and send the reflected beam to a separate photodetector. Before measuring devices, we calibrate the setup using a commercial dielectric mirror with a known reflectivity. After, the device is placed in the setup, its tip, tilt and position in relation to the beam waist is carefully adjusted, and its measurements are compared to those of the dielectric mirror in order to obtain the transmission and reflection coefficients as a function of wavelength. For a detailed description of the calibration procedure and setup details, I refer to the thesis of Moura [67].

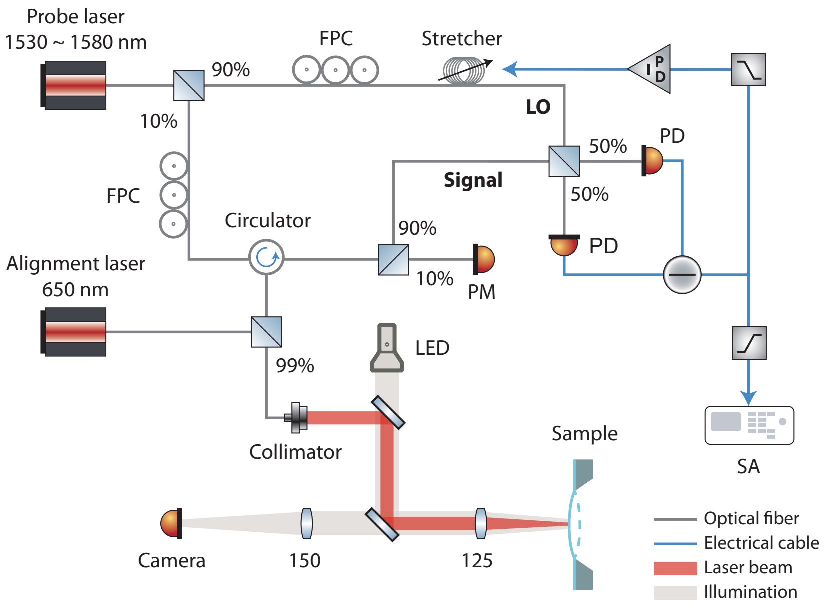
Probe laser
1530 ~ 1580 nm
90%
10%
FPC
Stretcher
PID
LO
50%
PD
Signal
50%
PD
FPC
Circulator
90%
10%
PM
Alignment laser
650 nm
99%
LED
Collimator
Sample
SA
Camera
150
125
Optical fiber
Electrical cable
Laser beam
Illumination

Figure B.2: Schematic of the mechanics characterization setup (taken from Moura [67]). FPC: fiber polarization controller; PID: proportional, integral, differential controller; SA: spectrum analyzer; PM: powermeter; PD: photodiode.

B.2 MECHANICAL CHARACTERIZATION

We characterize the resonators' mechanical properties using a fiber-based homodyne interferometer (compare Figure B.2). A laser beam is split into signal and local oscillator (LO) paths. The signal is focused onto the center pad of the membrane resonators. Light reflected from the devices is split from the incident beam path using a fiber circulator and then combined with the LO using a tunable fiber coupler, in order to precisely set the coupling ratio to 50:50. The coupler output is measured using a balanced detector. The low frequency output of the detector is used to lock the phase of the signal and LO, using a PID controller and a fiber stretcher which is connected to the LO path. Locking the phase between the LO and back-reflected signal beam on the phase quadrature allows us to be sensitive to the displacement of our mechanical resonators. The high frequency detector output contains the information we are interested in retrieving, and is fed into a Spectrum Analyzer (SA). Finally, a piezo actuator attached to the stage can drive the mechanical modes of interest, whose mechanical quality factors are then determined by means of ring-down measurements.

C

PROCESS RECIPES

In this chapter, process recipes for the fabricated devices are attached. For devices based on SiN the recipes are fully developed and readily usable. The fabrication process of the phononic shield membranes inherently also contains the process flow of simple square membranes in the first part, followed by the phononic shield fabrication in part two.

For the double membrane arrays, the full process flow is provided for the case of an array with two high reflectivity trampoline resonators that have been successfully used to study the optical, mechanical and optomechanical properties discussed in Chapter 5 and publication [30].

For the case of the structures of Chapter 6 where the goal was to work towards the integration of single and double membrane structures on top of a DBR, only the current status is provided and is still far from fully developed but can be seen as a good starting point for further process development.

On the following pages, process recipes for the structures fabricated throughout this thesis can be found:

1. Phononic shield membranes (Chapter 4)
2. Double PhC tethered membrane arrays (Chapter 5)
3. All-integrated DBR-membrane structures on III-V material platform with InGaP as device layer (in process development, Chapter 6)

Claus Gärtner - University of Vienna

Phononic shield membranes

50nm high stress LPCVD silicon nitride on 500um silicon wafer

Sample Name: ________________ Date: __________________ Version: ____

Step 0: Sample preparation and cleaning

Date: _____________

Si wafer coated with resist for dicing and debris protection (back and front side)
First start to protect the device side, then the less important back side
use any protective photoresist that is easy to remove.
Bake dicing resist at 100C for 3 min

Cleaving into 10x10 mm samples with resist on top for device layer protection

Part I: Fabrication of the square membrane

Step 1: E-beam Lithography: 350um square membrane

Date: ______________

The window size of the backside defines the final membrane size: dependent on Si substrate thickness
For 500um thick wafers and a square membrane of 350um in sidelength: L = 1050um

Resist Coating: AR-P 6200.09 (CSAR 62)

EB Resist (AR-P 6200.09) _______ spin at (3) _______ krpm for (60) _______ sec; Thickness = 350 nm
Tempering on a hotplate at (150) _____ °C for (3) ____ min, cool (5) ____ min
Expose image (330) _______ uC/cm^2 @ 100 keV
pentylacetate (60) _____ sec; MIBK:IPA (1:1) rinse (60) _____ sec; IPA rinse (60) _____ sec, N2 gun

Step 2: SiN dry etching [AMS Cryo Etcher]

Date: ______________

Recipe: CHF3_IGOR
CHF3 (60) _____ sccm; O2 (6) _____ sccm; Coil power (500) _____ W; RF power (50) _____ W;
Pressure (0.1) _____ ubar, Temperature (20) _____ C, He flow (0.7) _____ sccm
Etch rate ~ 80nm/min SiN, etch selectivity to CSAR ~ 1:1

Use thermal conductance oil for stable temperature of the sample and clean it off afterwards with ethanol.
Solvent clean: PRS baker at 80C, DI and IPA

Step 3: Organics clean

Date: ______________

Piranha clean [H2SO4 : H2O2 (3:1)] at (100) ___ °C for (8) ____ min
first pour H2SO4 into beaker, then slowly add H2O2 and stablize to 100°C.

CAREFUL: very exothermic reaction

Step 4: Wet release in 30% KOH

Date: ______________

http://lelandstanfordjunior.com/KOHcalcfaq.html
Etch rate in **30% KOH at 75C along** (100)-plane: ~60um/hour)
use one-sided holder in order to protect sample edges from etching
30% KOH at (75) ___ °C for (8.5) ____ hours
Di rinses (2x)

Step 5: KOH residue clean (IONIC CLEAN)

Date: ______________

HCl : H2O (1:5) for (10) ____ min
removes traces of metals -> potassium ions after KOH etch!
DI rinses (2x), IPA (2x), N2 gun
make sure there are no water residues on the the membrane after N2 blow drying

Part II: Fabrication of phononic shield

Step 6: PECVD oxide hard mask deposition

Date: ______________

Recipe: "PECVD oxide HQual."
Use dummy silicon shields to guarantuee uniform deposition

Frontside deposition at (300) ___ °C for (50) ____ min, oxide thickness (3500) ______ nm
Backside deposition at (300) ___ °C for (10) ____ min, oxide thickness (700) ______ nm

Oxide color chart: **https://cleanroom.byu.edu/color_chart**

Step 7: E-beam Lithography of phononic shield pattern

Date: ______________

Resist Coating: AR-P 6200.18
EB Resist (AR-P 6200.18) _______ spin at (2) _______ krpm for (60) _______ sec; Thickness = 1100 nm
Tempering on a hotplate at (150) _____ °C for (3) ____ min, cool (5) ____ min
Expose image (330) _______ uC/cm^2 @ 100 keV
pentylacetate (60) _____ sec; MIBK:IPA (1:1) rinse (60) _____ sec; IPA rinse (60) _____ sec, N2 gun

Step 8: Oxide (+SiN) dry etching [AMS BOSCH]

Date: ______________

Bias as low as possible for maximized etch selectivity. CAREFUL: polymer deposition below bias threshold
Mount sample on silicon carrier wafer with thermal conductance oil

Repetitive cycles of (2) ____ min etching, (80)____seconds Ar cooling, total etch time (~20)____ min
C4F8 (50) _____ sccm; He (100) ____ sccm; CH4 (10) ____ sccm;
Coil power (2500) _____ W; RF power (200) _____ W; DC bias (25)____ V
Pressure (?) _____ ubar, Temperature (0) _____ C, He flow (3.5) _____ sccm
Oxide etch rate ~ 210nm/min, resist etch rate ~ 50nm/min, etch selectivity ~4

O2 Descum for (2) _____ min
O2 (200) ____ sccm; Coil power (1000) ______ W; RF power (0)____W

Unmount sample by immersing carrier wafer in ethanol and gently pushing it off. Ethanol clean

Step 9: Organics clean

Date: ______________

Baker PRS at (80) ___ °C for (10) ____ min
Di rinses (2x), IPA (2x), N2 gun

[Optional] **Piranha clean [H2SO4 : H2O2 (3:1)] at (100) ___ °C for (8) ____ min**
first pour H2SO4 into beaker, then slowly add H2O2 and stablize to 100°C.
CAREFUL: very exothermic reaction
Di rinses (2x), IPA (2x), N2 gun

Step 10: DRIE [Estrellas]

Date: ______________

Recipe: 500um wafer, 50um features
Mount sample on **silicon oxide** carrier wafer with thermal conductance oil

Use ***LF Pulsed mode***
DRIE cycles of (1775) ____ ; total etch time (~69)____ min
Oxide etch rate ~ 7.5um/min, oxide etch rate ~ 40nm/min, etch selectivity ~190

Back to ***HF mode***

O2 Descum for (15) _____ min
O2 (100) ____ sccm; Coil power (2000) ______ W; RF power (20)____W
Do not exceed platen temperature of 200°C!

Step 11: Organics clean and HF oxide strip Date: ______________

Unmount sample by immersing carrier wafer in ethanol and gently pushing it off. Ethanol clean
Baker PRS at (80) ___ °C for (10) ____ min
Di rinses (2x)

HF (40%) dip for (5)___ sec
HF (10%) for (1) ____ min
Di rinses (2x)
Make sure that entire oxide is stripped!

Oxide etch rates in HF
40% HF: >16um/min
10% HF: 600nm/min

Piranha clean [H2SO4 : H2O2 (3:1)] at (100) ___ °C for (8) ____ min
first pour H2SO4 into beaker, then slowly add H2O2 and stablize to 100°C.
CAREFUL: very exothermic reaction
Di rinses (2x), IPA (2x), N2 gun

Step 12: Critical point drying [LEICA] Date: ______________

DI (2x) → IPA (2x) → (ultra pure IPA)
Recipe "Gaertner"

Double membrane arrays with high-reflectivity SiN membranes

200nm high stress LPCVD silicon nitride on 200um silicon wafer

Sample Name: ________________ Date: __________________ Version: ____

Step 0: Sample preparation and cleaning Date: ______________

Si wafer coated with resist for dicing and debris protection (back and front side)
First start to protect the device side, then the less important back side
use any protective photoresist that is easy to remove.
Bake dicing resist at 100C for 3 min

Cleaving into 10x10 mm samples with resist on top for device layer protection

Part I: Fabrication of frontside tethered PhC membrane

Step 1: E-beam Lithography (AR-P 6200.13) Date: ______________

Frontside: EB Resist (AR-P 6200.13) _______ spin at (3) _______ krpm for (60) _______ sec; Thickness = 450 nm
Tempering on a hotplate at (150) _____ °C for (3) ____ min, cool (2) ____ min
Backside: EB Resist (AR-P 6200.13) _______ spin at (3) _______ krpm for (60) _______ sec; Thickness = 450 nm
Tempering on a hotplate at (150) _____ °C for (3) ____ min, cool (2) ____ min

Frontside exposure (total baking time of 6min)
Expose image (330) _______ uC/cm^2 @ 100 keV
PhC design parameters:
lattice constant, a = 1375nm
hole diameter, d = 1050nm

Development
pentylacetate (60) _____ sec; MIBK:IPA (1:1) rinse (60) _____ sec; IPA rinse (60) _____ sec, N2 gun

Step 2: SiN dry etching Date: ______________

AMS cryo; recipe: CHF3_IGOR
Etch time: (3) _____ min for fully opening PhC holes
CHF3 (60) _____ sccm; O2 (6) _____ sccm; Coil power (500) _____ W; RF power (50) _____ W;
Pressure (0.1) _____ ubar, Temperature (20) _____ C, He flow (0.7) _____ sccm
Etch rate ~ 80nm/min SiN, etch selectivity to CSAR ~ 1:1

Use thermal conductance oil for stable temperature of the sample and clean it off afterwards with ethanol.
Solvent clean + PRS baker at 80C, followed by consecutive DI and IPA rinses
Cross-check: PhC holes should appear white under optical microscope when fully opened.

Step 3: Organics clean Date: ______________

Baker PRS at (80) ___ °C for (10) ____ min, cool (2) ____ min
Di rinses (2x)

Piranha clean [H2SO4 : H2O2 (3:1)] at (100) ___ °C for (8) ____ min
first pour H2SO4 into beaker, then slowly add H2O2 and stablize to 100°C.
CAREFUL: very exothermic reaction

Di rinses (2x), IPA (2x), N2 gun

Part II: Fabrication of backside tethered PhC membrane

Step 4: E-beam Lithography (AR-P 6200.13) Date: ______________

Frontside protection:

EB Resist (AR-P 6200.13) _______ spin at (3) _______ krpm for (60) _______ sec; Thickness = 450 nm
Tempering on a hotplate at (150) _____ °C for (3) ____ min, cool (2) ____ min

Backside: EB Resist (AR-P 6200.13) _______ spin at (3) _______ krpm for (60) _______ sec; Thickness = 450 nm
Tempering on a hotplate at (150) _____ °C for (3) ____ min, cool (2) ____ min

Backside exposure (total baking time of 3min)
Expose image (330) _______ uC/cm^2 @ 100 keV
PhC design parameters: (account for differences in baking time)
lattice constant, a = 1378nm
hole diameter, d = 1050nm

Development
pentylacetate (60) _____ sec; MIBK:IPA (1:1) rinse (60) _____ sec; IPA rinse (60) _____ sec, N2 gun

Step 5: SiN dry etching Date: ______________

AMS cryo; recipe: CHF3_IGOR
Etch time: (3) _____ min for fully opening PhC holes
CHF3 (60) _____ sccm; O2 (6) _____ sccm; Coil power (500) _____ W; RF power (50) _____ W;
Pressure (0.1) _____ ubar, Temperature (20) _____ C, He flow (0.7) _____ sccm
Etch rate ~ 80nm/min SiN, etch selectivity to CSAR ~ 1:1

Use thermal conductance oil for stable temperature of the sample and clean it off afterwards with ethanol.
Solvent clean + PRS baker at 80C, followed by consecutive DI and IPA rinses
Cross-check: PhC holes should appear white under optical microscope when fully opened.

Step 6: Organics clean Date: ______________

Baker PRS at (80) ___ °C for (10) ____ min, cool (2) ____ min
Di rinses (2x)

Piranha clean [H2SO4 : H2O2 (3:1)] at (100) ___ °C for (8) ____ min
first pour H2SO4 into beaker, then slowly add H2O2 and stablize to 100°C.
CAREFUL: very exothermic reaction

Di rinses (2x), IPA (2x), N2 gun

Part III: Wet release, cleaning and drying

Step 7: Wet release in 30% KOH Date: ______________

http://lelandstanfordjunior.com/KOHcalcfaq.html
Etch rate in **30% KOH** at 75C along (100)-plane: ~60um/hour)

30% KOH at (75) ___ °C for (110) ____ min
Di rinses (2x)

Step 8: KOH residue clean (IONIC CLEAN) Date: ______________

HCl : H2O (1:5) for (10) ____ min
removes traces of metals -> potassium ions after KOH etch!

Step 9: Critical point drying Date: ______________

DI (2x) → IPA (2x) → (ultra pure IPA)
Recipe "Gaertner" in LEICA tool

Tensile-Stressed InGaP Membranes: *Dispersively Coupled III-Vs*

DBR with 1 Membrane

Sample Name: ________________ Date: __________________ Version: ____

Step 0: Sample preparation and cleaning Date: ______________

Handling and storage: protect EPI structure with resist (SiN / SiO2 hard mask deposition before/after)

Cleaving into 10x10 mm samples with resist on top to protect the surface from splinters

Wafer Clean: InP baserd wafers (TU Delft) + solvents

H3PO4 (73 vol. %) : Di = 1 : 10 for (60) _______ sec (optional, still to be tested)

acetone (60) _______ sec; IPA (60) _______ sec; dry with N2

Microscope surface inspection: CLEAN !! CLEAN !! CLEAN !!

Step 1: InGaP + AlGaAs Strip Date: ______________

STS ICP tool: Chlorine based etch at elevated temperature : Etch time (45) _______ sec

No need of heat conducting grease

Etch gas chemistry: Cl2 (4.5) _____ sccm / N2 (4.5) _____ sccm / Ar (21) _____ sccm

Pressure (2) ____ mTorr; Temp. (190) _____ °C

ICP power (800) _____ W; RF power (50) _____ W -> bias voltage (300) _____ V

Etch rates: EPI ~ 400 nm/min; SiN ~ 25 nm/min => Selectivity ~ 16 (depends on feature size)

DI rinse immediately after chlorine based etches for (5) _____ min

AlGaAs strip with 1% HF solution (maybe heated for better solubility of Al byproducts)

~ 50:1 DI:48% HF (total of ~ 15sec) __________ sec (gently moving sample)

Dip in and out vertically / up side down.

Rinse in heated DI (2x) at (80) _____ °C for (5) _____ min [softmask paper: 10 min cold DI rinse]

Nitrogen blow drying

Cleaning off HF by-products / salts: AlF3, Al(OH)3, … with KOH

[optional if needed] 30% H2O2 for (60) __ [side effects: **oxidizing organics** and **1nm GaAs layer**]

Rinse in DI water for (60) _____ sec

[optional] Rinse in methanol / ethanol for (60) _____ sec for decrystallization of Aluminium hydroxid crystals

30% KOH [200g in 466ml DI] (150) ______ sec [thorough clean of Al(OH)3 residues + de-oxidation]

Rinse in heated DI (2x) at (80) _____ °C for (5) _____ min

Solvent rinse in IPA

Step 2: Hard mask deposition and Ebeam Lithography (EBL) Date: ______________

PECVD I: silicon nitride thickness (98) _______ nm for (7) _______ min in total

Standard recipe: PECVD Nitride HQual - grow rate ~ 12.8nm/min [14 nm/min stated]

Consistency check: Nitride thickness of _____ nm (100 nm) should give a _________ colour (blue)

[optional] split into two PECVD runs to reduce probability of pin holes in the mask structure

EBL: Transfer of membrane pattern into hard mask

Resist Coating: AR-P 6200.09 (CSAR 62); Thickness = (200) ______ nm

EB Resist (AR-P 6200.09) _______ spin at (3) _______ krpm for (60) _______ sec; Thickness = 200 nm

Tempering on a hotplate at (150) _____ °C for (3) ____ min, cool (5) ____ min

Expose image (310) _______ uC/cm2 @ 100 keV

pentylacetate (60) _____ sec; MIBK:IPA rinse (60) _____ sec; IPA rinse (60) _____ sec, N2 gun

Step 3: Dry etching (+ laser monitor for etch control) Date: ______________

RIE F2 tool: Fluorine based etch chemistry with end point detection

Optional: O2 descum for (10) _____ sec [cleaning openings from resist residues]

O2 (20) _____ sccm; RF power (25) _____ W; Pressure (50) _____ ubar

Etch gas chemistry: Etch time (12) _______ min for (200) ______ nm

CHF3 (50) _____ sccm; RF power (25) _____ W; Pressure (open valve ~8.4) _____ ubar

Etch rates: SiN ~ 18.8 nm/min; Resist ~ 5.5 nm/min; Selectivity ~ 3.4

Resist strip: Etch time (120) _______ sec

O_2 (20) _____ sccm; RF power (25) _____ W; Pressure (50) _____ ubar

Etch rate ~ 70nm/min

STS ICP tool: Chlorine based etch at elevated temperature : Etch time (60) _______ sec

Use heat conducting grease and seasoning of etch chamber for 5 min

Etch gas chemistry: Cl_2 (7) _____ sccm / N_2 (2) _____ sccm / Ar (21) _____ sccm

Pressure (2) ____ mTorr; Temp. (190) _____ °C

ICP power (800) _____ W; RF power (50) _____ W -> bias voltage (300) _____ V

Etch rates: EPI ~ 450 nm/min; SiN ~ 25 nm/min => Selectivity ~ 18 (depends on feature size)

Clean substrate from conducting grease with ethanol by gently wiping it off with a swipe and thorough rinsing

DI rinse immediately after chlorine based etches for (5) _____ min

Step 4: Wet etch processing and Critical Point Drying (CPD)

Date: ______________

[Optional] Hard mask strip (see process modifications)

RIE F2 tool: Fluorine based etch chemistry: Etch time (3) _______ min

Etch gas chemistry: CHF_3 (50) _____ sccm / CF_4 (50) _____ sccm

RF power (25) _____ W -> bias voltage (-405) ______ V; Pressure (open valve ~ 8.3) _____ ubar

Etch rates: SiN ~ 18.8 nm/min; Resist ~ 5.5 nm/min; Selectivity ~ 3.4

Organic residue clean and hydrophilic suface preparation: Etch time (60) _______ sec

O_2 (20) _____ sccm; RF power (25) _____ W; Pressure (50) _____ ubar

Etch rate ~ 180nm/min

Surface preparation right before wet processing!

Sacraficial Layer Removal I [Selective AlGaAs etch]: Etch rate dependence on high and low stress!

1% HF solution: (800ml:17ml - DI:48% HF) _______ min for _______ um membrane dimensions

rinse in heated DI at (80) _____ °C for (5) ______ min; (2x)

Sacraficial Layer Removal II [Non-Selective AlGaAs and GaAs]

H_3PO_4:H_2O_2:DI (1:5:15): etch rate ~ 1.4 um/min

Cleaning of by-products / salts from HF etch and 1nm GaAs layer removal by digital etching

30% KOH [200g in 466ml DI] (140) ______ sec

pure H_2O_2 for (30) ______ sec

Rinse in DI (2x) water for (3) _____ min

30% KOH [200g in 466ml DI] (140) ______ sec

Hot DI rinse (2x) at (80) _____ °C for (5) _____ min

Critical Point Dryer: DI (2x) → IPA (2x) → (ultra pure IPA)

Step 5: SiN deposition (AR coating) [for the sake of completeness, TBD]

Date: ______________

PECVD I: target **silicon nitride** thickness (xxx) _______ nm for (xxx) _______ min in total

Standard recipe: **LS Nitride** - grow rate ~ 14 nm/min

Consistency check: Nitride thickness of _____ nm (100 nm) should give a _________ colour (blue….)

Considerations:

1) Protect SiN backside AR coating with Germanium (H_2O_2 or XeF_2 works for stripping)

2) Protect SiN backside AR coating with Silicon (removal with XeF_2 or SF_6)

Advantageous, since in gas phase so no plasma needed and AlGaAs might be passivated

D

III-V WAFER DESIGNS

Here, I present the designed wafers used to study single membranes and double-membrane arrays monolithically integrated on top of a DBR. The epitaxial wafer structures presented here were used in Chapter 6 with the ultimate goal of reaching enhanced coupling strength and measurement rates for a multi-element optomechanical system with respect to the single membrane case. The designs incorporate a high-reflectivity distributed Bragg reflector (DBR) with a transmission in the few ppm range, consisting of 41.5 periods of quarter-wave (Al)GaAs layers (marked in light blue). Device layers are color-coded in purple, sacrificial layers in green and dark blue. Additionally, the refractive index of each material layer is given for room and cryogenic temperatures.

Deviating from the simulated cavity configuration, we opted for thinner sacrificial layers of only λ for the bottom and $\lambda/4$ for the upper sacrificial layer, respectively. In addition, a 1 nm thick GaAs is added as a cap layer in order to ensure high quality film growth for the InGaP membranes. It shall further be noted that we initially aimed for single-sided operation in our cavity where we detect the cavity-interacted light in reflection. We therefore designed the DBR of very low transmittance of nominally only 4 ppm on the order of scattering and absorption.

Presented here are the designs for two epitaxial wafers of the first generation for both low and high strain InGaP device layers, only differing in the In content of 47 % and 41 %, respectively.

41.5 period GaAs/AlGaAs DBR with double InGaP membrane

V2: Low Strain Membrane, optimized for LT performance @ 1064.5 nm

layer #	**repeat**	**Al content**	**In content**	**description**	**thickness (nm)**	**index (300 K)**	**index (~10K)**	**comments**
0	1	0.00	--	GaAs substrate	tbd	3.48041	3.41729	
1	1	0.00	--	GaAs Buffer layer	--	3.48041	3.41729	
2	1	0.92	--	AlGaAs	272	2.97717	2.944	etch stop
3	1	0.00	--	GaAs	78.0	3.48041	3.41729	quarter wave
4	41	0.92	--	AlGaAs	90.6	2.97717	2.944	DBR layers
5		0.00	--	GaAs	78.0	3.48041	3.41729	--
6	1	0.92	--	AlGaAs	1065.3	2.97717	2.944	sacrificial layer
7	1	0.00	--	GaAs	1.0	3.48041	3.41729	GaAs cap
8	1	--	0.47	InGaP	85.5	3.2196	3.1134	membrane
9	1	0.00	--	GaAs	1.0	3.48041	3.41729	GaAs cap
10	1	0.92	--	AlGaAs	264.6	2.97717	2.944	sacrificial layer
11	1	0.00	--	GaAs	1.0	3.48041	3.41729	GaAs cap
12	1	--	0.47	InGaP	85.5	3.2196	3.1134	membrane
13	1	0.00	--	GaAs	1.0	3.48041	3.41729	GaAs cap

Total thick. (w/o) buffer	8767.5	nanometers

Requirements:

1) Please maintain thickness error to below 0.5%, particularly for InGaP and AlGaAs sacrificial layers

2) all layers UID, ideal background doping below 10^15 cm^3

3) RMS roughness below 2 Ang (for an AFM scan window of 10 µm x 10 µm)

4) composition control - ideally within 1%

41.5 period GaAs/AlGaAs DBR with double InGaP membrane
V1: High Strain Membrane, optimized for LT performance @ 1064.5 nm

layer #	repeat	Al content	In content	description	thickness (nm)	index (300 K)	index (~10K)	comments
0	1	0.00	--	GaAs substrate	tbd	3.48041	3.41729	
1	1	0.00	--	GaAs Buffer layer	--	3.48041	3.41729	
2	1	0.92	--	AlGaAs	272	2.97717	2.944	etch stop
3	1	0.00	--	GaAs	78.0	3.48041	3.41729	quarter wave
4	41	0.92	--	AlGaAs	90.6	2.97717	2.944	DBR layers
5		0.00	--	GaAs	78.0	3.48041	3.41729	--
6	1	0.92	--	AlGaAs	1065.3	2.97717	2.944	sacrificial layer
7	1	0.00	--	GaAs	1.0	3.48041	3.41729	GaAs cap
8	1	--	0.41	InGaP	85.9	3.2078	3.1002	membrane
9	1	0.00	--	GaAs	1.0	3.48041	3.41729	GaAs cap
10	1	0.92	--	AlGaAs	264.6	2.97717	2.944	sacrificial layer
11	1	0.00	--	GaAs	1.0	3.48041	3.41729	GaAs cap
12	1	--	0.41	InGaP	85.9	3.2078	3.1002	membrane
13	1	0.00	--	GaAs	1.0	3.48041	3.41729	GaAs cap

Total thick. (w/o) buffer 8768.3 nanometers

Requirements:
1) Please maintain thickness error to below 0.5%, particularly for InGaP and AlGaAs sacrificial layers
2) all layers UID, ideal background doping below 10^15 cm^3
3) RMS roughness below 2 Ang (for an AFM scan window of 10 µm x 10 µm)
4) composition control - ideally within 1%

BIBLIOGRAPHY

[1] Martin A Afromowitz. “Refractive index of Ga1-xAlxAs.” In: *Solid State Communications* 15.1 (1974), pp. 59–63. ISSN: 00381098. DOI: 10.1016/0038-1098(74)90014-3.

[2] Mario N. Armenise, Carlo E. Campanella, Caterina Ciminelli, Francesco Dell’Olio, and Vittorio M.N. Passaro. “Phononic and photonic band gap structures: Modelling and applications.” In: *Physics Procedia* 3.1 (2010), pp. 357–364. ISSN: 18753892. DOI: 10.1016/j.phpro.2010.01.047. URL: http://dx.doi.org/10.1016/j.phpro.2010.01.047.

[3] A Arokiasamy. “Simulation of vibrations of rectangular and square membranes using computer graphics.” In: *Simulation Modelling Practice and Theory* 10.1-2 (2002), pp. 3–12. ISSN: 1569190X. DOI: 10.1016/S1569-190X(02)00101-6. URL: www.elsevier.com/locate/simpat.

[4] M. Aspelmeyer, T. J. Kippenberg, and F. Marquardt. “Cavity optomechanics.” In: *Rev. Mod. Phys.* 86 (2014), p. 1391. DOI: 10.1103/RevModPhys.86.1391.

[5] Markus Aspelmeyer, Tobias J. Kippenberg, and Florian Marquardt. *Cavity optomechanics: Nano- and micromechanical resonators interacting with light*. Ed. by Markus Aspelmeyer, Tobias J. Kippenberg, and Florian Marquardt. Berlin, Heidelberg: Springer Berlin Heidelberg, 2014, pp. 1–357. ISBN: 9783642553127. DOI: 10.1007/978-3-642-55312-7. URL: http://link.springer.com/10.1007/978-3-642-55312-7.

[6] Andreas Barg, Leonardo Midolo, Gabija Kiršanske, Petru Tighineanu, Tommaso Pregnolato, Ataç Imamolu, Peter Lodahl, Albert Schliesser, Søren Stobbe, and Eugene S. Polzik. “Carrier-mediated optomechanical forces in semiconductor nanomembranes with coupled quantum wells.” In: *Physical Review B* 94.15 (2018), pp. 1–9. ISSN: 24699969. DOI: 10.1103/PhysRevB.98.155316. arXiv: 1708.05885.

[7] Mohammad J Bereyhi, Alberto Beccari, Sergey A Fedorov, Amir H Ghadimi, Ryan Schilling, Dalziel J Wilson, Nils J Engelsen, and Tobias J Kippenberg. “Clamp-Tapering Increases the Quality Factor of Stressed Nanobeams.” In: *Nano Letters* 19.4 (2019), pp. 2329–2333. ISSN: 15306992. DOI: 10.1021/acs.nanolett.8b04942. URL: https://pubs.acs.org/doi/10.1021/acs.nanolett.8b04942..

[8] M. Bhattacharya and P. Meystre. "Multiple membrane cavity optomechanics." In: *Phys. Rev. A* 78 (4 Oct. 2008), p. 041801. DOI: `10.1103/PhysRevA.78.041801`. URL: `https://link.aps.org/doi/10.1103/PhysRevA.78.041801`.

[9] Ferdinand Brennecke, Stephan Ritter, Tobias Donner, and Tilman Esslinger. "Cavity Optomechanics with a Bose-Einstein Condensate." In: *Science* 322.5899 (2008), pp. 235–238. ISSN: 0036-8075. DOI: `10.1126/science.1163218`. URL: `http://science.sciencemag.org/content/322/5899/235`.

[10] Daniel W.C. Brooks, Thierry Botter, Sydney Schreppler, Thomas P. Purdy, Nathan Brahms, and Dan M. Stamper-Kurn. "Nonclassical light generated by quantum-noise-driven cavity optomechanics." In: *Nature* 488.7412 (Aug. 2012), pp. 476–480. ISSN: 00280836. DOI: `10.1038/nature11325`. URL: `http://www.nature.com/articles/nature11325`.

[11] Maximilian Bückle, Valentin C. Hauber, Garrett D. Cole, Claus Gärtner, Ute Zeimer, Jörg Grenzer, and Eva M. Weig. "Stress control of tensile-strained In1-xGaxP nanomechanical string resonators." In: *Applied Physics Letters* 113.20 (Nov. 2018), p. 201903. ISSN: 00036951. DOI: `10.1063/1.5054076`. URL: `http://aip.scitation.org/doi/10.1063/1.5054076`.

[12] Steven J Byrnes. "Multilayer optical calculations." In: (2016). arXiv: `1603.02720`. URL: `https://pypi.python.org/pypi/tmm.%20http://arxiv.org/abs/1603.02720`.

[13] Jasper Chan, T. P. Mayer Alegre, Amir H. Safavi-Naeini, Jeff T. Hill, Alex Krause, Simon Gröblacher, Markus Aspelmeyer, Oskar Painter, Simon Groeblacher, Markus Aspelmeyer, and Oskar Painter. "Laser cooling of a nanomechanical oscillator into its quantum ground state." In: *Nature* 478.7367 (Oct. 2011), pp. 89–92. ISSN: 1476-4687. DOI: `10.1038/nature10461`. arXiv: `1106.3614`. URL: `http://arxiv.org/abs/1106.3614%20http://www.ncbi.nlm.nih.gov/pubmed/21979049`.

[14] Jasper Chan, T. P.Mayer Alegre, Amir H. Safavi-Naeini, Jeff T. Hill, Alex Krause, Simon Gröblacher, Markus Aspelmeyer, and Oskar Painter. "Laser cooling of a nanomechanical oscillator into its quantum ground state." In: *Nature* 478.7367 (Oct. 2011), pp. 89–92. ISSN: 00280836. DOI: `10.1038/nature10461`. arXiv: `1106.3614`.

[15] Jasper Chan, Matt Eichenfield, Ryan Camacho, and Oskar Painter. "Optical and mechanical design of a "zipper" photonic crystal optomechanical cavity." In: 17.5 (2008), pp. 555–560. ISSN: 1094-4087. DOI: `10.1364/OE.17.003802`. arXiv: `0812.4683`. URL: `http://arxiv.org/abs/0812.4683%7B%5C%%7D0Ahttp://dx.doi.org/10.1364/OE.17.003802`.

[16] Jasper Chan, Amir H. Safavi-Naeini, Jeff T. Hill, Seán Meenehan, and Oskar Painter. "Optimized optomechanical crystal cavity with acoustic radiation shield." In: *Applied Physics Letters* 101.8 (2012). ISSN: 00036951. DOI: 10.1063/1.4747726. arXiv: 1206.2099.

[17] X. Chen, C. Chardin, K. Makles, C. Caër, S. Chua, R. Braive, I. Robert-Philip, T. Briant, P.-F. Cohadon, A. Heidmann, T. Jacqmin, and S. Deléglise. "High-finesse Fabry-Perot cavities with bidimensional Si_3N_4 photonic-crystal slabs." In: *Light Sci. Appl.* 6 (2017), e16190. DOI: 10.1038/lsa.2016.190.

[18] Cheng Wei Cheng, Kuen Ting Shiu, Ning Li, Shu Jen Han, Leathen Shi, and Devendra K. Sadana. "Epitaxial lift-off process for gallium arsenide substrate reuse and flexible electronics." In: *Nature Communications* 4 (2013), p. 1577. ISSN: 20411723. DOI: 10.1038/ncomms2583. URL: http://dx.doi.org/10.1038/ncomms2583.

[19] Wen Hsien Chuang, Thomas Luger, Rainer K Fettig, and Reza Ghodssi. "Mechanical property characterization of LPCVD silicon nitride thin films at cryogenic temperatures." In: *Journal of Microelectromechanical Systems* 13.5 (2004), pp. 870–879. ISSN: 10577157. DOI: 10.1109/JMEMS.2004.836815. URL: http://www.umdmsal.com/sites/default/files/publications/2004/2004-130.Chuang-JMEMS-UMD.pdf.

[20] Martijn A Cohen. *Optomechanics in a 3D microwave cavity*. 2019.

[21] Garrett D. Cole, Pen Li Yu, Claus Gärtner, Karoline Siquans, Ramon Moghadas Nia, Jonas Schmöle, Jason Hoelscher-Obermaier, Thomas P. Purdy, Witlef Wieczorek, Cindy A. Regal, and Markus Aspelmeyer. "Tensile-strained InxGa1-xP membranes for cavity optomechanics." In: *Applied Physics Letters* 104.20 (May 2014), p. 201908. ISSN: 00036951. DOI: 10.1063/1.4879755. URL: http://aip.scitation.org/doi/10.1063/1.4879755.

[22] Garrett D. Cole, Wei Zhang, Michael J. Martin, Jun Ye, and Markus Aspelmeyer. "Tenfold reduction of Brownian noise in high-reflectivity optical coatings." In: *Nature Photonics* 7.8 (July 2013), pp. 644–650. ISSN: 17494885. DOI: 10.1038/nphoton.2013.174. URL: http://www.nature.com/doifinder/10.1038/nphoton.2013.174.

[23] Garrett D Cole, Simon Gröblacher, Katharina Gugler, Sylvain Gigan, and Markus Aspelmeyer. "Monocrystalline Alx Ga1-x As heterostructures for high-reflectivity high- Q micromechanical resonators in the megahertz regime." In: *Applied Physics Letters* 92.26 (2008), p. 261108. ISSN: 00036951. DOI: 10.1063/1.2952512. URL: https://doi.org/10.1063/1.2952512.

[24] J. M. Dallesasse and N. Holonyak. “Oxidation of Al-bearing III-V materials: A review of key progress.” In: *Journal of Applied Physics* 113.5 (2013). ISSN: 00218979. DOI: 10.1063/1.4769968.

[25] Uroš Delić, Manuel Reisenbauer, Kahan Dare, David Grass, Vladan Vuletić, Nikolai Kiesel, and Markus Aspelmeyer. “Motional Quantum Ground State of a Levitated Nanoparticle from Room Temperature.” In: (Nov. 2019). arXiv: 1911.04406. URL: http://arxiv.org/abs/1911.04406.

[26] Gregory C. DeSalvo. “Wet Chemical Digital Etching of GaAs at Room Temperature.” In: *Journal of The Electrochemical Society* 143.11 (2006), p. 3652. ISSN: 00134651. DOI: 10.1149/1.1837266. URL: https://corescholar.libraries.wright.edu/physics/682.

[27] Vincent Dumont, Simon Bernard, Christoph Reinhardt, Alex Kato, Maximilian Ruf, and Jack C. Sankey. *Flexure-Tuned Membrane-at-the-Edge Optomechanical System*. Tech. rep. 2019. arXiv: 1905.04594. URL: http://arxiv.org/abs/1905.04594.

[28] S. A. Fedorov, A. H. Ghadimi, R. Schilling, T. J. Kippenberg, N. J. Engelsen, D. J. Wilson, and M. J. Bereyhi. “Elastic strain engineering for ultralow mechanical dissipation.” In: *Science* 360.6390 (May 2018), pp. 764–768. ISSN: 0036-8075. DOI: 10.1126/science.aar6939. URL: http://science.sciencemag.org/content/360/6390/764/tab-pdf%20http://www.ncbi.nlm.nih.gov/pubmed/29650701%20www.sciencemag.org/cgi/content/full/science.aar6939/DC1.

[29] Moritz Forsch, Robert Stockill, Andreas Wallucks, Igor Marinković, Claus Gärtner, Richard A. Norte, Frank van Otten, Andrea Fiore, Kartik Srinivasan, and Simon Gröblacher. “Microwave-to-optics conversion using a mechanical oscillator in its quantum ground state.” In: *Nature Physics* (Oct. 2019), pp. 1–6. ISSN: 1745-2473. DOI: 10.1038/s41567-019-0673-7. arXiv: 1812.07588.

[30] Claus Gärtner, João P. Moura, Wouter Haaxman, Richard A. Norte, and Simon Gröblacher. “Integrated Optomechanical Arrays of Two High Reflectivity SiN Membranes.” In: *Nano Letters* 18.11 (Nov. 2018), pp. 7171–7175. ISSN: 1530-6984. DOI: 10.1021/acs.nanolett.8b03240. arXiv: 1809.06372. URL: http://pubs.acs.org/doi/10.1021/acs.nanolett.8b03240.

[31] A H Ghadimi, S A Fedorov, N J Engelsen, M J Bereyhi, R Schilling, D J Wilson, and T J Kippenberg. “Elastic strain engineering for ultralow mechanical dissipation.” In: *Science* 360.6390 (May 2018), pp. 764–768. ISSN: 10959203. DOI: 10.1126/science.aar6939. URL: http://www.ncbi.nlm.nih.gov/pubmed/29650701.

[32] Robert D. Gould, Safa Kasap, and Asim K. Ray. “Thin Films.” In: *Springer Handbook of Electronic and Photonic Materials*. Cham: Springer International Publishing, 2017, pp. 1–1. DOI: 10.1007/978-3-319-48933-9_28. URL: http://link.springer.com/10.1007/978-3-319-48933-9%7B%5C_%7D28.

[33] Simon Gröblacher, Klemens Hammerer, Michael R Vanner, and Markus Aspelmeyer. “Observation of strong coupling between a micromechanical resonator and an optical cavity field.” In: *Nature* 460.7256 (Aug. 2009), pp. 724–7. ISSN: 1476-4687. DOI: 10.1038/nature08171. arXiv: 0903.5293. URL: http://www.ncbi.nlm.nih.gov/pubmed/19661913.

[34] Simon Gröblacher, Jared B. Hertzberg, Michael R. Vanner, Garrett D. Cole, Sylvain Gigan, K. C. Schwab, and Markus Aspelmeyer. “Demonstration of an ultracold micro-optomechanical oscillator in a cryogenic cavity.” In: *Nature Physics* 5.7 (June 2009), pp. 485–488. ISSN: 1745-2473. DOI: 10.1038/nphys1301. URL: http://www.nature.com/doifinder/10.1038/nphys1301.

[35] M. Gross, C. Fabre, P. Pillet, and S. Haroche. “Observation of Near-Infrared Dicke Superradiance on Cascading Transitions in Atomic Sodium.” In: *Phys. Rev. Lett.* 36 (1976), p. 1035. DOI: 10.1103/PhysRevLett.36.1035.

[36] J. Guo, R. A. Norte, and S. Gröblacher. “Integrated optical force sensors using focusing photonic crystal arrays.” In: *Opt. Express* 25.8 (2017), pp. 9196–9203. DOI: 10.1364/OE.25.009196. URL: http://www.opticsexpress.org/abstract.cfm?URI=oe-25-8-9196.

[37] Jingkun Guo, Richard A. Norte, and Simon Gröblacher. “Feedback cooling of a room temperature mechanical oscillator close to its motional groundstate.” In: (Nov. 2019). ISSN: 10797114. DOI: 10.1103/PhysRevLett.123.223602. arXiv: 1911.01586. URL: http://arxiv.org/abs/1911.01586.

[38] C. Gut, K. Winkler, J. Hoelscher-Obermaier, S. G. Hofer, R. Moghadas Nia, N. Walk, A. Steffens, J. Eisert, W. Wieczorek, J. A. Slater, M. Aspelmeyer, and K. Hammerer. “Stationary optomechanical entanglement between a mechanical oscillator and its measurement apparatus.” In: (Dec. 2019). arXiv: 1912.01635. URL: http://arxiv.org/abs/1912.01635.

[39] Michael J. Hartmann and Martin B. Plenio. “Steady State Entanglement in the Mechanical Vibrations of Two Dielectric Membranes.” In: *Phys. Rev. Lett.* 101 (20 Nov. 2008), p. 200503. DOI: 10.1103/PhysRevLett.101.200503. URL: https://link.aps.org/doi/10.1103/PhysRevLett.101.200503.

[40] K. Hennessy, A. Badolato, A. Tamboli, P. M. Petroff, E. Hu, M. Atatüre, J. Dreiser, and A. Imamoğlu. "Tuning photonic crystal nanocavity modes by wet chemical digital etching." In: *Applied Physics Letters* 87.2 (2005). ISSN: 00036951. DOI: `10.1063/1.1992656`. URL: `https://aipscitation-org.uaccess.univie.ac.at/doi/pdf/10.1063/1.1992656?class=pdf`.

[41] A. P. Higginbotham, P. S. Burns, M. D. Urmey, R. W. Peterson, N. S. Kampel, B. M. Brubaker, G. Smith, K. W. Lehnert, and C. A. Regal. "Harnessing electro-optic correlations in an efficient mechanical converter." In: *Nature Physics* 14.10 (Oct. 2018), pp. 1038–1042. ISSN: 17452481. DOI: `10.1038/s41567-018-0210-0`. arXiv: `1712.06535`.

[42] Jason Hoelscher-Obermaier. "Generation and Detection of Quantum Entanglement in Optomechanical Systems." PhD thesis. 2017.

[43] Sebastian G. Hofer and Klemens Hammerer. "Quantum Control of Optomechanical Systems." In: *Advances in Atomic, Molecular and Optical Physics*. Vol. 66. 2017, pp. 263–374. DOI: `10.1016/bs.aamop.2017.03.003`. URL: `http://dx.doi.org/10.1016/bs.aamop.2017.03.003`.

[44] Sebastian G Hofer, Witlef Wieczorek, Markus Aspelmeyer, and Klemens Hammerer. "Quantum entanglement and teleportation in pulsed cavity optomechanics." In: *Physical Review A - Atomic, Molecular, and Optical Physics* 84.5 (2011), p. 52327. ISSN: 10502947. DOI: `10.1103/PhysRevA.84.052327`. URL: `https://journals-aps-org.uaccess.univie.ac.at/pra/pdf/10.1103/PhysRevA.84.052327`.

[45] S. Hong, R. Riedinger, I. Marinković, A. Wallucks, S. G. Hofer, R. A. Norte, M. Aspelmeyer, and S. Gröblacher. "Hanbury Brown and Twiss interferometry of single phonons from an optomechanical resonator." In: *Science* 358 (2017), pp. 203–206. DOI: `10.1126/science.aan7939`.

[46] F Y Huang. "Theory of strain relaxation for epitaxial layers grown on substrate of a finite dimension." In: *Physical Review Letters* 85.4 (2000), pp. 784–787. ISSN: 00319007. DOI: `10.1103/PhysRevLett.85.784`. URL: `https://journals.aps.org/prl/pdf/10.1103/PhysRevLett.85.784`.

[47] Matthias Imboden and Pritiraj Mohanty. *Dissipation in nanoelectromechanical systems*. 2014. DOI: `10.1016/j.physrep.2013.09.003`. URL: `http://dx.doi.org/10.1016/j.physrep.2013.09.003`.

[48] IOFFE Inst. *NSM Archive - Physical Properties of Semiconductors*. 2015. URL: `http://www.matprop.ru/semicond` (visited on 08/13/2019).

[49] A. M. Jayich, J. C. Sankey, B. M. Zwickl, C. Yang, J. D. Thompson, S. M. Girvin, A. A. Clerk, F. Marquardt, and J. G.E. Harris. "Dispersive optomechanics: A membrane inside a cavity." In: *New Journal of Physics* 10 (2008). ISSN: 13672630. DOI: 10.1088/1367-2630/10/9/095008. URL: http://www.njp.org/.

[50] John D. Joannopoulos, Steven G. Johnson, Joshua N. Winn, and Robert D. Meade. *Photonic Crystals: Molding the Flow of Light (Second Edition)*. 2nd ed. Princeton University Press, 2008. ISBN: 0691124566.

[51] Surabhi Joshi, Sherman Hung, and Srikar Vengallatore. "Design strategies for controlling damping in micromechanical and nanomechanical resonators." In: *EPJ Techniques and Instrumentation* 1.1 (Dec. 2014), p. 5. ISSN: 2195-7045. DOI: 10.1140/epjti5. URL: http://epjtechniquesandinstrumentation.springeropen.com/articles/10.1186/epjti5.

[52] Nikolai Kiesel, Florian Blaser, Uroš Delić, David Grass, Rainer Kaltenbaek, and Markus Aspelmeyer. "Cavity cooling of an optically levitated submicron particle." In: *Proceedings of the National Academy of Sciences of the United States of America* 110.35 (Aug. 2013), pp. 14180–14185. ISSN: 00278424. DOI: 10.1073/pnas.1309167110. arXiv: 1304.6679.

[53] T. Kipf and G. S. Agarwal. "Superradiance and collective gain in multimode optomechanics." In: *Phys. Rev. A* 90 (2014), p. 053808. DOI: 10.1103/PhysRevA.90.053808.

[54] T. J. Kippenberg, S. M. Spillane, and K. J. Vahala. "Demonstration of ultra-high- Q small mode volume toroid microcavities on a chip." In: *Applied Physics Letters* 85.25 (2004), pp. 6113–6115. ISSN: 00036951. DOI: 10.1063/1.1833556. arXiv: 0412042 [physics].

[55] Dustin Kleckner, Brian Pepper, Evan Jeffrey, Petro Sonin, Susanna M. Thon, and Dirk Bouwmeester. "Optomechanical trampoline resonators." In: *Optics Express* 19.20 (Sept. 2011), p. 19708. ISSN: 1094-4087. DOI: 10.1364/oe.19.019708. URL: https://www.osapublishing.org/oe/abstract.cfm?uri=oe-19-20-19708.

[56] J. W. Lee, S. J. Pearton, C. R. Abernathy, W. S. Hobson, F. Ren, and C. S. Wu. "Investigation of wet etching solutions for In0.5Ga0.5P." In: *Solid State Electronics* 38.11 (1995), pp. 1871–1874. ISSN: 00381101. DOI: 10.1016/0038-1101(95)00012-I.

[57] Y.-S. Lee, M. DeVre, D. Lishan, and R. Westerman. *Smooth, anisotropic etching of indium containing structures using a high density ICP system*. Tech. rep. 2003, pp. 78–79. DOI: 10.1109/iciprm.2003.1205316. URL: https://csmantech.org/OldSite/Digests/2003/2003PDF/8-16.pdf.

[58] Rick Leijssen, Giada R. La Gala, Lars Freisem, Juha T. Muhonen, and Ewold Verhagen. “Nonlinear cavity optomechanics with nanomechanical thermal fluctuations.” In: *Nat. Commun.* 8 (2017), p. 16024. DOI: `10.1038/ncomms16024`.

[59] M Levinshtein, S Rumyantsev, and M Shur. *Handbook Series on Semiconductor Parameters*. Vol. 2. WORLD SCIENTIFIC, Nov. 1996. ISBN: 978-981-02-2935-1. DOI: `10.1142/2046-vol2`. URL: `https://www.worldscientific.com/worldscibooks/10.1142/2046-vol1%20https://www.worldscientific.com/worldscibooks/10.1142/2046-vol2`.

[60] Jie Li, André Xuereb, Nicola Malossi, and David Vitali. “Cavity mode frequencies and strong optomechanical coupling in two-membrane cavity optomechanics.” In: *J. Opt.* 18.8 (2016), p. 084001. DOI: `10.1088/2040-8978/18/8/084001`.

[61] LIGO Scientific Collaboration. “Observation of a kilogram-scale oscillator near its quantum ground state.” In: *New Journal of Physics* 11 (2009), p. 073032. ISSN: 1367-2630. DOI: `10.1088/1367-2630/11/7/073032`.

[62] J. Liu, K. Usami, A. Naesby, T. Bagci, E. S. Polzik, P. Lodahl, and S. Stobbe. “High-Q optomechanical GaAs nanomembranes.” In: *Applied Physics Letters* 99.24 (2011), p. 243102. ISSN: 00036951. DOI: `10.1063/1.3668092`. URL: `https://doi.org/10.1063/1.3668092`.

[63] Victor Liu and Shanhui Fan. “S^4 : A free electromagnetic solver for layered periodic structures.” In: *Comput. Phys. Commun.* 183.10 (2012), pp. 2233–2244. ISSN: 0010-4655. DOI: `10.1016/j.cpc.2012.04.026`. URL: `http://www.sciencedirect.com/science/article/pii/S0010465512001658`.

[64] J.W. Matthews and A.E. Blakeslee. “Defects in epitaxial multilayers.” In: *Journal of Crystal Growth* 27 (Dec. 2007), pp. 118–125. ISSN: 00220248. DOI: `10.1016/s0022-0248(74)80055-2`. URL: `https://www.sciencedirect.com/science/article/pii/S0022024874800552`.

[65] L. Midolo, T. Pregnolato, G. Kiršanske, and S. Stobbe. “Softmask fabrication of gallium arsenide nanomembranes for integrated quantum photonics.” In: *Nanotechnology* 26.48 (2015). ISSN: 13616528. DOI: `10.1088/0957-4484/26/48/484002`. arXiv: `arXiv:1506.00376v1`. URL: `https://iopscience-iop-org.uaccess.univie.ac.at/article/10.1088/0957-4484/26/48/484002/pdf`.

[66] Jonathan Moghal, Johannes Kobler, Jürgen Sauer, James Best, Martin Gardener, Andrew A.R. Watt, and Gareth Wakefield. “High-performance, single-layer antireflective optical coatings comprising mesoporous silica nanoparticles.” In: *ACS Applied*

Materials and Interfaces 4.2 (2012), pp. 854–859. ISSN: 19448244. DOI: `10.1021/am201494m`.

[67] João P. Moura. “Making light jump - Photonic crystals on trampoline membranes for optomechanics experiments.” PhD thesis. 2019. ISBN: 9789085933908.

[68] João P. Moura, Richard A. Norte, Jingkun Guo, Clemens Schäfermeier, and Simon Gröblacher. “Centimeter-scale suspended photonic crystal mirrors.” In: *Opt. Express* 26 (2018), pp. 1895–1909.

[69] A. Naesby and A. R. Dantan. “Microcavities with suspended subwavelength structured mirrors.” In: *arxiv:1804.00909* (2018).

[70] B. Nair, A. Naesby, and A. Dantan. “Optomechanical characterization of silicon nitride membrane arrays.” In: *Opt. Lett.* 42.7 (Apr. 2017), pp. 1341–1344. DOI: `10.1364/OL.42.001341`. URL: `http://ol.osa.org/abstract.cfm?URI=ol-42-7-1341`.

[71] Ramon Moghadas Nia. “Multimode optomechanics in the strong cooperativity regime: towards optomechanical entanglement with micromechanical membranes.” PhD thesis. 2018.

[72] William H. P. Nielsen, Yeghishe Tsaturyan, Christoffer B. Møller, Eugene S Polzik, and Albert Schliesser. “Multimode optomechanical system in the quantum regime.” In: 114.1 (2016), pp. 62–66. DOI: `10.1073/pnas.1608412114`. arXiv: `1605.06541`.

[73] R. A. Norte, J. P. Moura, and S. Gröblacher. “Mechanical Resonators for Quantum Optomechanics Experiments at Room Temperature.” In: *Phys. Rev. Lett.* 116 (2016), p. 147202. DOI: `10.1103/PhysRevLett.116.147202`.

[74] Richard A. Norte. “Nanofabrication for On-Chip Optical Levitation, Atom-Trapping, and Superconducting Quantum Circuits.” PhD thesis. 2015.

[75] A. D. O’Connell, M. Hofheinz, M. Ansmann, Radoslaw C. Bialczak, M. Lenander, Erik Lucero, M. Neeley, D. Sank, H. Wang, M. Weides, J. Wenner, John M. Martinis, and A. N. Cleland. “Quantum ground state and single-phonon control of a mechanical resonator.” In: *Nature* 464 (2010), pp. 697–703. DOI: `10.1038/nature08967`.

[76] T a Palomaki, J D Teufel, R W Simmonds, and K W Lehnert. “Entangling Mechanical Motion with Microwave Fields.” In: *Science (New York, N.Y.)* October (May 2013). ISSN: 0031-899X. DOI: `10.1126/science.1244563`. URL: `http://www.ncbi.nlm.nih.gov/pubmed/24091706`.

[77] John S. Parker, Erik J. Norberg, Robert S. Guzzon, Steven C. Nicholes, and Larry A. Coldren. “High verticality InP/InGaAsP etching in Cl2/H2/Ar inductively coupled plasma for photonic integrated circuits.” In: *Journal of Vacuum Science & Technology B, Nanotechnology and Microelectronics: Materials, Processing, Measurement, and Phenomena* 29.1 (2011), p. 011016. ISSN: 2166-2746. DOI: `10.1116/1.3522659`. URL: `https://coldren.ece.ucsb.edu/sites/coldren.ece.ucsb.edu/files/publications/parker%7B%5C_%7Dhigh%7B%5C_%7Dverticality%7B%5C_%7Dinpingaasp%7B%5C_%7Detching.pdf`.

[78] R. People and J. C. Bean. “Calculation of critical layer thickness versus lattice mismatch for GexSi1-x/Si strained-layer heterostructures.” In: *Applied Physics Letters* 47.3 (Aug. 1985), pp. 322–324. ISSN: 00036951. DOI: `10.1063/1.96206`. URL: `http://aip.scitation.org/doi/10.1063/1.96206`.

[79] Paolo Piergentili, Letizia Catalini, Mateusz Bawaj, Stefano Zippilli, Nicola Malossi, Riccardo Natali, David Vitali, and Giovanni Di Giuseppe. “Two-membrane cavity optomechanics.” In: *New J. Phys.* 20 (2018), p. 083024. DOI: `10.1088/1367-2630/aad85f`.

[80] Ullrich Pietsch, Václav Holý, and Tilo Baumbach. *High-Resolution X-Ray Scattering*. Advanced Texts in Physics. New York, NY: Springer New York, 2004. ISBN: 978-1-4419-2307-3. DOI: `10.1007/978-1-4757-4050-9`. URL: `http://link.springer.com/10.1007/978-1-4757-4050-9`.

[81] Marcel W Pruessner, Todd T King, Daniel P Kelly, Rohit Grover, Lynn C Calhoun, and Reza Ghodssi. “Mechanical property measurement of InP-based MEMS for optical communications.” In: *Sensors and Actuators, A: Physical* 105.2 (2003), pp. 190–200. ISSN: 09244247. DOI: `10.1016/S0924-4247(03)00102-X`. URL: `http://citeseerx.ist.psu.edu/viewdoc/download?doi=10.1.1.487.3870%7B%5C&%7Drep=rep1%7B%5C&%7Dtype=pdf`.

[82] C. Reinhardt, T. Müller, A. Bourassa, and J. C. Sankey. “Ultralow-Noise SiN Trampoline MEMS for Sensing and Optomechanics.” In: *Phys. Rev. X* 6 (2016), p. 021001. DOI: `10.1103/PhysRevX.6.021001`.

[83] R. Riedinger, A. Wallucks, I. Marinković, C. Löschnauer, M. Aspelmeyer, S. Hong, and S. Gröblacher. “Remote quantum entanglement between two micromechanical oscillators.” In: *Nature* 556 (2018), pp. 473–477. DOI: `10.1038/s41586-018-0036-z`.

[84] Ralf Riedinger, Sungkun Hong, Richard A Norte, Joshua A Slater, Juying Shang, Alexander G. Krause, Vikas Anant, Markus Aspelmeyer, and Simon Gröblacher. “Non-classical correlations

between single photons and phonons from a mechanical oscillator." In: *Nature* 530.7590 (2016), pp. 313–316. ISSN: 14764687. DOI: 10.1038/nature16536. URL: https://www-nature-com.uaccess.univie.ac.at/articles/nature16536.pdf.

[85] Massimiliano Rossi, David Mason, Junxin Chen, Yeghishe Tsaturyan, and Albert Schliesser. "Measurement-based quantum control of mechanical motion." In: *Nature* 563.7729 (Nov. 2018), pp. 53–58. ISSN: 14764687. DOI: 10.1038/s41586-018-0643-8. arXiv: 1805.05087. URL: http://www.nature.com/articles/s41586-018-0643-8.

[86] Sergey L Rumyantsev, Michael Shur, M. E. (Mikhail Efimovich) Levinshteĭn, and World Scientific (Firm). *Handbook series on semiconductor parameters. Vol. 2, Ternary and quaternary III-V compounds*. English. Includes bibliographical references. Singapore, London : World Scientific, 1999. ISBN: 9789812832085. URL: http://www.vlebooks.com/vleweb/product/openreader?id=none&isbn=9789812832085.

[87] Pedram Sadeghi, Manuel Tanzer, Simon L Christensen, and Silvan Schmid. "Influence of clamp-widening on the quality factor of nanomechanical silicon nitride resonators." In: (2019). arXiv: 1905.06730. URL: https://arxiv.org/pdf/1905.06730.pdf%20http://arxiv.org/abs/1905.06730.

[88] Amir H. Safavi-Naeini, Thiago P. Mayer Alegre, Martin Winger, and Oskar Painter. "Optomechanics in an ultrahigh-Q two-dimensional photonic crystal cavity." In: *Appl. Phys. Lett.* 97 (2010), p. 181106. URL: https://aip.scitation.org/doi/10.1063/1.3507288.

[89] Amir H. Safavi-Naeini, Simon Gröblacher, Jeff T. Hill, Jasper Chan, Markus Aspelmeyer, and Oskar Painter. "Squeezed light from a silicon micromechanical resonator." In: *Nature* 500.7461 (2013), pp. 185–189. ISSN: 00280836. DOI: 10.1038/nature12307.

[90] J. C. Sankey, C. Yang, B. M. Zwickl, A. M. Jayich, and J. G. E. Harris. "Strong and tunable nonlinear optomechanical coupling in a low-loss system." In: *Nature Phys.* 6 (2010), p. 707. URL: http://dx.doi.org/10.1038/nphys1707.

[91] Silvan Schmid, Guillermo Villanueva, and Michael Lee Roukes. "Fundamentals of Nanomechanical Resonators." In: (2016). URL: http://infoscience.epfl.ch/record/220923.

[92] Michael Schmidt, Max Ludwig, and Florian Marquardt. "Optomechanical circuits for nanomechanical continuous variable quantum state processing." In: *New J. Phys.* 14 (2012), p. 125005. DOI: 10.1088/1367-2630/14/12/125005.

[93] Keith C. Schwab and Michael L. Roukes. "Putting mechanics into quantum mechanics." In: *Physics Today* 58.7 (2005), pp. 36–42. ISSN: 00319228. DOI: 10.1063/1.2012461.

[94] A. B. Shkarin, N. E. Flowers-Jacobs, S. W. Hoch, A. D. Kashkanova, C. Deutsch, J. Reichel, and J. G.E. Harris. "Optically mediated hybridization between two mechanical modes." In: *Physical Review Letters* 112.1 (Jan. 2014). ISSN: 00319007. DOI: 10.1103/PhysRevLett.112.013602. arXiv: 1306.0613.

[95] Randy J. Shul and Stephen J. Pearton, eds. *Handbook of Advanced Plasma Processing Techniques*. Berlin, Heidelberg: Springer Berlin Heidelberg, 2000. ISBN: 978-3-642-63096-5. DOI: 10.1007/978-3-642-56989-0. URL: http://link.springer.com/10.1007/978-3-642-56989-0.

[96] A.E. Siegman. *Lasers*. University Science Books, 1986. ISBN: 9780935702118. URL: https://books.google.nl/books?id=1BZVwUZLTkAC.

[97] S. M. Spillane, T. J. Kippenberg, K. J. Vahala, K. W. Goh, E. Wilcut, and H. J. Kimble. "Ultrahigh-Q toroidal microresonators for cavity quantum electrodynamics." In: *Physical Review A - Atomic, Molecular, and Optical Physics* 71.1 (2005), pp. 1–10. ISSN: 10502947. DOI: 10.1103/PhysRevA.71.013817. arXiv: 0410218 [quant-ph].

[98] C. Stambaugh, H. Xu, U. Kemiktarak, J. Taylor, and J. Lawall. "From membrane-in-the-middle to mirror-in-the-middle with a high-reflectivity sub-wavelength grating." In: *Ann. Phys.* 527.1-2 (2015), pp. 81–88. DOI: 10.1002/andp.201400142.

[99] Dan M. Stamper-Kurn. "Cavity optomechanics with cold atoms." In: (2012). DOI: 10.1007/978-3-642-55312-7_13. arXiv: 1204.4351. URL: http://arxiv.org/abs/1204.4351.

[100] P. Strasser, R. Wüest, F. Robin, D. Erni, and H. Jäckel. "Detailed analysis of the influence of an inductively coupled plasma reactive-ion etching process on the hole depth and shape of photonic crystals in InPInGaAsP." In: *Journal of Vacuum Science & Technology B: Microelectronics and Nanometer Structures* 25.2 (2007), p. 387. ISSN: 10711023. DOI: 10.1116/1.2712198.

[101] M Strassner, J Daleiden, N Chitica, D Keiper, B Stalnacke, S Greek, and K Hjort. *III–V semiconductor material for tunable Fabry–Perot filters for coarse*. 2000. URL: www.elsevier.nlrlocatersna.

[102] Orazio Svelto. *Principles of Lasers*. Springer US, 2010. DOI: 10.1007/978-1-4419-1302-9. URL: https://doi.org/10.1007/978-1-4419-1302-9.

[103] J. D. Teufel, T. Donner, Dale Li, J. W. Harlow, M. S. Allman, K. Cicak, A. J. Sirois, J. D. Whittaker, K. W. Lehnert, and R. W. Simmonds. "Sideband cooling of micromechanical motion to the quantum ground state." In: *Nature* 475.7356 (July 2011), pp. 359–363. ISSN: 00280836. DOI: 10.1038/nature10261. arXiv: 1103.2144.

[104] JD Thompson, BM Zwickl, AM Jayich, Florian Marquardt, SM Girvin, and JGE Harris. "Strong dispersive coupling of a high-finesse cavity to a micromechanical membrane." In: *Nature* 452.7183 (2008), pp. 72–75. DOI: 10.1038/nature06715.

[105] Sofia Tönnberg. "Optimisation and characterisation of LPCVD silicon nitride thin film growth." In: *Master Thesis* (2006). URL: http://publications.lib.chalmers.se/records/fulltext/18906.pdf.

[106] Y. Tsaturyan, A. Barg, E. S. Polzik, and A. Schliesser. "Ultracoherent nanomechanical resonators via soft clamping and dissipation dilution." In: *Nature Nanotechnology* 12.8 (June 2017), pp. 776–783. ISSN: 17483395. DOI: 10.1038/nnano.2017.101. arXiv: 1608.00937. URL: http://www.nature.com/doifinder/10.1038/nnano.2017.101.

[107] Yeghishe Tsaturyan, Andreas Barg, Anders Simonsen, Luis Guillermo Villanueva, Silvan Schmid, Albert Schliesser, and Eugene S. Polzik. "Demonstration of suppressed phonon tunneling losses in phononic bandgap shielded membrane resonators for high-Q optomechanics." In: 124304.2006 (2013). DOI: 10.1364/OE.22.006810. arXiv: 1312.7776. URL: http://arxiv.org/abs/1312.7776%7B%5C%%7D0Ahttp://dx.doi.org/10.1364/OE.22.006810.

[108] J. H. Van Der Merwe. "Crystal interfaces. Part II. Finite overgrowths." In: *Journal of Applied Physics* 34.1 (Jan. 1963), pp. 123–127. ISSN: 00218979. DOI: 10.1063/1.1729051. URL: http://aip.scitation.org/doi/10.1063/1.1729051.

[109] E. Verhagen, S. Deléglise, S. Weis, A. Schliesser, and T. J. Kippenberg. "Quantum-coherent coupling of a mechanical oscillator to an optical cavity mode." In: *Nature* 482.7383 (2012), pp. 63–67. ISSN: 00280836. DOI: 10.1038/nature10787. URL: https://www-nature-com.uaccess.univie.ac.at/articles/nature10787.pdf.

[110] L G Villanueva and S Schmid. "Evidence of surface loss as ubiquitous limiting damping mechanism in SiN micro- and nanomechanical resonators." In: *Physical Review Letters* 113.22 (2014). ISSN: 10797114. DOI: 10.1103/PhysRevLett.113.227201. arXiv: 1405.6115. URL: https://journals-aps-org.uaccess.univie.ac.at/prl/pdf/10.1103/PhysRevLett.113.227201.

[111] M. M. A. J. Voncken, J. J. Schermer, A. T. J. van Niftrik, G. J. Bauhuis, P. Mulder, P. K. Larsen, T. P. J. Peters, B. de Bruin, A. Klaassen, and J. J. Kelly. "Etching AlAs with HF for Epitaxial Lift-Off Applications." In: *Journal of The Electrochemical Society* 151.5 (2004), G347. ISSN: 00134651. DOI: 10.1149/1.1690293.

[112] M. J. Weaver, F. Buters, F. Luna, H. Eerkens, K. Heeck, S. de Man, and D. Bouwmeester. "Coherent optomechanical state transfer between disparate mechanical resonators." In: *Nat. Commun.* 8 (2017), p. 824. DOI: 10.1038/s41467-017-00968-9. URL: https://doi.org/10.1038/s41467-017-00968-9.

[113] D. J. Wilson. "Cavity Optomechanics with High-Stress Silicon Nitride Films." PhD thesis. 2012, p. 217.

[114] H. Xu, D. Mason, Luyao Jiang, and J. G. E. Harris. "Topological energy transfer in an optomechanical system with exceptional points." In: *Nature* 537 (2016), pp. 80–83. DOI: 10.1038/nature18604.

[115] A. Xuereb, C. Genes, and A. Dantan. "Strong Coupling and Long-Range Collective Interactions in Optomechanical Arrays." In: *Phys. Rev. Lett.* 109 (22 Nov. 2012), p. 223601. DOI: 10.1103/PhysRevLett.109.223601.

[116] André Xuereb and Peter Domokos. "Dynamical scattering models in optomechanics: going beyond the 'coupled cavities' model." In: *New J. Phys.* 14 (2012), p. 095027. DOI: 10.1088/1367-2630/14/9/095027.

[117] P. L. Yu, K Cicak, N S Kampel, Y Tsaturyan, T P Purdy, R W Simmonds, and C A Regal. "A phononic bandgap shield for high-Q membrane microresonators." In: *Applied Physics Letters* 104.2 (2014), pp. 1–5. ISSN: 00036951. DOI: 10.1063/1.4862031. arXiv: 1312.0962.

[118] P. L. Yu, K Cicak, N S Kampel, Y Tsaturyan, T P Purdy, R W Simmonds, and C A Regal. "A phononic bandgap shield for high-Q membrane microresonators." In: *Applied Physics Letters* 104.2 (2014), p. 23510. ISSN: 00036951. DOI: 10.1063/1.4862031. URL: https://doi.org/10.1063/1.4862031.

[119] P.-L. L. Yu, T. P. Purdy, and C. A. Regal. "Control of material damping in High-Q membrane microresonators." In: *Physical Review Letters* 108.8 (Feb. 2012), p. 083603. ISSN: 10797114. DOI: 10.1103/PhysRevLett.108.083603. URL: http://link.aps.org/doi/10.1103/PhysRevLett.108.083603%20https://journals-aps-org.uaccess.univie.ac.at/prl/pdf/10.1103/PhysRevLett.108.083603%20https://journals-aps-org.uaccess.univie.ac.at/prl/supplemental/10.1103/PhysRevLett.108.083603/supplement.pdf.

[120] Mingyun Yuan, Martijn A Cohen, and Gary A Steele. "Silicon nitride membrane resonators at millikelvin temperatures with quality factors exceeding 108." In: *Applied Physics Letters* 107.26 (2015). ISSN: 00036951. DOI: 10.1063/1.4938747. URL: http://dx.doi.org/10.1063/1.4938747].

[121] Mian Zhang, Gustavo S. Wiederhecker, Sasikanth Manipatruni, Arthur Barnard, Paul McEuen, and Michal Lipson. "Synchronization of Micromechanical Oscillators Using Light." In: *Phys. Rev. Lett.* 109 (2012), p. 233906. DOI: 10.1103/PhysRevLett.109.233906.

[122] Yong Xing Zhang and Yong Jia. "Fluoride adsorption onto amorphous aluminum hydroxide: Roles of the surface acetate anions." In: *Journal of Colloid and Interface Science* 483 (2016), pp. 295–306. ISSN: 10957103. DOI: 10.1016/j.jcis.2016.08.054. URL: http://dx.doi.org/10.1016/j.jcis.2016.08.054.

[123] Weidong Zhou, Deyin Zhao, Yi Chen Shuai, Hongjun Yang, Santhad Chuwongin, Arvinder Chadha, Jung Hun Seo, Ken X. Wang, Victor Liu, Zhenqiang Ma, and Shanhui Fan. "Progress in 2D photonic crystal Fano resonance photonics." In: *Progress in Quantum Electronics* 38.1 (2014), pp. 1–74. ISSN: 00796727. DOI: 10.1016/j.pquantelec.2014.01.001. URL: http://dx.doi.org/10.1016/j.pquantelec.2014.01.001.

[124] D. Zoepfl, M. L. Juan, C. M. F. Schneider, and G. Kirchmair. "Single-photon strong cooperativity in microwave magnetomechanics." In: (Dec. 2019). arXiv: 1912.05489. URL: http://arxiv.org/abs/1912.05489.

[125] B M Zwickl, W E Shanks, A M. Jayich, C Yang, A C.Bleszynski Jayich, J D Thompson, and J. G.E. Harris. "High quality mechanical and optical properties of commercial silicon nitride membranes." In: *Applied Physics Letters* 92.10 (2008), p. 103125. ISSN: 00036951. DOI: 10.1063/1.2884191. URL: https://doi.org/10.1063/1.2884191.

COLOPHON

This document was typeset using the typographical look-and-feel `classicthesis` developed by André Miede and Ivo Pletikosić. The style was inspired by Robert Bringhurst's seminal book on typography "*The Elements of Typographic Style*". `classicthesis` is available for both LaTeX and LyX:

`https://bitbucket.org/amiede/classicthesis/`

Happy users of `classicthesis` usually send a real postcard to the author, a collection of postcards received so far is featured here:

`http://postcards.miede.de/`

Thank you very much for your feedback and contribution.

Final Version as of March 17, 2020 (classicthesis v4.6).